

Automatic Construction of Immobilisation Masks for use in  
Radiotherapy Treatment of Head-and-Neck Cancer

Mohammad Hashem Odeh Ryalat

A thesis submitted for the degree of  
Doctor of Philosophy  
at the University of East Anglia  
April 2017

Automatic Construction of Immobilisation Masks for use in  
Radiotherapy Treatment of Head-and-Neck Cancer

Mohammad Hashem Odeh Ryalat

© This copy of the thesis has been supplied on condition that anyone who consults it is understood to recognise that its copyright rests with the author and that no quotation from the thesis, nor any information derived therefrom, may be published without the author's prior, written consent.

# Abstract

Current clinical practice for immobilisation for patients undergoing brain or head and neck radiotherapy is normally achieved using Perspex or thermoplastic shells that are moulded to patient anatomy during a visit to the mould room. The shells are “made to measure” and the methods currently employed to make them require patients to visit the mould room. The mould room visit can be depressing and some patients find this process particularly unpleasant. In some cases, as treatment progresses, the tumour may shrink and therefore there may be a need for a further mould room visits. With modern manufacturing and rapid prototyping comes the possibility of determining the shape of the shells from the CT-scan of the patient directly, alleviating the need for making physical moulds from the patients’ head.

However, extracting such a surface model remains a challenge and is the focus of this thesis. The aim of the work in this thesis is to develop an automatic pipeline capable of creating physical models of immobilisation shells directly from CT scans. The work includes an investigation of a number of image segmentation techniques to segment the skin/air interface from CT images. To enable the developed pipeline to be quantitatively evaluated we compared the 3D model generated from the CT data to ground truth obtained by 3D laser scans of masks produced by the mould room in the frame of a clinical trial. This involved automatically removing image artefacts due to fixations from CT imagery, automatic alignment (registration) between two meshes, measuring the degree of similarity between two 3D volumes, and automatic approach to evaluate the accuracy of segmentation.

This thesis has raised and addressed many challenges within this pipeline. We have examined and evaluated each stage of the pipeline separately. The outcomes of the pipeline as a whole are currently being evaluated by a clinical trial (IRAS ID:209119, REC Ref.:16/YH/0485). Early results from the trial indicate that the approach is viable.

# Publications

- Mark Fisher, Christopher Applegate, Mohammad Ryalat, Stephen Laycock, Mark Hulse, Daniel Emmens, Duncan Bell, et al. Evaluation of 3-D printed immobilisation shells for head and neck IMRT. *Open Journal of Radiology*, 4(04):322, 2014.
- Mohammad Hashem Ryalat, Daniel Emmens, Mark Hulse, Duncan Bell, Zainab Al-Rahamneh, Stephen Laycock, and Mark Fisher. Evaluation of particle swarm optimisation for medical image segmentation. In *Advances in Systems Science: Proceedings of the International Conference on Systems Science 2016 (ICSS 2016)*, volume 539, page 61. Springer, 2016.
- Mohammad Hashem Ryalat, Stephen Laycock, and Mark Fisher. A fast and automatic approach for removing artefacts due to immobilisation masks in X-ray CT. In *Biomedical and Health Informatics (BHI), 2017 IEEE-EMBS International Conference on*, pages 33-36. IEEE, 2017.
- Mohammad Hashem Ryalat, Stephen Laycock, and Mark Fisher. Automatic removal of mechanical fixations from CT imagery with particle swarm optimisation. In *International Conference on Bioinformatics and Biomedical Engineering*, pages 419-431. Springer, 2017.

# List of Abbreviations

2D	: Two Dimensional
3D	: Three Dimensional
BF	: Brute Force
CAD	: Computer-Aided Design
CAM	: Computer-Aided Manufacturing
CBCT	: Cone Beam Computed Tomography
CT	: Computed Tomography
DICOM	: Digital Imaging and COmmunications in Medicine
DPSO	: Darwinian Particle Swarm Optimisation
DRLSE	: Distance Regularized Level Set Evolution
DSC	: Dice Similarity Coefficient
EM	: Expectation-Maximization
FAB	: Forward-And-Backward
FDM	: Fused Deposition Modelling
FDPSO	: Fractional Darwinian Particle Swarm Optimisation
FN	: False Negative
FNR	: False Negative Rate
FP	: False Positive
FPR	: False Positive Rate
HD	: Hausdorff Distance
HMRF-EM	: Hidden Markov Random Field with Expectation-Maximization
HNC	: Head-and-Neck Cancer
ICP	: Iterative Closest Point
IMRT	: Intensity Modulated Radiation Therapy
IRAS	: Integrated Research Application System
LINAC	: Linear Accelerator
LOM	: Laminated Object Manufacturing

LSF	:	Level Set Function
MRFM	:	Markov Random Field Models
MRI	:	Magnetic Resonance Imaging
MSDE	:	Mean Surface Distance Error
MVCT	:	MegaVoltage computed tomography
NNUH	:	Norfolk and Norwich University Hospital
NOO	:	Number Of Observations
PCA	:	Principal Component Analysis
PET	:	Positron Emission Tomography
PS	:	Procrustes Superimposition
PSO	:	Particle Swarm Optimisation
PVE	:	Partial Volume Effects
REC	:	Research Ethics Committee
RMSDs	:	Root Mean Square Distances
RMSE	:	Root Mean Square Error
ROI	:	Region Of Interest
RP	:	Rapid Prototyping
RT	:	Radiation Therapy
SDCCV	:	Signed Distances with a Colour-Coded Visualization
SLA	:	Stereolithography technique
SLS	:	Selective Laser Sintering
SPC	:	Specificity
STL	:	STereoLithography file format
SVD	:	Singular Value Decomposition
TC	:	Tanimoto Coefficient
TN	:	True Negative
TNR	:	True Negative Rate
TP	:	True Positive
TPR	:	True Positive Rate
UV	:	UltraViolet
WSSS	:	Within-set Sum of Squares

# Table of Contents

<b>Abstract</b>	<b>i</b>
<b>Publications</b>	<b>ii</b>
<b>List of Abbreviations</b>	<b>iii</b>
<b>1 Introduction</b>	<b>1</b>
1.1 Research Aim . . . . .	1
1.2 Motivation . . . . .	3
1.3 Radiotherapy Planning Process . . . . .	5
1.4 Overview of our proposed treatment approach . . . . .	8
1.5 List of Contributions . . . . .	9
1.6 Thesis Structure . . . . .	10
<b>2 Background</b>	<b>12</b>
2.1 Radiation Therapy (RT) . . . . .	12
2.2 Common Radiology Imaging Modalities . . . . .	14
2.3 Three dimensional laser scanning . . . . .	16
2.4 Three Dimensional Printing in Medical Applications . . . . .	17
2.5 Image Segmentation . . . . .	22
2.6 Measures of Overlap of Labelled Regions . . . . .	25
2.7 Summary . . . . .	28
<b>3 Research Workflow</b>	<b>29</b>
3.1 Research Workflow . . . . .	29
3.2 Data Sets . . . . .	32
3.3 Summary . . . . .	37
<b>4 Automatic Removal of Immobilisation Masks from CT Imagery with Particle Swarm Optimisation</b>	<b>38</b>
4.1 Introduction . . . . .	39
4.2 Background . . . . .	40

4.3	The Proposed Approach . . . . .	45
4.4	Experimental Work . . . . .	48
4.4.1	Evaluation of PSO-based algorithms . . . . .	49
4.4.2	Removal of the Immobilisation mask . . . . .	52
4.5	Results, Validation and Discussion . . . . .	55
4.6	Summary . . . . .	58
<b>5</b>	<b>Image Segmentation</b>	<b>59</b>
5.1	Technical Background . . . . .	59
5.1.1	Otsu's method . . . . .	60
5.1.2	K-Means . . . . .	60
5.1.3	Expectation-Maximization (EM) . . . . .	61
5.1.4	Hidden Markov Random Field Model and Expectation-Maximization (HMRF-EM) . . . . .	62
5.1.5	Distance Regularized Level Set Evolution (DRLSE) . . . . .	63
5.2	Our Customisation/Handling of the DRLSE Technique . . . . .	66
5.2.1	Setting the Initial Level Set Binary Function . . . . .	66
5.2.2	Handling the Multi-Contour Case . . . . .	68
5.3	Experiments . . . . .	69
5.4	Results . . . . .	71
5.5	Summary . . . . .	75
<b>6</b>	<b>Automatic 3D Alignment</b>	<b>78</b>
6.1	Iterative Closest Point (ICP) . . . . .	78
6.1.1	Variants of ICP . . . . .	80
6.2	Customised version of ICP . . . . .	83
6.3	Experimental Work & Results . . . . .	86
6.4	Summary . . . . .	89
<b>7</b>	<b>Overlap Measurement</b>	<b>92</b>
7.1	Introduction . . . . .	93
7.2	Materials and Methods . . . . .	98
7.2.1	Data Sets . . . . .	98
7.2.2	Methods . . . . .	98
7.3	The Slicing Process . . . . .	99
7.3.1	Simplifying the Mesh . . . . .	99
7.3.2	Plane/Triangle Intersection . . . . .	101
7.3.3	Projection of Intersection Points into Image Pixels . . . . .	103
7.3.4	Filling the Slices . . . . .	105
7.4	Experimental Work . . . . .	106
7.5	Results . . . . .	106
7.6	Discussion . . . . .	114

7.7	Summary	120
<b>8</b>	<b>Pre-clinical Trial</b>	<b>122</b>
8.1	Introduction	122
8.2	The Proposed Pipeline	124
8.2.1	Reading a stack of 2D CT images and constructing a 3D model	125
8.2.2	Extracting the vertices from the triangulated mesh and simplifying it	129
8.2.3	Alignment, Slicing, and Measuring the Overlap Ratio	131
8.3	Experimental Work	133
8.4	Results	135
8.5	Conclusion and Discussion	136
<b>9</b>	<b>Clinical Trial</b>	<b>139</b>
9.1	Overview of the Clinical Trial	139
9.2	Experiments and Results	142
9.3	Discussion	149
9.4	Summary	154
<b>10</b>	<b>Conclusions</b>	<b>156</b>
10.1	Conclusions	156
10.2	Future Work	159
	<b>Bibliography</b>	<b>161</b>
<b>A</b>	<b>Applying our Overlap Measurement in Related Applications of Surface Simplification</b>	<b>196</b>
A.1	Introduction	196
A.2	Comparing Two Surface-Simplification Techniques	197
A.3	Determining the Optimal Correction Value in Poisson Surface Reconstruction Technique	199
<b>B</b>	<b>Related Documents of the Clinical Trial</b>	<b>203</b>

# List of Tables

2.1	Comparison between RP techniques (advantages) . . . . .	19
2.2	Comparison between RP techniques (disadvantages) . . . . .	19
3.1	Description of data sets used in this Thesis. . . . .	34
3.2	Showing in which chapter each data set is used. . . . .	36
4.1	Initial parameters of the PSO, DPSO and FODPSO algorithms . . .	50
4.2	Average fitness values of Brute-Force, PSO, DPSO and FODPSO algorithms for different number of thresholds over different five data sets	51
4.3	Average execution time (in sec) of the Brute-Force, PSO, DPSO and FODPSO algorithms for different number of thresholds over different five data sets . . . . .	53
4.4	Standard deviation of fitness for PSO, DPSO and FODPSO after running each algorithm 15 times over different five data sets. . . . .	54
4.5	The average values of TP, FP, TN, FN, TPR, FPR, TNR and FNR for each dataset . . . . .	56
4.6	The values of TPR, SPC, and NOO for each dataset . . . . .	57
5.1	The Average Similarity Ratio (ASR), for each segmentation technique, between the CT segmented slices and the ground-truth, Standard deviation (STD), 90 <sup>th</sup> percentile, and the time (in sec) required to segment the whole dataset. . . . .	74
5.2	The similarity ratio for the slices 20 to 25 (around patient's nose). . .	75
6.1	Comparing the basic ICP algorithm with the customised ICP in terms of execution time and average distance . . . . .	88

7.1	Description of data sets used in this study. . . . .	98
7.2	Description of the test cases used in the experimental part and their corresponding data sets. . . . .	107
7.3	Surface ~ Surface overlap measurements for different test cases of axial, sagittal and coronal views. . . . .	108
7.4	Surface ~ Volume overlap measurements for different test cases of axial, sagittal and coronal views. . . . .	111
7.5	Volume ~ Volume overlap measurements for different test cases of axial, sagittal and coronal views. . . . .	112
7.6	Volume ~ Volume overlap measurements when the values of the same specific column in each slice are inverted. . . . .	113
7.7	Correlation coefficients, $p_{value}$ , lower and upper bounds for a 95% confidence interval for each coefficient between <i>Dice_3S</i> , <i>RMSE</i> and <i>HD</i> . . . . .	114
8.1	The syntax for a binary stl file . . . . .	129
8.2	Dice value, Standard deviation and the 90 <sup>th</sup> percentile for the three objects. . . . .	136
9.1	Basic description of our clinical trial. . . . .	140
9.2	Statistics generated by our pipeline to represent the similarity ratio between the CT slices and the slices that are calculated from the outer surface of the mask for the “Perspex Mask” data set. . . . .	144
9.3	Values represent how many pixels labelled with {-1, 0, +1, +2, +3, +4, +5, +6, +7} and the percentage of this label over the whole set of labelled pixels. . . . .	151
A.1	Testing <i>Dice_3S</i> on different reduced (simplified) versions of the pelvis and knee data sets. The QECD technique was used here to reduce the size of objects . . . . .	198
A.2	Testing the overlap measurement on different reduced versions of the pelvis and knee data sets. The UMR technique was used here to reduce the size of objects . . . . .	199



# List of Figures

1.1	Examples of perspex shells. . . . .	2
1.2	Examples of thermoplastic shells. . . . .	2
1.3	The treatment process for HNC patients. The green blocks would replace those shown in red if the mask was printed directly from the CT scan. The black blocks belong to the common stages between the two approaches. . . . .	7
1.4	(a) A general schema represents our proposed treatment approach. (The photo of the 3D-printing of the mask (f) is from [1]). . . . .	9
2.1	A comparison between five different RP techniques in terms of accuracy and cost. . . . .	20
2.2	Edge types. . . . .	24
2.3	General description for edge-detection algorithms. . . . .	24
3.1	(a) A general schema represents the evaluation process in our study (b) A schema points in which chapter each phase of the evaluation process is presented. . . . .	30
3.2	Example of CT slice which involves immobilisation mask. . . . .	31
3.3	Different segmentation techniques generate different CT models. Each CT model is evaluated with regard to laser-scan model. . . . .	32

3.4	The different data sets used in this study. (a), (b), (c), (d) and (e) display surface meshes represent respectively real pelvis, real knee, plastic object in a shape of nested cubes, plastic object in a shape of dome, and the Cantonese head. (f) and (g) represent one CT image slice for two CT data sets of human head from TCIA. (h) represents one CT image slice for one of the three data sets that we got from Leeds. (i) represents the perspex mask and (j) represents the surface mesh of this mask. . . . .	33
3.5	Plastic objects in a shape of (a) Cubes and (b) Dome. Examples of CT image slices of (c) Cubes and (d) Dome. The hand-held laser scanner (Artec Space SpiderTM from Artec 3D, Luxembourg) that we used to scan the plastic objects are shown in (e). . . . .	35
4.1	A chart represents the basic assumption of Otsu's method. . . . .	41
4.2	Overview of the proposed approach. . . . .	46
4.3	A CT image in DICOM format and the same image after segmentation using the FODPSO algorithm along with their pixel region tool. . . .	48
4.4	Examples of pixels mislabeled by FDPSO. Upper row: pixels mislabeled as $\{M\}$ ; Lower row: pixels mislabeled as $\{B\}$ . . . . .	49
4.5	Applying FODPSO using different number of thresholds. . . . .	52
4.6	An example of a CT slice from the first dataset. . . . .	55
4.7	One CT slice example from each dataset (Input & Output). . . . .	56
4.8	(left) Example of a CT image includes a noise in the middle column (Middle) A CT image has a disconnected representation of the mask pixels (Right) Defining new start points to seek horizontally. . .	57
5.1	A schema represents the problems and drawbacks accompanying the conventional level set formulation (left part) and the reasons that make the DRLSE able to overcome these problems (right part). . . . .	64
5.2	Level set function which (a) develops irregularity through its evolution and (b) another level set function in which the regularity is preserved during the evolution (imported from [2]). . . . .	65

5.3	A schema showing the procedure that we follow to derive the initial level set binary function. . . . .	67
5.4	Examples of images that have more than one contour. . . . .	69
5.5	Structure of Contour Matrix. . . . .	69
5.6	A schema illustrates the procedure that we follow to evaluate the accuracy of the five segmentation techniques. . . . .	71
5.7	Random segmented CT slices generated by applying Otsu, K-means, EM, DRLSE, and HMRF-EM techniques to segment the CT slices of the Perspex mask. . . . .	73
5.8	The first three images represent three images generated when slicing the laser-scan mesh and the last three images represent the same images after applying automatic filling. . . . .	73
5.9	Constructed models generated from CT segmented slices after applying (a) Otsu (b) K-means (c) EM (d) DRLSE and (e) HRMF-EM. . . . .	73
5.10	Similarity ratio slice by slice for different segmentation techniques. The process that we follow to find these similarity ratio is presented in Chapter 7. . . . .	76
6.1	ICP phases and common approaches. . . . .	81
6.2	Three objects (left): head (middle): cubes (right): dome. . . . .	87
6.3	(left): The REVscan <sup>TM</sup> laser scanner from Handyscan 3D (right): Artec space spider <sup>TM</sup> laser scanner from Artec 3D. . . . .	87
6.4	The two models (top): before alignment (bottom): after alignment . .	88
6.5	The outcomes after performing the alignment when using (top): the basic form of ICP, (bottom): customised (adjusted) ICP. . . . .	89
6.6	Convergence plots when applying the basic ICP and the customised (adjusted) ICP over (top): the Cantonese head , (middle): cubes and (bottom): dome. . . . .	91
7.1	The proposed model of measuring the degree of overlap between two medical volumes. . . . .	100

7.2	2D binary image generated after applying Algorithm 5 over the Pelvis dataset (a): Without activating the automatic fill (b): activating the automatic fill. . . . .	105
7.3	Bar charts that <i>Dice_3S</i> generates for axial (a and d), sagittal (b and e) and coronal (c and f) perspectives. These charts are produced when it is run to find the ratio of overlap between the original surface of the Pelvis dataset and the same surface after translating it 2% in y-direction (a, b and c) and 5% in y-direction (d, e and f) (Row#14 and Row#15 in Table 7.3). (b) and (e) show that the number of images that have a zero similarity ratio (i.e. identified by a red ellipse) when the dataset is translated 5% is greater than that number of images when it is translated 2%. . . . .	110
7.4	The values of the same specific column are inverted (from white to black) in each slice. . . . .	112
7.5	A screen shot for the Matlab GUI tool of <i>Dice_3S</i> . . . . .	116
7.6	The three different perspectives intersect the voxel space in different positions producing more accurate results for partial volume estimate. . . . .	118
7.7	Bar charts generated by <i>Dice_3S</i> to find similarity ratios between a head displayed in Figure 7.8(a) and another edited version of that head displayed in Figure 7.8(b). (left): axial, (middle): sagittal, and (right): coronal . . . . .	119
7.8	(a) Delineation of a head shows the axial, sagittal and coronal perspectives (imported from [3] and edited) (b) The region that has a low overlap is displayed in red. . . . .	119
8.1	A schema represents the pipeline of the proposed approach . . . . .	126
8.2	The first step of the pipeline includes image segmentation and surface reconstruction. . . . .	127
8.3	Graphical representation of the concepts of pixel-spacing and spacing-between-slices. . . . .	128
8.4	The second phase of the pipeline: Extracting the vertices. . . . .	129

8.5	A simple mesh includes 12 rows of vertices before simplifying (imported form [4] and edited). . . . .	130
8.6	The same mesh in Figure 8.5 but after simplifying it to be composed of 4-rows. . . . .	130
8.7	Examples of laser slices and its corresponding slices after filling. . . .	132
8.8	Two regions of interest defined by the user. . . . .	133
8.9	Building 3D models from 2D medical images. (a-d): head (e-h): cubes and (i-l): dome. The first column displays the original images (DICOM images), the second column displays the segmented images, the third column displays the segmented images after the automatic cropping and the fourth column displays the constructed 3D models. . . . .	134
8.10	A proposed pipeline that can be used if two meshes are the inputs. .	138
9.1	Flowchart represents the stages of the clinical trial. . . . .	141
9.2	A histogram representing the similarity ratio slice by slice for the “Perspex Mask” data set generated by our pipeline. . . . .	144
9.3	A flowchart represents the procedure to calculate the physical distances between the two surfaces (CT-derived model and laser-scan model). .	145
9.4	(left) A CT image segmented using DRLSE technique and filled, (right) Its corresponding image computed from laser model and filled. . . . .	145
9.5	(left) A CT image after detecting the edges, (right) Its corresponding laser image after detecting the edges. . . . .	146
9.6	Screen shots of five composite slice images which are spaced apart in different locations on the face. The red colour represents the border of CT image, the green colour represents the border of laser image, and the yellow colour represents the pixels where the two images are superimposed. . . . .	146
9.7	Investigation for the pixels in different regions of a composite image. Red squares belong to the border of the CT image, green squares belong to the border of the laser image, and yellow squares represent pixels where the two images are superimposed. . . . .	148

9.8	Representation of the approach that is used to find the distances between the borders in composite images. Red squares belong to the border of the CT image, green squares belong to the border of the laser image, and yellow squares represent pixels where the two images are superimposed. . . . .	149
9.9	Histograms represent the total distance between the laser slice and the CT slice in pixels. . . . .	150
9.10	Constructed model generated from the CT corresponding to the patient for whom the perspex mask was made. The scan does not involve scanning the patients to the top vertex of the skull. . . . .	152
9.11	A photo shows the Perspex mask that we have scanned by the hand-held laser scanner. . . . .	153
9.12	A photo shows the Perspex mask and the red circle shows the extension that is used to fix the mask over the couch. . . . .	154
9.13	A photo shows the laser mesh acquired for the Perspex mask and the red circles show some examples of incomplete/gaps on the surface of the mesh. . . . .	154
A.1	Comparison between the QECD and the UMR techniques. Interpolation has been used to find the interpolated values at specific file sizes for the UMR . . . . .	200
A.2	Average similarity ratio for different Offsetting values. The red ellipses in the figure represent the point at which the parameter $\alpha$ reaches the maximum value of similarity ratio. . . . .	202

# Chapter 1

## Introduction

This chapter forms an introduction to this thesis in which we present the aims and the motivations of the research in Section 1.1 and Section 1.2 respectively. It also presents a brief overview on the current treatment pathway for patients requiring head and neck radiotherapy in Section 1.3. Section 1.4 presents a general description about our proposed treatment approach in which Head-and-Neck cancer patients are no longer need to visit the mould room. Section 1.5 listed the contributions of this thesis. Thesis organisation is presented in Section 1.6.

### 1.1 Research Aim

Radiotherapy is normally delivered in fractions over a period of time and patients need to be carefully and consistently positioned during treatment to ensure tumours are accurately targeted. Patients undergoing treatment of the head and neck are normally immobilised by fitting a facial mask. Two types of facial masks (immobilisation masks) are commonly used in hospitals nowadays for the purpose of immobilisation [5]. The first one, see Figure 1.1, is the Polycarbonate or Perspex (hard plastic) mask which is formed from a model created from a Plaster of Paris mould of the patient's face and in some cases extending to the neck and shoulders. Alternative soft plastic immobilisation systems (thermoplastic), see Figure 1.2, require a plastic mesh to



Figure 1.1: Examples of perspex shells.



Figure 1.2: Examples of thermoplastic shells.

be heated and draped over the patient's face. Immobilisation masks are fitted by radiotherapists and technicians during a mould room appointment scheduled before treatment commences. Both approaches are invasive and some patients find the mould room visit unpleasant and distressing. With modern advanced manufacturing comes the possibility of automatically producing an immobilisation mask from a 3D computer model built using CT scans. This non-invasive approach would improve the patient experience, improve efficiency and save time.

Successful radiation therapy treatment outcomes rely on accurate targeting of cancerous tissue while minimising the dose to surrounding healthy organs. Consequently, the process of immobilisation for head-and-neck cancer patients during the treatment sessions is a big challenge. The core goal of this research is focused on demonstrating that the model needed to construct a mask could be produced automatically from the CT with similar accuracy as those currently made by the moulding process.

## 1.2 Motivation

Head-and-Neck Cancer (HNC) refers to a group of different malignant tumors that develop in or around the throat, larynx, nose, sinuses, and mouth [6]. Staging of the cancer may be determined by medical imaging, biopsy and blood tests [7]. HNC is the eighth most common cancer in the UK (2014), accounting for 3% of all new cases [8]. Figures published from the United States estimate that 61,760 people developed head and neck cancer in 2015 [9].

Acquiring CT data is necessary and indispensable step in treatment planning, and so reusing these data to construct a 3D-printed model of the mask does not introduce any additional steps to the treatment pathway. The existence of these data motivate us to reuse it to produce a printed mask instead of looking for another additional acquisition method that can produce a high quality 3D model. Consequently, this research addresses the problem of how to create high quality models with smooth iso-surfaces.

As stated in Section 1.1, immobilisation for HNC patients is currently accomplished through the use of perspex/thermoplastic shells. This process requires direct moulding to the patient's face and in some cases to the neck. Consequently, a visit to the mould room is a prerequisite. The patient may have undergone previous surgery to remove malignant tissue and taking the mould can be painful and is sometimes a cause of distress. In some cases additional moulds are required as treatment progresses and the tumour shrinks.

Many UK radiotherapy centres are currently using the Orfit soft-drape masks in treatment sessions [10, 5]. Extended discussions have taken place between the research group and radiologists and radiotherapist in Ipswich Hospital NHS Foundation Trust, Suffolk, UK and St James's University Hospital NHS Foundation Trust, Leeds, UK in order to investigate the nature of the problem and to discuss deeply the feasibility

of generating 3D printed shells for HNC patients. Those discussions and meetings as well as other recent studies [5, 11] indicate that constructing 3D-printed masks for HNC patients is worthy of further investigation. This research is motivated by many challenges arising from the following points:

- The current perspex/thermoplastic shells used in radiation therapy cause distress, anxiety, stress, pain and worry.
- The current process of producing shells is manually intensive, physically demanding, and requires a dedicated facility (i.e. the mould room) and specialist staff [12].
- Visiting mould room and the moulding process itself are time consuming.
- The current process does not use digital data to store shell's measurement and features. So there is a need to store the shell itself for future comparison and consequently this shortage of digital data complicates the comparative studies over time [12].
- Since the recent developments in 3D printing indicate that this technique may present a cheap and affordable choice in many industrial and medical applications, it is worth exploring the use of this technique in our research. It may present in the future a cheaper choice than using the current perspex/thermoplastic shells.
- There is an increasing interest worldwide toward the development of new health-care technologies and especially in the field of image guided planning for surgery and radiotherapy to enhance precision/targeting. For example, one of the funding opportunities offered by the Engineering and Physical Sciences Research Council (EPSRC) is: frontiers of physical intervention grand challenges. One of the specific impacts that could be achieved under this grand challenge is “Advances in physics modelling and image guided planning for surgery and radiotherapy to improve precision/targeting, leading to fewer side-effects, faster recovery, and better outcomes” [13].
- The need for a high level of accuracy of radiation beams and the need for a precise

immobilisation for the patient during the treatment session create a strong motivation for us to focus on creating a 3D-printed immobilisation mask for HNC patients.

### 1.3 Radiotherapy Planning Process

A course of Radiotherapy Treatment is typically prescribed for patients diagnosed with Head-and-Neck Cancer (HNC). It directs high energy ionising radiation to destroy malignant cells, but it must be accurately targeted to limit harm to healthy cells. A typical course of radiotherapy treatment for HNC is delivered in fractions over several weeks and masks Figure 1.1 and Figure 1.2 are employed to ensure the patient can be consistently repositioned for each dose fraction.

The radiation therapy process consists of various steps. It starts with data acquisition using for example a CT scan. This is followed by treatment planning stages including tumour localisation then treatment planning and beam positioning, and at the end radiation delivery. Producing a 3D radiation treatment plan requires defining the target volume and organs at risk accurately, and these in turn require image segmentation either manually or automatically as is clarified in the next paragraphs. Radiation treatment is delivered in fractions, each session taking 15-30 minutes and the whole process, from beginning to end, takes four to six weeks[14, 15].

Since radiation damages both healthy and malignant cells, precise positioning of the patient prior and during the treatment sessions is a basic and important component in achieving a successful outcome [16]. The dose given to surrounding healthy tissues and ‘organs at risk’ which are particularly sensitive to radiation should be minimised [17].

Tumour localisation, the accurate placement of radiation beams and the precise calculation of dose distributions are of great importance in reducing side effects of radiotherapy treatment [18]. In order to understand the nature of the radiotherapy

planning process and to appreciate to what extent this process is critical we present a brief description about these consecutive stages:

*Stage1: Tumour localisation, identifying of target volume and organs at risk.*

The radiotherapy planning process starts with the identifying of the location and the form of the tumour. After that, the detecting of the target volume should take place by identifying the volume which has to be totally covered by the therapeutic dose. This stage involves the definition of tumour margins and safety margins which are detected according to histology and the organs at risk. Errors and uncertainties which are produced during this stage significantly impact the efficiency of treatment planning and the result of the whole process [18].

*Stage2: Modelling of anatomy and image segmentation.*

In this phase, organs and tissues which will be irradiated have to be involved in the treatment planning process. Moreover these tissue and organs have to be modelled in three dimensions. The commonly approach used for extracting 3D information is the manual segmentation of CT slices. Automatic or semi-automatic segmentation can also be used since manual segmentation is time consuming, extremely tedious and needs a great amount of efforts.

*Stage3: Treatment design and dose calculation.*

After finishing the delineation of anatomical structures and modelling of it in 3D, a selection of the best directions from which to direct radiation beams at the target volume is taken place. Numerous beams of radiation focused from different angles at the target in order to allow for a better separation between the target volume and the critical structures. The calculations of irradiation dose has three prerequisite [18]: The precise patient geometry, the distribution of electron densities within the body, and the physical beam characteristics of the irradiation units. The first and second prerequisite (i.e. patient geometry and electron densities) can be acquired from CT

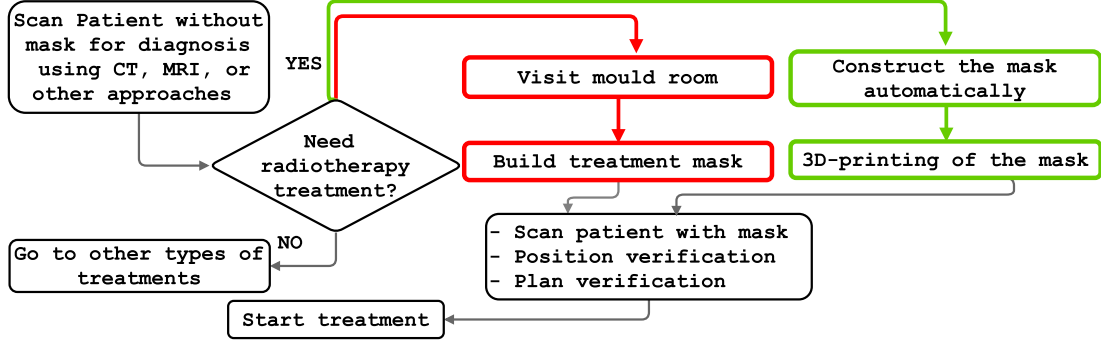


Figure 1.3: The treatment process for HNC patients. The green blocks would replace those shown in red if the mask was printed directly from the CT scan. The black blocks belong to the common stages between the two approaches.

slices.

#### *Stage4: Transfer of treatment to the patient*

This is the final stage in which the settings that have been defined in the previous stages are transferred to the patient during the treatment sessions.

Figure 1.3 illustrates the current patient treatment approach for Head-and-Neck cancer in addition to our proposed treatment approach. The stages that are coloured in black in the figure are common stages between the current treatment approach and our approach. The red blocks belong to the current approach whereas the green blocks belong to our proposed approach. Notice that most of the stages are common between the two approach except that we replace the visit to the mould room with the automatic construction of the mask using computer algorithms. Treatment of HNC is slightly different from general cases of radiotherapy treatment since it involves a mould room visit and because the CT planning scan is done with the patient wearing the mask.

## 1.4 Overview of our proposed treatment approach

We have presented in the previous section a general description about our proposed treatment approach. In this section we present more scientific description of the main phases of our proposed treatment approach. We mentioned that the current treatment process requires direct moulding to patient anatomy. The proposed approach of treatment enables the immobilisation masks to be obtained directly from the CT data without requiring patients to visit the mould room. The phases of the proposed approach are presented in Figure 1.4 in which the process starts by reading a stack of CT images for those patients who have a Head-and-Neck cancer. This CT scan is routinely performed on those patients as part of their radiotherapy planning process. Then the image segmentation process takes place. The aim of the image segmentation is to label pixels as belonging to the foreground or background. The details of the image segmentation process is presented in Chapter 5. The foreground area, which represents the region of the patient's head, is then dilated (see Figure 1.4 (c)). The aim of the dilation process is to gradually enlarge the boundaries of regions of foreground pixels to form a representation of mask to be fitted around patient's face.

A volume is constructed from those dilated images using the Marching Cubes algorithm [19](see Figure 1.4). The digitally constructed model represents a larger volume than the head itself. From that constructed model we extract the mask as a mesh. This mesh is sent later to 3D printer to produce a physical immobilisation mask. Notice that we just present in this section a general description about our proposed approach to construct automatically radiotherapy treatment immobilisation masks. In the next chapters we present all the details of the proposed approach and the evaluation process.

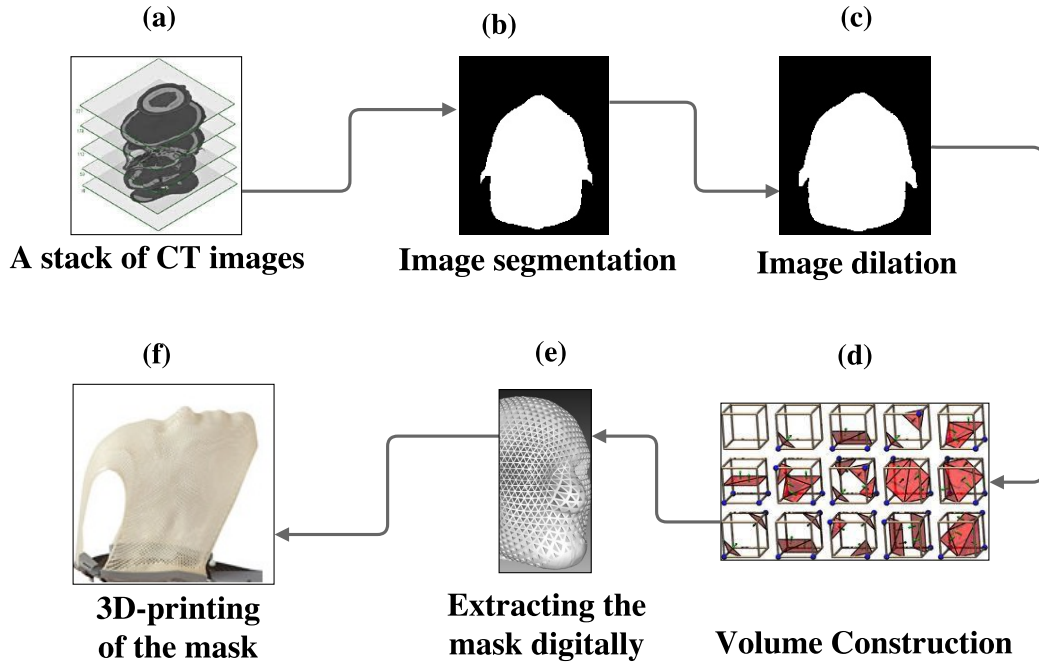


Figure 1.4: (a) A general schema represents our proposed treatment approach. (The photo of the 3D-printing of the mask (f) is from [1]).

## 1.5 List of Contributions

This thesis makes the following contributions to enhance the treatment of HNC:

- It presents an automatic approach to generate a 3D model from which an immobilisation mask can be constructed for use in radiotherapy treatment of Head-and-Neck cancer using the CT volume currently acquired for treatment planning purposes.
- It presents a novel, fast, and automatic approach to remove image artefacts due to fixations (i.e. immobilisation masks as it is depicted in Figure 3.2 Chapter 3) in CT images with Particle Swarm Optimisation and without affecting pixel values representing tissues.
- It investigates the use of five different segmentation techniques to segment the air/skin boundary interface in CT images and evaluates the outcomes generated

by each technique.

- It presents a customised version of the iterative closest point algorithm in order to automatically align (register) two 3D meshes. This version exceeds the conventional algorithm in terms of accuracy and speed.
- It presents an approach to 3D-overlap measurement for medical volumes. The proposed approach does not just produce a figure-of-merit but it also gives complementary statistical information that enables the observer to assess the scale and positions of regions/volumes of match and mismatch.
- It presents a novel pipeline to automatically evaluate the accuracy of segmentation of CT images when a laser-scan mesh is available as a ground-truth.
- It presents and evaluates the early outcome of a clinical trial (IRAS ID:209119, REC Ref.:16/YH/0485) which is designed to provide data and a framework to evaluate computer algorithms designed to construct immobilisation masks for Head-and-Neck cancer patients.

## 1.6 Thesis Structure

The remainder of chapters of this thesis are organised as follows. Chapter 2 presents background information on radiation therapy, common radiology imaging modalities, laser scanners, 3D-printing, image segmentation and the common overlap measurements which are used to evaluate the outcomes of image segmentation. Chapter 3 describes the procedures by which we evaluate the reliability of our work and the data sets that have been used in this thesis. In Chapter 4 we present a fast and automatic approach that removes image artefacts due to fixations in CT images which are captured with the immobilisation mask fitted. The presented approach in Chapter 4

prepares the CT data sets to be ready for automatic segmentation. This segmentation is investigated in Chapter 5 in which five segmentation techniques are applied and evaluated.

Chapter 6 presents a customised version of the iterative closest point algorithm that we develop to align between the CT-derived model and the ground-truth (laser-scan model). Chapter 7 develops a 3D-overlap measurement for medical volume images which will be used later to evaluate the accuracy of the constructed CT-derived model when compared to the ground-truth. Chapter 8 introduces a novel pipeline to be used to evaluate the accuracy of segmenting a CT volume by comparing to a 3D ground-truth model acquired using a laser scanner. A pre-clinical trial is presented to evaluate the reliability of the proposed pipeline. Chapter 9 presents the early outcome of a clinical trial that we conduct to evaluate the reliability of the whole system. Chapter 10 concludes this thesis and discusses the possibilities of future work.

# Chapter 2

## Background

This chapter aims to present to the reader an overview of the process of Radiation Therapy (RT) and a general description about the common radiology imaging modalities such as Computed Tomography (CT) and Magnetic Resonance Imaging (MRI). In addition, an overview is presented on laser scanners and three-dimensional (3D) printing and its applications in medical fields. The chapter ends by presenting an overview of the image segmentation concepts and a description on the common overlap measures of labelled regions that are used to evaluate the outcomes of image segmentation. Other literature and background information are presented in relevant chapters to keep the transitions within chapters more simple and understandable.

### 2.1 Radiation Therapy (RT)

Radiation Therapy (RT) is the use of high-energy radiation from x-rays, gamma rays, neutrons, and other sources to kill cancer cells [20]. X-rays used in radiation therapy employ voltages between 6 MV and 20 MV [21]. Radiation therapy, also referred to as radiotherapy, can be given either externally or internally. External radiotherapy employs a large machine called a linear accelerator to direct high-energy X-rays at the area requiring treatment whereas internal radiotherapy, known as brachytherapy, uses a small piece of radioactive material placed inside the body near the cancerous

cells or a radioactive liquid that is swallowed or injected.

There are three major methods used in treatment of cancer: Radiation therapy, chemotherapy, and surgery. Contrary to other medical specializations that depend principally on the clinical knowledge and experience of medical specialists, radiotherapy, with its use of ionising radiation in treatment of cancer, depends on modern technology and collaborative efforts of a number of professionals whose coordination significantly affects the result of the treatment [22].

The radiation therapy process includes numerous phases. The main phases are: data acquisition, typically using a CT scanner, tumour localisation, planning treatment, and radiation delivery. As it known in Radiology, radiation damages both healthy and malignant cells. Consequently, radiation should be oriented to the malignant cells precisely. Positioning the patient accurately is very important to get successful outcome [16]. A precise procedure for patient positioning saves time and reduces errors in targeting cancerous cells at the tumour site.

There are several different types of radiation therapy systems such as: Linear accelerator, Tomotherapy and CyberKnife.

- Linear Accelerator (LINAC)

LINAC accelerator is the most commonly used radiation therapy system for patients with cancer. It customizes high energy x-rays to be consistent with a tumors shape and damage cancer cells while saving surrounding normal tissue. It can be used for a stereotactic radiosurgery so it is used to treat all parts/organs of the body [23].

- Tomotherapy

This system of radiation therapy merges the Intensity Modulated Radiation Therapy (IMRT) delivery with an internal image guided system that uses a

MegaVoltage computed tomography scanning (MVCT). It is capable of delivering IMRT by radiating tumours helically with a combination of the use of sophisticated computer controlled radiation beam collimation and the use of on-board CT scanner for treatment site imaging.

- CyberKnife

The CyberKnife is an image-guided frameless radiosurgery system. The system involves primarily a robotic controller, an X-ray radiographic locating system and a light weight 6 MV linear accelerator head [24].

Intensity Modulated Radiation Therapy (IMRT) is now the fundamental means of delivering radiation to the tumour site in the correct dose and location without influencing the surrounding healthy cells [25]. That is because in IMRT radiation beams are shaped to be similar to the shape of tumour, and this allows a more precise conformal radiation dose to be delivered to the tumour site [26]. The next section will present an overview of the common radiology imaging modalities.

## 2.2 Common Radiology Imaging Modalities

This section presents an overview of some common imaging modalities used by oncologists to diagnose and treat disease.

### X-ray imaging

In 1895, Rontgen published his initial results of using X-rays and since then X-ray imaging has been used heavily in medical applications. The important reasons that stand behind the widespread use of X-rays are the simplicity to be generated and detected, and because it is still the cheapest choice for acquiring medical images [27]. In medical diagnostics, the used X-rays are generated by acceleration voltages chosen between 25 kV and 150 kV, while those employed in radiation therapy use voltages

between 6 MV and 20 MV [9]. X-ray imaging modality is considered the first modality used in medical applications and it has been used to develop other medical imaging techniques.

## Computed Tomography (CT)

Godfrey Hounsfield, an English scientist, developed the process of Computed Tomography (CT) in the early 1970s. CT images, or CT slices, are produced using X-rays. The mechanism that CT imaging follows can be described as rebuilding a two dimensional image slice using one dimensional X-ray projections that are acquired from different angles [28] and then a three dimensional volume could be generated from the resulting stack of two dimensional CT slices.

The idea of X-ray CT is to reconstruct a 2D image slice using 1D X-ray projections that are acquired from different angles [28], and then stack the CT slices to reconstruct a 3D volume. This volume could be used in several medical applications such as medical diagnosis and the planning of surgical or radiotherapy treatment. This may, in turn require image segmentation, surface rendering, image registration etc.

Since the 1970s, the means of acquiring CT images have been improved in numerous generations of scanners. The basic aspects of differences between these generations are:

- Geometry of the X-ray source
- Scanning configuration
- Scanning motions
- Detector arrangement

## Magnetic Resonance Imaging (MRI)

Magnetic Resonance Imaging (MRI) is a medical imaging technique used in radiology to investigate the anatomy and physiology of the body. It uses a powerful magnetic

field and radio waves to produce detailed images of the inside of the body. The outcomes of an MRI scan is used to help plan treatments, diagnose conditions, and evaluate the effectiveness of previous treatment. An MRI scan is a painless and safe process since MRI scans do not implicate exposure to ionizing radiation.

MRI was developed in 1973 by Lauterbur and Mansfield. In MRI, the hydrogen nuclei, which make up 80% of all atoms in the human body, are lined up as a nuclear magnetised atoms by strong magnetic fields. After that, radio frequency fields are used to change the alignment of the previous magnetised atoms. This produces magnetic signals from the hydrogen nuclei which are then detected by the MRI scanner and rebuilt as an MRI image [29].

Laser scanners are used in our research to acquire surfaces to be used later as a ground-truth in evaluation process. We present in the next section basic concepts of laser scanning technology.

### 2.3 Three dimensional laser scanning

3D laser scanning is a non-contact technology that digitally acquires the shape of real objects using a line of laser light. 3D laser scanners generate a point cloud model of data from the surface of an object. The idea that stands behind the laser scanner is that the scanner projects a line of laser light onto the surface while sensor cameras continuously record the changing distance and shape of the laser line in three dimensions as it sweeps along the object.

The term laser scanning is used with two connected, but separate concepts. The first concept which was presented by Marshall et al. [30] refers to the controlled deflection of laser beams, visible or invisible. These laser beams are employed in used in different fields like their use for material processing, ceramic laser treatments, laser printers, rapid prototyping, laser engraving machines, etc. The second concept

which is of our interest in this thesis, often called 3D object laser scanning, refers to the controlled steering of laser beams followed by a distance measurement at every pointing direction in order to capture shapes of objects.

Laser scanner machines are common in industry and medicine as a non-invasive method for producing a 3D digital surface models [31]. Physical anthropologists, forensic scientists, and conservators used laser scanner machines to record, recreate, and analyze objects and human remains, involving craniofacial features[32, 33, 34, 35, 36]. The laser surface scanner is considered by craniofacial investigators as one of the most common types of surface data acquisition machine nowadays [37]. This technique provides an accurate and precise approach for identifying craniofacial surface landmarks [31].

## 2.4 Three Dimensional Printing in Medical Applications

As our aim in this research is to construct 3D models of radiotherapy immobilisation mask to be printed later using 3D printing technology, this section aims to present general ideas about 3D printing and its applications in medical fields. 3D printing is a process of creating 3D solid objects from a digital file where the construction of a 3D printed object is achieved using additive processes in which an object is built by laying down consecutive layers of material under computer control until the entire object is created. These layers can be considered as a collection of lightly sliced horizontal cross-section of the resultant object. According to the kind of production method used, 3D printing is also named Rapid Prototyping (RP), solid free form or layered manufacturing.

## Methods of Rapid Prototyping

Rapid Prototyping (RP) involves a number of established manufacturing techniques and experimental technologies. Rengier et al. [38] presented an overview of established rapid prototyping techniques used in the medical fields where Wendel et al. [39] described in details some selective additive processing technologies. The current common RP techniques are:

- Stereolithography technique (SLA)

SLA is a technology used for creating models and patterns in a layer by layer fashion using photopolymerization. Photopolymerization is the process by which a machine, called a stereolithograph apparatus (SLA), converts liquid plastic into solid objects [40]. (e.g. 3DSYSTEMS company, Rock Hill, SC, USA, <http://www.3dsystems.com>).

- Three-Dimensional printing techniques (3DP)

Inkjet printing (INK) techniques are the most common form of 3DP techniques. These techniques are based on different kinds of fine powders such as plaster or starch. An inkjet-like printing head goes across a bed of powder, depositing a liquid binding material in the shape of the section. After that, a new layer of powder is spread across the top of the object, and the procedure is repeated again. Unbound powder is automatically detached when the model is complete [41]. (e.g. Z Corporation, Burlington, MA, USA which was acquired by 3DSYSTEMS).

- Selective Laser Sintering (SLS)

SLS is an additive manufacturing technique that uses a laser as the power source to sinter powdered material. In SLS, small particles of plastic, ceramic or glass are fused together by heat to form a solid object. (e.g. EOS, GmbH, Munich,

Table 2.1: Comparison between RP techniques (advantages)

Technique	Good strength	Low cost	High speed	Variety of materials	Large part size
SLA					X
3DP		X	X		
SLS	X			X	
FDM	X	X			
LOM		X			X

Table 2.2: Comparison between RP techniques (disadvantages)

Technique	Moderate strength	High cost	Low speed	Limited materials	powdery surface
SLA	X				
3DP	X				
SLS		X			X
FDM			X		
LOM				X	

Germany, <http://www.eos.info>).

- Fused Deposition Modelling (FDM) Small beads of fused thermoplastic material is extruded through a nozzle to lay down plastic according to slice information. (e.g. Stratasys Inc., Eden Prairie, MN, USA, <http://www.stratasys.com>).
- Laminated Object Manufacturing (LOM)  
This technique employs a laser cutter to shape layers of paper or plastic films that are glued together. (e.g. Cubic Technologies, Torrance, CA, USA, <http://www.cubictechnologies.com>).

Table 2.1 shows the important advantages for each one of the RP techniques where Table 2.2 displays the basic disadvantage for each one. A comparison between the five different techniques in terms of accuracy and cost are presented in Figure 2.1. Notice that the attributes can change according to the specific printing system used.

As Figure 2.1 shows, the SLA technique has the highest accuracy among others where the LOM and INK have the lowest. According to [39], the accuracy of SLA reaches  $<0.05\text{mm}$ , followed by SLS which has accuracy in the range (0.05 - 0.1) mm. The accuracy of FDM is closed to SLS such that the accuracy of FDM reaches 0.1 mm. LOM technique has low accuracy (0.15mm) comparing to others, where the

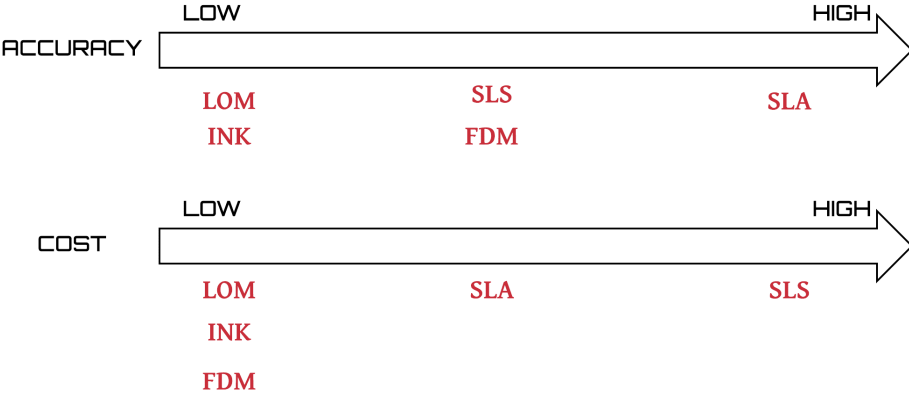


Figure 2.1: A comparison between five different RP techniques in terms of accuracy and cost.

accuracy of 3DP reaches, described using dots per inch (dpi) metric,  $0.1/600 \times 540$  dpi. In terms of cost, it is difficult to supply exact numbers and figures because the cost depends on the size and complexity of samples, but we can describe the cost relatively. As displayed in Figure 2.1, SLS is the most expensive one, followed by SLA, where the remaining techniques have closed values in terms of cost. The following subsection presents some common applications of 3D printing and specially in medical fields.

## Applications of 3D Printing

Rapid prototyping has afforded new technologies that help in visualization of intricate structures. It has been employed in different fields like: industry, biomedical engineering, forensic science, education, customizable labware ([42], digital preservation and study of cultural heritage artefacts (e.g. [43] 3D printing was used to study the fine details of a Cantonese chess piece with complex internal structure), space vehicles manufacturing (in [44] NASA explores the potential of 3D printing in the development of the next generation space exploration vehicle) and many other numerous applications.

In addition to the numerous applications of rapid prototyping and 3D printing that are mentioned above, they are also used in different medical applications. Using 3D printing in medicine saves the time in most cases as well as reducing errors [45]. The following list include some of the medical fields which benefit from the 3D printing technology:

- It is used in prosthesis design [46, 47].
- It allows the production of a realistic, physical, understandable and true 3-D object which are of useful clinical value (e.g. in [48] the 3D-printed model provides a better understanding of a large osteochondroma arising from the scapula).
- 3D-printed models aid surgeons, radiologists and junior trainees in their works [49, 50].
- It makes the process of communication with patients easier [40].
- It helps plan surgical management [48].
- It is important for planning maxillofacial and craniofacial surgery [41, 51].
- It is used for neurosurgical procedures and repairing of skull defects. (e.g. [52] used it to create an implant for the surgical reconstruction of a large cranial defect).
- It used in orthopaedics diagnosis and for treating disorders of the spine [53], pelvis [54] and shoulder. (e.g. in [55] the 3D printed model helped the surgeons preoperatively decide the proper location for positioning of pedicle screws).
- 3D-printed models help in diagnosis and treatment of cardiovascular disease [56, 57], (e.g. [58] used 3D-printed models to determine patients suitability for

percutaneous pulmonary valve implantation).

- Producing phantoms for medical research [59].

Accurate segmentation of the CT slices leads to more accurate final outcomes in our research. The following section presents an overview of images segmentation.

## 2.5 Image Segmentation

Image segmentation is the process of partitioning an image into multiple meaningful segments (i.e. dividing into multiple regions) [60]. These regions correspond to different objects or parts of objects. In medical imaging, these regions normally correspond to different tissue classes, organs, or other biologically relevant structures [61]. As image segmentation forms a basic part of the work in this thesis and since successful segmentation of 2D CT image slices can significantly assist the next reconstruction of a 3D model, we present in this section an overview on the image segmentation concepts. There is no standard classification of the image segmentation algorithms in literature. Algorithms are categorised in [62] in accordance with their primary methodologies based on thresholds, clustering techniques and deformable models. Image segmentation is one of the most important steps that should take place in the treatment process in order to benefit from the medical images produced by the modern imaging modalities such as computed tomography (CT) and magnetic resonance imaging (MRI).

Segmentation of medical images can be performed manually, automatically (computerized) or using a combination of methods. Manual segmentation is time-consuming comparing to automatic segmentation and the results may be prone to observer variability whereas using computer-aided segmentation techniques have significantly improved the accuracy of the segmentation outcomes [63, 62].

Many image segmentation algorithms use a threshold value as a basis for segmentation. Thresholds can be chosen manually or automatically. Manual selection of a threshold value requires prior information and occasionally trial experiments while automatic segmentation uses image information such as the image histogram and pixel intensities to determine the threshold value automatically. The algorithms that are categorised as thresholds-based algorithms can be classified as:

- Edge-based algorithms.
- Region-based algorithms.
- Hybrid algorithms.

### **Edge-based algorithms**

The existence of edges represents an important features of images. Edges, in digital image processing, represent a part of the image where the intensity of the image local area changes greatly. In other words, edges represent points in an images where brightness changes abruptly. Edges can be generally categorised into four types: step, ramp, line and roof. A step edge, as shown in Figure 2.2(a), represents a complete transition from one segment to another whereas a ramp edge, as in Figure 2.2(b), represents a smoother transition between the two segments. A line edge represents two edges in close proximity. See Figure 2.2(c) for illustration. Figure 2.2(d) and 2.2(e) represent the two types of roof edges. Roof edges occur when two adjacent ramps exist in an image. Edges are commonly present between objects and backgrounds, objects and objects, primitives and primitives [64] (i.e. the primitive represent an image element from which more complex images can be reconstructed such as line, arc, etc.).

The general approach to detect edges in images is to investigate the change of intensity level in an image as changes reflect discontinuities that separate parts in the

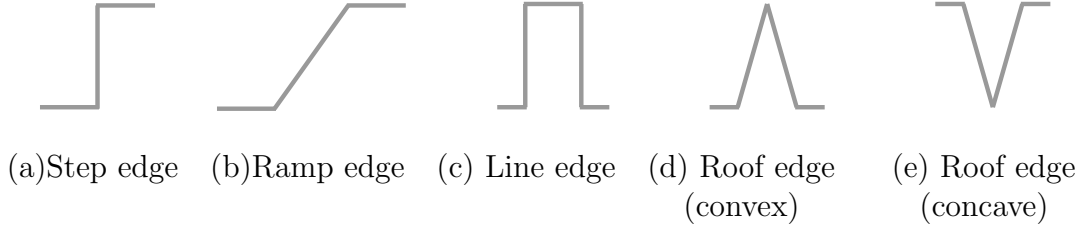


Figure 2.2: Edge types.

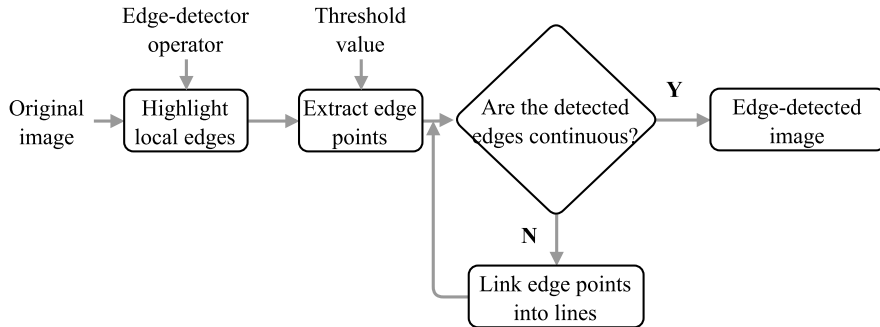


Figure 2.3: General description for edge-detection algorithms.

image. The general methodology of edge-detection algorithms is presented in Figure 2.3. The first step as shown in Figure 2.3 is to use an edge estimator to highlight local edges in images. After that, a threshold value should be selected, manually or automatically, depending on the strength of edges. The detected edge may not be continuous due to several reasons such as noise etc., so some of algorithms try to link edge points into lines by using some post-processing steps such as morphological operations.

Edge detection algorithms are further categorized as static or dynamic. Static algorithms use one threshold for the whole image while dynamic thresholding adjusts the threshold depending on local information. Edge detection is the most common method for identifying meaningful discontinuities in intensity values.

The following are the common approaches classified as edge-based algorithms: Canny edge detection (presented in [65]); Sobel; Laplacian; Prewitt and Roberts.

### **Region-based algorithms**

The basic idea in this group of algorithms is to look for pixels that share similar characteristics like intensity. One of the differences between the algorithms in this group lies in their search strategy. The following are common algorithms classified as region-based: Seeded region growing presented in [66] by Adams and Bischof, adaptive region growing presented in [67] by Pohle and Toennies, adaptive region growing based on centerline estimation presented in [68] by Yi and Ra, a bayes-based region-growing presented in [69] by Pan and Lu.

### **Hybrid algorithms**

Watershed algorithms are typical examples of hybrid algorithms. The following is some of the common algorithms classified as watershed algorithms: watershed algorithm based on immersion simulations presented in [70] by Vincent and Soille, improved watershed transform using prior information presented in [71] by Grau et al, using K-means clustering and improved watershed algorithm presented in [72] by Ng et al, and watershed segmentation using prior shape and appearance knowledge presented in [73] by Hamarneh and Li.

The process of image segmentation needs to be followed by evaluating the accuracy of segmentation. Common measurements of overlapped regions used to evaluate the accuracy of segmentation are presented in the next section.

## **2.6 Measures of Overlap of Labelled Regions**

There are a number of measurements that are useful for evaluating results derived from image segmentation algorithms. The two most popular measures of region overlap are the Tanimoto Coefficient (TC) and the Dice Similarity Coefficient (DSC) [74]. The following paragraphs presents the common measurements used to evaluate the overlap of labelled regions.

## Tanimoto Coefficient (TC)

Tanimoto Coefficient (TC) [75] is a statistic used for comparing the similarity of two sample sets. TC, also known as Jaccard Similarity [76], evaluates similarity between finite sample sets through dividing the size of the intersection over the size of the union of the sample sets as shown in Equation (2.6.1).

$$TC = \frac{N(A \cap B)}{N(A \cup B)} \quad (2.6.1)$$

Where  $N()$  refers to the number of pixels in the enclosed set. A high value of TC shows a well correspondence between the two sets. A value of one points to complete correspondence where a value of zero indicates that there is no any correspondence. Rogers and Tanimoto [77] presented the concept of similarity ration over bitmaps. The definition of the Tanimoto similarity ratio over bitmaps is the number of joint bits, divided by the number of nonzero-bits in either sample as shown in Equation (2.6.2).

$$TSR(A, B) = \frac{\sum_i^n (A_i \wedge B_i)}{\sum_i^n (A_i \vee B_i)} \quad (2.6.2)$$

Where  $TSR(A, B)$  refers to the Tanimoto similarity ratio,  $n$  refers to the total number of bits in set A or set B (i.e. set A should contains the same number of bits as set B),  $A_i$  represents the  $i^{\text{th}}$  bit of A,  $\wedge$  and  $\vee$  are bitwise logical ‘and’, ‘or’ operators respectively.

Equation (2.6.3) clarify how the calculation of TC is performed over two binary images where G represents the ground truth image, S represents the segmented image,  $g_i$  represents the  $i^{\text{th}}$  bit of G and  $s_i$  represents the  $i^{\text{th}}$  bit of S.

$$TC(G, S) = \frac{\sum_i^n (g_i \wedge s_i)}{\sum_i^n g_i^2 + \sum_i^n s_i^2 - \sum_i^n (g_i \wedge s_i)} \quad (2.6.3)$$

## Dice Similarity Coefficient (DSC)

Dice Similarity Coefficient (DSC) [74] is a statistic used for comparing the similarity of two sample sets. DSC is used as a spatial overlap index and a reproducibility validation measurement [78]. If there are no spatial overlap between two sets of binary segmentation, DSC takes a value of zero where it takes a value of one when there are a complete overlap. Equation (7.3.2) displays how DSC is calculated.

$$TC = \frac{2N(A \cap B)}{N(A) + N(B)} \quad (2.6.4)$$

Where  $N()$  refers to the number of pixels in the enclosed set. The definition of the Dice similarity ratio over bitmaps is shown in Equation 2.6.5 .

$$DSR(A, B) = \frac{2 \sum_i^n (A_i \wedge B_i)}{\sum_i^n A_i + \sum_i^n B_i} \quad (2.6.5)$$

## Hausdorff Distance (HD)

Hausdorff Distance (HD), named after Felix Hausdorff, is a measurement used to measure how far two subsets of a metric space are from each other. HD represents the greatest of all the distances from a point in one set to the closest point in the other set. Given Equation 2.6.6 where  $\|.\|$  represents the Euclidean norm

$$h(A, B) = \max_{a \in A} \min_{b \in B} \|a - b\| \quad (2.6.6)$$

then Hausdorff distance is computed as shown in Equation 2.6.7 .

$$H(A, B) = \max(h(A, B), h(B, A)) \quad (2.6.7)$$

HD was used heavily in the literature and in many applications. It was used for example [79] to measure the difference between two different representations of the

same 3D object particularly for efficient display of complex 3D model.

## 2.7 Summary

This chapter presented some background information that is related to our work in this thesis. It started by describing the radiation therapy treatment phases and then several different types of radiation therapy systems were introduced. The X-ray imaging, CT and MRI imaging systems were presented as these common medical image modalities are related to our research. Moreover, basic concepts about 3D laser scanning were discussed. The chapter also presented some discussion on different applications of 3D printing in medical applications and the principal methods used for rapid prototyping. An overview of basic concepts of image segmentation and the common measures of overlap of labelled regions are presented in this chapter since these measurements are used to assess the accuracy of image segmentation. The next chapter presents the research workflow, a brief description of the evaluation pipeline and the group of data sets which are employed in this research.

# Chapter 3

## Research Workflow

This chapter presents an overview of the progression of chapters presented later in this thesis. It also describes generally the strategies and procedures by which we evaluate the reliability of our work. Finally we present a description of the data sets that have been used through the different stages of preparing this thesis.

### 3.1 Research Workflow

Evaluation of surface models built from Computed Tomography (CT) is of vital importance to validate the outcomes of the segmentation and registration of medical images. 3D models obtained through laser scanning have been used in numerous studies as a ground-truth [80, 81, 82, 83, 84, 85, 86, 87, 88]. In a related context, laser scanners were used in a few studies to verify the accuracy of 3D-printing models of bones created from previously acquired CT-derived data [89, 90, 91]. Moreover, the following studies recommended laser scanners to be used to provide a ground truth for the model being acquired[92, 93, 94].

We evaluate the accuracy of surface models built from CT images by employing laser-scan model as a ground-truth. Figure 3.1(a) represents a general pipeline that we apply in order to evaluate models built from data acquired in pre-clinical and clinical studies presented in chapters 8 and 9. For the clinical study patients undergoing

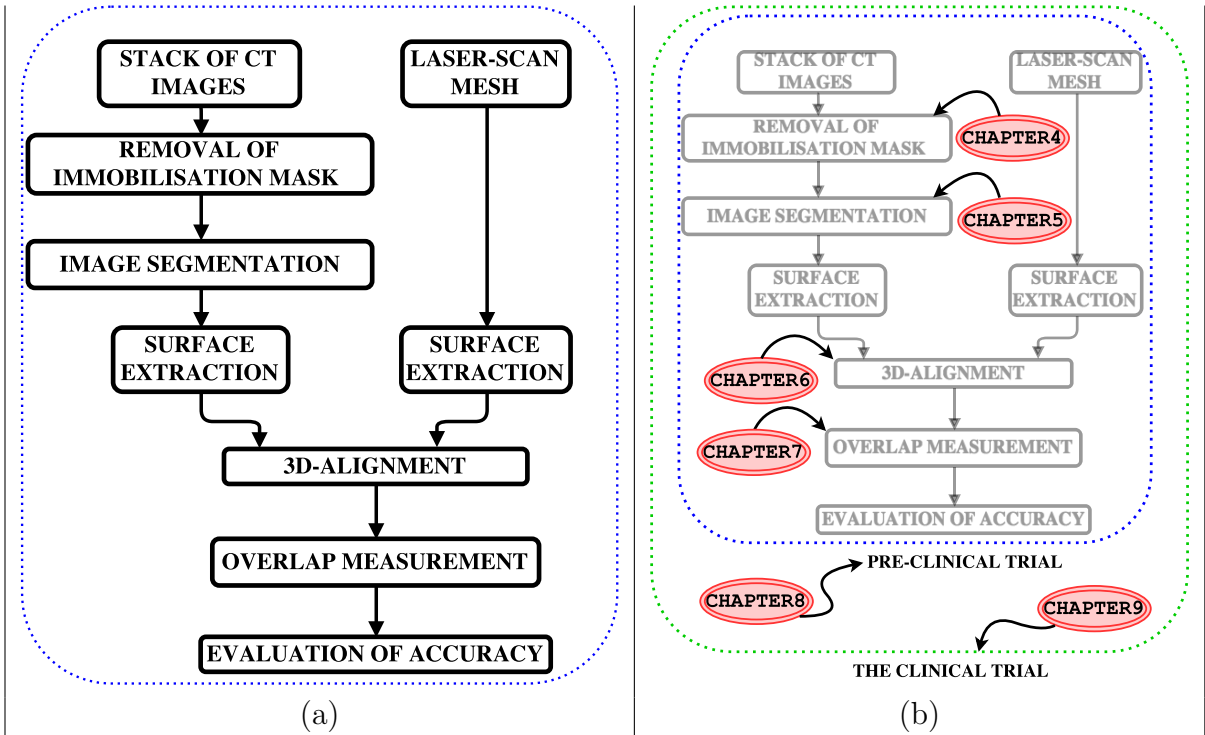


Figure 3.1: (a) A general schema represents the evaluation process in our study (b) A schema points in which chapter each phase of the evaluation process is presented.

radiotherapy treatment for head and neck cancer at the Norfolk and Norwich University Hospital (NNUH) NHS Foundation Trust are recruited by the oncology team. Treatment progresses normally and the CT planning data are acquired. Additional data, captured by a hand held laser scanner are also gathered (see Chapter 9 for more details about the clinical trial).

As we mentioned in Chapter 1 immobilisation masks are used to immobilise patients undergoing radiotherapy treatment for tumours affecting the head and neck. Consequently the CT slices of those patients that are normally acquired within oncology departments include immobilisation masks (see Figure 3.2). Manually editing the data to remove artefacts due to the mask is time consuming and error prone. This challenge is addressed in this thesis in Chapter 4 and a fast and automatic approach to edit the immobilisation mask in CT images is presented and evaluated.

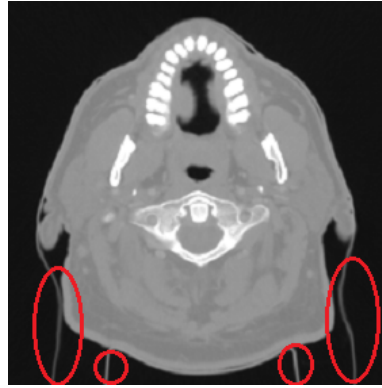


Figure 3.2: Example of CT slice which involves immobilisation mask.

After automatically removing the artefacts and preprocessing the CT images, the head is segmented from successive CT slices. We tested five different segmentation techniques for this purpose. The experimental work and the outcomes of the segmentation process is presented in Chapter 5. We then use the Marching Cubes to construct a 3D model of patient's head. To avoid confusion, it is important here to mention that there are some common steps between the evaluation pipeline process presented in this chapter and the proposed treatment pipeline presented in Chapter 1.

As Figure 3.1(a) shows, The 3D-alignment between the laser-scan model and the CT-derived model is one of the essential parts of this evaluation pipeline. The details of the process that we follow to automatically align the two models are presented in Chapter 6. The overlap measurements are calculated after our system aligns automatically both of the 3D models. The overlap measurements produces readings that determine to which degree is the overlap between the laser-scan model as a ground-truth and the CT-derived model as an examined model. More details on the overlap measurements are explained in Chapter 7.

The evaluation of different segmentation techniques is performed by applying each segmentation technique over the stack of 2D images (see Figure 3.3). So the resultant

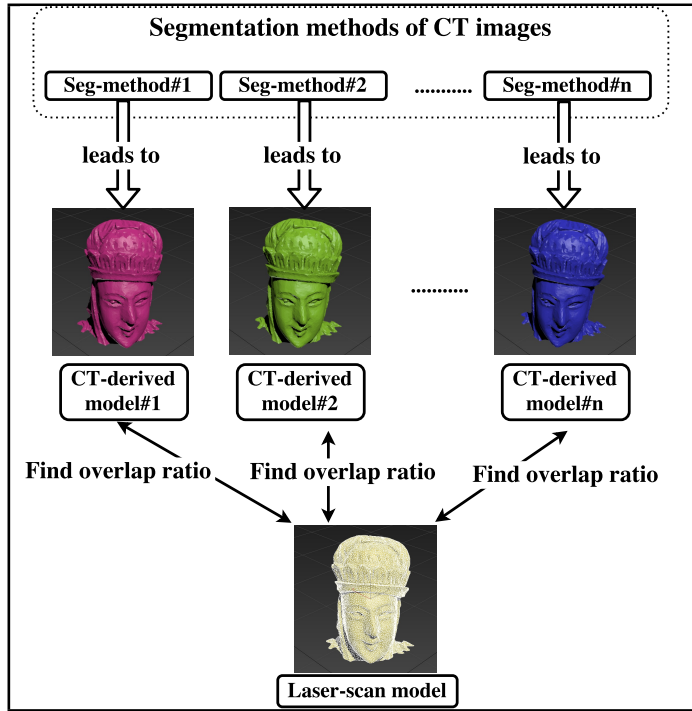


Figure 3.3: Different segmentation techniques generate different CT models. Each CT model is evaluated with regard to laser-scan model.

overlap measurement is considered as an evaluation of the accuracy of the applied segmentation technique.

Figure 3.1(b) illustrates graphically the evaluation pipeline process and which chapter covers each stage of this evaluation pipeline. A pre-clinical trial is presented in Chapter 8 in which the evaluation pipeline was employed over some 3D printed homogeneous objects. In Chapter 9 we present the details, experiments and outcomes of our clinical trial (IRAS project ID:209119, REC reference:16/YH/048).

## 3.2 Data Sets

This section presents an overview on the different data sets that are used through this thesis. The description, properties and sources of these data sets are tabulated in Table 3.1.

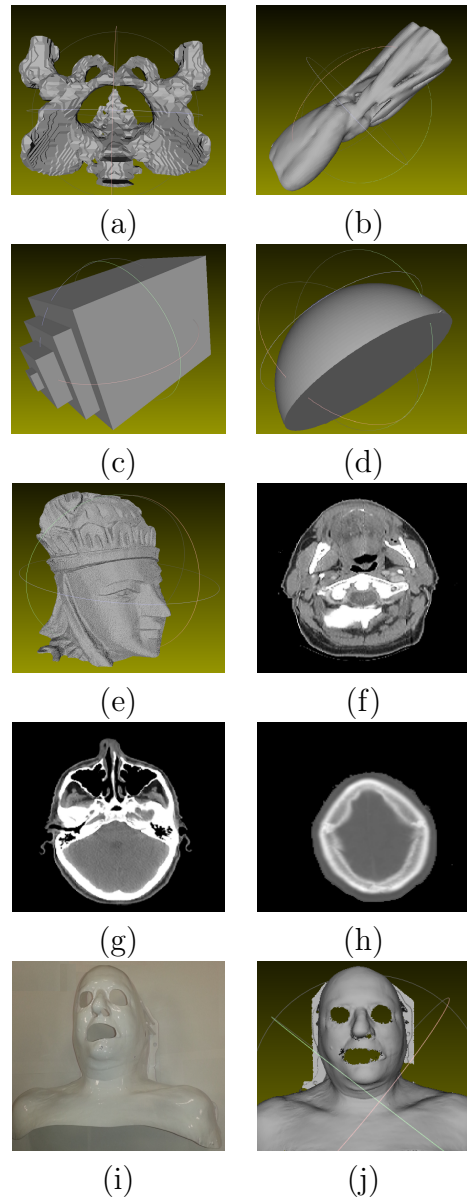


Figure 3.4: The different data sets used in this study. (a), (b), (c), (d) and (e) display surface meshes represent respectively real pelvis, real knee, plastic object in a shape of nested cubes, plastic object in a shape of dome, and the Cantonese head. (f) and (g) represent one CT image slice for two CT data sets of human head from TCIA. (h) represents one CT image slice for one of the three data sets that we got from Leeds. (i) represents the perspex mask and (j) represents the surface mesh of this mask.

Table 3.1: Description of data sets used in this Thesis.

Name & Format	Source	Properties
<b>Pelvis</b>		
STL file	Able Software Corp (Lexington, USA)	Mesh surface/ Pelvis File-size =750 KB (7625 vertices)
<b>Knee</b>		
STL file	The Biomedical 3D Printing Community (embodi3D LLC)	Mesh surface/ Knee File-size =2665 KB (26651 vertices)
<b>Cubes, Dome</b>		
STL file + CT DICOM images	Ipswich Hospital NHS Foundation Trust, Suffolk, UK	CT images (helical, pitch = 0.562:1, collimation 16x0.625 mm (10mm), 512 x 512 x 60 for the cubes, 512 x 512 x 129 for the dome). STL file-size of cubes=6299 KB and of dome=155478 KB
<b>Cantonese head</b>		
STL file + CT DICOM images	Combining X-Ray Micro-CT Technology and 3D Printing project [43]	CT images (helical, pitch = 0.562:1, collimation 16x0.625 mm (10mm), 512 x 512 x 180). STL file-size =849 KB
<b>Head1, Head2</b>		
CT DICOM images	The Cancer Imaging Archive (TCIA): a project funded by the National Cancer Institute	CT images (512x512x130, 512x512x156, pixel-spacing 1.08x1.08 mm 0.98x0.98 mm, slice-thickness 3.14 mm)
<b>Head3, Head4, Head5</b>		
CT DICOM images	St James's University Hospital NHS Foundation Trust, Leeds, UK	CT images (512x512x155, 512x512x146, 512x512x151, helical, pixel-spacing 1.367x1.367 mm, slice-thickness 2.5 mm)
<b>Clinical Trial/Perspex Mask</b>		
STL file + CT DICOM images	Collaborative project (UK) between the University of East Anglia, University Campus Suffolk and Norfolk and Norwich University Hospital	CT images (512x512x90, helical, pixel-spacing 0.9765x0.9765 mm, slice-thickness 2.5 mm). STL file-size = 6198 KB

The first dataset [95], shown in Figure 3.4(a), represents a surface produced from pelvis CT images and saved in STereolithography (STL) file format. The second dataset [96], shown in Figure 3.4(b), represents a surface produced from knee CT images and saved in STL format.

The third and the fourth data sets, shown in Figure 3.4 (c) and (d) respectively, represent two plastic objects in a shape of nested cubes and dome (hemisphere). These two objects were initially designed digitally with known dimensions and then printed in the 3D-printing lab in Computing Sciences School at University of East Anglia. The fifth data set, shown in Figure 3.4 (e), represents a 3D-printed scaled head of a Cantonese chess piece that were delicately carved from ivory throughout the 19<sup>th</sup> Century. This object was produced using a 3D printer by Laycock et al. [43]. CT data

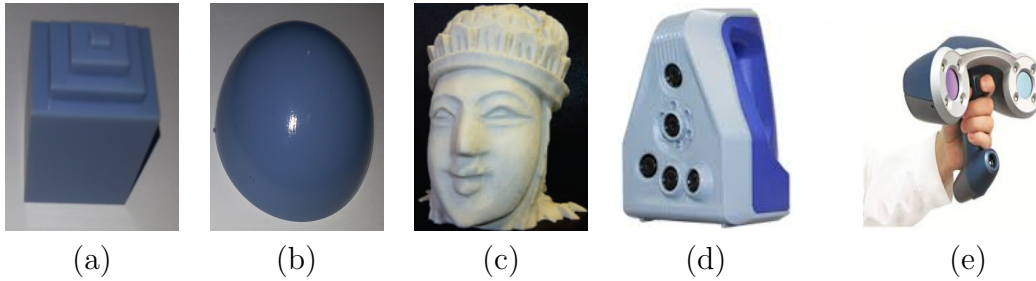


Figure 3.5: Plastic objects in a shape of (a) Cubes and (b) Dome. Examples of CT image slices of (c) Cubes and (d) Dome. The hand-held laser scanner (Artec Space SpiderTM from Artec 3D, Luxembourg) that we used to scan the plastic objects are shown in (e).

sets of those three objects (i.e. cubes, dome, and the Cantonese head) were acquired at Ipswich Hospital, UK. We also scanned these three objects using a hand-held laser scanner (Artec Space SpiderTM laser scanner from Artec 3D, Luxembourg) for the cubes and the dome, and (REVscanTM laser scanner from Handyscan 3D Creaform, Canada) for the Cantonese head. We performed the laser-scanning for the cubes and the dome in University Campus Suffolk, UK, and performed the laser-scanning for the Cantonese head in a local company (Nexus training & resources for engineering, Gt Yarmouth, Norfolk, UK [97]). Figure 3.5(a), (b) and (c) display photos for the nested cubes, dome and the Cantonese head respectively. The two hand-held laser scanners that we used to scan these three objects are shown in Figure 3.5(d) and (e).

Two other data sets (Head1 and Head2) were downloaded from the Cancer Imaging Archive (TCIA)/Head-Neck-Cetuximab [98, 99]. These two data sets represent stack of CT image slices for two subjects who have had CT scanning for their heads. Examples of two CT images slices of those two humans are displayed in Figure 3.4 (f) and (g). We also used three other data sets (Head3, Head4 and Head5) from St James's University Hospital at Leeds, UK. These three data sets also represent stack of CT images for three subjects. An examples of a CT image from those images is displayed in Figure 3.4 (h). The eleventh dataset, shown in Figure 3.4 (i), represents

Table 3.2: Showing in which chapter each data set is used.

Data Set	Ch.4	Ch.5	Ch.6	Ch.7	Ch.8	Ch.9
Cubes			X	X	X	
Dome			X	X	X	
Cantonese			X		X	
Pelvis				X		
Knee				X		
Head1	X			X		
Head2	X			X		
Head3	X					
Head4	X					
Head5	X					
Clinical Trial		X				X

a Perspex mask of a patient who have a neck cancer. The CT scan of this patient is gotten based on our registered clinical trial (IRAS project ID:209119, REC reference:16/YH/0485, Sponsor: University of East Anglia, Health Research Authority, NHS, UK). We also had a laser-scan for the Perspex mask itself using a hand-held laser scanner (Artec Space SpiderTM laser scanner from Artec 3D, Luxembourg).

Since each stage (and then each chapter) of the work plan has its own field and evaluation procedure, we employed different data sets in this thesis. Table 3.2 shows in which chapter each data set has been used. In Chapter 4 our aim was to validate the accuracy of our approach to remove immobilisation masks from CT imagery and then we used five different CT data sets (738 CT images) to run our approach. The “Perspex Mask” data set is employed in Chapter 5 to evaluate the accuracy of different segmentation techniques. In Chapter 6 we were interested in development of an automatic approach to align 3D models and then we used three objects of which we have different scans of different poses to prove the accuracy of the alignment approach. The target of Chapter 7 is to develop and validate the reliability of a proposed model for overlap measurements. This model accepts as inputs two surfaces, two volumes, or one surface and one volume. Consequently we used different groups of data sets

which represent surfaces and volumes. Our interest in Chapter 8 is to evaluate the accuracy of our automatic pipeline over homogeneous objects for which we have two scans (i.e. laser-scan and CT-scan). For that reason we run the experiments of this chapter over the cubes, dome and the Cantonese head. The experimental works that are displayed in Chapter 9 are run over the clinical trial data sets.

### 3.3 Summary

This chapter presented an overview of the chapters of this thesis. It described the topics that have been covered in each chapter. The evaluation pipeline was also described in this chapter since the main steps of this pipeline forms the core of the next chapters. The description, properties and sources of the data sets which were used in this thesis are presented in details. The next chapter presents the automatic approach that we developed to remove artefacts in CT slices in order to be ready for segmentation.

# Chapter 4

## Automatic Removal of Immobilisation Masks from CT Imagery with Particle Swarm Optimisation

Radiotherapy planning CT data sets for those patients who have HNC are currently captured with the immobilisation mask fitted. Manually editing the CT images to remove artefacts due to the mask is time consuming and error prone. This chapter presents a fast and automatic approach that removes image artefacts due to fixations in CT images without affecting pixel values representing tissue. The proposed approach is tested on five CT data sets. The results show that the proposed approach achieves an average specificity of 92.01% and sensitivity of 99.39%. We also present results showing how fractional order Darwinian particle swarm optimisation has been employed to speed up the process.

Section 4.1 provides an introduction to the artefacts in CT images due to the mask for those patients who have Head-and-Neck Cancer. Section 4.2 presents a description on Particle Swarm Optimisation and its uses in medical image segmentation. The proposed approach for the removal of immobilisation masks from CT images is explained in Section 4.3. The experimental work performed to evaluate the approach

is discussed in Section 4.4 and the results are presented in Section 4.5.

## 4.1 Introduction

CT data used for planning HNC radiotherapy treatment contain artefacts due to the mask (see Figure 3.2 in Chapter 3) which can make planning more difficult and can affect the process of constructing the volume from the CT images as it is required in our research.

Segmentation of the brain, lateral ventricles, and skull are made more complicated by artefacts due to the mask. For example [11] and [5] need to edit the CT images to render a reconstructed 3D CT volume of the head. Removing the mask by manually editing individual CT image slices, is time consuming and prone to errors particularly in the regions where the mask contacts the skin. Development of a robust approach to automatically remove the masks from the CT slices represents an appreciable saving in time and avoids the possibility committing manual errors.

There are numerous studies related to the segmentation and identification of the head/intra-cranial structures in the CT images [100, 101, 102, 103] but in our knowledge, the study that is included in this chapter is the first to present a fully automatic approach for removing CT image artefacts due a fixation mask. Our algorithm employs an extension of Otsu's method [104], which classifies pixels as belonging to one of many classes using multi-level thresholding. Exhaustive search for multiple thresholds requires the evaluation of  $(n + 1)(D - n + 2)^n$  combinations of thresholds [105, 106] where  $n$  represents the number of thresholds and  $D$  represents the absolute difference between the maximum and minimum image pixel value. Since pixel intensities in DICOM images (Digital Imaging and COmmunications in Medicine) are represented by 16-bit signed integers this can be very time consuming. The range of values that DICOM images do normally have lies in [-1000, 3000]. So if

we need, for example, to apply the exhaustive search (i.e. brute-force) method to look for the optimal five thresholds that segment a DICOM image, then we need for  $(5 + 1)(4000 - 5 + 2)^5 = 6.1210 * 10^{18}$  combinations of thresholds to be evaluated. Taking into consideration that this evaluation of large number of combinations is repeated normally more than 100 times (since scanning human head using CT scanner with normal resolution leads to produce a stack of CT slices of more than 100 images), then this implies that the exhaustive search method will be absolutely undesirable in terms of speed. To address this we test three optimisation techniques: Particle Swarm Optimisation (PSO)[107], Darwinian Particle Swarm Optimisation (DPSO)[108] and Fractional Darwinian Particle Swarm Optimisation (FDPSO) [109] in order to speed up the segmentation process.

## 4.2 Background

### Otsu's Method

Otsu's method [104] is a common approach in image segmentation field used to automatically perform clustering-based image thresholding [110]. The basic assumption of Otsu's approach, as shown in Figure 4.1, is that the image contains two classes of pixels (i.e. foreground pixels and background pixels). It then computes the optimum threshold separating the two classes so that their inter-class variance (i.e. between-class variance or the variance within the class) is maximal. An extension of the basic assumption of Otsu's method to multi-level thresholding, is presented in [111]. We refer to this extension as multi-Otsu method.

### Optimisation Techniques

Numerous artificial intelligence and machine learning algorithms have been widely applied in image segmentation field to segment non-medical images (e.g. modified

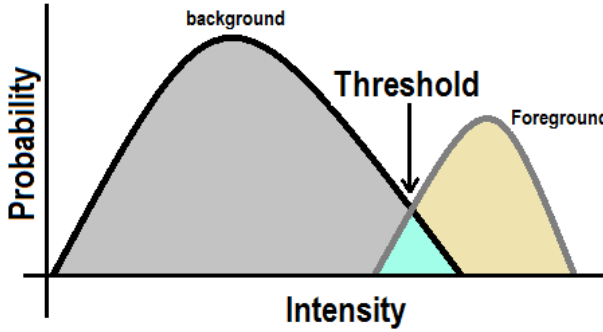


Figure 4.1: A chart represents the basic assumption of Otsu's method.

bacterial foraging algorithm was used in [112], artificial bee colony in [113], Cuckoo search algorithm and wind driven optimization in [114], particle swarm optimisation based in [115], differential evolution in [116] and genetic algorithms in [117]).

Numerous studies have also applied the PSO, DPSO and FODPSO algorithms on image segmentation (e.g. the authors of [118] applied those algorithms over hyperspectral remote sensing images which contain numerous number of data channels). In the context of medical images, there are a number of studies that applied the traditional form of the PSO algorithm to segment medical images (e.g [119, 100, 120, 121, 122]).

## PSO-based techniques

Particle swarm optimization (PSO) is a population based stochastic optimization algorithm developed in 1995 [107] inspired by social behaviour of bird flocking or fish schooling in search of food. It is basically initialized with a population of random solutions and searches for optima by updating generations. The basic drawback of the PSO algorithm is that there is a possibility, as other optimisation algorithms, to be trapped in a local optima. Darwinian particle swarm optimization (DPSO) introduced in 2005 [108] as an extension to the PSO algorithm by adding the natural selection mechanism (i.e. survival of the fittest) to improve the ability of the PSO

algorithm to escape from local optima. In DPSO, many parallel PSO algorithms, each one forms a swarm, operate on the same search space. The fractional-order Darwinian PSO (FODPSO) [109] algorithm was published in 2012 as an extension to the DPSO algorithm. In the FODPSO, fractional calculus concepts are used in order to control the convergence rate of the DPSO.

### Particle Swarm Optimisation (PSO)

Particle swarm optimisation (PSO) algorithm is inspired in the way swarms act and its elements move in a synchronized way. It is based on a population initialized with a random solutions called particles. Each particle is distinguished by its own position and velocity. Equations (4.2.1) and (4.2.2) describes how the velocity  $v_{id}$  and position  $X_{id}$  are updated at each iteration  $k$ . Each particle has a kind of memory which stores the position where it had the lowest cost ( $X_{pbest_{id}}$ ), and the position of the best particle in the population ( $X_{gbest_d}$ ).

$$V_{id}(k) = wv_{id}(k-1) + c_1r_{1id}(k)(X_{pbest_{id}} - X_{id}) + c_2r_{2id}(k)(X_{gbest_d} - X_{id}) \quad (4.2.1)$$

$$X_{id}(k) = X_{id}(k-1) + V_{id}(k) \quad (4.2.2)$$

In equations (4.2.1) and (4.2.2),  $w$  represents the inertia weight,  $r_1$  and  $r_2$  are random numbers with a uniform distribution in the range  $[0,1]$ , and  $c_1$  and  $c_2$  are assigned weights to the local and global best solutions respectively.

Algorithm 1 represents the basic steps that PSO algorithm follows until it reaches the stopping criteria. It is obvious that the algorithm starts by initialising some parameters for the swarm. Those parameters include the population-size, number-of-iterations,  $c_1$ (cognitive weight),  $c_2$ (Social weight),  $w$ (Inertial factor), and  $V_{max}$  and  $V_{min}$  to set the limits of velocities. After that, the algorithm iterates through all particles to calculate the fitness function. Notice that the fitness function in this study will be the inter-class variance between pixels intensities. Our aim is to search for the

---

**Algorithm 1** Steps of PSO Algorithm

---

```

Initialize parameters of particles;
repeat
    forall particles do
        calculate fitness  $f$ 
    end
    forall particles do
        update  $V_{id}(k)$  according to equation (4.2.1)
        update  $X_{id}(k)$  according to equation (4.2.2)
    end
     $t = t + 1$ 
until stopping condition;

```

---

threshold(s) that maximise this fitness value to global optima. The algorithm will iterate again through all particles to update the value of the velocity  $V_{id}(k)$  and the location of the new position  $X_{id}(k)$ . Those iterations will be repeated until stopping criteria happen. These criteria includes setting a maximum number of iterations or stopping after executing a fixed number of iterations without giving any enhancement.

### Darwinian Particle Swarm Optimisation Algorithm (DPSO)

A general problem with optimization algorithms is that of becoming trapped in a local optimum. This leads a specific technique to work well on one problem but may fail on another one. Tillett et.al. proposed an approach, named Darwinian PSO [108] and based on natural selection, in which when a search have a tendency to a local optimum, the search in that area is basically ignored and another area is searched instead. More than one swarm exist in DPSO. Each swarm separately behaves like a normal PSO algorithm with some rules controlling the group of swarms that are intended to simulate natural selection.

Algorithm 2 displays the internal processes that are performed by the DPSO algorithm. The algorithm starts by setting initial values in a collection of parameters.

Those parameters include number of swarms, maximum and minimum possible number of swarms, maximum and minimum possible population size in addition to the basic parameters of the traditional PSO. It is worthy to notice that the swarm in the DPSO algorithm spawns (reproduce) a new particle if it finds a new global optimum, and a particle is removed if the swarm has been unsuccessful in achieving a better fitness in a fixed number of steps.

---

**Algorithm 2** Steps of DPSO Algorithm

---

```

Initialize parameters of swarms;
repeat
    forall swarms do
        forall particles do
            calculate fitness  $f$ 
        end
        forall particles do
            Update particle Bests
        end
        forall particles do
            Move particle
        end
        if swarm gets better then
            Reward swarm, spawn particle and extend swarm life
        end
        if swarm has not enhanced then
            Delete particle and reduce swarm life
        end
    end
    forall swarms do
        Allow the swarm to spawn
    end
    Delete failed swarms
until stopping condition;

```

---

### Fractional Order Darwinian Particle Swarm Optimisation Algorithm (FODPSO)

The name ‘fractional’ PSO derives from the use of fractional calculus. The fractional calculus is a generalization of the ordinary differentiation and integration to

non-integer order [123]. There are numerous uses of fractional calculus in physics, mechanics, chemistry, computational mathematics and others. The basic idea that stands behind the FODPSO algorithm is that this algorithm utilises the fractional calculus concepts in order to control the convergence rate of the DPSO algorithm. Those systems that comprise the using of fractional processes reveal residual memory and their fractional order is understood as a measure of the memory strength [124, 125].

Equation 4.2.3 presents the Grunwald-Letnikov description based on the concept of fractional differential of a general signal  $x(t)$ :

$$D^\alpha[x(t)] = \lim_{h \rightarrow 0} \left[ \frac{1}{h^\alpha} \sum_{k=0}^{+\infty} \frac{(-1)^k \Gamma(\alpha + 1) x(t - kh)}{\Gamma(k + 1) \Gamma(\alpha - k + 1)} \right] \quad (4.2.3)$$

where  $\Gamma$  is the gamma function and  $\alpha$  is the fractional coefficient such that  $\alpha \in \mathbb{C}$ . It is worthy to notice that while an integer-order derivative is evaluated as an finite series, the fractional-order derivative is evaluated as an infinite number of terms. Consequently, integer-order derivative behaves like a local operator, while fractional-order derivative behaves like a structure that has a memory of all past events [109].

### 4.3 The Proposed Approach

The basic steps of the proposed approach [126] are presented in Figure 4.2. The algorithm applies FDPSO ‘slice-by-slice’ to segment the image to six different classes under Otsu’s criterion. Section 4.4 explains that we found segmenting the image into six different classes empirically classifies all or most of the pixels belonging to the mask as one class. Algorithm 1 implements a heuristic search method to find pixels in the labelled image that represent the immobilization mask and background.

Algorithm 1 further refines the output of the FODPSO segmentation. We assume the top middle pixel represents the image background (air) and search the labeled

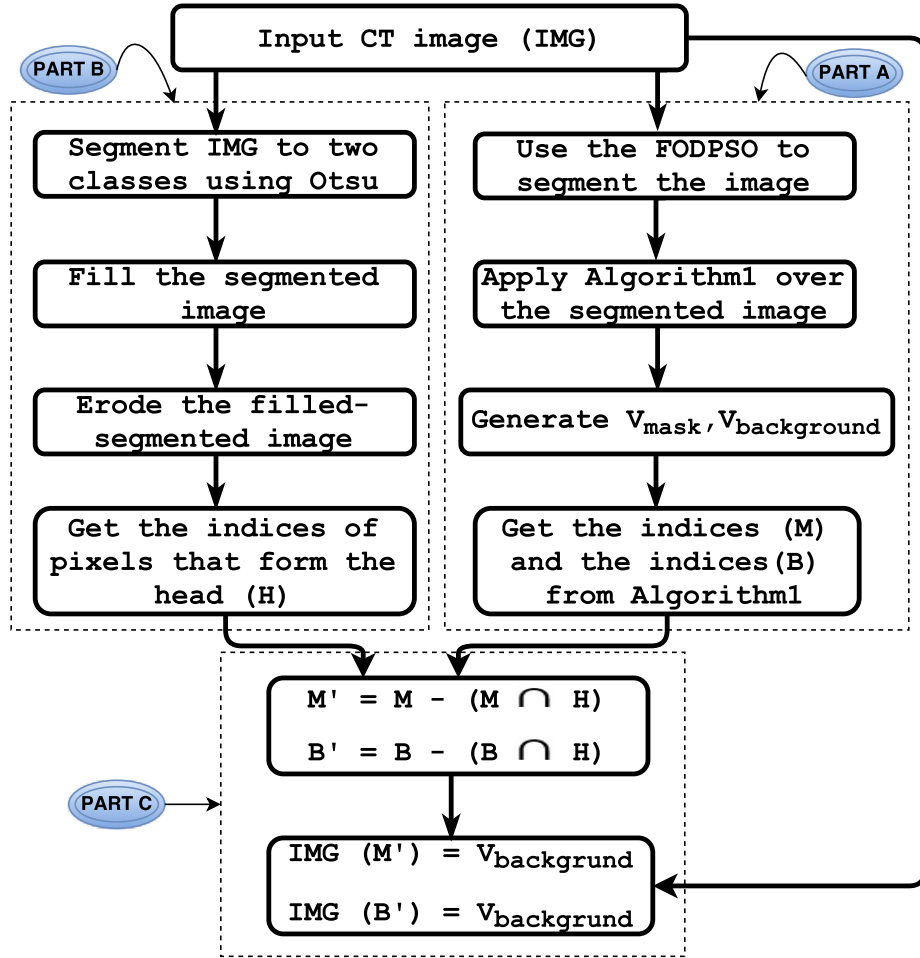


Figure 4.2: Overview of the proposed approach.

image until we find a different pixel value (See the pixel in red square in Figure 4.3). This pixel is assumed to belong to the class mask. Using these pixel labels we identify sets of pixels  $\{M\}$  and  $\{B\}$  that represent the mask and background respectively.

Figure 4.4 illustrates that  $\{M\}$  and  $\{B\}$  sometimes include erroneous pixels because the FODPSO segmentation process groups these as one cluster. The sets  $\{M\}$  and  $\{B\}$  contain pixels that are misclassified because the FDPSON algorithm only uses intensity to cluster pixels. In our experiments, illustrated in Figure 4.4 we found that the misclassified pixels are always located inside the skull. we correct this problem by recovering the coordinates of those pixels located within the skull and excluding

---

**Algorithm 1** Finding the pixels that represent the immobilization mask and those that represent the background pixels

---

```

1: height  $\leftarrow$  height_of_image
2: width  $\leftarrow$  width_of_image
3: mid_col  $\leftarrow$  the index of the middle column in the image
4: s  $\leftarrow$  Get the segmented image.
5: for row  $\leftarrow 2, \text{height}$  do
6:   if s (row, mid_col)  $\neq$  s (1, mid_col) then
7:     v_mask  $\leftarrow$  s (row, mid_col)
8:     v_bg_in_CT_img  $\leftarrow$  IMG (row - 1, mid_col)
9:     Break
10:   end if
11: end for
12: indices_of_mask_pixels (M)  $\leftarrow$  find (s == v_mask)
13: indices_of_bg_pixels (B)  $\leftarrow$  find (s == s (1, mid_col))

```

---

these from  $\{M\}$  by a sequence of operations that split the original CT image to two clusters (i.e. foreground(head) and background(air)) using Otsu's method. We then automatically flood-fill holes that may appear inside the skull using the morphological reconstruction operator described in [127]. Subsequently we proceed by performing an erosion [128] over the filled image. The aim of this process is to erode away the boundaries of the skull thus areas of foreground pixels shrink in size. This will guarantee that none of the pixels that belong to the mask will be excluded later and the only pixels that will be excluded are those which are exist inside the skull. The index of those pixels which represent the skull are recovered from the eroded image as  $\{H\}$ . Equations (4.3.1) and (4.3.2) identify the sets  $\{M'\}$  and  $\{B'\}$  that exclude those pixels within  $\{M\}$  and  $\{B\}$  that are also with the skull  $\{H\}$ .

$$M' = M - (M \cap H) \quad (4.3.1)$$

$$B' = B - (B \cap H) \quad (4.3.2)$$

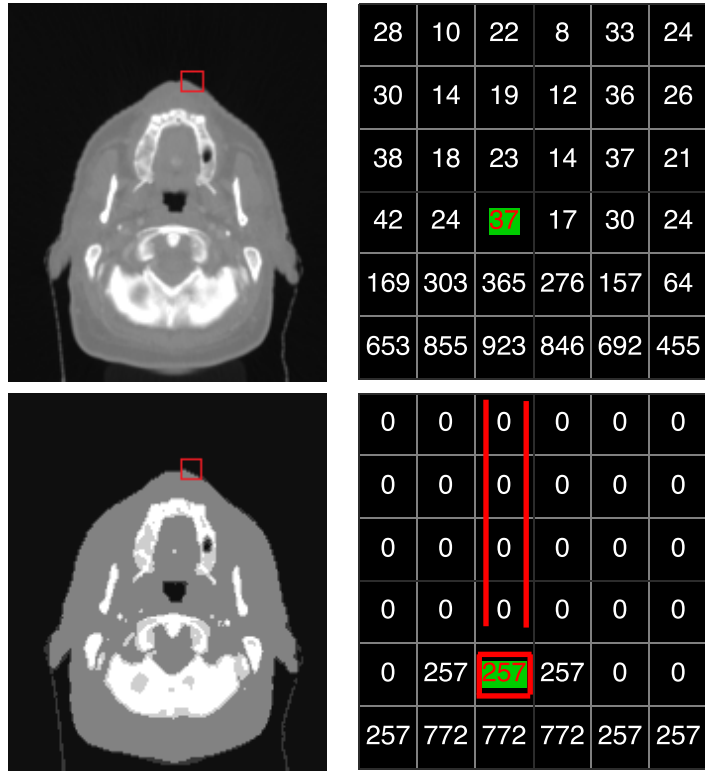


Figure 4.3: A CT image in DICOM format and the same image after segmentation using the FODPSO algorithm along with their pixel region tool.

## 4.4 Experimental Work

### Data set

Five CT data sets from anonymized patients have been used in this study. The first three data sets (512x512x155, 512x512x146, 512x512x151, helical, pixel-spacing 1.367x1.367 mm, slice-thickness 2.5 mm) were acquired at St James's University Hospital NHS Foundation Trust, Leeds, UK and the other two data sets (512x512x130, 512x512x156, pixel-spacing 1.08x1.08 mm 0.98x0.98 mm, slice-thickness 3.14 mm) were downloaded from the Cancer Imaging Archive (TCIA)/Head-Neck-Cetuximab [98, 99].

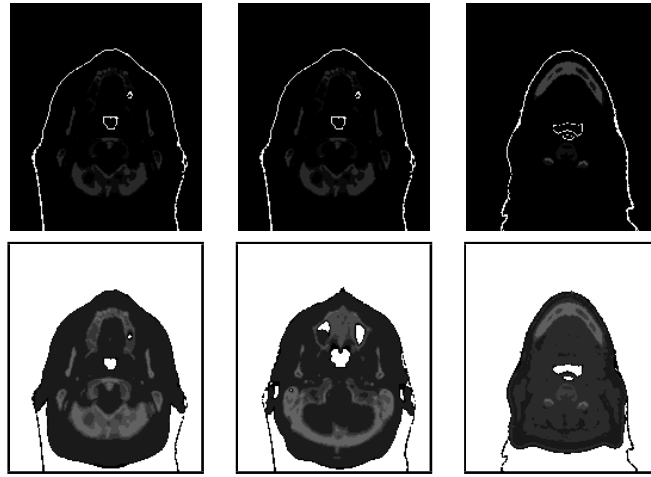


Figure 4.4: Examples of pixels mislabeled by FDPSO. Upper row: pixels mislabeled as  $\{M\}$ ; Lower row: pixels mislabeled as  $\{B\}$ .

## Experiments

The experimental work in this chapter consists of two aspects. In the first aspect we evaluate the PSO-based algorithms for medical image segmentation in terms of speed, accuracy and stability of outcomes. In the second aspect, we evaluate the performance of the automatic approach which is described in Section 4.3.

### 4.4.1 Evaluation of PSO-based algorithms

PSO-based algorithms need to define search space, candidate solutions and global optima. In our case, the pixel intensities of the image will form the search space, the possible threshold values (i.e.  $[min\_intensity, max\_intensity]$ ) will form the candidate solutions, and maximising the interclass variance (i.e. Otsu criterion) will be our global optimisation function. In addition to that, PSO-based algorithms need to initialise some parameters (e.g population size, number of swarms, ...). We chose these empirically. Table 4.1 displays those values. The initial values of those parameters were adjusted experimentally to lead for faster convergence. We found that there is no significant influence on the CPU execution time and the fitness value when a slightly

Table 4.1: Initial parameters of the PSO, DPSO and FODPSO algorithms

Parameter	PSO	DPSO	FODPSO
Population size	180	35	35
Number of iterations	25	25	25
Cognitive weight	0.8	1.1	1.1
Social weight	0.8	0.9	0.9
Inertial factor	1.2	1.2	1.2
Vmax	3	3	3
Vmin	-3	-3	-3
Number of swarms	N/A	5	5
Max number of swarms	N/A	7	7
Min number of swarms	N/A	3	3
Max population size	N/A	50	50
Min population size	N/A	20	20
Stagnancy	N/A	8	8
Fractional coefficient	N/A	N/A	0.8

change is made on the values of those parameters. However, we recommend using those values for any future studies in the field of DICOM images segmentation since we found those values are the most efficient values that speed up the convergence rate.

Evaluating the accuracy of the PSO, DPSO and FODPSO is performed by measuring the fitness (i.e. inter-class variance) for each algorithm and comparing the outputs with the brute-force (BF) method. BF method performs an exhaustive search by evaluating the outcomes of all combinations of threshold values. The fitness in this context refers to the inter-class variance between pixels intensities as it is presented in Section 4.2. Table 4.2 presents the average fitness values generated by the PSO, DPSO and FODPSO algorithms against the fitness value generated by the BF method. It is clear from Table 4.2 that FODPSO algorithm generates either exactly the same or a slightly less fitness value compared to the BF method. This indicates that applying the FODPSO algorithm for segmentation leads to a very high accurate outcomes.

Table 4.2: Average fitness values of Brute-Force, PSO, DPSO and FODPSO algorithms for different number of thresholds over different five data sets

Dataset	Thr.	Brute-Force	PSO	DPSO	FODPSO
Dataset#1 (155 images)	1	3269.09	<b>3269.09</b>	<b>3269.09</b>	<b>3269.09</b>
	2	3773.38	3773.37	<b>3773.38</b>	<b>3773.38</b>
	3	3829.39	3829.36	<b>3829.38</b>	<b>3829.38</b>
	4	3855.43	3854.92	3855.25	<b>3855.39</b>
	5	3871.88	3871.81	3871.72	<b>3871.82</b>
Dataset#2 (146 images)	1	3488.54	3488.49	<b>3488.54</b>	<b>3488.54</b>
	2	4067.33	4067.21	<b>4067.30</b>	<b>4067.30</b>
	3	4142.05	4141.87	4141.91	<b>4142.02</b>
	4	4178.69	4178.11	<b>4178.67</b>	<b>4178.67</b>
	5	4197.88	4197.09	4197.09	<b>4197.86</b>
Dataset#3 (151 images)	1	2374.66	2374.39	2374.54	<b>2374.54</b>
	2	2635.29	2634.50	2634.88	<b>2635.26</b>
	3	2657.87	2654.98	2655.29	<b>2657.84</b>
	4	2679.31	2677.82	2679.19	<b>2679.27</b>
	5	2688.69	2685.58	2686.44	<b>2688.64</b>
Dataset#4 (130 images)	1	3749.77	<b>3749.77</b>	<b>3749.77</b>	<b>3749.77</b>
	2	4264.51	4264.01	4264.32	<b>4264.51</b>
	3	4363.87	4363.12	4363.72	<b>4363.86</b>
	4	4418.97	4417.99	<b>4418.96</b>	<b>4418.96</b>
	5	4435.87	4431.89	4435.82	<b>4435.85</b>
Dataset#5 (156 images)	1	2870.42	2870.18	<b>2870.42</b>	<b>2870.42</b>
	2	3386.32	3385.83	3386.12	<b>3386.32</b>
	3	3462.11	3460.76	3460.76	<b>3462.10</b>
	4	3516.13	3515.73	3516.08	<b>3516.11</b>
	5	3535.57	3533.12	3534.84	<b>3535.53</b>

Table 4.3 displays the average CPU processing time that PSO, DPSO, FODPSO and BF methods need to segment the whole images in each data set. The table confirms that the FODPSO algorithm is always slightly faster than the DPSO algorithm and the DPSO algorithm is significantly faster than the PSO algorithm. It is worth noting that the speed of BF search is similar to, but less than the speed of FODPSO when the number of thresholds equals one. But as the number of thresholds increases, the difference between the speed of BF and the speed of the other three optimisation

algorithms becomes significant. In our case (i.e. removing artefacts due to immobilization masks) we are interested in the case when the number of thresholds equals 5, and then the use of the FODPSO algorithm will make a significant enhancement in terms of speed. We empirically found that segmenting the image into six different classes (i.e 5 thresholds) classifies all or most of the pixels belonging to the mask as one class and this interprets our interest in choosing the number 5 as the number of thresholds. The fractional coefficient used in FODPSO allows the convergence rate of the algorithm to be controlled and this explains why FODPSO outperforms the DPSO algorithm.

The standard deviation was used as an evaluation measurement of stability. Table 4.4 shows that FODPSO produces the most stable results when compared to the PSO and DPSO, and the standard deviation increases as the number of thresholds increase in most cases. Typical results of segmentation using the FODPSO algorithm over one sample image using different number of thresholds is shown in Figure 4.5.

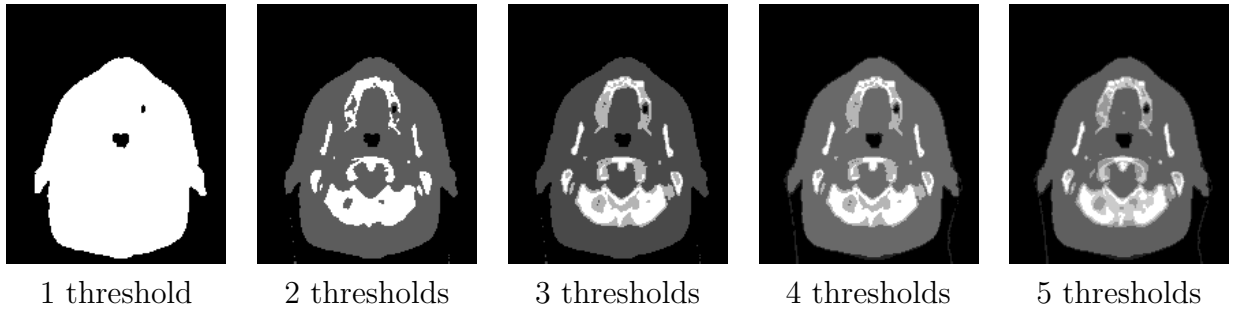


Figure 4.5: Applying FODPSO using different number of thresholds.

#### 4.4.2 Removal of the Immobilisation mask

Figure 4.6(a) displays an example of one of the CT slices from the first data set. A previous study [106] evaluated the use of Particle Swarm Optimisation for medical image segmentation and demonstrated the the FODPSO algorithm delivered high accuracy, stability and speed. We found that segmenting the image to six different

Table 4.3: Average execution time (in sec) of the Brute-Force, PSO, DPSO and FODPSO algorithms for different number of thresholds over different five data sets

Dataset	T.holds	Brute-Force	PSO	DPSO	FODPSO
Dataset#1	1	10.86	33.81	12.15	<b>9.72</b>
	2	235.52	73.12	58.38	<b>56.75</b>
	3	25951	90.85	74.90	<b>72.53</b>
	4	2408545	111.01	90.04	<b>86.82</b>
	5	> 1week	131.06	103.25	<b>98.03</b>
Dataset#2	1	7.28	20.95	8.37	<b>6.96</b>
	2	221.46	65.56	53.39	<b>50.27</b>
	3	24429	84.90	71.50	<b>67.20</b>
	4	1709952	104.41	83.91	<b>79.08</b>
	5	> 1week	123.61	97.84	<b>93.42</b>
Dataset#3	1	7.25	20.20	7.03	<b>6.20</b>
	2	232.58	69.35	56.92	<b>54.85</b>
	3	25118	88.02	70.82	<b>66.54</b>
	4	1809433	107.73	86.51	<b>82.36</b>
	5	> 1week	127.18	100.57	<b>94.81</b>
Dataset#4	1	8.06	16.15	8.51	<b>7.97</b>
	2	195.84	58.54	47.82	<b>46.69</b>
	3	21717	75.35	61.32	<b>60.80</b>
	4	1908530	92.85	76.12	<b>72.91</b>
	5	> 1week	109.67	86.73	<b>84.16</b>
Dataset#5	1	9.26	49.02	8.75	<b>8.09</b>
	2	238.19	70.40	57.81	<b>57.59</b>
	3	26148	90.99	76.13	<b>72.12</b>
	4	2173860	111.82	90.04	<b>84.29</b>
	5	> 1week	132.30	104.59	<b>97.21</b>

classes tends to lead to better results as this number classifies all or most of the pixels belonging to the mask as one class. The FODPSO algorithm delivers significant benefits in terms of execution speed over the BF approach (i.e. exhaustive search) which takes a very long time when the number of clusters equals six. In Section 4.5 we tabulate the time required by the FODPSO algorithm against the time needed by other techniques in order to segment the stack of CT slices comprising each data set. Figure 4.6(b) displays the image after it was segmented to six different clusters using the FODPSO algorithm.

Table 4.4: Standard deviation of fitness for PSO, DPSO and FODPSO after running each algorithm 15 times over different five data sets.

Dataset	T.holds	PSO	DPSO	FODPSO
Dataset#1	1	<b>0</b>	<b>0</b>	<b>0</b>
	2	0.0001	<b>0</b>	<b>0</b>
	3	0.0036	0.0003	<b>0.0002</b>
	4	1.2873	0.0114	<b>0.0105</b>
	5	0.0206	1.2195	<b>0.0190</b>
Dataset#2	1	0.0001	<b>0</b>	<b>0</b>
	2	0.0009	0.0002	<b>0.0001</b>
	3	0.0021	0.0005	<b>0.0002</b>
	4	0.0122	0.0120	<b>0.0113</b>
	5	0.0787	0.0342	<b>0.0341</b>
Dataset#3	1	0.0023	0.0001	<b>0</b>
	2	0.0082	0.0009	<b>0.0001</b>
	3	0.0810	0.0569	<b>0.0015</b>
	4	0.0254	0.0143	<b>0.0061</b>
	5	0.5932	0.5437	<b>0.2903</b>
Dataset#4	1	0.0011	0.0002	<b>0</b>
	2	0.0008	0.0002	<b>0.0001</b>
	3	0.0110	0.0089	<b>0.0073</b>
	4	0.0196	0.0159	<b>0.0161</b>
	5	1.7163	0.0938	<b>0.0884</b>
Dataset#5	1	0.0005	0.0003	<b>0.0001</b>
	2	0.0012	0.0004	<b>0.0001</b>
	3	0.0082	0.0027	<b>0.0011</b>
	4	0.0243	0.0199	<b>0.0190</b>
	5	1.3081	0.0373	<b>0.0361</b>

In Figure 4.6(c-e) we present the output that is generated by part-B of the proposed approach. The image was firstly segmented to two classes (foreground and background) using Otsu’s method. It was then filled automatically and eroded as it displayed in 4.6(e). Part-A and part-B of the proposed approach produced three data structures of indices ( $M$ ,  $B$ , and  $H$ ) and those indices were used to form the final output image which is displayed in Figure 4.6(f). Finally, Figure 4.7 illustrates randomly-selected input images and their outputs after applying the approach.

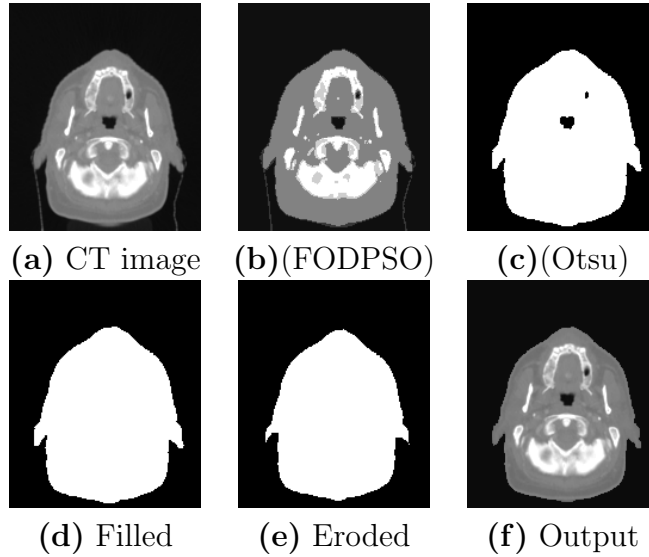


Figure 4.6: An example of a CT slice from the first dataset.

## 4.5 Results, Validation and Discussion

### The Performance of the Approach

We used the **Sensitivity** and the **Specificity** to evaluate the proposed approach as both of them are statistical measures of the performance of a binary classification test. We have identified the True Positive Rate (TPR), False Positive Rate (FPR), True Negative Rate (TNR) and False Negative Rate (FNR) in this context as:

- TPR: percentage of mask pixels correctly identified as mask.
- FPR: percentage of not-a-mask pixels incorrectly identified as mask.
- TNR: percentage of not-a-mask pixels correctly identified as not-a-mask.
- FNR: percentage of mask pixels incorrectly identified as not-a-mask.

The pixels that represent the immobilisation mask were identified by an expert in 25 CT images (5 randomly-selected from each dataset) and compared to the number of pixels identified by the proposed approach. Table 4.5 displays the average values, rounded to the whole number, of TP, FP, TN and FN for each dataset and

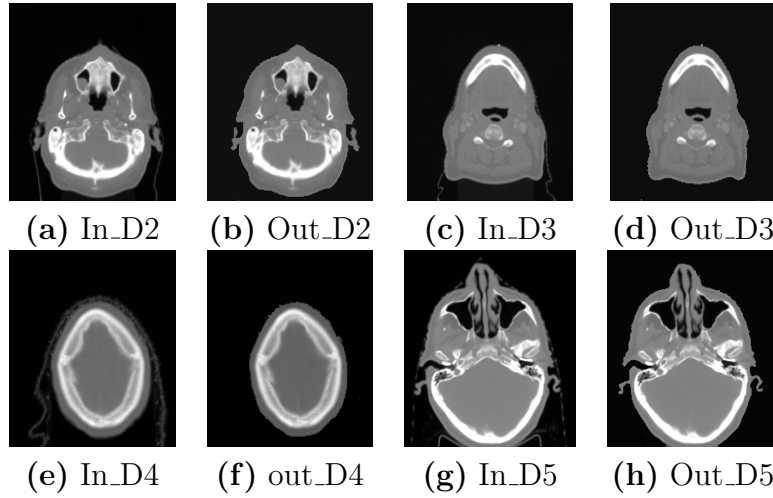


Figure 4.7: One CT slice example from each dataset (Input & Output).

the percentage values of TPR, TNR, FPR and FNR. Table 4.6 displays the sensitivity, also called the true positive rate (TPR), specificity (SPC) and the Number-Of-Observations (NOO) for each dataset.

Table 4.5: The average values of TP, FP, TN, FN, TPR, FPR, TNR and FNR for each dataset

Dataset	TP	TN	FP	FN	TPR	FPR	TNR	FNR
Dataset#1	389	30,239	100	23	94.41%	99.67%	0.33%	5.59%
Dataset#2	403	30,152	154	42	90.56 %	99.49%	0.51%	9.44%
Dataset#3	429	30,199	93	30	93.64%	99.69%	0.31%	6.54%
Dataset#4	1714	29,060	465	203	89.41%	98.42%	1.58%	10.59%
Dataset#5	841	45,371	148	71	92.21%	99.67%	0.33%	7.79%

As is shown in Table 4.6 the average value of the sensitivity (TPR) is 92.01% which indicates to the proportion of positives that are correctly identified (i.e. the percentage of mask pixels which are correctly identified by the proposed approach as mask pixels) and the average value of the specificity (SPC) is 99.39% which points to the proportion of negatives that are correctly identified (i.e. the percentage of not-a-mask pixels who are correctly identified as not-a-mask pixels). The heading 'NOO' in the table indicates to the number of observations which is equivalent to the

Table 4.6: The values of TPR, SPC, and NOO for each dataset

Dataset	TPR	SPC	NOO
Dataset#1	0.9441	0.9967	30751
Dataset#2	0.9056	0.9949	30751
Dataset#3	0.9346	0.9969	30751
Dataset#4	0.8941	0.9842	31442
Dataset#5	0.9221	0.9967	46431
Average	<b>0.9201</b>	<b>0.9939</b>	34,025

number of pixels in each image.

## Handling Exceptions

We applied our approach over five different data sets (total= 738 images) and noticed that the approach did not work on 13 images of them for two reasons. Firstly some CT images include a noise in the middle column on the top of the mask itself, as displayed in Figure 4.8-left and secondly some CT images have disconnected representation of the mask pixels, as displayed in Figure 4.8-middle. We handled the first exception by applying the median filter over the background area in order to remove the noise from the background area, and we handled the second exception by changing the seeking mechanism in Algorithm 1 by searching the segmented image horizontally and vertically from different five start points as displayed in Figure 4.8-right.



Figure 4.8: (left) Example of a CT image includes a noise in the middle column (Middle) A CT image has a disconnected representation of the mask pixels (Right) Defining new start points to seek horizontally.

## 4.6 Summary

This chapter presented an automatic approach for segmenting immobilization masks in Head-and-Neck CT data sets. The approach identifies the pixels that belong to the immobilization mask and replaces their intensity value with that of air, thereby eliminating the mask from the output image. Five different data sets were tested to evaluate the accuracy of the approach. Sensitivity and specificity were used as statistical measures of the performance of the approach in this chapter. The evaluation indicates that the proposed approach is robust and of practical use. Some enhancements to speed up the process using Particle Swarm Optimisation were also presented and tested in the chapter.

Since this chapter presented an approach that removes the fixation and prepares the CT slices for the segmentation process, the next chapter presents the different segmentation techniques that were investigated to segment the CT images before constructing a 3D volume of the head.

# Chapter 5

## Image Segmentation

This chapter presents the part of the thesis which addresses image segmentation. The chapter begins by presenting in Section 5.1 a brief overview on five different segmentation techniques which are employed in this research to segment the CT images. Section 5.2 illustrates the steps that we developed within the framework of Distance Regularized Level Set Evolution (DRLSE) to set the initial level set binary function and to handle the case when more than one contour is found in the final output image. The experimental work is presented in Section 5.3 and the results in Section 5.4 include the outcomes after applying the five segmentation techniques over our dataset. Section 5.5 draws a conclusion for this chapter.

### 5.1 Technical Background

We have presented in Chapter 2 an overview on the basic concepts of image segmentation and we present in this section a brief overview over the five image segmentation techniques that are employed in this research. The five segmentation techniques that we applied and run over our data sets are: Otsu, K-means, Expectation Maximization, Hidden Markov Random Field Model with Expectation-Maximization, and Distance Regularized Level Set Evolution. We have chosen these techniques since they are common image segmentation techniques, widely accepted and tested, and have been

successfully employed for medical image segmentation. In addition to that, since image segmentation techniques are normally categorised in accordance with their primary methodologies based on (1) thresholds, (2) clustering techniques and (3) deformable models [62] then these five techniques represent representative sample for the three main categories of segmentation techniques.

### 5.1.1 Otsu’s method

Otsu’s method [104] is a common method in image segmentation which selects the threshold to minimise the inter-class variance of the foreground and background pixels. It comprises iterating through all the possible threshold values. The details of this method were presented in Chapter 4 Section 4.2.

### 5.1.2 K-Means

The term “K-means” was first used in 1967 [129]. Image segmentation using the K-means approach is one of the common examples of the state-of-the-art clustering methods for image segmentation [130] and it is used in different applications including medical image segmentation [131, 132, 133, 134, 135]. The aim of the K-means approach is to partition  $n$  observations into  $m$  clusters in which each observation belongs to the cluster with the nearest mean. In the context of image segmentation, the K-means takes an  $n$  of pixel values ( $x_1, x_2, \dots, x_n$ ) and partition these pixels into  $m$  sets  $S = \{S_1, S_2, \dots, S_m\}$  in order to minimise the within-set sum of squares ( $wsss$ ) as shown in Equation (5.1.1).

$$wsss = \sum_{i=1}^m \sum_{x \in S_i} \|x - \mu_i\|^2 \quad (5.1.1)$$

where  $\mu_i$  is the mean of pixel values in set  $S_i$ . Notice that  $m$  equals 2 in the case of binary image segmentation since we have just two sets (i.e. black and white).

In this case, consider  $c_m$  is the centre of cluster and  $p(x, y)$  is an input pixel. The K-means algorithm for binary image segmentation is described as follows:

1. Set  $m = 2$ .
2. Initialize the centroids for each cluster with random intensities.
3. For each pixel in the image, calculate the distance  $d$  of their intensities from the centroid intensities as shown in Equation (5.1.2)

$$d = \| p(x, y) - c_m \| \quad (5.1.2)$$

4. Assign all the pixels to the nearest centre based on distance  $d$ .
5. Update the new positions of the centres as shown in Equation (5.1.3)

$$c_m = \frac{1}{m} \sum_{x \in c_m} \sum_{y \in c_m} p(x, y) \quad (5.1.3)$$

6. Repeat from step 3 to 5 for specific number of iterations or until the difference satisfies a threshold value.

The next subsection presents an overview of another algorithm employed in image segmentation named Expectation Maximization.

### 5.1.3 Expectation-Maximization (EM)

The Expectation-Maximization (EM) algorithm presents an intuitive iterative parameter estimation scheme. It relies on finding the maximum likelihood estimates of parameters. Each iteration of the EM algorithm involves two procedures: maximization and expectation. In this approach, alternating steps of expectation and maximization are executed iteratively until convergence [131]. The maximization computes the maximum likelihood estimates by maximizing the expected likelihood

detected on the last expectation step and the parameters detected on the maximization step are then used to initiate another expectation step [136]. The EM algorithm was explained and named in [137]. This algorithm has been employed in image segmentation in different studies [138, 139, 140, 141, 142]. A very detailed description of the EM algorithm is presented in [143, 144].

#### 5.1.4 Hidden Markov Random Field Model and Expectation-Maximization (HMRF-EM)

Markov Random Field Models (MRFM) have been used for image segmentation in different studies [145, 146, 147] by incorporating the spatial relationships among neighbouring labels as a Markovian prior [148]. The Hidden Markov Random Field with Expectation Maximization (HMRF-EM) approach was first presented in [149] in which the authors incorporated the HMRF and the EM approaches into a unified framework. In this framework the likelihood probability parameters are estimated through the EM algorithm [150].

The algorithm can be described as follows. Suppose that we have an image  $M$  consisting of  $n$  pixels  $(m_1, m_2, \dots, m_n)$  where  $m_i$  represents the intensity of pixel  $i$ . The target of HMRF-EM is to infer a configuration of the set of all possible labels  $L = (l_1, l_2, \dots, l_n)$  where  $l_i \in L$  by seeking the labelling  $L^*$  as shown in Equation (5.1.4)

$$L^* = P(M \mid L, \vartheta)P(L) \quad (5.1.4)$$

where the joint likelihood probability is shown in Equation (5.1.5)

$$P(M \mid L, \vartheta) = \prod_i P(M_i \mid L_i, \theta_{L_i}) \quad (5.1.5)$$

where  $P(M_i \mid L_i, \theta_{L_i})$  is a Gaussian distribution function and  $\theta_{L_i} = (\mu_{L_i}, \sigma_{L_i})$ . Notice that  $\vartheta = \{\theta_l \mid l \in L\}$  is the parameter set that is found by the EM algorithm.

HMRF-EM has been employed in image segmentation in different studies [141, 151, 152, 153, 154, 155].

### 5.1.5 Distance Regularized Level Set Evolution (DRLSE)

The level set method was introduced by Osher and Sethian [156]. In the level set method the interface is described by the zero level set [157]. It works by representing a contour as the zero level set of a higher dimensional function, called a level set function (LSF), and formulating the motion of the contour as the evolution of the level set function [2]. The level set framework is now used on a numerous applications, including capturing moving fronts [158], image segmentation [159, 160, 161, 162], image reconstruction [163], moving liquid interfaces [164, 165], image analysis [166], reservoir simulations [167], optimal shape design [168], and computer vision [169]. The details of employing the conventional level set method in the field of image segmentation and active contour models are presented in [170, 169, 171].

The Distance Regularized Level Set Evolution (DRLSE)[2] is a new variational level set form in which the regularity of the LSF is preserved through the evolution process. The derived level set evolution has a unique Forward-And-Backward (FAB) diffusion effect to preserve a desired shape of the LSF. The diagram in Figure 5.1 displays the problems that normally accompany the conventional level set formulation and how the DRLSE technique overcomes these problems.

It is obvious from Figure 5.1 that irregularities is the main drawback that happens during the evolution of conventional level set formulation. The concept of the irregularity in this context is illustrated in Figure 5.2 in which Figure 5.2(a) displays a level set function (LSF) which developed irregularities during its evolution. The LSF evolution in this figure constantly degrades the LSF to a function with undesirable irregularities (i.e. very steep shape in some regions and very flat shape in

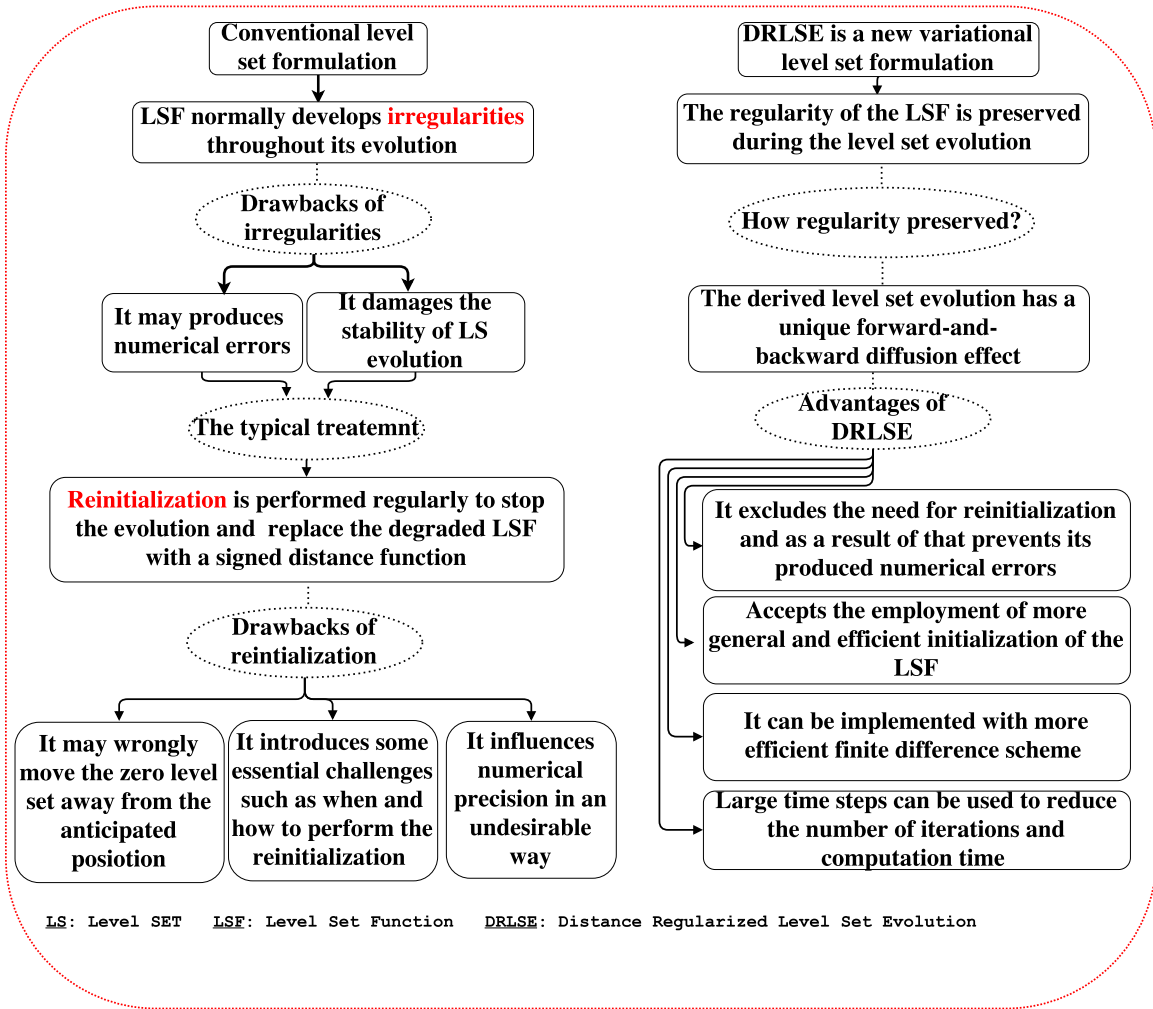


Figure 5.1: A schema represents the problems and drawbacks accompanying the conventional level set formulation (left part) and the reasons that make the DRLSE able to overcome these problems (right part).

other regions). Figure 5.2(b) displays a level set function which applied the DRLSE in its evolution to preserve the regularity through its evolution. The irregularity may lead to numerical errors and destroy the stability of level set evolution. However, the typical treatment for the irregularities problem is the use of the reinitialization. Although the reinitialization is able to replace the degraded LSF with a signed distance function, but there are some drawbacks produced by performing the reinitialization. The drawbacks of the reinitialization include possible wrong movement of the zero

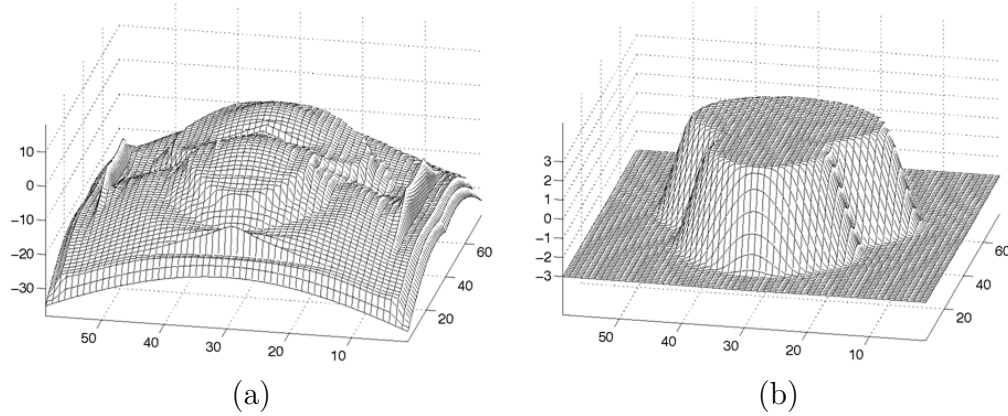


Figure 5.2: Level set function which (a) develops irregularity through its evolution and (b) another level set function in which the regularity is preserved during the evolution (imported from [2]).

level set away from the anticipated position and defining numerical precision in an undesirable way.

On the other hand, the derived level set evolution in DRLSE technique has a unique FAB diffusion effect. Hence, the DRLSE has a number of advantages:

- It eliminates the need for reinitialization and then it avoids all of the reinitialization's drawbacks.
- It accepts the employment of more general initialization of the LSF.
- It can be implemented with more efficient difference scheme.
- It can use large time steps to reduce the number of iterations and computation time.

The authors of the DRLSE technique have applied it to an edge-based active contour model for image segmentation and proved its efficiency and accuracy. They have used this technique to segment a CT image with a tumor in human liver and to segment MR image of a human bladder. The active contour model in the DRLSE

permit the employment of large time steps to reduce iteration numbers and computation time while preserving the numerical accuracy to a very great degree. Given that the active contour models including conventional level set method are not designed to process large amounts of data [172], then the enhancement on the computation time that is offered by the DRLSE will be an important feature.

## 5.2 Our Customisation/Handling of the DRLSE Technique

Applying the DRLSE technique requires to set the initial level set binary function in accordance with your specific application. In addition to that it is possible to have more than one contour as a final output when applying the DRLSE. We present in this section the procedure that we follow to set the initial level set binary function and illustrate the algorithm that we develop to handle the multi-contour case.

### 5.2.1 Setting the Initial Level Set Binary Function

As the DRLSE technique requires the use of an initial LSF, we present a procedure to derive the initial LSF to be used in the context of segmentation. The procedure that we follow to set the initial LSF is illustrated in Figure 5.3. This procedure allows the Region  $R_0$  to be close to the region to be segmented where  $R_0$  represents the region which surrounds the object to be segmented by an initial contour. Consequently a small number of iterations are required to move the zero level set to the desired border of the object.

The process of deriving the initial LSF starts, as illustrated in Figure 5.3, by reading the CT image and applying Otsu method over that image. Notice that the segmented image is stored as temporary image. Automatic image filling is then performed over the temporary image and followed by dilation process to allow the

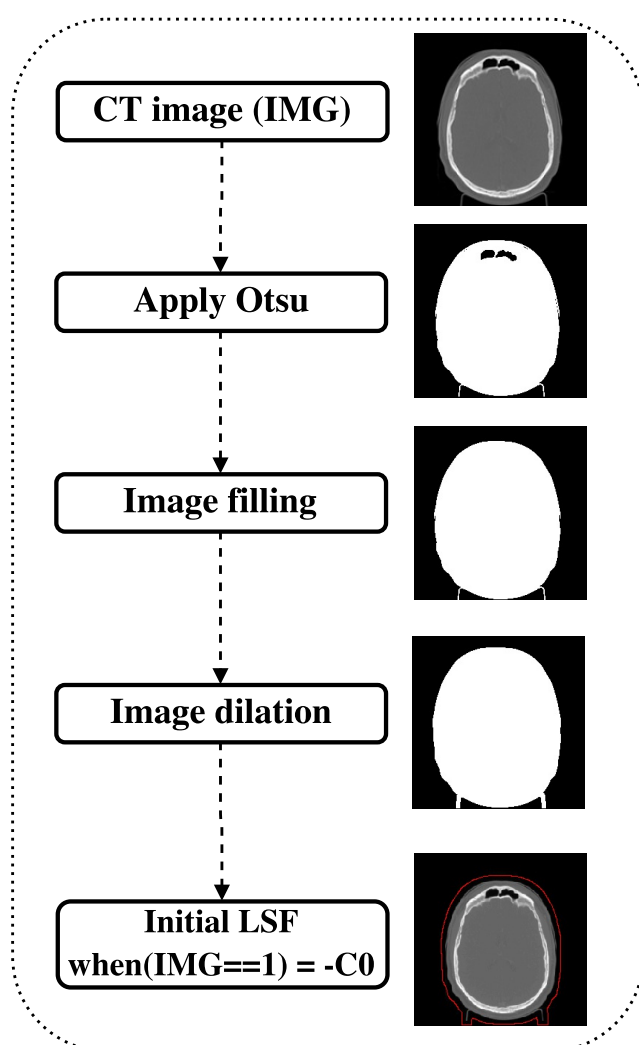


Figure 5.3: A schema showing the procedure that we follow to derive the initial level set binary function.

boundary of object to expand. The borders of the temporary image is then extracted to form the initial LSF for the CT image (see the red contour around the head in the bottom image in Figure 5.3).

### 5.2.2 Handling the Multi-Contour Case

The DRLSE technique may lead to produce more than one contour during its evolution (See Figure 5.4). We present here Algorithm 2 in which we develop a procedure to deal with the case of more than one contour in the final output of the DRLSE technique. The structure of *ContourMatrix* in Algorithm 2 is illustrated in Figure 5.5. As it is shown in the figure, the data structure *ContourMatrix* represents a two-row matrix. The element that lies in first column and second row represents the number of vertices that form the contour line. The remaining columns represent the vertices itself for the contour line. In the case of multi-contour the *ContourMatrix* contains a separate definition for each contour line. For example, the *ContourMatrix* in Figure 5.5 indicates that there are four contour lines. The dotted red circles show the starts of each one of the contour line definitions. The first contour consists of four vertices, the second of three vertices, the third of ninety-five vertices and the last of three vertices. Algorithm 2 is employed when we find that the *ContourMatrix* consists of more than one contour line. The basic operation of this algorithm is to search for the start location of the largest contour line (i.e. the one that has the maximum number of points) and extract the vertices that belong to that contour. This operation is performed in the algorithm through the while loop (line 5 - line 12) by getting the element that lies in first column and second row and storing it in *max\_size*. After that, the algorithm repeatedly skips a number of elements equals to the value of *size\_of\_current\_contour* and compares the value of the new *size\_of\_current\_contour*

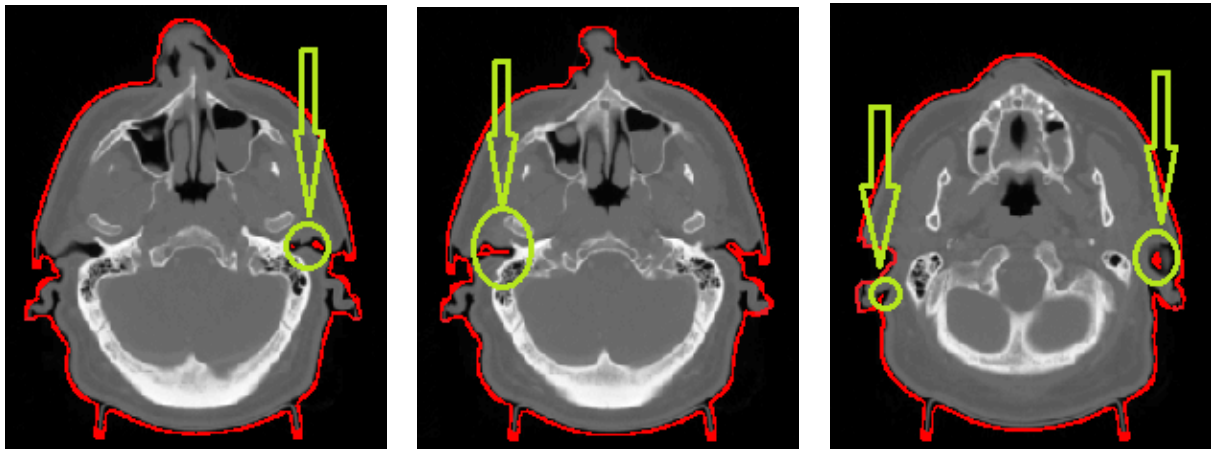


Figure 5.4: Examples of images that have more than one contour.

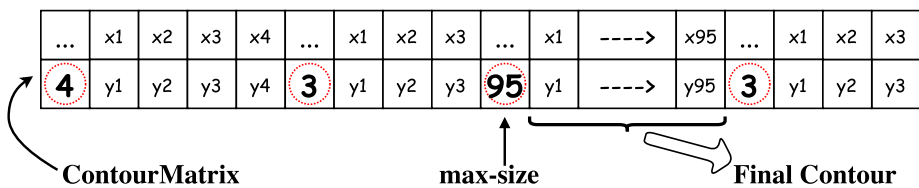


Figure 5.5: Structure of Contour Matrix.

with the value of the `max_size` until it reaches the end of `ContourMatrix`. The algorithm then continues by setting on the pixels which lie inside the largest contour and return the final result as a segmented image consisting of ones and zeros.

### 5.3 Experiments

The experiments in this chapter are performed over the “Perspex Mask” data set which is a part of the data sets of our clinical trial (IRAS project ID:209119, REC reference:16/YH/0485, Sponsor: University of East Anglia, Health Research Authority, NHS, UK). The details of this data set is presented in Chapter 3.

Although a large concentration has been given to propose new segmentation techniques in the literature, a slight interest given to derive a uniform framework to be used in comparing different segmentation approaches and evaluate their performance

---

**Algorithm 2** Handling multi-contour when the DRLSE technique is used in segmentation

---

```

1: loc  $\leftarrow$  1
2: max_size  $\leftarrow$  0
3: size_of_current_contour  $\leftarrow$  0
4: start  $\leftarrow$  0
5: while loc  $<$  (No. of columns of ContourMatrix) do
6:   size_of_current_contour  $\leftarrow$  ContourMatrix(2, loc)
7:   if size_of_current_contour  $>$  max_size then
8:     max_size  $\leftarrow$  size_of_current_contour
9:     start  $\leftarrow$  loc
10:  end if
11:  loc  $\leftarrow$  loc + size_of_current_contour + 1
12: end while
13: for i  $\leftarrow$  1, max_size do
14:   FinalContour(ContourMatrix(2, start + i), ContourMatrix(1, start + i)) = 1
15: end for

```

---

[173]. Accuracy of a segmentation algorithm can be defined as the level to which the segmentation outcomes agree with the ground truth, a so called "gold standard" [174]. In the case when dealing with images of real patients, the ground truth is considered not known. There are some choices that can be considered as a replacement or a substitution for the ground truth [175]. These choices include, but not limited to, using the laser-scan mesh, using manual segmentation by experts, different imaging modality, or another segmentation algorithm known to give accurate outcomes. We employed in our clinical trial the laser-scan mesh as a ground-truth.

The schema that is presented in Figure 5.6 illustrates the procedure that we follow to evaluate the accuracy of each segmentation technique (i.e. evaluate the the similarity ratio between the laser-scan model as a ground-truth and the outcome of each one of the five segmentation techniques). For each one of the segmentation techniques, the stack of CT slices (in DICOM format) is read and segmented. After that a 3D model is constructed from these segmented slices using Marching Cubes algorithm [19]. The laser-scan 3D model, which represents the ground-truth, is then

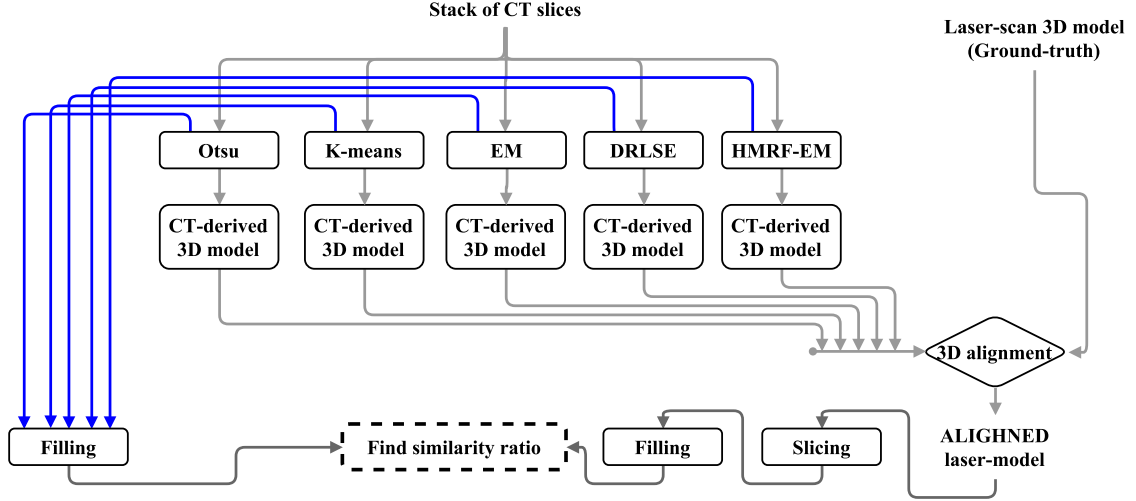


Figure 5.6: A schema illustrates the procedure that we follow to evaluate the accuracy of the five segmentation techniques.

automatically aligned with the CT-derived 3D model. The details of the process of alignment are presented in Chapter 6. The aligned laser-model is then sliced in *z* – *direction* as it is presented in details in Chapter 7. At that point the slices image resulted from the slicing process for the laser-scan model and the segmented CT slices are automatically filled and compared. The comparison is performed between each segmented filled CT slice and its corresponding filled laser image slice. The overlap measurement that we used is Dice similarity coefficient (DSC) [74] which finds the similarity ratio between each corresponding slices from each model. The average similarity ratio is then calculated to represent the final outcome. It is worth mentioning here that the details of the procedure illustrated in Figure 5.6 are clarified and tested in detail in Chapter 6, Chapter 7 and Chapter 8.

## 5.4 Results

The stack of CT slices which represent the head of the patient are segmented five times each time by one of the segmentation techniques that are mentioned before.

Figure 5.7 displays random segmented CT slices generated when applying the Otsu, K-means, EM, DRLSE, and HMRF-EM segmentation techniques to segment the CT slices of the “Perspex Mask” data set. The figure also displays the slices that are generated from the laser-mesh and used as a ground-truth. The techniques display the pixels which belong to the background in black colour and the pixels which belong to the object in white colour. It is clear from the figure that the EM algorithm does not identify well, in some images, the foreground and background pixels. This will lead later to construct the 3D model of the head in an incorrect way. Figure 5.8 displays three random slices that are generated when we sliced the laser-scan mesh. The constructed models that are generated from each group of segmented images are displayed in Figure 5.9.

Table 5.1 displays, for each segmentation technique, the average similarity ratio between the segmented CT slices and the slices obtained from the ground-truth (i.e. laser-scan mesh). Notice that the exact details of the procedure that we follow to obtain these readings are presented in the next three chapters. We present these readings here to give a perception about the performance of each one of the segmentation techniques.

Exploring the values in Table 5.1 leads to a number of observations. The first one is that the DRLSE technique exceeds the other four techniques in terms of accuracy. This is obvious from the table since the value of the calculated average similarity ratio for the DRLSE technique is the highest one. This in turn makes the DRLSE technique a good candidate to be used for segmentation of CT slices for those patients who have Head-and-Neck cancer in order to construct an immobilisation mask for them. The second observation on the readings is that all the employed segmentation techniques, except the EM technique, achieved satisfactory similarity ratio and close to each other results which indicates that the selection of a specific segmentation technique will not

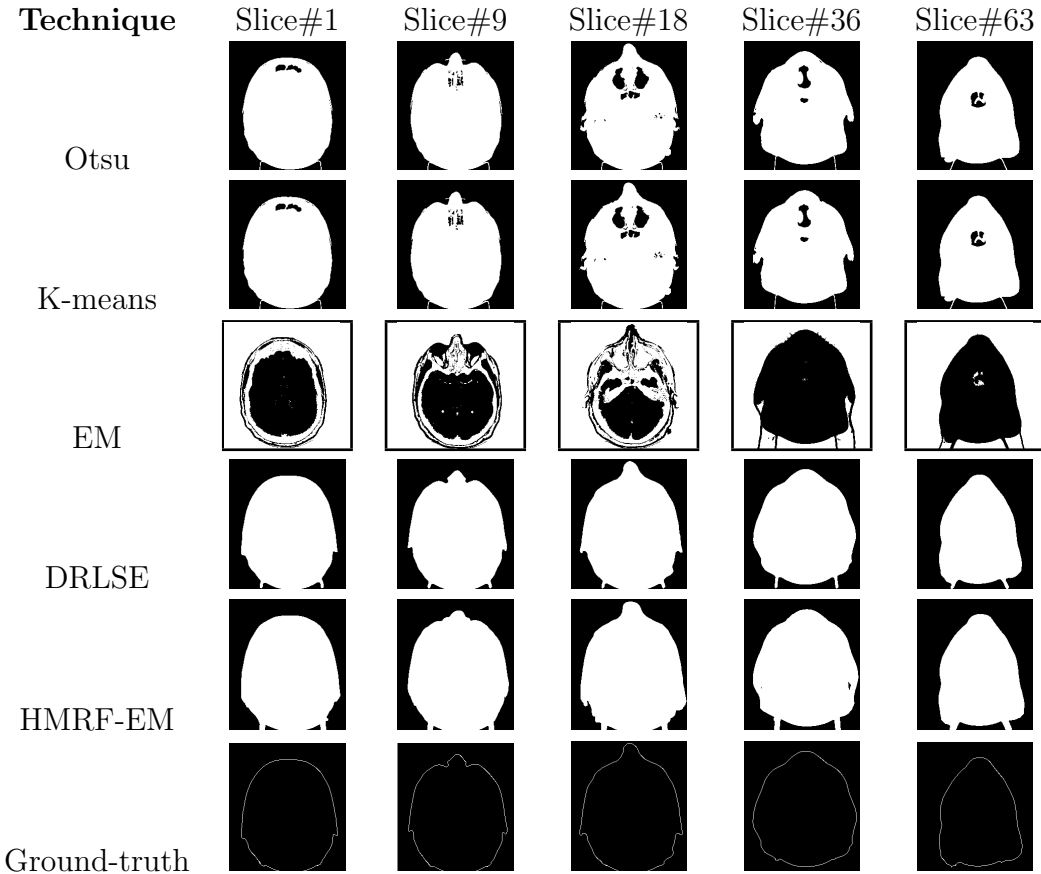


Figure 5.7: Random segmented CT slices generated by applying Otsu, K-means, EM, DRLSE, and HMRF-EM techniques to segment the CT slices of the Perspex mask.



Figure 5.8: The first three images represent three images generated when slicing the laser-scan mesh and the last three images represent the same images after applying automatic filling.

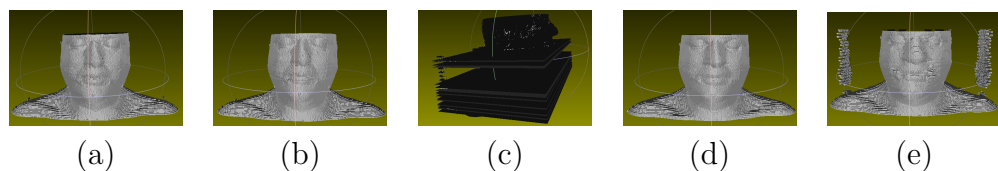


Figure 5.9: Constructed models generated from CT segmented slices after applying (a) Otsu (b) K-means (c) EM (d) DRLSE and (e) HRMF-EM.

Table 5.1: The Average Similarity Ratio (ASR), for each segmentation technique, between the CT segmented slices and the ground-truth, Standard deviation (STD), 90<sup>th</sup> percentile, and the time (in sec) required to segment the whole dataset.

Technique	ASR	Max. val	Min. val	STD	90 <sup>th</sup> perc.	Time(s)
Otsu	0.9601	0.9796	0.9369	0.00968	0.9711	12.63
K-means	0.9564	0.9747	0.9334	0.01253	0.9714	14.58
EM	0.3537	0.9579	0.0249	0.21215	0.3937	103.83
DRLSE	0.9656	0.9777	0.9462	0.00796	0.9729	114.27
HMRF-EM	0.9597	0.9756	0.9417	0.00813	0.9693	822.36

have a big influence on the final outcome of the process.

The third observation is that the value of the standard deviation when a slice by slice comparison takes place by all the employed segmentation techniques, except the EM technique, is very low which indicates that the results generated by the four segmentation techniques (Otsu, K-means, DRLSE, and HMRF-EM) are stable and similarity ratios between each slice and its corresponding slice are not spread out over a wider range of values. This fact is also supported when we see in the table the difference between the maximum and the minimum similarity ratio for the four techniques. The fourth observation is that the outcomes of the DRLSE are the most stable and tend to be closest one to the mean with a standard deviation equals (0.00796) which makes it again the most convenient candidate for head segmentation in CT slices. Notice that we have presented in this chapter the use of similarity ratio for evaluation. While this similarity ratio enables the techniques to be ranked it doesn't give any insight into absolute errors. These absolute errors and other evaluation for the whole process are presented in Chapter 9.

Figure 5.10 displays histograms representing the similarity ratio slice by slice for each one of the five segmentation techniques. The similarity ratio is measured here by calculating the Dice similarity coefficient (DSC) between each corresponding slices. DSC produces a value between 0 and 1 which indicates to which degree the similarity

Table 5.2: The similarity ratio for the slices 20 to 25 (around patient's nose).

Otsu	K-means	EM	DRLSE	HRMF-EM
0.9531	0.9479	0.3850	<b>0.9570</b>	0.9515

is between the two corresponding slices. The results shown in the histograms support the observations that we got from Table 5.1 in which we noticed that results generated by (Otsu, K-means, DRLSE, and HMRF-EM) are close to each other and there are no high variance over the whole set of slices. It is worth noting, in Figure 5.10, that there is a small decrease in the similarity ratio, for the four segmentation techniques mentioned before, around the region of patient's nose (slices 20 - 25) but this small decrease is very low and has no real effect on the accuracy of the derived model. The reasons for that decrease is explained in the discussion part of Chapter 9. Table 5.2 displays the average similarity ratio over the slices (20-25) in which we can observe that the DRLSE produced the higher similarity ratio when compared to the other four techniques. Anyway, as manufacturing the immobilisation mask includes defining a hole on the nose region for breathing purposes then the accuracy around that area is not a priority in our case.

## 5.5 Summary

This chapter evaluated five different segmentation techniques. A brief technical background on these segmentation techniques is presented in the beginning of this chapter. We also developed a post processing algorithm to handle the case when the DRLSE produces more than one contour in the final output. This algorithm in addition to our work to set the initial level set binary function for head segmentation in CT images is explained in a separate section. The experiments, results, and outcomes of this chapter encourage us to apply the DRLSE technique for segmentation of the skin/air interface of the head as this technique leads to relatively better results than the other

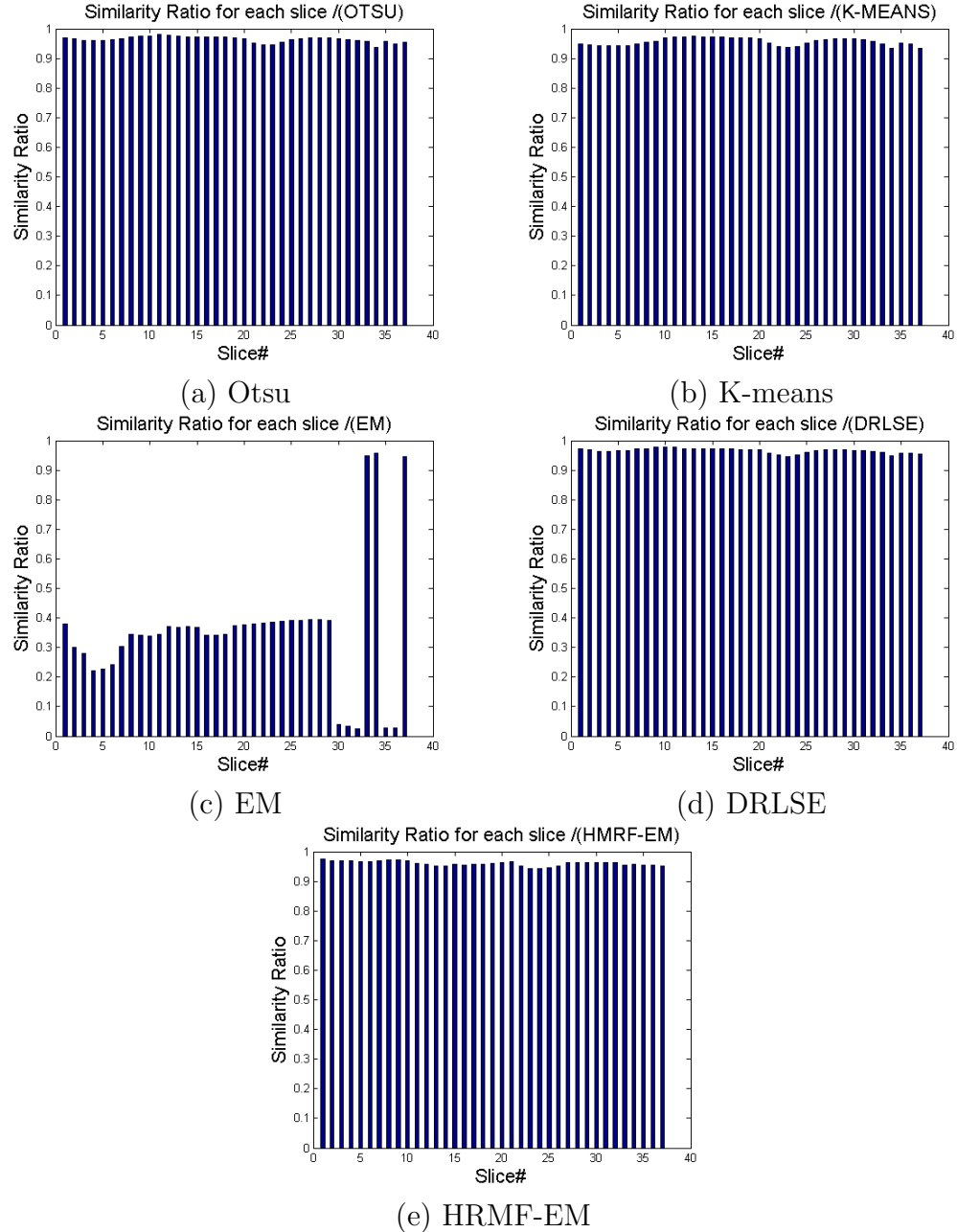


Figure 5.10: Similarity ratio slice by slice for different segmentation techniques. The process that we follow to find these similarity ratio is presented in Chapter 7.

four techniques.

As the experiments in this chapter produced CT-derived model from the segmented CT slices, we are now in a place which qualifies us to move on and perform a 3D automatic alignment between the CT-derived model and the laser-scan model. The following chapter presents the details of the process that we developed in order to perform an alignment (i.e. registration) between the two models.

# Chapter 6

## Automatic 3D Alignment

It was presented in Chapter 3 Section 3.1 that the laser-scan digital models will be used as a ground-truth for evaluating the accuracy of the CT-derived models. This evaluation requires an accurate alignment between the ground-truth (i.e. laser-scan model) and the input model (i.e. CT-derived model). Consequently an automatic approach should be developed to align (register) the laser-scan model and the CT-derived model. This chapter presents the details of the approach that we follow to align the two models automatically. Section 6.1 presents an overview on one of the most well-known techniques used for geometric alignment of 3D data-models named the Iterative Closest Point (ICP) algorithm. Section 6.2 describes a customised version of ICP that we developed in order to speed up the alignment process and increase the accuracy of it. Experimental work and results are displayed in Section 6.3. Finally, in Section 6.4, we present a summary describing the main parts of this chapter.

### 6.1 Iterative Closest Point (ICP)

The ICP algorithm is a frequently and widely used method for 3D alignment [176, 177]. It is an optimization algorithm that performs a number of iterations in order to minimize root mean square distances (RMSDs) of corresponding points between

two data sets and consequently to align them. The two datasets, the input and the target, are normally given to ICP as a set of sparse representation of points. As the relative positions of these points is not known and as noisy data are a problem with all kinds of 3D acquisition methods [178], performing an accurate registration between them represents a challenging task and needs a robust algorithm. The ICP algorithm is one of the popular algorithms in this field which focuses on two issues: (1) discovering the best correspondence between points in each dataset and (2) determining the most accurate transformation from input dataset to target dataset. The ideal transformation is identified to be the one that let the least squares reaches the minimum [179].

ICP was introduced mainly to find the transformation that aligns between two data sets by minimizing the root mean square errors between the corresponding points in each dataset. After that, ICP was employed in different applications and research areas. For example, in [180] ICP was used to register two sequences of eight surfaces of the left ventricle of the heart, obtained from two different medical imaging modalities. In [181], ICP was used for camera pose refinement. In [182], a high-standard vehicle control system was proposed in which ICP was used to evaluate and obtain state quantities of vehicles with roadside sensors. [183] used ICP in scanned model reconstruction. [184] and [185] employed ICP in 3D face pose estimation.

The followings represent the main steps of the ICP algorithm:

Step1: Input for two data sets. (We will call the first one a target mesh and the second one an input mesh).

Step2: Observing corresponding points in both meshes. Finding the corresponding points can be done through different approaches. The common approach is to find, for each point in the input mesh, the closest point in the target mesh. The other approaches used to find the corresponding points are presented in Section 6.1.1 which

discusses the different variants of the ICP algorithm.

Step3: Computing transformation matrices (rotation and translation) in order to minimize the total distance between the two meshes.

Step4: Moving the input mesh to match the reference target mesh according to the transformation matrices resulted from step3.

Step5: Loop (from step2 to step4) until the total distance between the two meshes becomes less than a threshold value or until a specific number of iterations is performed.

### 6.1.1 Variants of ICP

The basic concept of ICP was presented in the early 1990s nearly at the same time by Besl and McKay [186] and Chen and Medioni [187]. The form which introduced in [186] is the most frequently cited one. ICP takes two 3D models, as an input, and an initial transform estimation that can find the correct alignment between the two models. It then improves the transform by repetitively producing sets of corresponding points from the two models and reducing the measured value of error.

Many variations of the ICP algorithm have been presented in literature. Good reviews about these variations were presented by [176] and [188]. If we look at ICP as an algorithm consisting of six phases, then we can classify the variations of ICP according to their effects on each one of these phases. We prepare a schema to represent these variations in Figure 6.1. The phases of the ICP algorithm are:

#### **Phase1: Selection**

In this phase, selection of all or some of points are carried out. More than one method have been proposed to perform the selection. The common approaches which have been proposed for the selection process include:

- A. Selecting all points as in the basic ICP proposed by [186].

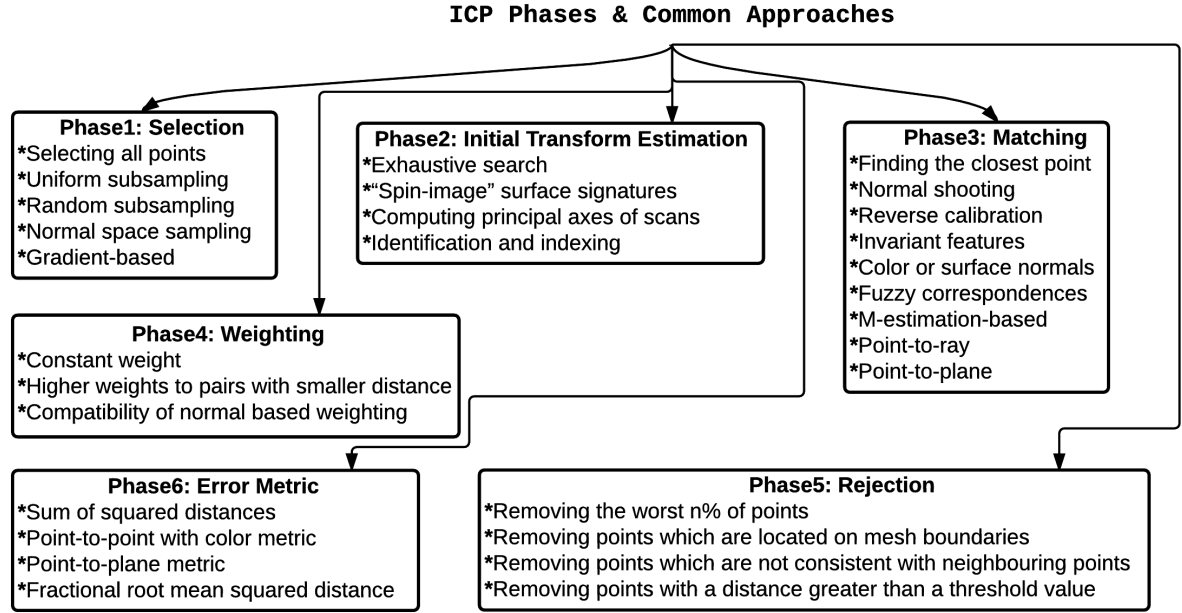


Figure 6.1: ICP phases and common approaches.

- B. Uniform subsampling [189].
- C. Random subsampling [190].
- D. Normal space sampling [176].
- E. Gradient-based or colour-based selection [191].

### Phase2: Initial transform estimation

Creating the initial transform can be performed in different ways.

- A. Exhaustive search for corresponding points [192, 193].
- B. 'Spin-image' surface signatures [194].
- C. Computing principal axes of scans [195].
- D. Identification and indexing of surface features [196, 197].

### Phase3: Matching

In this phase, each selected point from the input dataset should be paired with a correspondent point from the target dataset. The following are some of the common methods used in literature to match the points:

- A. Finding the closest point in the target dataset as proposed in the basic ICP [186].
- B. Normal shooting [187].
- C. Reverse calibration [198, 199].
- D. Using the invariant features [200, 201], colour or surface normals [202] in the distance metric.
- E. Using fuzzy correspondences [203].
- F. M-estimation-based method for correspondences [204].
- G. Point-to-ray [205] or point-to-plane [206] metrics.
- H. Mahalanobis distance for correspondence.

#### Phase4: Weighting

In this phase, different weights are assigned to the corresponding points. The classification of algorithms which are grouped under this field depends on the approach that each algorithm use to assign weights. The following are some of the common approaches used to assign weights:

- A. Constant weight
- B. Providing higher weights to pairs with smaller distance.
- C. Compatibility of normal based weighting in which Equation 6.1.1 will be used to find the compatibility of normals between the two paired points given that the plane which contains the first point has a normal named  $n_1$  and the plane which contains the second point has a normal named  $n_2$ .

$$Weight = n_1 \cdot n_2 \quad (6.1.1)$$

#### Phase5: Rejecting Some Pairs of Points

The main target of this phase is to remove outliers which have a big influence on the registration outcomes when working on least-squares minimization. The common proposed approaches in this field are:

- A. Removing the worst n% of points [207, 202].
- B. Removing points which are located on mesh boundaries [189].
- C. Removing points which are not consistent with neighbouring points [205].
- D. Removing points with a distance greater than a threshold value [176]. This threshold value could be defined as in [190] in which the authors rejected the corresponding points with distances greater than 2.5 times the standard deviation of distances.

#### **Phase6: Setting an error metric and minimizing it**

In this phase, an error metric should be used and iteratively minimized in order to reach to a better registration results. The common error metric used in the literature are:

- A. Sum of squared distances between paired points. This metric was used by most algorithms in this field [188].
- B. Point-to-point with colour metric [208].
- C. Point-to-plane metric [187].
- D. Using fractional root mean squared distance (FRMSD) which includes the fraction of inliers when finding the distance [209].

In the next section we present a customised version of the ICP algorithm that we applied to align between the laser-scan model and the CT-derived model.

## **6.2 Customised version of ICP**

Since using the basic form of the ICP algorithm to match the corresponding points between two datasets may lead the process of ICP to converge but to a local minimum [209], and since many variations of the ICP algorithm have been presented in the literature, we implemented numerous forms of ICP in order to find the best form which presents the optimal alignment and registration between the two models in the shortest amount of time. The settings that we chose in order to achieve the best

performance in terms of time and accuracy of registration are:

- *In terms of selection*, we allow the ICP to include all the points in the registration process. This will help the ICP algorithm to align the two models better and will not divert the algorithm to incorrect matching. We have not used subsampling in the selection process although random subsampling [190], uniform subsampling [189] and normal space sampling [210] have been used in some cases in some studies because the sampling process is a critical issue and can lead to misalignment between the two models. The experiments that we implemented indicate that there is no considerable time saving when we used subsampling.
- *In terms of matching*, we pair each point from the laser-scanned model with a corresponding point from the CT-derived model according to the closest point rule as proposed in [186].
- *In terms of setting an error metric to be minimized*, we use the ‘sum of squared distances’ between paired points since this metric is used by most studies in this field [188].

Since 3D meshes normally have a large number of points, the registration/alignment process could be time consuming. We applied some additional steps in order to shorten the required time for the alignment process:

- *A KD tree* data structure is used to specify how point matching should be done quickly. The aim of using KD trees to search for closest points is that it transforms the process of searching the closest point to searching inside a binary tree. In this process, the set of points is divided according to the value of the median of first coordinates of all points. The point that corresponds to the median is set to be the root of the binary tree. Then, the two consequential subsets are divided according to the value of the median of their second coordinates. This process can be extended to higher dimensional spaces as it is the case in our alignment problem since we have

three coordinates for each point. The concept and details of the KD tree is presented in [211].

- *Point to point minimisation* is employed when surface normals for the points are not available and *point to plane minimisation* is employed when surface normals are available. Point to point minimisation is based on the Singular Value Decomposition (SVD) and is usually the fastest method. Point normals will be found through Principal Component Analysis (PCA) procedure of the 4-nearest neighbours. This implies that the error metric, which defines the objective function, sums the squared distances of input-model points to target-model points. Equation 6.2.1 represents the objective function where  $\mathbf{R}$  and  $\mathbf{T}$  represent the final rotation and translation matrices respectively,  $\mathbf{d}$  and  $\mathbf{g}$  represent the  $i^{\text{th}}$  point in an input and target models respectively, and  $n$  represents the total number of corresponding points. Point to plane minimisation will often yield higher accuracy. It uses linearized angles and requires surface normals for all points.

$$TotalDist = \sum_{i=0}^n (Rd_i + T - g_i)^2 \quad (6.2.1)$$

- *Extrapolation* is used so the iteration direction will be evaluated and extrapolated if possible using the approach outlined by Besl and McKay [186].

- *Detecting convergence* is activated thus allowing a good short-term performance. We will refer to the ICP algorithm that uses the above mentioned settings as ‘customised ICP’ or adjusted throughout this chapter. ICP will return the final translation  $\mathbf{T}$  and rotation  $\mathbf{R}$  matrices which are required to transform the vertices of the laser-scanned model from its initial position and orientation to a new position and orientation as presented in (6.2.2) where  $\mathbf{P}$  and  $\mathbf{Q}$  represent the vertices of the laser-scanned model before and after the alignment respectively.

$$Q = R * P + T \quad (6.2.2)$$

The customised version of ICP that we applied achieved great results in terms of speed and accuracy of alignment as it will be presented in Section 6.3, but we tried to search for another 3D alignment approach to explore if we can get more accurate results. We applied the basic form of a technique named Procrustes Superimposition (PS) [212] which is performed by optimally translating, rotating and uniformly scaling the objects. PS method did not achieve competitive results in some cases and completely failed to align the two models in other cases.

### 6.3 Experimental Work & Results

The three objects that were used in these experiments are shown in Figure 6.2. We chose these objects at this stage because it is easy to acquire CT data for these objects (i.e. no ethical approval needed) and at this stage in the project we didn't have ethical approval. The first object is a 3D-printed scaled head of a Cantonese chess piece, the second dataset is a plastic object in a shape of nested cubes and the third dataset represents a plastic hemisphere. The details of these data sets are presented in Chapter 3. The head was scanned using a hand-held laser scanner (REVscanTM laser scanner from Handyscan 3D Creaform, Canada) where the other two objects were scanned using (Artec Space SpiderTM laser scanner from Artec 3D, Luxembourg) in order to use the resultant 3D meshes as a ground-truth. The two hand-held laser scanners which were used to scan the objects are displayed in Figure 6.3.

A comparison between the results that we got from the customised ICP against the basic form of the ICP is presented in this section. Figure 6.4 (top) shows the two models (i.e. the CT-derived model and laser-scan model) before performing an alignment

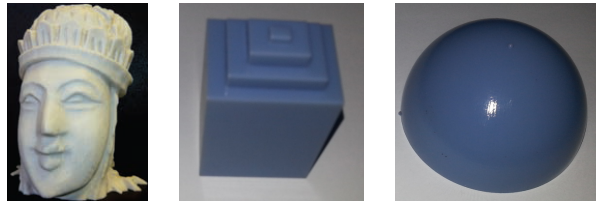


Figure 6.2: Three objects (left): head (middle): cubes (right): dome.



Figure 6.3: (left): The REVscan<sup>TM</sup> laser scanner from Handyscan 3D (right): Artec space spider<sup>TM</sup> laser scanner from Artec 3D.

and Figure 6.4 (bottom) shows the two models after applying the customised ICP. The two models, as shown in Figure 6.4 (top), were completely misaligned, having different coordinate systems, different image resolution and different point-set densities. Applying the customised ICP algorithm leads to a high level of superimposing and registration between the two models.

### Enhancements produced by the customised ICP algorithm

Table 6.1 presents a comparison between the basic form of the ICP algorithm and the customised one in terms of execution time and average distance between the two models. It is obvious from the table that the customised ICP requires much less time to converge than the basic form of ICP. This is due to the use of the KD tree, point to point minimisation and the ability to detect convergence. It is worthy to be noted that the average distances that we got for the three objects were smaller than the CT pixel-spacing value.

Figure 6.5 displays the two models after performing the alignment using the basic

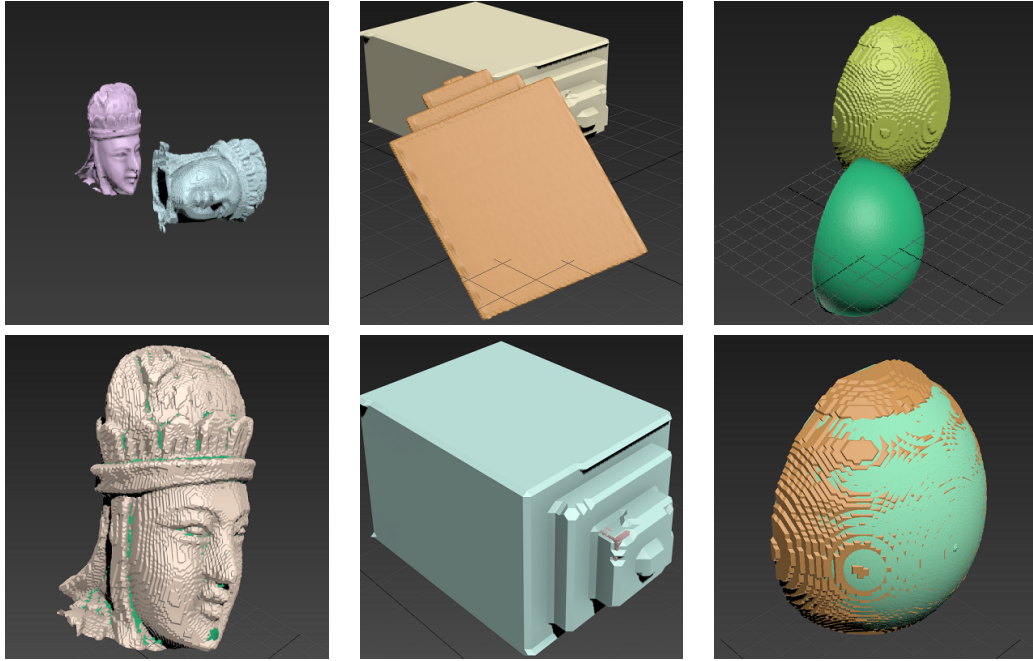


Figure 6.4: The two models (top): before alignment (bottom): after alignment

Table 6.1: Comparing the basic ICP algorithm with the customised ICP in terms of execution time and average distance

Method	Average distance(mm)			Execution time(sec)		
	head	cubes	dome	head	cubes	dome
Basic ICP	2.8651	3.5256	0.7346	61.80	263.26	423.45
customised ICP	0.60392	0.6192	0.47472	3.28	26.96	9.10

form of the ICP and the two models after performing the alignment using the customised ICP. It is obvious that the two models were superimposed very well when the customised ICP was used whereas the models were not well aligned when the basic form of the ICP was used. There is a high possibility for the basic form of the ICP algorithm to be trapped in local minima. This is very clear in the case of the cubes as column 2 displays in Figure 6.5.

Figure 6.6 displays the convergence plots when we applied the basic form of the ICP algorithm over the three objects (left column) and the convergence plots for the same objects when we applied the customised form of the ICP algorithm (right

column). The plots show that both of the forms are able to converge but to a local minima in the case of the basic form of the ICP algorithm.

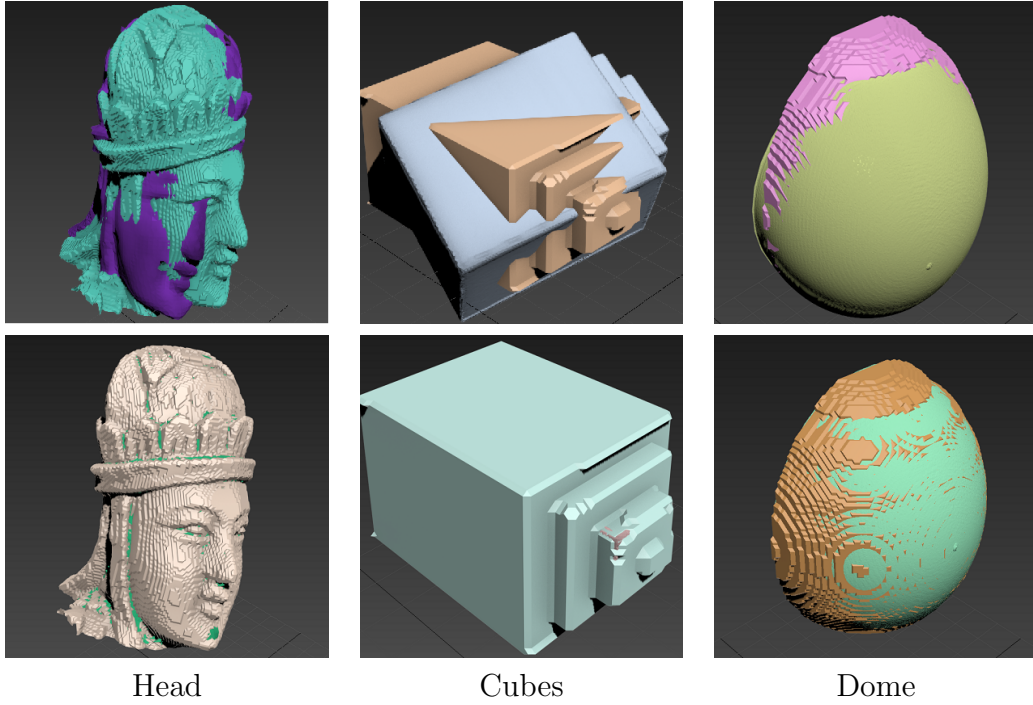


Figure 6.5: The outcomes after performing the alignment when using (top): the basic form of ICP, (bottom): customised (adjusted) ICP.

## 6.4 Summary

This chapter presented a detailed description of the ICP algorithm; one of the well-known algorithms used for 3D alignment. It then presented an overview on many variations of the ICP algorithm. We developed a customised version of the ICP algorithm in order to achieve the best performance in terms of time and accuracy of alignment. The outcomes of the experiments show that the average distances between the aligned models were smaller than the CT pixel-spacing value which ensures the accuracy of the employed approach. The outcomes, in this chapter, are presented visually and in tabular format to get a clear evidence on the accuracy and correctness of the output. The next chapter will present the details of a proposed 3D overlap

measurement approach that we developed to be used as measurement to find the degree of alignment between 3D models.

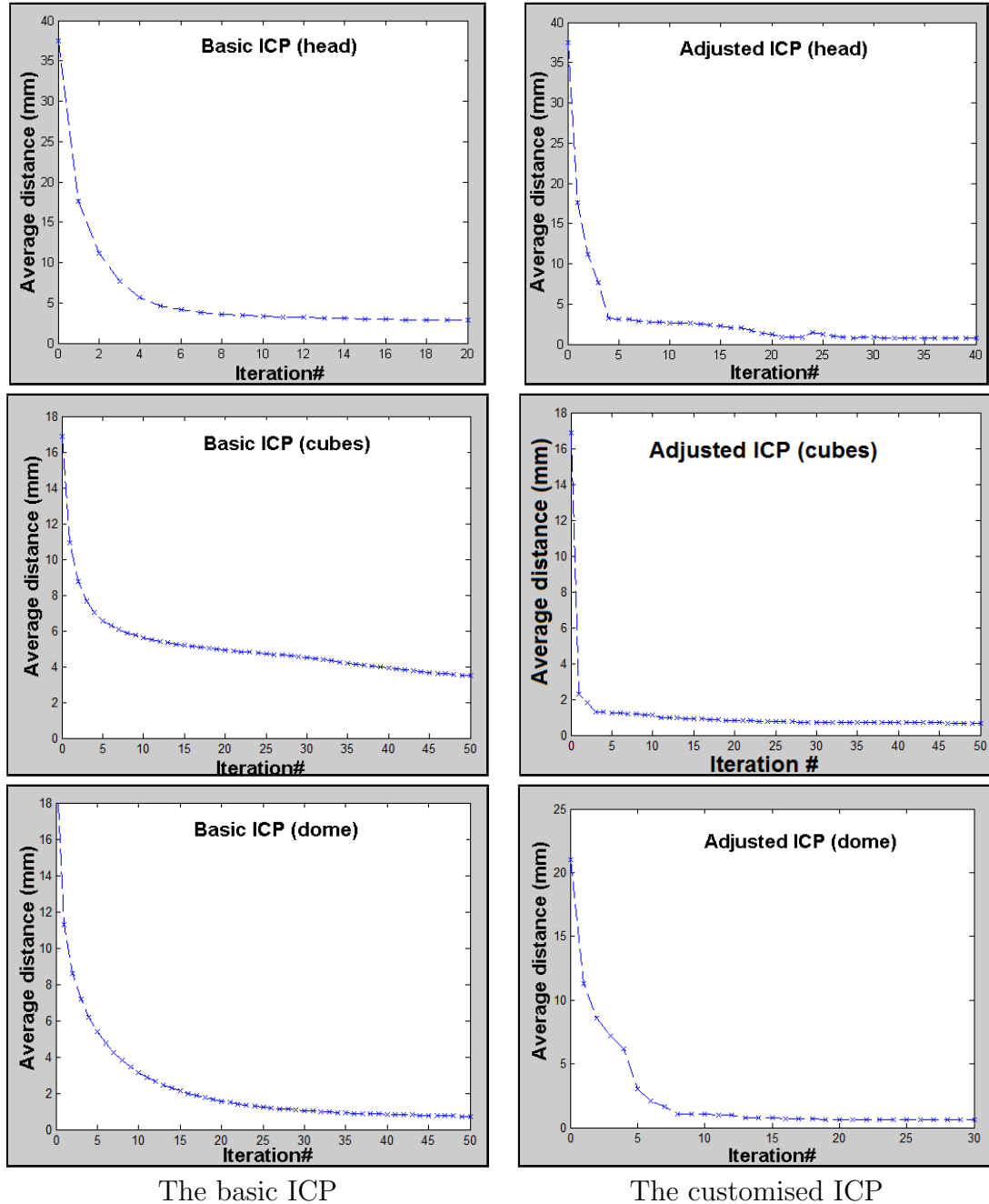


Figure 6.6: Convergence plots when applying the basic ICP and the customised (adjusted) ICP over (top): the Cantonese head , (middle): cubes and (bottom): dome.

# Chapter 7

## Overlap Measurement

The evaluation of the accuracy of 3D medical image segmentation and registration is normally performed by measuring the overlap ratio between the examined model and the ground-truth. Consequently the reliability and accuracy of the applied overlap measurement play a key role in the evaluation process. This chapter presents a 3D-overlap measurement for medical volume images. For convenience we will refer to the proposed overlap measurement as “*Dice\_3S*” similarity measurement throughout this chapter. While the current overlap measurements employed in biomedical fields were initially designed for computer graphics applications, the *Dice\_3S* similarity measurement extends 2D overlap measures that are popular for evaluating 2D medical image segmentation to 3D medical volumes. *Dice\_3S* does not just produce a figure-of-merit of the proportion of the region match but it also gives complementary statistical information that enables the observer to assess the scale and positions of regions/volumes of match and mismatch. The information is organised for each one of the axial, sagittal and coronal planes which makes this measurement convenient for medical images. Six different datasets are used in this chapter to test and validate the results. We use two strategies in order to evaluate the proposed model (*Dice\_3S*). The first is examining the correlation between *Dice\_3S* and other overlap measurements which are widely used and accepted. The second is analyzing our model’s

outcomes for particular test cases in which we know in advance how the trend of the correct outputs should be. The results support the importance of employing the presented overlap measurement, *Dice\_3S*, to evaluate the outcomes of the segmentation and registration of medical images.

We have also employed *Dice\_3S* in two different applications which are related to the quality of surface simplification of volume images. For convenience, we present the experimental work and results that are related to the surface simplification in Appendix A.

## 7.1 Introduction

A typical medical volume image is a stack of 2D slice images acquired by an X-ray CT, Magnetic Resonance Imaging (MRI), or Positron Emission Tomography (PET). The 3D overlap measurement is a measure that finds the proportion of overlap between two 3D models (i.e. between two medical volumes in our context).

The accuracy of a segmentation and registration algorithm can be defined as the level to which the outcomes agree with the ground truth, a so called “gold standard” [174]. In this study, we employ the mesh which is generated from the laser scan as a ground truth. The need for a robust and accurate overlap measurement to be used as a measure in biomedical engineering is of great significance. This measurement should quantify the region agreement between two volumes and consequently will reflect the quality of the registration and segmentation processes.

A good example motivating the need for 3D overlap measurement is cone-beam CT. Radiotherapy treatment is increasingly using cone-beam CT for monitoring pre-treatment patient set-up. Hence it needs registration of CT volumes (rather than images). The accuracy of the registration and segmentation processes plays a key role in medical applications. In registration, a group of methods are employed to

establish anatomical or functional correspondence between images/volumes obtained at different times, with different modalities, or of different subjects [213, 214]. Registration is of vital importance for image-guided radiosurgery [215], image-guided radiation therapy [216], interventional radiology [217], and image-guided minimally invasive surgery [218]. For example, in image-guided minimally invasive surgery, the registration of pre- and intra-interventional data supply a surgeon with notifications about the current position of the used instruments relative to the planned trajectory and the definitive target [219]. In external beam radiotherapy, registration of planning CT images and daily pre-treatment images lead to more accurate positioning for a patient, which is important for accurate targeting of cancerous tissue while minimising the dose to surrounding healthy organs [11]. Moreover, 3D image registration is of vital importance in dental surgery [220] and has numerous applications in that field [221, 222].

The segmentation is also one of the primary procedures that are required in medical applications. The importance of segmentation comes from its ability to delineate, characterise, and visualise regions of interest in medical volumes [223]. Segmentation of medical volumes can be performed manually, automatically (computerized) or using a combination of methods. However, manual segmentation is time-consuming compared to automatic segmentation and the results may be prone to observer variability whereas using computer-aided segmentation techniques have significantly improved the accuracy of the segmentation outcomes [175] [62]. Both of the segmentation methods (i.e. manual and automatic) need a reliable overlap measurement to quantify the quality of the segmentation process and can be evaluated numerically using appropriate measurements [224].

There are three measurements that are widely used by researchers to measure the overlap between medical volumes. These measurements are: Hausdorff Distance

(HD), Mean Surface Distance Error (MSDE), and Signed Distances with a Colour-Coded Visualization (SDCCV). The distances in MSDE and SDCCV are calculated for each point of the first surface by computing its Euclidean distance to the corresponding point of the second surface. The average value of absolute distances is calculated in MSDE whereas signed distances are calculated for each point in SDCCV. Examples of studies that applied the MSDE and SDCCV for evaluation include [225, 83, 88, 80, 226, 227, 228, 229]. It is worth noting that there is no definite line between MSDE and SDCCV and numerous studies applied the two concepts interchangeably as both of them use the Euclidean distance (i.e. Root Mean Square Error (RMSE)) as a base for the comparison.

Hausdorff Distance (HD) is used to measure how far two subsets of a metric space are from each other. It can be applied to determine the degree of similarity between two models that are superimposed on one another [230]. Examples of studies used HD for evaluation include [231, 232, 233, 234, 235]. HD represents the greatest of all the distances from a point in one set to the closest point in the other set. Given Equation (7.1.1) where  $\|\cdot\|$  represents the Euclidean norm

$$h(A, B) = \max_{a \in A} \min_{b \in B} \|a - b\| \quad (7.1.1)$$

then Hausdorff distance is computed as shown in Equation (7.1.2).

$$H(A, B) = \max(h(A, B), h(B, A)) \quad (7.1.2)$$

A review of current overlap measurements leads to some observations:

- Signed distances with colour-coded visualisation does not quantify the outcome as a single number (i.e. figure of merit).
- Most of overlap measurements including the HD, MSDE and SDCCV measure the degree of agreement with regard to the surface points but not for each voxel inside the object.

- Those overlap measurements are initially designed for general purposes and specially for computer graphics applications but not particularly for medical application. This means that those measurements are more appropriate to 3D surface models than 3D solid models.
- HD is sensitive to outliers in the input data [236] which is a common case in medical images.
- MSDE and SDCCV are sensitive to point positions and they are classified as distance-based measurements more than overlap-based measurements [237].
- HD can sometimes produce misleading results since it finds the greatest of all the distances from a point in one set to the closest point in the other set (i.e. the maximum of minimums).
- It is not an easy for distance-based error measurements including the HD, MSDE and SDCCV to measure a precise geometric error on a highly curved surfaces since the error calculated by these measurements on such a region is usually small [238].
- None of those overlap measurements present an analysis with regard to the axial, sagittal and coronal planes whereas this analysis is convenient in different clinical cases.

*Dice\_3S* similarity measurement produces a proportion (a number between 0 and 1) to reflect the ratio of overlap between two 3D models where 1 indicates a complete match and 0 a complete mismatch. This overlap measurement forms a framework to quantify the degree of agreement between two volume images. In this framework, the overlap proportion can be measured between one surface and another surface, one surface and one volume (i.e 3D grid), and one volume and another volume. These

three cases are common and required in numerous medical applications. *Dice\_3S* does not just produce, as a final output, a figure of merit of the proportion of the region match but it gives complementary figures that allow the scale and location of regions/volumes of match and mismatch to be visualised and subjected to statistical analysis. These complementary figures make *Dice\_3S* a specialised and comprehensive tool to measure the overlap between medical images in particular.

*Dice\_3S* examines the overlap ratio taking the axial, sagittal and coronal planes into consideration. This makes it the appropriate choice for medical volume images. It is very important to not only derive global measures but to analyse the local distribution of these errors since local distributions may immediately show where/which kinds of anatomical shapes are not correctly matched [232]. The complementary figures, which are offered by the overlap measurement, give the facility to help in identifying where/which regions are not correctly matched or mismatched.

The Dice similarity coefficient (DSC) is one the most popular and used 2D overlap measure to evaluate the outcome of the image segmentation. *Dice\_3S* applies DSC, which was presented earlier in this thesis in Section 2.6, in three dimensions (axial, sagittal, and coronal). *Dice\_3S* slices the examined objects in three dimensions and applies DSC over the collection of all slices in each direction. This explains the reason for naming the proposed model as *Dice\_3S*. Since *Dice\_3S* applies DSC, it is insensitive to outliers. *Dice\_3S* is designed to be overlap-based oriented measurement and it is able to locate geometric errors on highly curved surfaces when the image fill property is deactivated as it will be discussed in Section 7.2.

The remainder of this chapter is organised as follows: Section 7.2 presents the data sets used in this study and describes the *Dice\_3S* model. Section 7.3 presents three algorithms that we follow to slice surfaces (i.e. divide them into layers). Section 7.4 presents the experimental work that is performed to evaluate the reliability of

*Dice\_3S*. The results are presented in Section 7.5 and discussions of these results are presented in Section 7.6. Section 7.7 draws the conclusions for this chapter.

## 7.2 Materials and Methods

### 7.2.1 Data Sets

There are six different data sets used in this chapter (see Table 7.1). The description, properties and sources of these data sets are presented in Chapter 3. The ‘Pelvis’ and the ‘Knee’ data sets are used to evaluate the performance of the overlap measurement when it is applied to measure the overlap between two surfaces. The ‘Cubes’ and the ‘Dome’ data sets are used to measure the overlap between one surface and one volume (3D-grid) since we have acquired a laser scan (surface) and a CT scan (volume) for those two objects. The ‘Head1’ and the ‘Head2’ data sets are used to evaluate the overlap measurement when it is applied to measure the overlap between two volumes.

Table 7.1: Description of data sets used in this study.

Dataset	Format
<b>Pelvis</b>	STL file
<b>Knee</b>	STL file
<b>Cubes, Dome</b>	STL file + CT DICOM images
<b>Head1, Head2</b>	CT DICOM images

### 7.2.2 Methods

The proposed similarity measurement (*Dice\_3S*), shown as a model in Figure 7.1, evaluates numerically the degree of overlap between two 3D models. It accepts two 3D models as inputs and classifies each input as a surface or a volume. According to that, the approach selects one of three paths to measure the proportion of overlap. The first one represents the case in which the two inputs are surfaces. This case is common in medical applications. An example of this case is performing registration between two

surfaces acquired for the same object by two acquisition devices. Another example of that case is evaluating the quality of segmentation of the 3D model by comparing it to a ground-truth surface [84, 89, 239, 90]. The second path represents the case in which one of the inputs is a surface and the other is a volume (i.e. 3D grid of volume data). An example of this case is when an evaluation is needed for a CT-derived model by comparing it with a surface mesh as a ground truth [11, 5, 106, 240, 82]. The third path represents the case when both the inputs are a 3D grid of voxels. An example of this case is when an object is CT-scanned by different CT scanners to evaluate the accuracy of each scanner [241, 242, 243, 244, 245].

In the case of surface  $\sim$  volume matching, the first step that *Dice\_3S* will perform is extracting the isosurface from the volume to form a surface. This extraction is done by a common algorithm called the Marching Cubes algorithm [19]. After that, the slicing process takes place by performing plane/triangle intersections for each surface in the three different planes (i.e. axial, sagittal and coronal). The slicing process consists mainly of :

- Simplifying the mesh
- Plane/triangle intersection
- Projection of intersection points into 2D-image pixels

The following section presents three algorithms that we follow to slice surfaces.

## 7.3 The Slicing Process

### 7.3.1 Simplifying the Mesh

The aim of this step is to extract the vertices from the mesh and then to remove the duplicated vertices, a process named simplifying the mesh. Removing duplicated

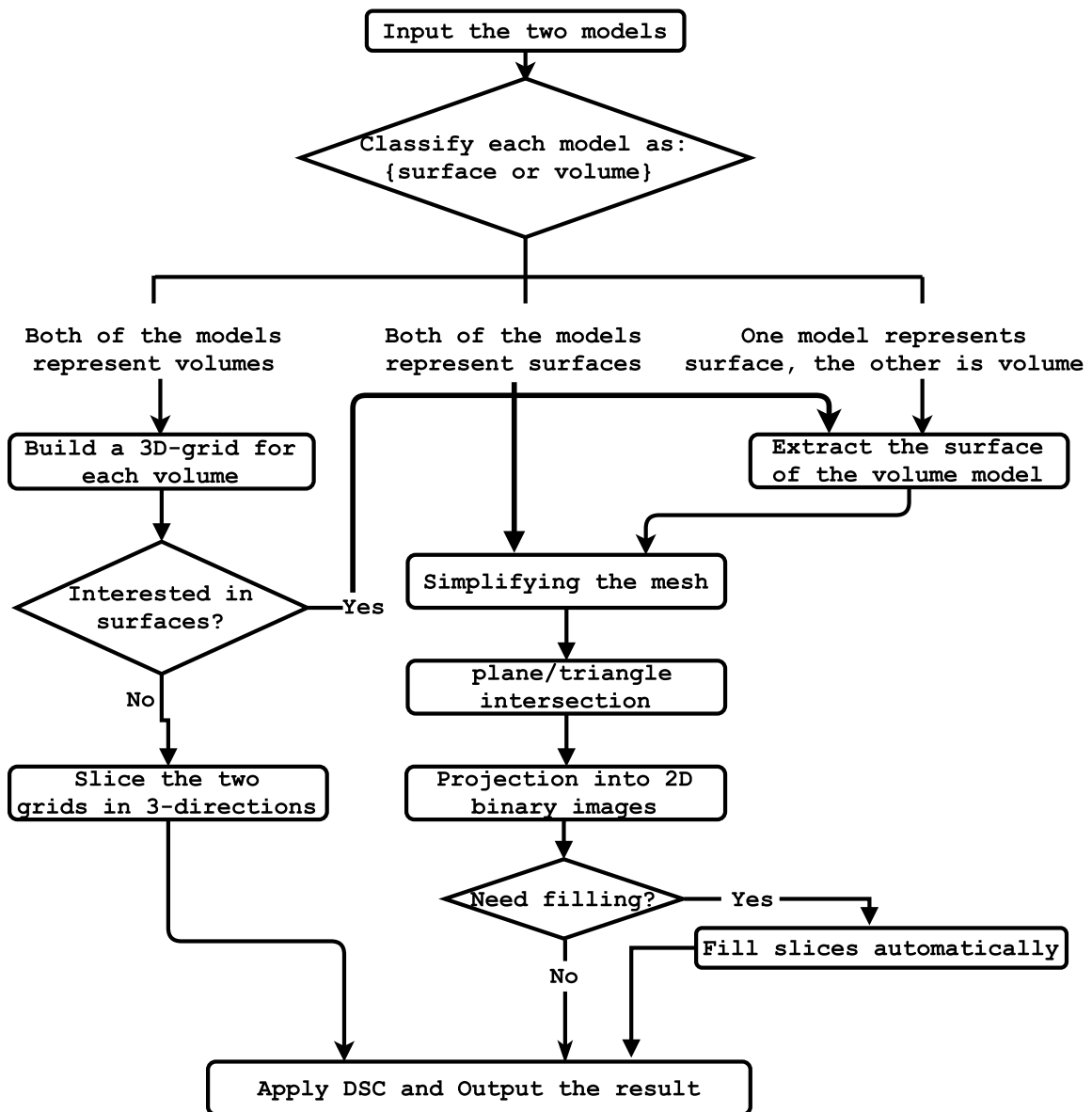


Figure 7.1: The proposed model of measuring the degree of overlap between two medical volumes.

vertices will reduce the computational cost and will not affect the quality of the outcomes.

Suppose that a mesh has  $N_f$  facets and  $N_v$  vertices, then the relation between the two values can be described as in Equation (7.3.1). Observing that the number of vertices is  $3 \times N_f$  and noting that many of the triangle facets share vertices, then there will be redundant vertices. Removing these duplicated vertices will make a significant difference in terms of the required memory and time.

$$N_f \leq N_v * 3 \quad (7.3.1)$$

The steps that trace the process that we follow to simplify the mesh is displayed in Algorithm 3. In the algorithm,  $\mathbf{V}_{\text{new}}$  will store the coordinates of triangles' vertices without repetition, and  $\mathbf{F}_{\text{new}}$  will keep a record of which vertices to connect according to the new ordered non-duplicated values stored inside  $\mathbf{V}_{\text{new}}$ . Both of the two structures  $\mathbf{V}_{\text{new}}$  and  $\mathbf{F}_{\text{new}}$  will be used later instead of  $\mathbf{V}$  and  $\mathbf{F}$  respectively as inputs to the next step when performing the plane/triangle intersection.

---

**Algorithm 3** Simplifying the mesh

---

**Declarations**

- 1:  $V$ : a structure of vertices before simplifying.
- 2:  $V_{\text{new}}$ : a structure of vertices after simplifying.
- 3:  $F$ : a structure of facets' labels before simplifying.
- 4:  $F_{\text{new}}$ : a structure of facets' labels after simplifying.

**Procedure**

- 5:  $V_{\text{new}} \leftarrow \text{unique\_rows\_of\_}(V)$
- 6: Sort  $V_{\text{new}}$
- 7: Create  $\text{index}N$  such that  $V(:) \leftarrow V_{\text{new}}(\text{index}N)$
- 8:  $F_{\text{new}} \leftarrow \text{index}N(F)$

---

### 7.3.2 Plane/Triangle Intersection

The aim of this step is to perform an intersection between the triangles of the mesh and the group of planes located at equal distance from each other. There are a group

---

**Algorithm 4** Getting intersection segments

---

```

1: current_perspective = {Axial, Sagittal, coronal}.
2: intersection_points: intersection points between each facet and planes.
3: for  $i \leftarrow 1, 3$  do
4:   for all plane( $p$ )  $\in$  current_perspective( $i$ ) do
5:     Get a point  $Q$  lies on that plane.
6:     Find the normal  $N$  of that plane.
7:     for row  $\leftarrow 1, \text{num\_of\_rows\_in\_F}_{\text{new}}$  do
8:       Construct a triangle ( $t$ ) of 3 vertices such that:
9:        $P1 \leftarrow V_{\text{new}}(F_{\text{new}}(\text{row}, 1), :)$ 
10:       $P2 \leftarrow V_{\text{new}}(F_{\text{new}}(\text{row}, 2), :)$ 
11:       $P3 \leftarrow V_{\text{new}}(F_{\text{new}}(\text{row}, 3), :)$ 
12:      Intersect  $p$  with  $t$ 
13:      if intersection_exist then
14:        intersection_points  $\leftarrow$  coordinates
15:      end if
16:    end for
17:  end for
18: end for

```

---

of planes located in axial direction, a group of planes in sagittal direction, and a group of planes in coronal direction. Notice that each plane is defined by a point that lies on it  $Q$  and a normal vector  $N$ , and each triangle is defined by three vertices ( $P1$ ,  $P2$  and  $P3$ ).

Algorithm 4 presents the procedure that we follow to get the intersection line segments between triangles and planes. In this algorithm we calculate the intersection points between each facet of the surface and planes to store those points in a structure named *intersection\_points*. It is worth noting that the process of getting the corners of each triangle (i.e.  $P1$ ,  $P2$  and  $P3$ ) is not performed directly in Algorithm 4 since we reorganised the order of storing the points when we simplified the mesh in the previous step. Instead of that, we use the stored labels inside  $\mathbf{F}_{\text{new}}$  as an index to pick the vertex from  $\mathbf{V}_{\text{new}}$  at that specific index. The loop which starts at line 7 will iterate through each facet in the mesh in order to find the intersection segments.

### 7.3.3 Projection of Intersection Points into Image Pixels

Since surface meshes have coordinates in a “space-domain” which represent a continuous range of values (float numbers), we follow a method to map these continuous values to discrete values and then project them into 2D images. Algorithm 5 represents the procedure that we follow to generate a stack of 2D binary images from the surface model. As Algorithm 5 displays, there are some declarations and initial calculations at the beginning of the algorithm followed by the procedure. The aim of that procedure is to translate the continuous range of values in 3D space to values located on the slice planes. These slice planes will produce a stack of binary images for each surface model. The two stacks of 2D images will be later compared via DSC [74].

The procedure starts by creating a black slice with a number of rows equal to *height* and a number of columns equal to *width*. These values of *height* and *width* are unified for each slice in the same perspective. So the algorithm will generate a stack of 2D slices of the same *height* and *width* for the axial perspective, another stack of 2D slices with different *height* and *width* for the sagittal perspective, and another one for the coronal perspective. After that, two main iterations take place. The first one (line 14-35) is responsible for quantisation by taking the *intersection\_points* generated from the previous step (i.e. plane/triangle intersection) and projecting each point to the nearest pixel location in the output slice. The second main iteration (line 36-42) employs the Bresenham’s line algorithm [246] to connect between the end points of each intersection segment and setting the corresponding pixels at those locations. The final output of Algorithm 5 will be a stack of binary images to represent the outer surface of the object.

---

**Algorithm 5** Generating 2D slices from the mesh

---

**Initializations**

- 1:  $minX$ : min value stored in (x) triangle's coordinates.
- 2:  $maxX$ : max value stored in (x) triangle's coordinates.
- 3:  $minY$ : min value stored in (y) triangle's coordinates.
- 4:  $maxY$ : max value stored in (y) triangle's coordinates.
- 5:  $width$ : the width of each slice.
- 6:  $height$ : the height of each slice.
- 7:  $r\_data$ : a row vector of length =  $height$ .
- 8:  $c\_data$ : a row vector of length =  $width$ .

**Initial Calculations**

- 9: Fill  $r\_data$  with evenly spaced points in  $[minX, maxX]$ .
- 10:  $space\_rows \leftarrow (maxX - minX)/(height - 1)$ .
- 11: Fill  $c\_data$  with evenly spaced points in  $[minY, maxY]$ .
- 12:  $space\_cols \leftarrow (maxY - minY)/(width - 1)$ .

**Procedure**

- 13: Create a black slice of size ( $width \times height$ )
- 14: **for all**  $row_i \in intersection\_points$  **do**
- 15:    $x \leftarrow the\_first\_element\_in\_row_i$
- 16:   **for**  $j \leftarrow 1, height$  **do**
- 17:      $cond1 = x \geq r\_data(j)$
- 18:      $cond2 = x < (r\_data(j) + space\_rows/2)$
- 19:     **if**  $cond1 \& cond2$  **then**
- 20:        $x\_index \leftarrow j$
- 21:     **else**
- 22:        $x\_index \leftarrow j + 1$
- 23:     **end if**
- 24:   **end for**
- 25:    $y \leftarrow the\_second\_element\_in\_row_i$
- 26:   **for**  $j \leftarrow 1, width$  **do**
- 27:      $cond1 = y \geq c\_data(j)$
- 28:      $cond2 = y < (c\_data(j) + space\_cols/2)$
- 29:     **if**  $cond1 \& cond2$  **then**
- 30:        $y\_index \leftarrow j$
- 31:     **else**
- 32:        $y\_index \leftarrow j + 1$
- 33:     **end if**
- 34:   **end for**
- 35: **end for**
- 36: **for all**  $end\_points \in intersection\_segments$  **do**
- 37:   Apply Bresenham algorithm to connect  $end\_points$ .
- 38:   Update  $x\_index$  and  $y\_index$
- 39:   **for**  $k \leftarrow 1, length\_of\_x\_index$  **do**
- 40:      $Slice(x\_index(k), y\_index(k)) \leftarrow 1$
- 41:   **end for**
- 42: **end for**

---

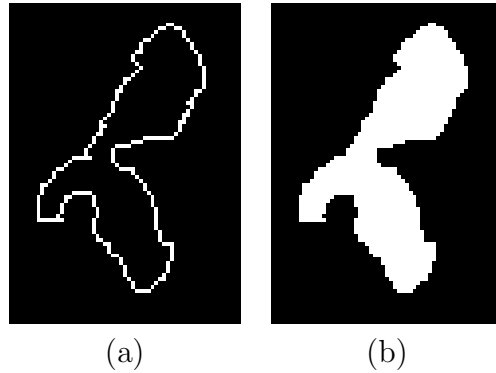


Figure 7.2: 2D binary image generated after applying Algorithm 5 over the Pelvis dataset (a): Without activating the automatic fill (b): activating the automatic fill.

### 7.3.4 Filling the Slices

The presented approach offers the option to fill or not to fill the slices which represent the outer surface of the object (see Figure 7.2). The algorithm that is described in [127] is used for filling the slices automatically. This algorithm performs a flood-fill operation on background pixels based on morphological reconstruction. We recommend deactivating the automatic-filling option when the contour is of interest (e.g when the focus of research is to find an exact boundary delimitation). We recommend activating the automatic-filling when the general alignment and overlap is of interest.

Equation 7.3.2 displays how DSC is calculated

$$DSC = \frac{2N(A \cap B)}{N(A) + N(B)} \quad (7.3.2)$$

Where A and B represent the first and second sets respectively and N() refers to the number of pixels in the enclosed set. *Dice\_3S* finds three separated values of DSC one for each plane (axial, sagittal, and coronal). These three values can be averaged to produce the mean or displayed individually according to the requirement of the examined case.

Since DSC measures the ratio between the number of white pixels common in the two images to a total number of white pixels in the two image, its value can change

dramatically when no-filling option is activated if the total number of white pixels common in the two images changes slightly.

## 7.4 Experimental Work

The experimental work in this chapter aims to evaluate the reasonability of the outcome generated by *Dice\_3S*. We use two strategies in order to analyze *Dice\_3S*. The first is examining the correlation between *Dice\_3S* and the outcome of the Root Mean Square Error measurement (*RMSE*) and Hausdorff distance (*HD*) as these two measurements are widely used and accepted by researchers. The second is analyzing our *Dice\_3S* outcomes for particular test cases (shown in Table 7.2) in which we know in advance how the trend of the outputs should be.

The experiments are designed to evaluate the reliability of the outcomes produced by 3D overlap measurements when a surface is compared with a surface, surface with a volume, and volume with a volume. Table 7.2 displays the test cases that have been performed and the data sets that have been used for each input.

The outcomes that are generated when applying the test cases are investigated and compared with the outcomes of the Root Mean Square Error (*RMSE*) and the Hausdorff Distance (*HD*) method. Note that *RMSE* measurement is the measurement that is used by *MSDE* and *SDCCV* to find the distances. The results of those comparisons are presented in Section 7.5.

## 7.5 Results

As mentioned in Section 7.4 we design the experiments to measure the overlap between two surfaces, between one surface and one volume, and between two volumes. This section focuses on presenting the results whereas Section 7.6 discusses these results.

Table 7.2: Description of the test cases used in the experimental part and their corresponding data sets.

<i>Inputs</i>	Sets	Test Cases
Surface ~ Surface	<b>Pelvis</b>	The same surface
	<b>Knee</b>	Rotate the surface 2 degrees in x direction Rotate the surface 2 degrees in y direction Rotate the surface 2 degrees in x direction Rotate the surface 2 degrees in 3 directions Rotate the surface 5 degrees in x direction Rotate the surface 5 degrees in y direction Rotate the surface 5 degrees in z direction Rotate the surface 5 degrees in 3 directions Rotate the surface 15 degrees in x direction Rotate the surface 15 degrees in y direction Rotate the surface 15 degrees in z direction Rotate the surface 15 degrees in 3 directions Translate the surface 2% in y direction Translate the surface 5% in y direction Translate the surface 25% in y direction Completely separate the objects
Surface ~ Volume	<b>Cubes</b> <b>Dome</b>	The same as test cases in the above
Volume~Volume	<b>Head1</b> <b>Head2</b>	The same volume Random voxels inverting (percenatge = 5%) Random voxels inverting (percenatge = 20%) Random voxels inverting (percenatge = 35%) Completely inverted voxels Inverting specific column in each slice

## Surface ~ Surface Overlap

Table 7.3 displays the values that are generated by *Dice\_3S*, RMSE, and HD when they are applied over the ‘Pelvis’ and ‘Knee’ data sets. These experiments over the ‘Pelvis’ and ‘Knee’ data sets are examples on applying the overlap measurements between two surfaces.

Figure 7.3 displays six bar charts that *Dice\_3S* generates for axial, sagittal and coronal perspectives when it is run to find the ratio of overlap between the original surface of the Pelvis dataset and the same surface after translating it 2% and 5% in y-direction (Row#14 and Row#15 in Table 7.3). Figure 7.3 (b) and (e), represents the bar charts of the sagittal plane which show that the number of images that have a zero similarity ratio (i.e. identified by a red ellipse) when the dataset is translated 5% is greater than the number of images when it is translated by 2%. This outcome is the expected result for translation in the y-direction only. Note that the bar charts

Table 7.3: Surface  $\sim$  Surface overlap measurements for different test cases of axial, sagittal and coronal views.

Row#	Case	Dice_3S				RMSE	HD
		Axial	Sagittal	Coronal	Average		
<b>Pelvis</b>							
1	Same	1.00000	1.00000	1.00000	1.0000	0.0000	0.00
2	Rot_2deg_xdir	0.91849	0.87023	0.8983	0.8957	0.7981	1811
3	Rot_2deg_ydir	0.86423	0.87877	0.8608	0.8679	0.9859	2531
4	Rot_2deg_zdir	0.86566	0.83477	0.88539	0.8619	0.9144	2597
5	Rot_2deg_3dir	0.82493	0.79827	0.82531	0.8162	1.2269	2490
6	Rot_5deg_xdir	0.8131	0.77446	0.7899	0.7925	1.4078	1871
7	Rot_5deg_ydir	0.71122	0.75858	0.70818	0.7260	1.6659	2549
8	Rot_5deg_zdir	0.72988	0.68254	0.76811	0.7268	1.6831	2544
9	Rot_5deg_3dir	0.65774	0.64804	0.64529	0.6504	2.1291	2501
10	Rot_15deg_xdir	0.54668	0.50139	0.51741	0.5218	3.0101	1985
11	Rot_15deg_ydir	0.43425	0.50979	0.40788	0.4506	4.1092	2635
12	Rot_15deg_zdir	0.42622	0.38793	0.46384	0.4260	4.1253	2533
13	Rot_15deg_3dir	0.34392	0.33966	0.31900	0.3342	5.3131	2564
14	Trans_02perc_ydir	0.87093	0.79052	0.87813	0.8465	0.9858	99
15	Trans_05perc_ydir	0.77063	0.6625	0.78236	0.7385	1.7848	248
16	Trans_25perc_ydir	0.11866	0.087385	0.13057	0.1122	7.6134	1240
17	Non_overlap	0.0000	0.0000	0.0000	0.0000	64.3856	8846
<b>Knee</b>							
18	Same	1.00000	1.00000	1.00000	1.0000	0.0000	0.00
19	Rot_2deg_xdir	0.9196	0.83161	0.8941	0.8818	2.6070	608
20	Rot_2deg_ydir	0.82128	0.92154	0.87666	0.8732	2.4930	24312
21	Rot_2deg_zdir	0.94411	0.95532	0.98071	0.9600	1.1942	23906
22	Rot_2deg_3dir	0.81134	0.81561	0.91447	0.8471	3.1930	24449
23	Rot_5deg_xdir	0.80689	0.68254	0.7503	0.7466	5.7851	1523
24	Rot_5deg_ydir	0.6515	0.82636	0.73783	0.7386	5.4974	24796
25	Rot_5deg_zdir	0.88337	0.9131	0.95502	0.9172	2.0253	24018
26	Rot_5deg_3dir	0.63208	0.66772	0.81023	0.7033	7.0673	25031
27	Rot_15deg_xdir	0.53832	0.3862	0.42773	0.4507	15.5593	4578
28	Rot_15deg_ydir	0.37252	0.60694	0.45142	0.4770	14.7794	24199
29	Rot_15deg_zdir	0.72557	0.81077	0.87932	0.8052	4.9550	24218
30	Rot_15deg_3dir	0.32311	0.39495	0.56676	0.4283	18.8890	24072
31	Trans_02perc_ydir	0.93367	0.86478	0.94484	0.9144	2.1983	514
32	Trans_05perc_ydir	0.83781	0.73161	0.86625	0.8119	4.9985	1286
33	Trans_25perc_ydir	0.38327	0.31021	0.46253	0.3853	20.6401	6523
34	Non_overlap	0.0000	0.0000	0.0000	0.0000	134.694	22483

in Figure 7.3 (a),(c),(d) and (f), which represent the axial and coronal planes, do not have images of zero similarity ratio since the translation was done in y-direction only.

## Surface $\sim$ Volume Overlap

Table 7.4 displays the values that are generated by *Dice\_3S*, RMSE, and HD when they are applied over the ‘Cubes’ and ‘Dome’ data sets. These experiments over the ‘Cubes’ and ‘Dome’ data sets are examples on applying the overlap measurements between one surface and one volume.

## Volume $\sim$ Volume Overlap

Table 7.5 displays the values that are generated by *Dice\_3S* when it is applied over ‘Head1’ and ‘Head2’. The test cases that are performed here are:

- The same volume image
- 5% random changes over the original voxel values
- 20% random changes over the original voxel values
- 35% random changes over the original voxel values
- Completely inverted-voxels of the same volume image

The values in Table 7.5 indicate that the results generated by *Dice\_3S* are reasonable when it is used to find the overlap between two volumes. In the first case when the volume is compared to itself the overlap measurement gives the degree of similarity equals one (i.e. total match) which is expected. In the case when we inverted the white voxels to black ones the overlap measurement gives the degree of similarity equals zero (i.e. no overlap) which is expected as well. The values also show a clear agreement between the degree the similarity of the two inputs and the value generated by the overlap measurement. As the percentage of random changes increases in the input model (i.e. less degree of similarity), the value generated by the overlap measurement decreases. This supports the ability of *Dice\_3S* to reflect

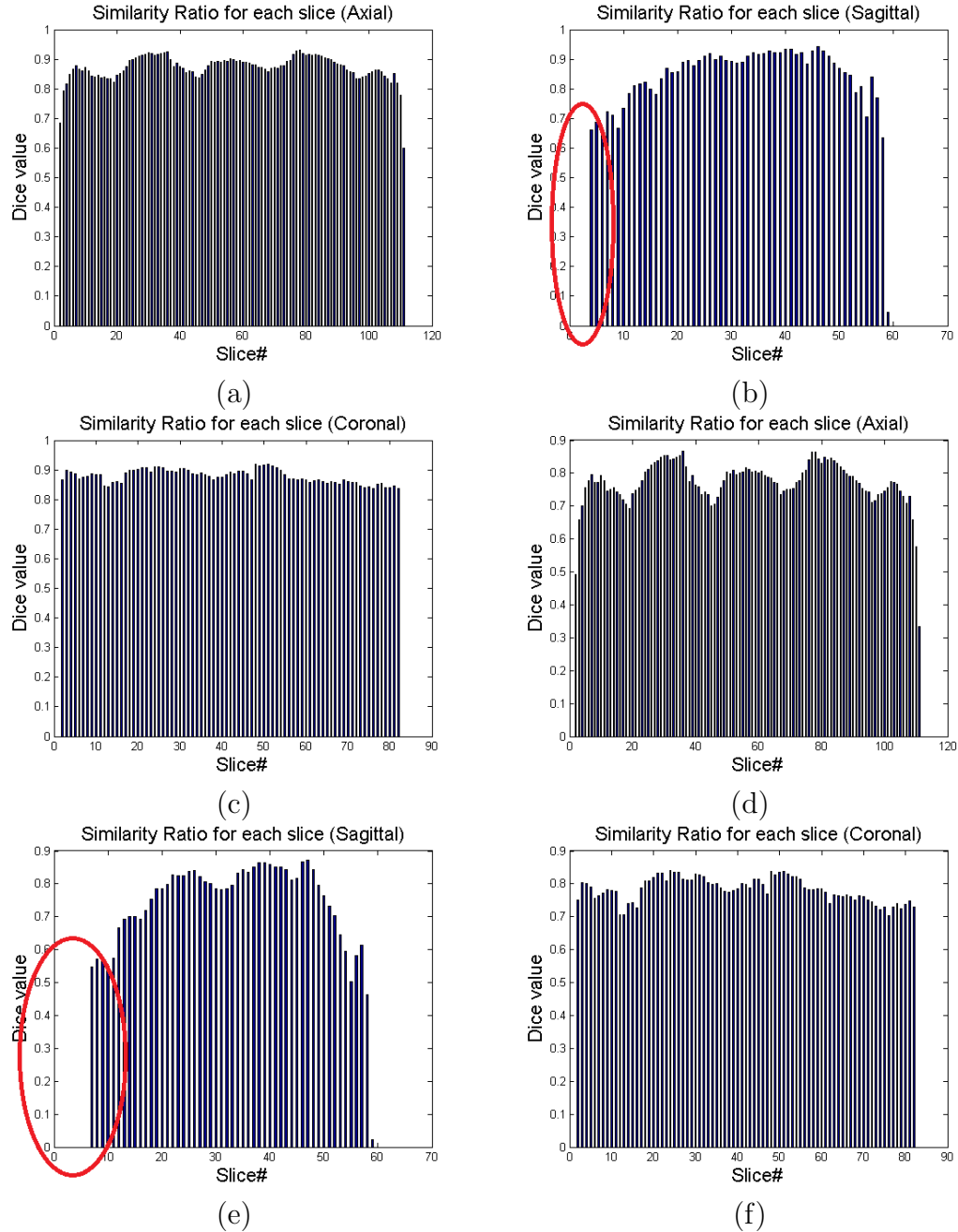


Figure 7.3: Bar charts that *Dice\_3S* generates for axial (a and d), sagittal (b and e) and coronal (c and f) perspectives. These charts are produced when it is run to find the ratio of overlap between the original surface of the Pelvis dataset and the same surface after translating it 2% in y-direction (a, b and c) and 5% in y-direction (d, e and f) (Row#14 and Row#15 in Table 7.3). (b) and (e) show that the number of images that have a zero similarity ratio (i.e. identified by a red ellipse) when the dataset is translated 5% is greater than that number of images when it is translated 2%.

Table 7.4: Surface ~ Volume overlap measurements for different test cases of axial, sagittal and coronal views.

Row#	Case	Dice_3S				RMSE	HD
		Axial	Sagittal	Coronal	Average		
<b>Cubes</b>							
1	<i>Same</i>	1.0000	1.0000	1.0000	<b>1.0000</b>	<b>0.0000</b>	<b>0.00</b>
2	<i>Rot_2deg_xdir</i>	0.96143	0.91862	0.94637	<b>0.9421</b>	<b>0.8103</b>	<b>419</b>
3	<i>Rot_2deg_ydir</i>	0.89718	0.96854	0.94634	<b>0.9374</b>	<b>0.6429</b>	<b>478</b>
4	<i>Rot_2deg_zdir</i>	0.98502	0.99687	0.99834	<b>0.9934</b>	<b>0.8788</b>	<b>473</b>
5	<i>Rot_2deg_3dir</i>	0.88539	0.90944	0.90868	<b>0.9012</b>	<b>1.3440</b>	<b>473</b>
6	<i>Rot_5deg_xdir</i>	0.90417	0.83176	0.86346	<b>0.8665</b>	<b>1.8172</b>	<b>419</b>
7	<i>Rot_5deg_ydir</i>	0.81104	0.92159	0.86346	<b>0.8654</b>	<b>1.6069</b>	<b>478</b>
8	<i>Rot_5deg_zdir</i>	0.96777	0.99388	0.99693	<b>0.9862</b>	<b>2.1954</b>	<b>466</b>
9	<i>Rot_5deg_3dir</i>	0.78912	0.81934	0.8146	<b>0.8077</b>	<b>2.7825</b>	<b>477</b>
10	<i>Rot_15deg_xdir</i>	0.76907	0.63786	0.64748	<b>0.6848</b>	<b>3.1058</b>	<b>255</b>
11	<i>Rot_15deg_ydir</i>	0.62499	0.78981	0.64749	<b>0.6874</b>	<b>2.5553</b>	<b>476</b>
12	<i>Rot_15deg_zdir</i>	0.96585	0.99265	0.99591	<b>0.9848</b>	<b>2.9046</b>	<b>489</b>
13	<i>Rot_15deg_3dir</i>	0.57462	0.63946	0.55562	<b>0.5899</b>	<b>3.9880</b>	<b>483</b>
14	<i>Trans_02perc_ydir</i>	0.94798	0.90552	0.94737	<b>0.9336</b>	<b>1.2386</b>	<b>23</b>
15	<i>Trans_05perc_ydir</i>	0.88442	0.79355	0.88189	<b>0.8533</b>	<b>3.0033</b>	<b>58</b>
16	<i>Trans_25perc_ydir</i>	0.55683	0.41948	0.54984	<b>0.5087</b>	<b>8.0510</b>	<b>294</b>
17	<i>Non-overlap</i>	0.0000	0.0000	0.0000	<b>0.0000</b>	<b>44.9030</b>	<b>1013</b>
<b>Dome</b>							
18	<i>Same</i>	1.00000	1.00000	1.00000	<b>1.0000</b>	<b>0.0000</b>	<b>0.00</b>
19	<i>Rot_2deg_xdir</i>	0.91849	0.87023	0.8983	<b>0.8957</b>	<b>0.5546</b>	<b>65</b>
20	<i>Rot_2deg_ydir</i>	0.86423	0.87877	0.8608	<b>0.8679</b>	<b>0.5762</b>	<b>2495</b>
21	<i>Rot_2deg_zdir</i>	0.86566	0.83477	0.88539	<b>0.8619</b>	<b>0.1164</b>	<b>2653</b>
22	<i>Rot_2deg_3dir</i>	0.82493	0.79827	0.82531	<b>0.8162</b>	<b>0.7182</b>	<b>2639</b>
23	<i>Rot_5deg_xdir</i>	0.81310	0.77446	0.7899	<b>0.7925</b>	<b>1.1001</b>	<b>162</b>
24	<i>Rot_5deg_ydir</i>	0.71122	0.75858	0.70818	<b>0.7260</b>	<b>1.1779</b>	<b>2727</b>
25	<i>Rot_5deg_zdir</i>	0.72988	0.68254	0.76811	<b>0.7268</b>	<b>0.1960</b>	<b>2654</b>
26	<i>Rot_5deg_3dir</i>	0.65774	0.64804	0.64529	<b>0.6504</b>	<b>1.5778</b>	<b>2617</b>
27	<i>Rot_15deg_xdir</i>	0.54668	0.50139	0.51741	<b>0.5218</b>	<b>3.1325</b>	<b>486</b>
28	<i>Rot_15deg_ydir</i>	0.43425	0.50979	0.40788	<b>0.4506</b>	<b>3.4278</b>	<b>2663</b>
29	<i>Rot_15deg_zdir</i>	0.42622	0.38793	0.46384	<b>0.4260</b>	<b>0.2668</b>	<b>2639</b>
30	<i>Rot_15deg_3dir</i>	0.34392	0.33966	0.3190	<b>0.3342</b>	<b>4.6057</b>	<b>2650</b>
31	<i>Trans_02perc_ydir</i>	0.87093	0.79052	0.87813	<b>0.8465</b>	<b>0.7953</b>	<b>168</b>
32	<i>Trans_05perc_ydir</i>	0.77063	0.6625	0.78236	<b>0.7385</b>	<b>1.7378</b>	<b>421</b>
33	<i>Trans_25perc_ydir</i>	0.11866	0.087385	0.13057	<b>0.1122</b>	<b>8.7223</b>	<b>2103</b>
34	<i>Non-overlap</i>	0.0000	0.0000	0.0000	<b>0.0000</b>	<b>74.3029</b>	<b>6441</b>

Table 7.5: Volume  $\sim$  Volume overlap measurements for different test cases of axial, sagittal and coronal views.

DataSet	Case	Axial	Sagittal	Coronal	Average
Head1	same	1.00000	1.00000	1.00000	<b>1.0000</b>
	perc=0.05	0.97507	0.97502	0.97522	<b>0.9751</b>
	perc=0.20	0.90055	0.90025	0.90045	<b>0.9004</b>
	perc=0.35	0.82631	0.82593	0.8265	<b>0.8262</b>
	inverted	0.00000	0.00000	0.00000	<b>0.0000</b>
Head2	same	1.00000	1.00000	1.00000	<b>1.0000</b>
	perc=0.05	0.97505	0.97519	0.9749	<b>0.9750</b>
	perc=0.20	0.90028	0.89805	0.89991	<b>0.8994</b>
	perc=0.35	0.82693	0.82684	0.82609	<b>0.8266</b>
	inverted	0.00000	0.00000	0.00000	<b>0.0000</b>

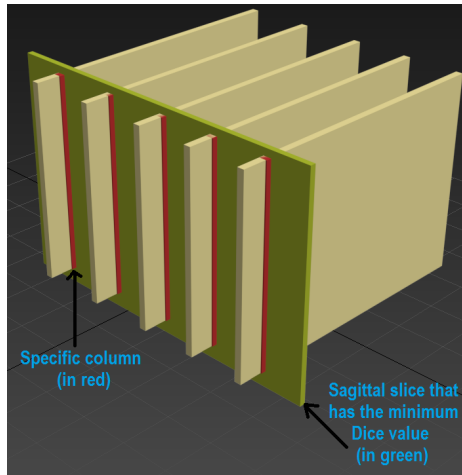


Figure 7.4: The values of the same specific column are inverted (from white to black) in each slice.

to which degree the overlap is between the two input models when both of the inputs represent volume data.

In order to evaluate the ability of the overlap measurement to produce correct outcomes for each plane (axial, sagittal or coronal) separately, we inverted the values of the same specific column in each slice (see Figure 7.4) from white to black and applied the overlap measurement. The values of these measurements are displayed in Table 7.6. The values indicate that the minimum value of similarity ratio occurs in the sagittal plane, which supports the ability of the overlap measurement to sense the source of any non-overlapped regions.

Table 7.6: Volume  $\sim$  Volume overlap measurements when the values of the same specific column in each slice are inverted.

DataSet	Plane	Avg. Dice	Max_Dice	Min_Dice
<b>Head1</b>	Axial	0.99939	1.0000	0.99837
	Sagittal	0.99805	1.0000	<b>0.0000</b>
	Coronal	0.99931	1.0000	0.99634
<b>Head2</b>	Axial	0.99942	1.0000	0.99736
	Sagittal	0.99802	1.0000	<b>0.0000</b>
	Coronal	0.99935	1.0000	0.99074

## Computing the Correlation

Measuring the linear dependence of two random variables represent the value of the correlation coefficient. The correlation coefficient has a value ranges from (-1) to (+1), where (+1) indicates to a total positive linear correlation (all data points lying on a line for which  $set2$  increases as  $set1$  increases), (-1) to a total negative linear correlation (all data points lying on a line for which  $set2$  decreases as  $set1$  increases), and (0) to no linear correlation between the two random variables. Table 7.7 displays the correlation coefficients,  $p_{value}$ , lower and upper bounds for a 95% confidence interval for each coefficient between  $Dice\_3S$ ,  $RMSE$  and  $HD$ . In this context  $p_{value}$  takes a value range from 0 to 1 for testing the hypothesis (i.e. null hypothesis) that there is no relationship between the observed phenomena. The more smaller value of  $p_{value}$  means the corresponding correlation coefficient is considered more significant. In other words, values close to 0 correspond to a low probability of observing the null hypothesis. Numerous studies presented interpretation of the values of correlation coefficients [247] but all such criteria are considered arbitrary to some extent [248].

The computations in the first part of Table 7.7 (i.e. between  $Dice\_3S$  and  $RMSE$ ) lead to some observations. Firstly, the results indicate that there is a good correlation between  $Dice\_3S$  and  $RMSE$  (average=-0.7559) giving that we have a very small number of points in each data set (17 values). This supports the fact that our proposed overlap measurement correlates with one of the most widely accepted

Table 7.7: Correlation coefficients,  $p_{value}$ , lower and upper bounds for a 95% confidence interval for each coefficient between  $Dice\_3S$ ,  $RMSE$  and  $HD$ .

Data set	Correlation	P-value	L-bound	R-bound
<b><math>Dice\_3S \sim RMSE</math></b>				
Pelvis	-0.6727	0.0031	-0.8715	-0.2838
Knee	-0.8115	0.0001	-0.9296	-0.5425
Cubes	-0.8838	0.0000	-0.9576	-0.7009
Dome	-0.6558	0.0043	-0.8641	-0.2558
Average	<b>-0.7559</b>	<b>0.0018</b>	N/A	N/A
<b><math>Dice\_3S \sim HD</math></b>				
Pelvis	-0.6004	0.0108	-0.8389	-0.1684
Knee	-0.1709	0.5119	-0.6021	0.3374
Cubes	-0.5768	0.0153	-0.8279	-0.1331
Dome	-0.6343	0.0062	-0.8545	-0.2211
Average	<b>-0.4956</b>	<b>0.1360</b>	N/A	N/A
<b><math>RMSE \sim HD</math></b>				
Pelvis	0.8803	0.0000	0.6927	0.9563
Knee	0.1741	0.5040	-0.3346	0.6042
Cubes	0.6698	0.0033	0.2789	0.8703
Dome	0.7117	0.0014	0.3512	0.8884
Average	<b>0.6089</b>	<b>0.1271</b>	N/A	N/A

measures. Secondly, the correlation coefficient value is a negative value. The reason of that is while the proportion of similarity ratio is getting bigger, the value of  $Dice\_3S$  increases whereas the value of  $RMSE$  decreases. The third observation is the small value of  $p_{value}$  (0.0018 as an average of the four data sets) which refers to a low probability of observing the null hypothesis.

We mentioned in Section 7.1 that  $HD$  can sometimes produce misleading results. This interprets the reason of the relatively low values of the correlation between ( $Dice\_3S$  and  $HD$ ) and ( $Dice\_3S$  and  $RMSE$ ) when compared to ( $Dice\_3S$  and  $RMSE$ ). The  $p_{value}$  that is generated when we computed the correlation between ( $HD$  and  $Dice\_3S$ ) and ( $HD$  and  $RMSE$ ) for the knee data set is very high (0.5119 and 0.5040) which indicates that the  $HD$  leads to misleading results in this case.

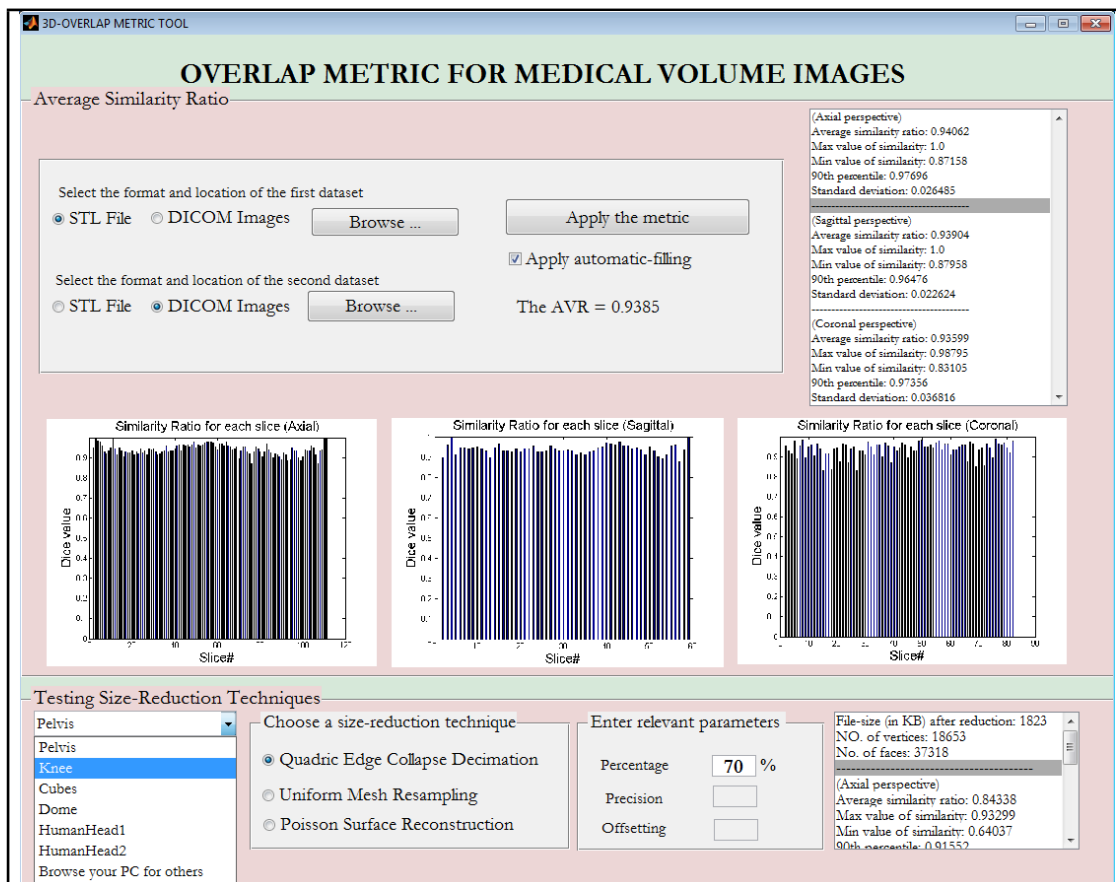
## 7.6 Discussion

The results that are generated by  $Dice\_3S$  support the fact of the ability of this measurement to avoid the drawbacks of the current overlap measurements. While

most of the current overlap measurements finds the degree of similarity with regard to the surface points, *Dice\_3S* is able to measure the similarities not only with two surfaces but even with solid models. Since *Dice\_3S* applies the DSC so this makes *Dice\_3S* insensitive to outliers whereas some of the current overlap measurements are sensitive.

The evaluation through slicing the object (dividing the object into layers) is appropriate for the applications that use 3D-printing since the 3D-printing process takes a 3D mesh and translates this model into individual layers [249, 42]. So the accuracy, that we got for the similarity ratio and the physical distances between individual slices, correlates with the accuracy that we will get when the object is manufactured through the 3D-printing process.

Figure 7.5 displays a screen shot for the Matlab GUI tool that we created to run *Dice\_3S*. Table 7.3 and Table 7.4 in Section 7.5 presented some observations that we are discussing here. The first observation is that the results that are generated by *Dice\_3S* are correlated with the results generated by the RMSE measure which is considered one of the most widely accepted measure used in research. This correlation reinforces the reliability of *Dice\_3S*. The second observation is that the outcomes of *Dice\_3S* presented in those two tables are rational and reasonable in the context of geometry and transformation. For example, the similarity ratio when the object is rotated 15 degrees is less than the similarity ratio when the object is rotated 5 degrees, and the similarity ratio for the later is less than the similarity ratio when the object is rotated 2 degrees (See as an example row#5, row#9 and row#13 in Table 7.4). Another example on the rationality of the outcomes, the similarity ratio when the object is translated 2% is greater than when it is translated 5% and the later is greater than when it is translated 25% (see as an example row#31-row#33 in Table 7.3). The third observation is that the complementary values generated by *Dice\_3S*

Figure 7.5: A screen shot for the Matlab GUI tool of *Dice\_3S*.

could help in recognising the cause of mismatch and then could lead to help any other alignment-algorithm to better alignment. For example (see row#14-row#16 and row#31-row#33 in Table 7.3 and the same rows in Table 7.4), when the object is translated in the y-direction (i.e. sagittal view), the outcomes indicate that the similarity ratio in sagittal view is the lowest when compared to the similarity ratio in axial and coronal views. Another example (see row#2, row#6 and row#10 in Table 7.4), when the object is rotated about the x-axis (i.e. axial view), the outcomes indicate that the similarity ratio in axial view is the highest when compared to the similarity ratio in sagittal and coronal views.

With regard to the use of image filling; We present in Appendix A in Table A.1, A.2 and A.3 the average similarity ratios with and without using the automatic fill of images. There are two observations on these values. The first one is that the overlap measurement becomes more sensitive when the automatic fill of images is deactivated since the number of common white pixels becomes low comparing to the total number of white pixels in the two images. The second observation is that the values generated when the image fill is activated agree with the values generated when the image fill is deactivated. This agreement is obvious in Table A.1, A.2 and A.3 for all rows with just one exception in row#10 and row#11 in Table A.2 where the similarity in row#11 is less than in row#10 (with-filling column) whereas the similarity in row#11 is greater than in row#10 (no-filling column). This can be understood when we know that the similarity values in both rows are very close to each other as the difference between the two values is less than 0.0006.

It is worth noting that *Dice\_3S* is robust to partial volume effects (See Figure 7.6). That is because *Dice\_3S* takes 3 perspectives (i.e. axial, sagittal and coronal) into consideration when it measures the proportion of overlap between two objects. This leads to more accurate results for partial volume estimate.

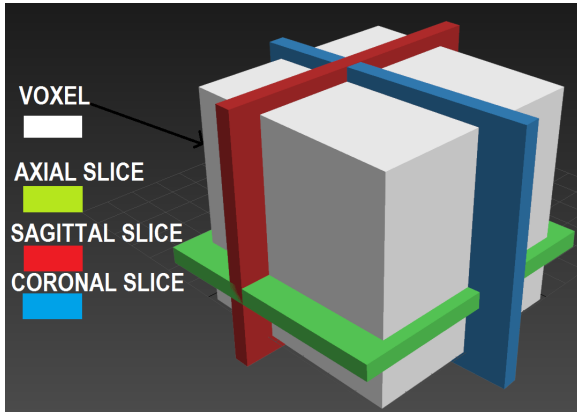


Figure 7.6: The three different perspectives intersect the voxel space in different positions producing more accurate results for partial volume estimate.

The standard deviation of the DSC for each image slice is supplied by *Dice\_3S* as a complementary value. High values of the standard deviation indicates that the similarity ratio between the corresponding 2D images are spread out over a wide range of values. This in turn means there are a proportion of outliers and then the figures that display the similarity ratio for each slice should be investigated to recognise the images which cause that.

The axial, sagittal and coronal analysis figures that are supplied by *Dice\_3S* can lead to recognise the regions/positions of mismatch or lower overlap. For example the bar charts, shown in Figure 7.7, are produced by *Dice\_3S* to find the proportion of overlap between a 3D model of a head and an edited version of that model. To simplify, a delineation of a head is shown in Figure 7.8(a) and the edited version of that model is shown in Figure 7.8(b). Notice that the editing is performed over the region that is shown in red colour. The slicing process in our approach generates (102,61,74) images in axial, sagittal and coronal directions respectively. Having a look over the three bar charts in Figure 7.7 it can be seen that there is a low proportion of similarity on the left half of the top region of the head (displayed in red in Figure 7.8(b)). The first 50% (30 images) in the sagittal chart have a lower value of similarity

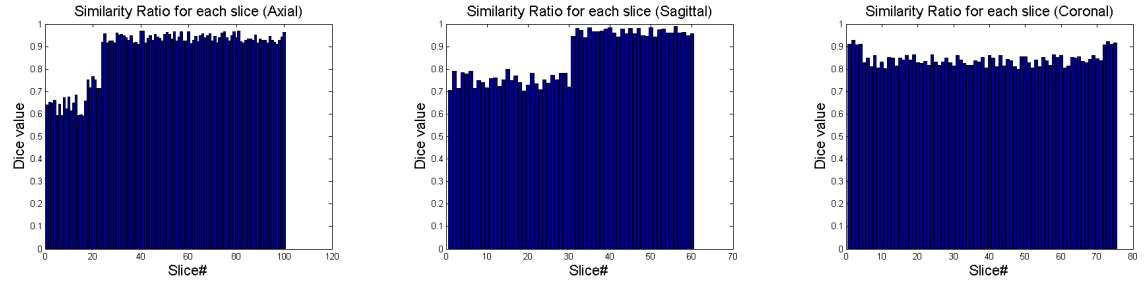


Figure 7.7: Bar charts generated by *Dice\_3S* to find similarity ratios between a head displayed in Figure 7.8(a) and another edited version of that head displayed in Figure 7.8(b). (left): axial, (middle): sagittal, and (right): coronal

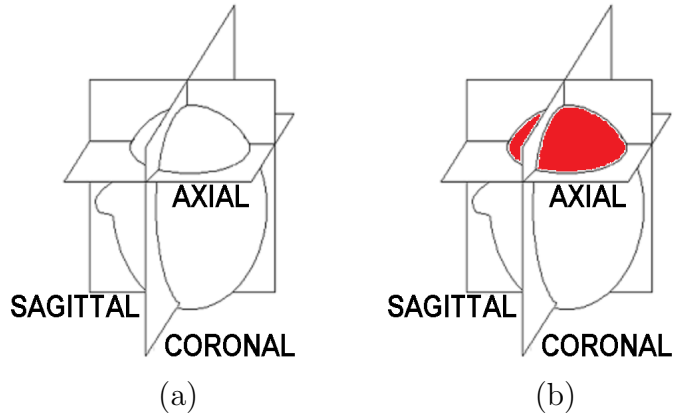


Figure 7.8: (a) Delineation of a head shows the axial, sagittal and coronal perspectives (imported from [3] and edited) (b) The region that has a low overlap is displayed in red.

than others which means a mismatch in the left half of the head, and the first 20% (20 images) in the axial chart have a lower value of similarity than others which means a mismatch in the top region of the head. The proportion of similarity of the images in the coronal direction show that all the images have convergent values which indicates that the problem does not occur at specific region when we direct from the front of the head to the back.

## 7.7 Summary

This chapter presented a model to measure the 3D-overlap ratio between medical volume images. The proposed overlap measurement (*Dice\_3S*) plays a key role in the process of quantifying the quality of the image segmentation and registration. It has a number of characteristics; firstly it presents a figure-of-merit to quantify the proportion of overlap between medical volume images. Secondly, it accepts as inputs two surfaces, two 3D-grid, or one surface and one 3D-grid. Thirdly, it gives complementary figures of statistical use that lead to recognise the amount and positions of regions of match and mismatch. Fourthly, it examines the overlap ratio taking the axial, sagittal and coronal planes into consideration which makes it convenient for medical applications. Fifthly, it is insensitive to outliers which makes this measurement of vital importance for medical images in particular. Sixthly it does not need to orient or position the objects under-evaluation in specific pose. It takes the two objects as they are and starts the evaluation without the need for any initialisation or specific setting and furthermore it is able to locate geometric errors on a highly curved surfaces.

An intensive evaluation, over six different data sets with different test cases, has been performed to validate the outcomes of *Dice\_3S*. The values that were generated by *Dice\_3S* were compared with the values that are generated by other three widely-accepted overlap measurements. The correlation and rationality of the outcomes of *Dice\_3S* are evident. The analysis that we presented in this study indicates that *Dice\_3S* presents complementary values that describe the regions of overlaps with regards to the axial, sagittal, and coronal planes which makes this measurement convenient for medical volume images.

Down-sampling (i.e. size-reduction) of medical volume images is a critical issue since high-density volume images need high resources (memory, graphic cards, CPU,

...) and since over-downsampling can decrease the quality of the volume image. We employed *Dice\_3S* to evaluate the effect caused by the Quadric Edge Collapse Decimation technique and the Uniform Mesh Resampling technique, and to find the optimal value of the parameter  $\alpha$  in Poisson Surface Reconstruction technique. The results of these experiments are displayed in Appendix A.

# Chapter 8

## Pre-clinical Trial

The evaluation of segmentation of CT medical images to construct CT-derived models is gaining importance since it is required in many applications such as radiotherapy treatment, the diagnosis of malignant tumours and guiding surgical and remedial procedures. This chapter presents a pre-clinical trial of an automatic segmentation pipeline that is the main component in a system designed to automatically generate a 3D model that in turn can be printed to create an immobilisation shell. The focus of this chapter is to introduce a novel pipeline that can be used to evaluate the accuracy of segmenting a CT volume by comparing to a 3D ground-truth model acquired using a laser scanner. Section 8.1 presents an overview on what has been used in the previous studies as a ground-truth. Section 8.2 explains in detail the steps of the proposed pipeline and how it can be employed to evaluate the accuracy of the segmentation methods. The experimental work is presented in Section 8.3 and the results are displayed in Section 8.4. Section 8.5 draws a conclusion for this chapter.

### 8.1 Introduction

This chapter introduces a novel pipeline that can be used to evaluate the accuracy of medical image segmentation techniques when a 3D mesh is employed as a ground-truth (e.g laser-scan mesh). In terms of selecting a ground-truth, there are numerous

studies that use a 2D manual segmentation as a ground-truth to evaluate the accuracy of the segmentation process for CT-derived models. For example: [250] used the manual segmentation as a ground-truth to segment and reconstruct a newborn's skull, [251] to segment the kidney into multiple components, [252] for segmentation of muscle and fat tissues from CT images to estimate body composition, [253] for crown segmentation from CT images with metal artefacts, [254] to segment the hematoma region from CT images and [255] for 3D medical image segmentation.

There are many other studies that used real physical measurements as a ground-truth using a calliper or a coordinate measuring machine and compared them with linear measurements of the images. For example: the authors in [256] used linear measurements to compare the depth and diameter of simulated bone defects in an acrylic block and a human mandible with predetermined machined dimensions to validate whether Cone Beam Computed Tomography (CBCT) measurements were precise. In [257], a geometric measuring object made of polymethylmethacrylate whose geometry is exactly known was used to determine the geometric accuracy of CBCT and to evaluate their convenience for implant planning. In [258], the authors determined the accuracy of measuring linear distances between landmarks commonly used in orthodontic analysis on a human skull using two CBCT systems and compared their readings with physical measures using a calliper. A calliper was used in [259] to evaluate the accuracy of the linear measurements obtained in CT images when compared with measurements obtained in dry skulls. In [240], three 3D scanning systems were evaluated using the physical linear measurements as a ground truth to evaluate the accuracy of standard anthropometric linear measurements. Other examples of using real physical measurements as a ground-truth include [260, 231, 261]

There are also many other studies which employed the laser-scan mesh as a ground-truth as it is presented in Chapter 3. Examples of those studies include [80, 81,

82, 83, 84, 85, 87, 88, 89, 90, 91]. Manual segmentation is time consuming and prone to error. Real physical measurements do not lead to accurate results in our research project since attempting to accurately measure the human head would be a challenging task. On the other hand, laser scanning is a fast process when compared to manual segmentation, not subjective as is the case in manual segmentation, and it can lead to an accurate representation given the precision of scanners available on the market.

## 8.2 The Proposed Pipeline

The proposed pipeline consists of various steps that produce in the end a value which represents the ratio of similarity between the two input models. The key to our pipeline is the process of generating 2D slices from a 3D mesh (i.e. laser-scan mesh). The generated 2D slices can then be compared with the stack of CT images. Since the CT-derived model and the laser-scan model may be completely misaligned, have different image resolution and/or different point-set densities, our pipeline handles all of these differences in order to produce an accurate alignment between the two models. This pipeline employs the whole 3D model surface for registration and not only certain landmarks. In addition to that, this pipeline presents a standardized methodology that can be used to assess the accuracy of various CT scanners when a specific segmentation approach is used.

In order to convert the 3D laser-scan mesh to a stack of 2D slices, the pipeline applies plane/triangle intersection in order to intersect the geometry of the scanned object with the slicing plane to obtain 2D slices from the 3D model. A graphical representation of the pipeline is presented in Figure 8.1. This pipeline is applied to align and evaluate a stack of 2D CT images of an object (normally saved in DICOM file format) and a 3D mesh acquired for that object via a laser scanner (saved in an stl

file format). The output produced by this pipeline is a ratio (a number between 0 and 1) which measures to which degree the CT-derived model is similar to the laser-scan model.

### 8.2.1 Reading a stack of 2D CT images and constructing a 3D model

The first step in our pipeline includes reading a group of 2D CT images, building a 3D volume that represents the CT-scanned object to which the CT slices belong and surface reconstruction. Surface reconstruction techniques are widely used in medical applications to build 3D models [262]. This step includes a group of sub steps (shown in Figure 8.2 and explained in next paragraphs).

#### 2D Image Segmentation

This step involves Implementing a 2D image segmentation technique to convert the images to binary. We used Otsu's method [104] to produce black/white images since the data sets that are being used represent homogeneous surfaces which should be easily segmented by Otsu's method.

#### Automatic Cropping

In this step an automatic preprocessing is performed by cropping segmented images to remove unrelated-components from the image that do not form a part of the object like the couch and most of the pixels that form the background of the image. This is done automatically by scanning each segmented image from the top most row, the left most column and the right most column to find the area that forms the borders of the target object. The next step is to search for the bottom border by finding the pixels that represent the couch which normally occupy most of the width of the image.

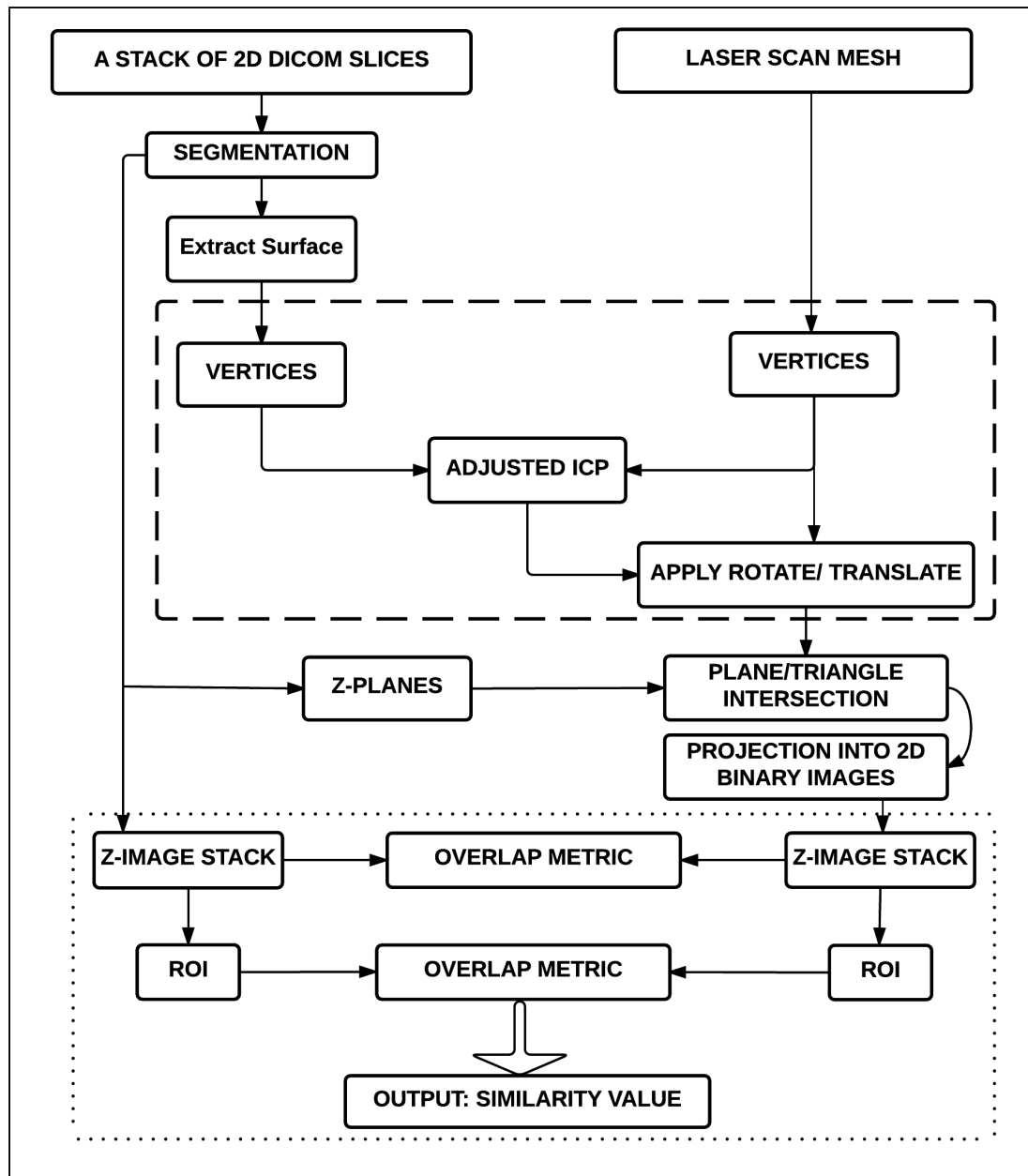


Figure 8.1: A schema represents the pipeline of the proposed approach

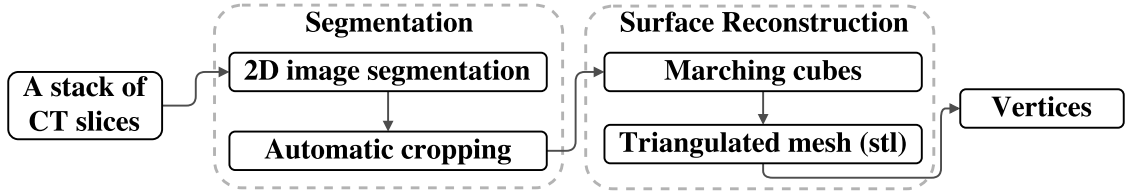


Figure 8.2: The first step of the pipeline includes image segmentation and surface reconstruction.

### Applying the Marching Cubes

We then use the Marching Cubes algorithm [19] to build a 3D model of the scanned object. The basic function of the Marching Cubes algorithm is to compute a triangulated mesh of the isosurface within a 3D matrix of scalar values at a specific isosurface value. The x, y and z coordinates of the stack of CT slices should be prepared before sending them to the Marching Cubes algorithm. This implies performing a mesh grid operation in which we produce a 3D coordinate array. It is of high importance in this step to consider the "pixel-spacing" and the "spacing-between-slices" parameters of the CT-scanner in order to produce an accurate 3D coordinate array which will be sent later to the Marching Cubes algorithm. Pixel-spacing is a value generated from the CT-scanner that specifies the physical distance measured between the centres of two adjacent pixels (see Figure 8.3) where spacing-between-slices gives the distance between two adjacent slices (perpendicular to the image plane). The triangulated mesh returned by the Marching Cubes algorithm includes a structure of vertices (V) and another structure of faces (F). Structure (V) specifies triangle vertex values whereas structure (F) defines which vertices to connect. The precise description of how the Marching Cubes algorithm generates triangles is presented in [19].

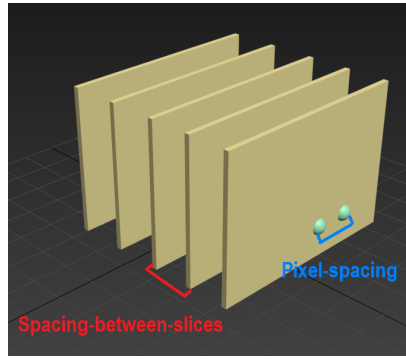


Figure 8.3: Graphical representation of the concepts of pixel-spacing and spacing-between-slices.

### Creating Triangulated Mesh

This step involves creating an stl (Stereo Lithography) file using the returned faces (F) and vertices (V) produced by the Marching Cubes algorithm. Stl file is a triangular representation of a three dimensional surface geometry. The surface is broken down into a series of small triangles (facets). Each facet is described by a perpendicular direction, named normal, and three vertices representing the corners of the triangle. Most of all today's 3D scanners are capable of producing output using the stl file format and this format is supported by many software packages, commonly used in computer-aided manufacturing (CAM), computer-aided design (CAD), rapid prototyping and 3D printing. Due to this we decided to build an stl file from the stack of CT slices and then we can let the two models go through the same pipeline. The stl format can be stored either in ASCII or in binary representation. Binary files are more common, since they are more compact. Table 8.1 shows the general format of a binary stl file.

All of the steps of our pipeline are performed automatically with no need for human intervention.

Table 8.1: The syntax for a binary stl file

UINT8[16]	Header
UINT32	Number of triangles
for each triangle	
REAL32[3]	Normal vector
REAL32[3]	Vertex 1
REAL32[3]	Vertex 2
REAL32[3]	Vertex 3
UINT16	Attribute byte count
end	

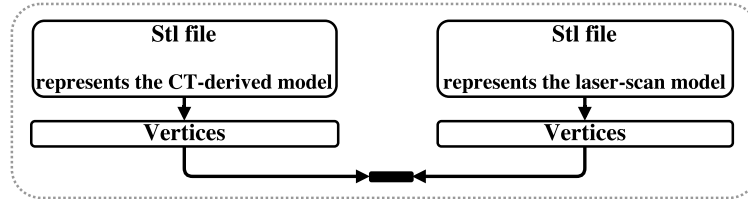


Figure 8.4: The second phase of the pipeline: Extracting the vertices.

### 8.2.2 Extracting the vertices from the triangulated mesh and simplifying it

After the end of the first step, two triangulated meshes each in stl file format will be produced. The first mesh is a 3D model generated from a stack of 2D CT slices and the second one is the laser-scan model, see Figure 8.4. In order to align and register these two models, we extract the vertices from each mesh and then remove duplicated vertices, a process named simplifying the mesh. Removing duplicated vertices will reduce the computation required for the alignment algorithm. The details of simplifying the mesh are presented in Chapter 7.

We present here just a simple example that shows how simplifying the mesh can decrease the size of the vertices array to 1/3 of its original size (see Figure 8.5). In the example, the vertices array ( $V$ ) consists of 12 rows before removing the duplicated values and the number of rows becomes 4 rows after simplifying the mesh (see Figure 8.6).

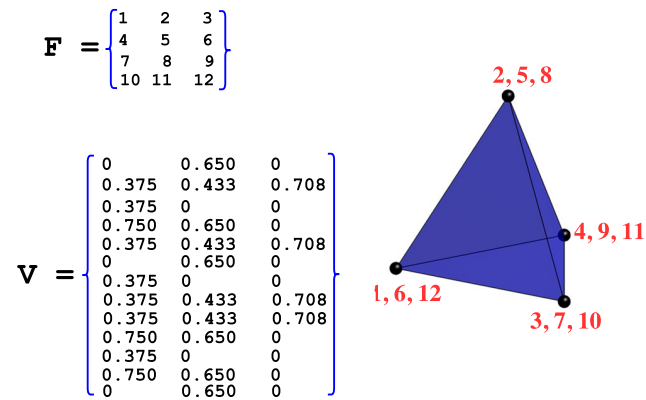


Figure 8.5: A simple mesh includes 12 rows of vertices before simplifying (imported from [4] and edited).

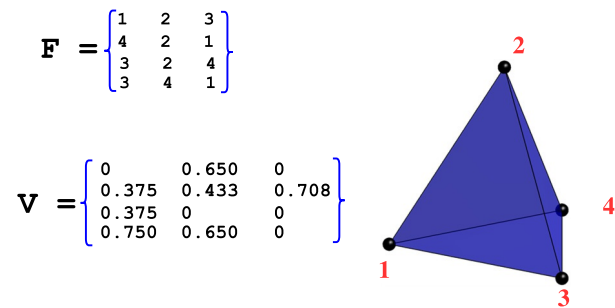


Figure 8.6: The same mesh in Figure 8.5 but after simplifying it to be composed of 4-rows.

### 8.2.3 Alignment, Slicing, and Measuring the Overlap Ratio

We now have two groups of non-duplicated vertices. The first group belongs to the model generated from CT slices whereas the second group of vertices belongs to the laser-scan model. Our adjusted ICP algorithm, which we presented in Chapter 6, is being used to align the CT-derived model and the laser-scan model.

The next step includes slicing the aligned laser-scan mesh by intersecting its triangles with the z-planes constructed at the same locations as the slices of the CT-derived model in order to be able to match each slice from the laser-scan model with its corresponding slice from the CT-derived model.

The vertices that we have so far represent the corners of 3D triangles which compose the surface of the mesh of the aligned laser-scan model. It is necessary at this stage to calculate the line segments which result from intersecting Z-planes with each triangle from the set of the triangles' vertices of the laser-scan model. Z-planes are set at the same locations as the CT slices. Notice that each plane is defined by a point  $Q$  (which is located in the CT slices) and a normal vector  $N$ , and each triangle is defined by three vertices ( $P1$ ,  $P2$  and  $P3$ ).

To calculate the intersection segment between a plane and a triangle, we firstly find in which side the vertices of each triangle ( $P1$ ,  $P2$  and  $P3$ ) lies regarding to the plane according to equations (8.2.1) (8.2.2) and (8.2.3). The equations apply dot product to determine the side in which each corner of each triangle lie regarding to the plane. For example, if  $d1$  and  $d2$  have the same sign, then that means  $P1$  and  $P2$  lie in the same side regarding to the plane, whereas if they have different signs then that means  $P1$  and  $P2$  lie on different sides. Knowing on which side each triangle vertex lies will lead us to the next stage in which we calculate the intersection segment between a plane and a triangle. The details and the algorithms that we derive to apply the plane/triangle intersection and to project the intersection points into image pixels

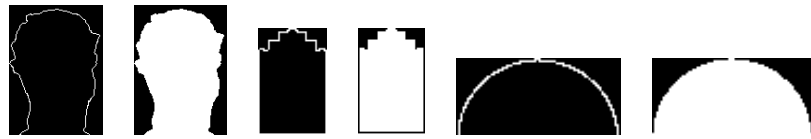


Figure 8.7: Examples of laser slices and its corresponding slices after filling.

are presented in Chapter 7.

$$d1 = (P1 - Q).N \quad (8.2.1)$$

$$d2 = (P2 - Q).N \quad (8.2.2)$$

$$d3 = (P3 - Q).N \quad (8.2.3)$$

Since laser-scan models provide just the surface of the scanned object whilst the CT scanner provides the internal structure of the scanned object in addition to the surface, we filled the images and then applied the overlap measurements. Figure 8.7 shows three examples on the filling operation of images obtained from the laser-scan model after applying the slicing process over that laser-scan model.

The overlap measurement is then performed between each slice from the stack of CT slices and its corresponding slice from the stack of laser-scan slices. The Dice measurement is used to find the level of similarity between the two corresponding slices. We define a measure that represents the total mean of similarity between the two groups of images according to the Dice measurement. This mean value is shown in (8.2.4) where  $n$  represents the total number of compared slices.

$$Avg - Dice = \frac{\sum_{i=1}^n Dice(CTSlice(i), laserSlice(i))}{n} \quad (8.2.4)$$

Since the 3D mesh that is generated by laser scanners may have some gaps and may suffer from incompleteness in some regions, then we define in our pipeline an

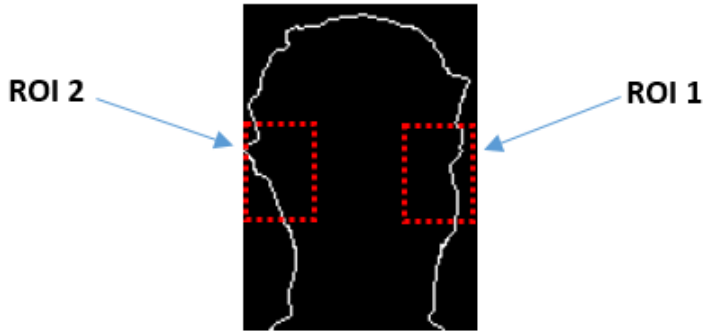


Figure 8.8: Two regions of interest defined by the user.

optional step in which we allow to define a region of interest (ROI). This means to define a window (region) over an area of a slice so the overlap measurements will be performed over just these defined regions. If, for example, the user is interested on the area that lies on the bottom right of the image, then the overlap measurement will be calculated over those pixels that lie on that region of interest only (see Figure 8.8).

### 8.3 Experimental Work

There are three data sets used in the experiments of this chapter: the cubes, dome and the Cantonese head. The description, properties and sources of these data sets are presented in Chapter 3. It is worth mentioning here that we have two scans for these objects (a CT scan and a laser scan).

This part will present the experiments that were applied over the three objects. Figure 8.9 shows the first steps that we did over the stack of CT slices to build a 3D triangulated mesh for each object. We started the process by implementing Otsu's segmentation algorithm to get segmented binary images (see Figure 8.9 (b), (f) and (j) ), and then we applied the automatic preprocessing steps to crop images (see Figure 8.9 (c), (g) and (k)). After that we applied the Marching Cubes algorithm over the stack of segmented images to build a 3D model for each object and converted

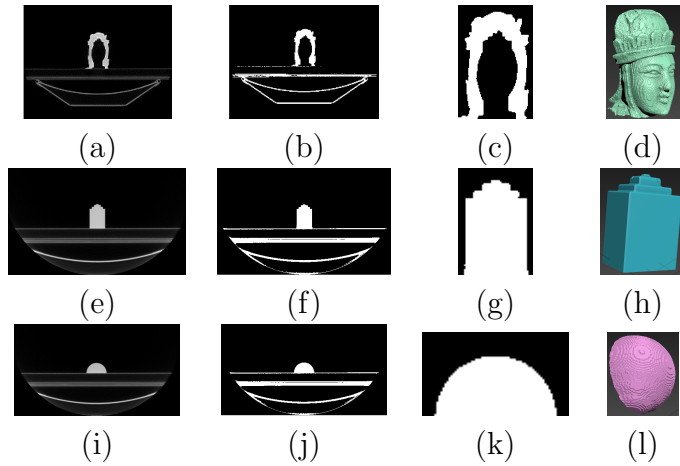


Figure 8.9: Building 3D models from 2D medical images. (a-d): head (e-h): cubes and (i-l): dome. The first column displays the original images (DICOM images), the second column displays the segmented images, the third column displays the segmented images after the automatic cropping and the fourth column displays the constructed 3D models.

that 3D model to stl file format as depicted in Figure 8.9 (d), (h) and (l). We then converted the two meshes to vertices and removed duplicated vertices. The details of this process were presented in Section 8.2.

After that, we moved to apply the adjusted ICP algorithm over the two models (i.e. the CT-derived model and laser-scan model). The two models, as displayed in the figures of Chapter 6, were completely misaligned, having different coordinate systems, different image resolution and different point-set densities. Applying the adjusted ICP algorithm achieved a high level of superimposing and alignment between the two models. More details and readings on applying the adjusted ICP over these objects are presented in Chapter 6.

We then calculated the plane/triangle intersections between the set of facets of the laser-scan model and the set of planes which are imported from CT images as it was described previously in Section 8.2. Finding those intersection segments formed the base to perform slicing of the aligned 3D laser-scan model. After that, we converted all laser slices to binary images.

Then we filled the slices as presented in Section 8.2 Figure 8.7 and calculated the overlap measurements between the two stacks of slices. The results of this phase are presented in the next section.

## 8.4 Results

As stated before, the reliability of the similarity value generated by the proposed pipeline is affected by the accuracy of the alignment process between the CT-derived model and the laser-scan model. The experimental results of applying the adjusted ICP are presented in Chapter 6. We will just present here the final readings that are generated by the pipeline to evaluate the accuracy of segmentation.

The average values of the Dice similarity measure were calculated according to Equation (8.2.4). Table 8.2 displays the average Dice value, standard deviation and the 90<sup>th</sup> percentile for the three objects. It is obvious that all the three objects achieved high level of Dice value which supports the claim that surface models derived from CT data are an excellent representation of the real scanned object. Notice that although the surface of the head contains many more complex structures, engravings and curvatures, it still achieved 96.96% which made us very assured that the proposed pipeline presents a robust approach to evaluate the accuracy of surface models built from CT images. We present in the table the 90<sup>th</sup> percentile and the low values of the standard deviation to indicate the stability of results over the whole collection of slices. Moreover, the success of applying this pipeline over three different objects each with its different characteristics increases the reliability of the output generated from the proposed pipeline.

Table 8.2: Dice value, Standard deviation and the 90<sup>th</sup> percentile for the three objects.

Measurements	head	cubes	dome
Average Dice value	96.96%	99.40%	98.61%
Standard deviation	0.073341	0.00268	0.022607
90 <sup>th</sup> percentile	0.9844	0.99689	0.99039

## 8.5 Conclusion and Discussion

This chapter presented a fully automatic approach that can be followed to evaluate the accuracy of CT-derived models. The experimental work and results indicated clearly that CT-derived models achieved very high values of similarity with the ground-truth. While most of the published studies in this field either require 2D manual segmentation or use linear physical measurements for the purpose of providing a ground-truth, the proposed pipeline presents an automatic approach for evaluation of CT-derived models using 3D triangulated-meshes acquired by a laser scanner as a ground-truth. Using a laser-scan model as a ground truth saves much time and effort. Manual segmentation and/or physical measurements are time-consuming and prone-to-error since they are done by humans where the recent advances in laser scanning technology makes it strongly relevant to be used as a ground-truth. The chapter presented a detailed description about the proposed approach in the form of a pipeline which shapes a framework that can be followed by researchers. MATLAB R2014a Image Processing Toolbox was used in implementing this pipeline.

Since the first element that affects the overall accuracy of the CT-derived models is the accuracy of the 2D-segmentation technique, then the proposed pipeline can be used for evaluation of the accuracy of 2D segmentation techniques. Applying different segmentation techniques in the proposed pipeline will produce different output similarity values. A higher similarity value means a higher matching between the CT segmented-images and the ground truth, and consequently means a more accurate 2D

segmentation technique convenient for extracting the surface of the scanned object.

The two inputs of the proposed pipeline could be two meshes scanned by two different 3D acquisition devices. Consequently, we can evaluate the accuracy of a 3D derived mesh produced by one of these devices assuming that the mesh produced by the other device forms the ground-truth. Figure 8.10 displays the pipeline that can be used to evaluate the accuracy of a mesh generated from a 3D acquisition device compared to another mesh generated from another device which has a higher resolution (i.e. ground truth). This pipeline is similar to the pipeline presented in Figure 8.1 except that this pipeline skips the steps that are responsible of segmentation and building a mesh from the stack of 2D slices, and it performs the plane/triangle intersection for both inputs not for only one input.

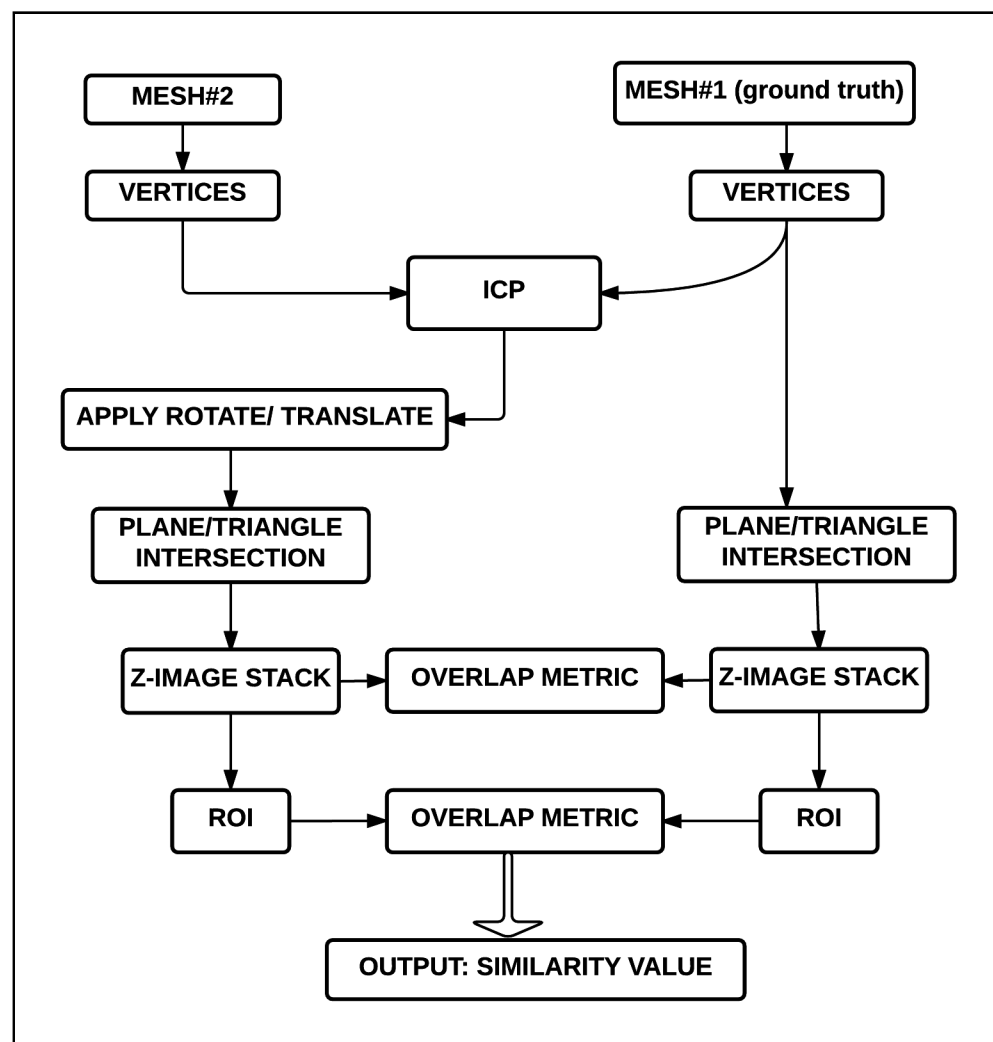


Figure 8.10: A proposed pipeline that can be used if two meshes are the inputs.

# Chapter 9

## Clinical Trial

This chapter starts by presenting, in Section 9.1, an overview of the clinical trial which forms a part of this thesis. The basic features of this trial and the design and methodology of it are also described. Section 9.2 describes the experimental work which was designed to evaluate the outcomes of constructing an immobilisation mask for the “Perspex Mask” data set. A detailed discussion is presented in Section 9.3 on the results generated and the possible sources of inaccuracies when applying our pipeline. Section 9.4 summarises the main points of this chapter. Related documents to our clinical trial are presented in Appendix B.

### 9.1 Overview of the Clinical Trial

This section presents an overview of the clinical trial and its basic features. Our clinical trial is registered under the permission and approvals of the (Health Research Authority, NHS, UK) and the (Research Ethics Committee (REC), Yorkshire & The Humber, UK) and sponsored by the University of East Anglia, UK. It was given the following ID under the Integrated Research Application System (IRAS project ID:209119) and the following reference under the Research Ethics Committee (REC reference:16/YH/0485). Our clinical trial is posted online (see [263, 264, 265]). Table 9.1 illustrates some basic information about this clinical trial.

Table 9.1: Basic description of our clinical trial.

<b>Title of the trial</b>	Acquisition of 3D facial geometry of patients' scheduled for RT 1.0
<b>Category</b>	Basic science study involving procedures with human participants.
<b>Site of the trial</b>	England
<b>Principal inclusion criteria</b>	Patients undergoing radiotherapy treatment for tumours affecting their head and neck.
<b>Principal exclusion criteria</b>	Age not in 18-69 years and patients who are not able to give written informed consent (in English).
<b>Identification process</b>	The oncology department, Norfolk and Norwich University Hospital will identify patients who are planned to have head and neck radiotherapy.
<b>Trial's Objective</b>	To compare 3D models of facial geometry built from CT and laser-scanner data sets in terms of accuracy and precision.
<b>Trial's Outcome</b>	providing patient specific data that will in turn enable algorithms developed to be quantitatively evaluated and compared, thus allowing us to determine if the approach is clinically viable.

## Methodology

The stages of the clinical trial are represented as a flowchart in Figure 9.1. Patients will follow a normal treatment pathway, using an immobilisation shell manufactured normally (i.e. ‘softdrape’ or ‘hard-shell’). Once the mask has been manufactured (by mould room technicians) it will be scanned (in the mould room) using the laser scanner. Researchers at UEA will need a copy of (pseudonymised) patient’s CT data. This will be held at the School of Computing Sciences, UEA (for more information see the clinical trial protocol in Appendix B).

Laser Scanning of patients will take place at the Norfolk and Norwich University Hospital (NNUH) NHS Foundation Trust. A researcher from UEA will perform the scan, supervised by a radiographer or nurse from NNUH. The participant will be asked to sit in an office chair and participant’s head will be scanned using a hand held laser scanner. The laser scanning session will take about 15 minutes and during

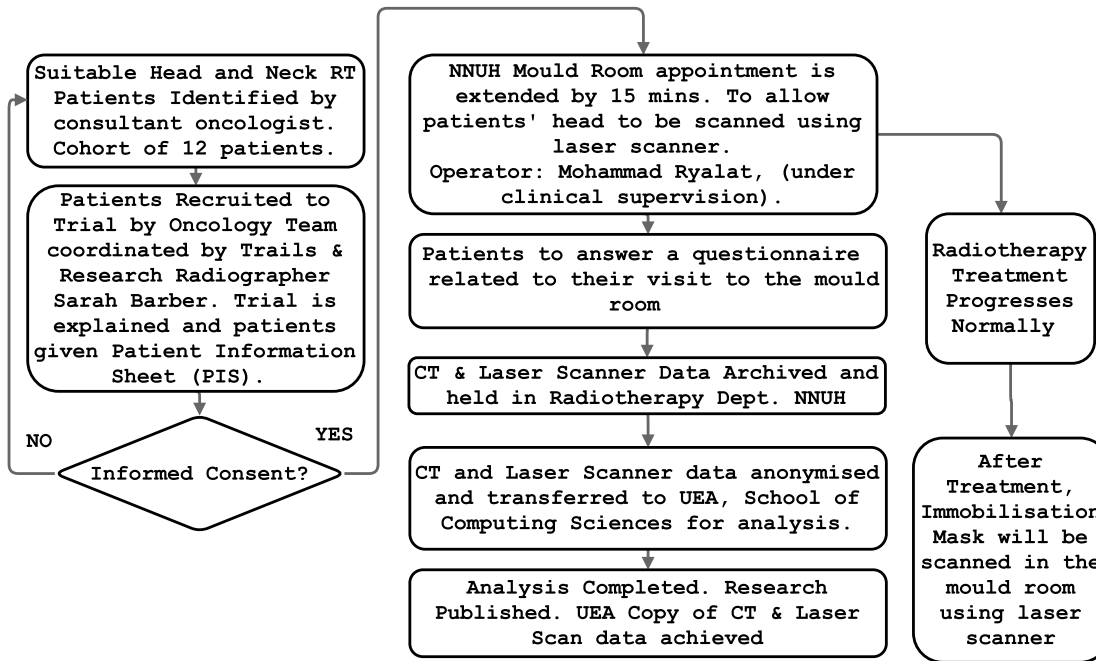


Figure 9.1: Flowchart represents the stages of the clinical trial.

this time participant will need to wear an eye mask. The process can be completed in stages with a break of 2-3 minutes between each session. The hand held laser scanner will be moved around the participant and the distance between participant's head and the laser machine will be in the range 20-60 cm (for more information about the laser scanning session see the participant information sheet in Appendix B).

The low power laser used in the scanner is no more powerful than a laser pointer. The laser machine is CE marked which means that the machine complies with the essential requirements of the relevant European health, safety and environmental protection legislation. This procedure will be applied one time only for each participant. Participant's eyes will be covered while being scanned.

### Objectives

The main three questions that this trial aims to answer:

1. To determine if a computer vision system can automatically generate 3-D printed

immobilisation masks having performance comparable to existing head and neck immobilisation systems from a CT scan?

2. To compare 3-D models of facial geometry built from CT and laser-scanner data sets in terms of accuracy and precision?
3. To identify if patients find the experience of making a facial mould using plaster of paris distressing and painful?

### **Outcome**

The potential broad outcomes for the trial which will reflect the research question aims:

1. We will place the mask on the patients face (virtually, using 3-D computer modelling) and report errors measured between the immobilisation shell and the patients skin. This will enable us to benchmark a range of algorithms used to segment the CT and extract a surface contour that could be used to print a shell.
2. By comparing results of computer modelling with those reported for thermoplastic masks we can determine if the approach is viable.
3. Patient responses to the questionnaire data will provide limited insight into their experience in the mould room.

Although the ethical and HRA approval that we have got relates to scanning patients and masks, the work reported in this chapter only relates to a mask (i.e. currently no patients have been scanned due to the unavailability of the laser scanner). More details and documents of our clinical trial are presented in Appendix B.

## **9.2 Experiments and Results**

Although our *Dice\_3S* measurement, presented in Chapter 7, provides a ‘figure of merit’ that can be used to assess the degree of agreement between the models it does not provide any information about the degree of immobilisation provided by the

mask. To address this we also provide absolute measurements of the space between the surfaces of the two models.

We present in this section two approaches in order to evaluate the accuracy of the outcomes that were generated when we applied our experiments over the “Perspex Mask” data set. In the first approach we use our pipeline that was presented in Chapter 8 to evaluate the similarity between the CT-derived model and the laser-scan model. In the second approach we measure the distances (in pixels) between the external border of the CT slices and their corresponding external borders of laser slices in order to have a good conception about the accuracy of physical measurements.

## Evaluation through our Pipeline

As explained in previous chapters, our pipeline presents statistics which represent the degree of similarity ratio between the CT slices of the patient’s head and its corresponding slices calculated from the laser-scan model. The overlap measurement that is used by the pipeline to find the similarity ratio between each two corresponding slices is the DSC. Table 9.2 shows the statistics generated by our pipeline to represent the similarity ratio between the CT slices and the slices that are calculated from the laser-scan model for the “Perspex Mask” data set. The readings in this table shows that the average similarity ratio equals 96.56% which indicates to a relatively high degree of similarity between the two groups of images. Figure 9.2 displays a histogram representing the similarity ratio slice by slice for the “Perspex Mask” data set. The results shown in the histogram support the readings that we got in Table 9.2 in which we notice that the standard deviation has a low value which indicates that the values of similarities between corresponding images are close to the mean. This in turn increases the robustness and reliability of the outcomes.

Table 9.2: Statistics generated by our pipeline to represent the similarity ratio between the CT slices and the slices that are calculated from the outer surface of the mask for the “Perspex Mask” data set.

Avg. Similarity ratio	Max. value	Min. value	Standard deviation	90 <sup>th</sup> percentile
96.56%	97.77%	94.62%	0.00796	97.29%

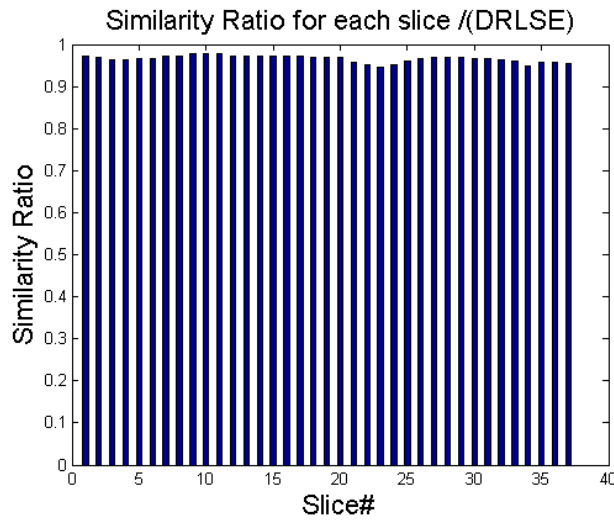


Figure 9.2: A histogram representing the similarity ratio slice by slice for the “Perspex Mask” data set generated by our pipeline.

## Evaluation through Physical Measurements

Figure 9.3 displays a flowchart which represents the procedure that we follow to calculate the physical distances between the surface of the CT-derived constructed model and the laser-scan model. In each iteration of this procedure two images are entered as inputs. The first input represents a filled segmented CT image (see Figure 9.4(left)) and the second one represents its corresponding filled image calculated from the laser model (see Figure 9.4(right)).

The next step in the procedure is to get the border of each image. This process involves creating a binary image having ones where the process finds edges and zeros elsewhere. We used the Sobel approach to detect edges in both images. Figure 9.5 shows the two images displayed in Figure 9.4 after getting the borders. We then

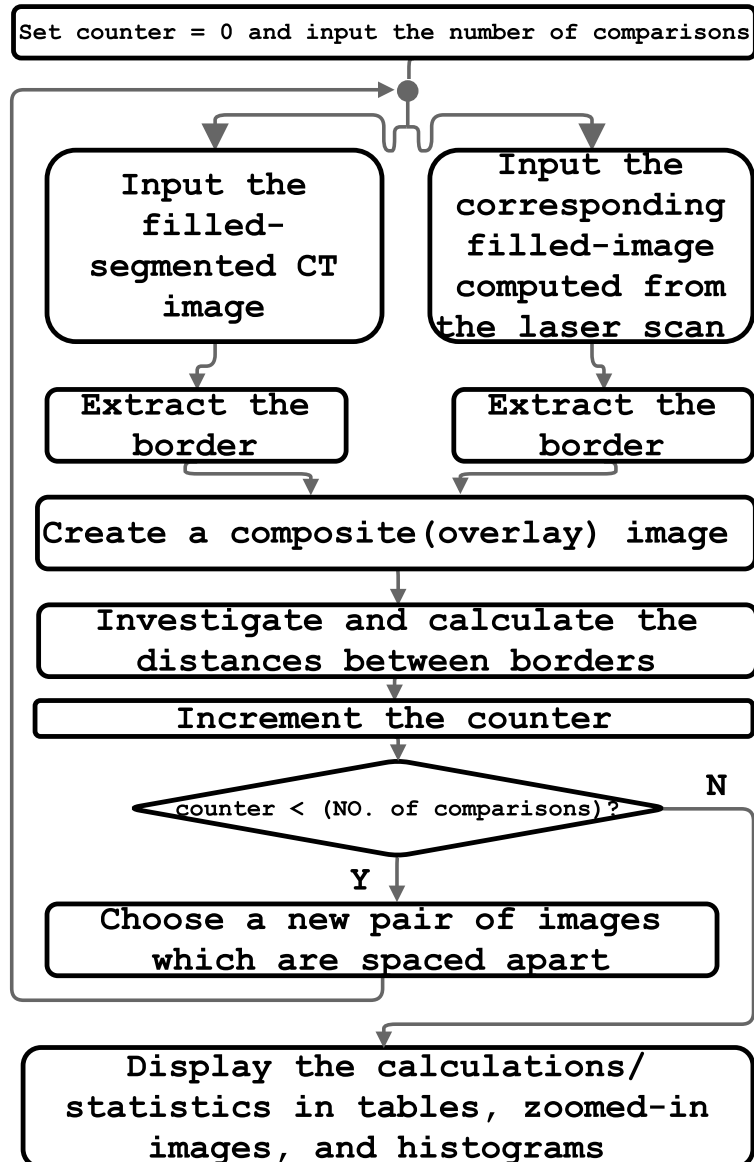


Figure 9.3: A flowchart represents the procedure to calculate the physical distances between the two surfaces (CT-derived model and laser-scan model).



Figure 9.4: (left) A CT image segmented using DRLSE technique and filled, (right) Its corresponding image computed from laser model and filled.



Figure 9.5: (left) A CT image after detecting the edges, (right) Its corresponding laser image after detecting the edges.

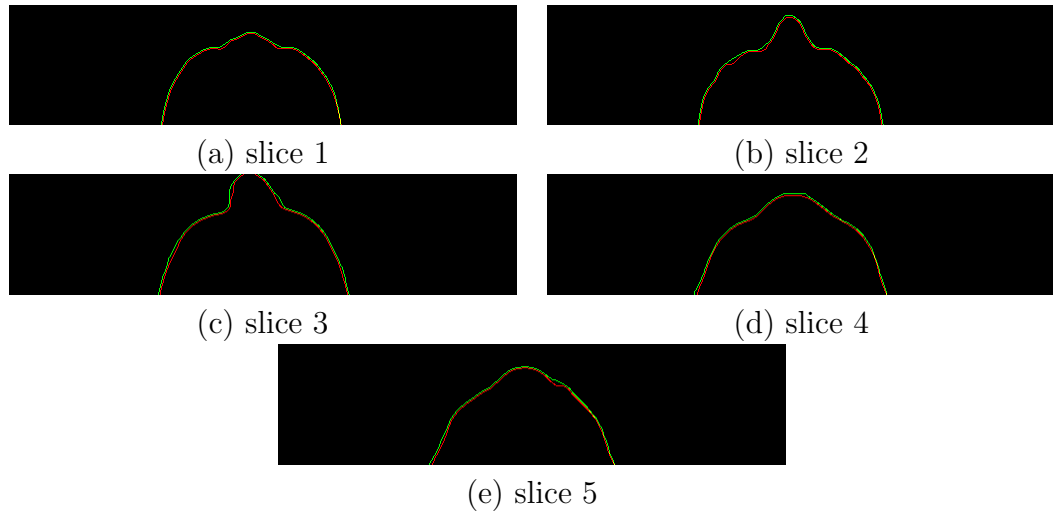


Figure 9.6: Screen shots of five composite slice images which are spaced apart in different locations on the face. The red colour represents the border of CT image, the green colour represents the border of laser image, and the yellow colour represents the pixels where the two images are superimposed.

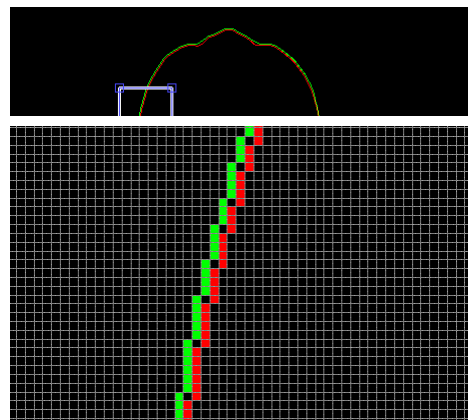
move in the procedure to create a composite image in which the two images are superimposed (overlaid). We present in Figure 9.6 screen shots of five composite slice images, which are spaced apart in different locations of the face, and selected from the two models (the laser-scan model and the CT-derived model). The red colour in the figure represents the border of the CT images, the green colour represents the border of the laser images, and the yellow colour represents the pixels where the two images are superimposed.

We measure the distances between the external border of CT slices and laser slices by investigating the pixels in the composite images. Figure 9.7 displays zoomed-in regions of a composite image. This display for the pixels enable us to easily find

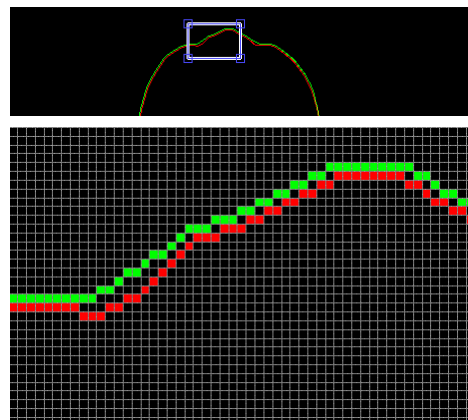
the physical distances between the borders of the two images since any CT image (DICOM format) has a ‘pixel-spacing’ property which specifies the physical distance between the centres of two adjacent pixels. The pixel-spacing equals 0.9765 mm in our “Perspex Mask” data set for both directions (i.e. x-direction and y-direction) which means that the real physical distance between the centres of each adjacent pixels is 0.9765 mm.

In order to derive statistics and generate histograms to represent the total number of pixels that have specific distances between the two corresponding images, we followed the approach, which is displayed in Figure 9.8. Since the CT scan images represent the patient’s head where the laser-scan images represent the external surface of the perspex mask (immobilisation mask) then we expect the border of the laser image to be wider than the border of the CT image. We labelled the case shown in Figure 9.8(a) with (-1) which indicates that the CT border for that pixel is wider than the laser border for its corresponding pixel. When the two borders are superimposed over a specific pixel we labelled that case with (0) which indicates that the distance between the two borders equals zero as shown in Figure 9.8(b). When the laser border on a specific pixel is adjacent and wider than the CT border on its corresponding pixel, as the case in Figure 9.8(c), we labelled this case with (+1) which means the laser border is wider than the CT border with only one pixel. This means that the laser border is 0.9765 mm wider than the CT border at that pixel location since the ‘pixel-spacing’ equals 0.9765 mm in our case. This implies that the laser border is wider ( $2 \times 0.9765$  mm) in 9.8(d) and wider ( $3 \times 0.9765$  mm) in 9.8(e) than the CT border at that locations.

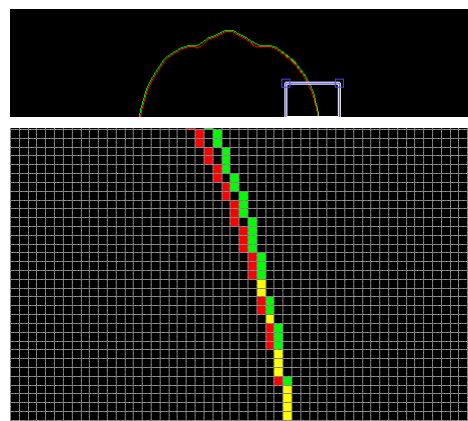
Table 9.3 displays readings for five composite images which are spaced apart in different locations of the face. The table shows, for each image, how many pixels are labelled with -1, 0, +1, +2, ..., +7 and what is the percentage of this label over



(a) Region1



(b) Region2



(c) Region3

Figure 9.7: Investigation for the pixels in different regions of a composite image. Red squares belong to the border of the CT image, green squares belong to the border of the laser image, and yellow squares represent pixels where the two images are superimposed.

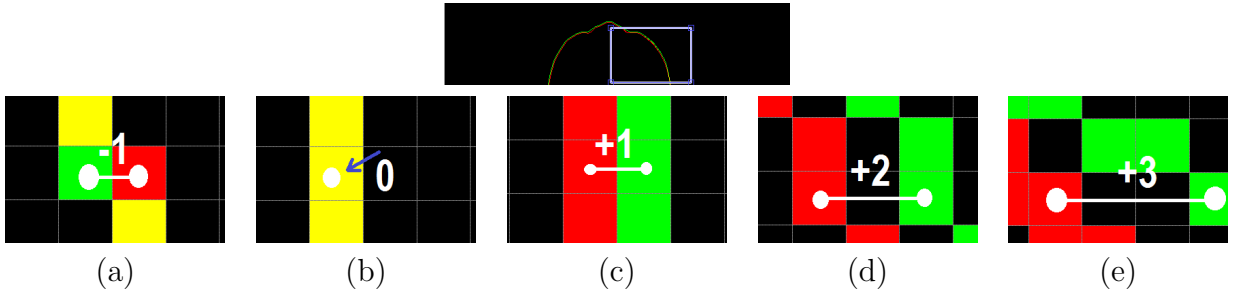


Figure 9.8: Representation of the approach that is used to find the distances between the borders in composite images. Red squares belong to the border of the CT image, green squares belong to the border of the laser image, and yellow squares represent pixels where the two images are superimposed.

the whole set of labelled pixels. Figure 9.9 shows the measurements in a form of histograms to represent the distances between the border of the laser slice and the border of the CT slice. It is obvious in the table and histograms that the majority of pixels have either a distance equal to one pixel (i.e 0.9765 mm) or a distance equal to two pixels (i.e.  $2 \times 0.9765 = 1.953$  mm). The average percentage, for the five images, of the pixels which have a distance labelled (+1) or (+2) is 87.62% which means in other words that the laser border is wider than the CT border with a distance equals either (0.9765 mm) or (1.953 mm) over 87.62% of the whole set of points. This difference in distance represents the thickness of the mask. More discussions and explanation about these measurements are presented in Section 9.3.

As we presented in Section 7.6, the evaluation through slicing the object (dividing the object into layers) is appropriate for the applications that use 3D-printing since the 3D-printing process takes a 3D mesh and translates this model into individual layers [249, 42].

### 9.3 Discussion

In this section we address some issues that may affect, one way or another, the accuracy of the outcomes that we got when we applied our whole pipeline over the

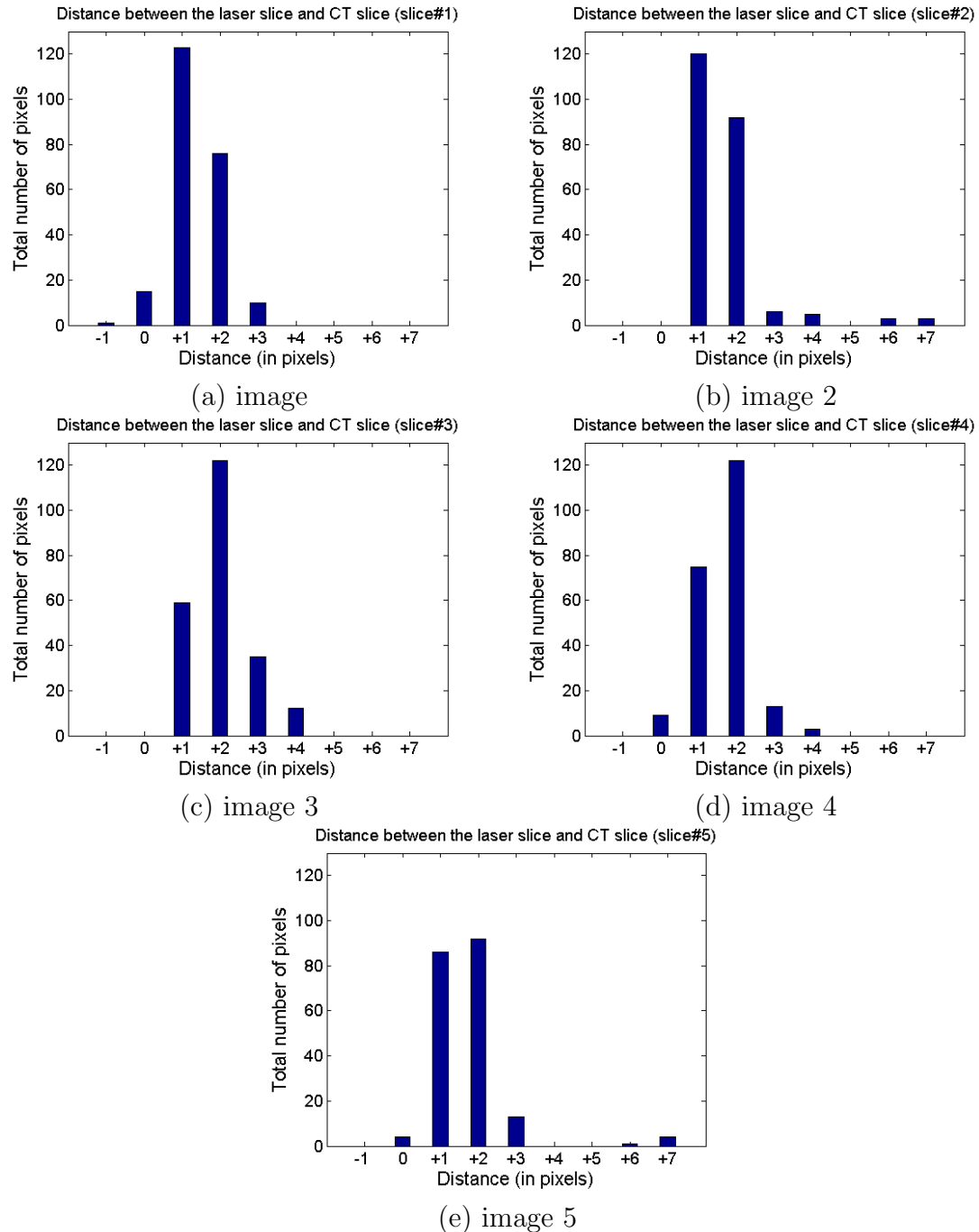


Figure 9.9: Histograms represent the total distance between the laser slice and the CT slice in pixels.

Table 9.3: Values represent how many pixels labelled with  $\{-1, 0, +1, +2, +3, +4, +5, +6, +7\}$  and the percentage of this label over the whole set of labelled pixels.

Image#	-1	0	+1	+2	+3	+4	+5	+6	+7
<b>Image1</b>									
<i>total</i>	1	15	123	76	10	0	0	0	0
<i>percentage</i>	0.44%	6.67%	<b>54.67%</b>	<b>33.78%</b>	4.44%	0.00%	0.00%	0.00%	0.00%
<b>Image2</b>									
<i>total</i>	0	0	120	92	6	5	3	3	
<i>percentage</i>	0.00%	0.00%	<b>52.40%</b>	<b>40.17%</b>	2.62%	2.18%	0.00%	1.31%	1.31%
<b>Image3</b>									
<i>total</i>	0	0	59	122	35	12	0	0	
<i>percentage</i>	0.00%	0.00%	<b>25.88%</b>	<b>53.51%</b>	15.35%	5.26%	0.00%	0.00%	0.00%
<b>Image4</b>									
<i>total</i>	0	9	75	122	13	3	0	0	
<i>percentage</i>	0.00%	4.05%	<b>33.78%</b>	<b>54.95%</b>	5.86%	1.35%	0.00%	0.00%	0.00%
<b>Image5</b>									
<i>total</i>	0	4	86	92	13	0	1	4	
<i>percentage</i>	0.00%	2.00%	<b>43.00%</b>	<b>46.00%</b>	6.50%	0.00%	0.00%	0.50%	2.00%

“Perspex Mask” data set.

- The data sets that we got from our clinical trial are for patients who have treatment in the neck region. This implies that the radiotherapy treatment plan for those patients does not involve scanning the patients to the top vertex of the skull. Those patients are scanned as far as the supraorbital ridge (see Figure 9.10).

According to that and since the alignment process (i.e. registration) works for two similar objects, the laser-scan model should be pre-processed by cutting (cropping) the region which represents the top region of the head since the CT-derived model of the “Perspex Mask” is incomplete (i.e. missing a group of slices representing the top region of the head). This cutting for the laser-scan model is performed using open-source software (MeshLab) for processing and editing 3D triangular meshes. As the cutting process is not exactly accurate then that may have an effect on the final outcome of the whole pipeline.

- One of the common problems in medical imaging which complicates the segmentation process is the partial volume effects (PVE). PVE, also named as tissue-fraction effect, happens when multiple tissues are part of a single pixel

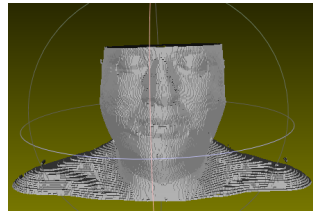


Figure 9.10: Constructed model generated from the CT corresponding to the patient for whom the perspex mask was made. The scan does not involve scanning the patients to the top vertex of the skull.

or voxel due to the finite spatial resolution of the imaging device. This will result in a blurring of intensity across boundaries [266]. PVE depends on the characteristics of the imaging device, scanned object and activity distribution [267]. PVE can cause errors in volume measurement in the range of 20%-60% [268, 269].

- Automatic segmentation, especially facial soft tissue, is still a complicated process due to the fact that the human head is one of the most complex parts of the body because it contains thin layers of tissue, which contain muscles that are often touching each other and this complicate the morphological characteristics of facial tissues [270]. Although there are several studies on brain tissue segmentation, there are only a few studies related to facial soft tissue [175]. The most salient drawback of those studies is that most of them involve manual segmentation [271, 272], but, as it known, manual segmentation is time consuming and prone to inter-expert and intra-expert variability [175].
- Medical images are prone to be affected by different types of noise sources [273, 274] such as the quantum structure of the X-ray beam, the structure of the film, or digital receptors. This image noise may affect the accuracy of the segmentation process and consequently may affect the accuracy of the whole process to construct our immobilisation mask.

- The thickness of the Perspex mask, see Figure 9.11, that we have scanned using the hand-held laser scanner is variable in different regions. We have measured the thickness of that mask in the mechanical workshop of University of East Anglia using a digital calliper and found that the thickness varies from region to region. The thickness values range from [1.25 - 2.13]mm which means that the mesh generated by scanning the outer surface of the mask does not represent the exact dimensions of the patient's head.



Figure 9.11: A photo shows the Perspex mask that we have scanned by the hand-held laser scanner.

- Since we use the Marching Cubes algorithm to construct the CT-derived model and since the exact position of the vertex along the edge is computed through linear interpolation in marching cubes, then this interpolation may have an effect over the whole process.
- The immobilisation masks, including the Perspex mask, are normally having some extension to be used for fixation purposes (see the red circle in Figure 9.12). On the other hand, the CT-derived model is constructed for the head itself without any other extensions. Consequently the two meshes (i.e. the CT mesh and the laser mesh) do not represent similar objects. This point requires some pre-processing for the laser mesh and this in turn may lead to a loss in accuracy through the whole process.
- The process of slicing the laser mesh into 2D images, which was presented in



Figure 9.12: A photo shows the Perspex mask and the red circle shows the extension that is used to fix the mask over the couch.

Chapter 7, needs the use of quantisation and mathematical rounding. This may define some inaccuracies in the final outcome.

- The existence of holes/gaps/incomplete regions on the surface of the laser mesh, see Figure 9.13, may affect the the accuracy of the whole pipeline.

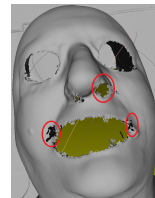


Figure 9.13: A photo shows the laser mesh acquired for the Perspex mask and the red circles show some examples of incomplete/gaps on the surface of the mesh.

## 9.4 Summary

This chapter presented at the beginning a brief description of the clinical trial and its main features. It moved then to illustrate two approaches which are used to evaluate the accuracy of the outcomes that were generated when we applied our experiments over the “Perspex Mask” data set. In the first approach, we used our pipeline to evaluate the degree of similarity between the CT constructed model and the ground-truth (laser mesh). The pipeline produced figures and statistics which indicated that there is a relatively high match between the two models. In the second approach, we investigated and calculated the distances between the borders of the CT images and

the borders of images got from the laser model. This investigation of pixels indicated that about 87% of points have distance-between-borders equals either (0.9765 mm) or (1.953 mm). These calculated distance-between-borders are considered acceptable for clinical practice as it is presented in [275, 5]. The chapter also presented extensive discussion on the possible sources that may cause any inaccuracy on the final outcomes. As a conclusion of this chapter we will raise two questions: (a) If we print this mask will it fit the patient? The answer based on the presented work is ‘very probably’. If it didn’t then some very minor changes to the algorithm would fix the problem. (b) Would the printed mask provide better immobilisation than the existing shell? This is a more difficult question and we think we would need to do further clinical trials with patients ‘wearing’ printed masks.

# Chapter 10

## Conclusions

### 10.1 Conclusions

This thesis presented an automatic pipeline which aims to evaluate the accuracy of the CT-derived models which are built using different segmentation techniques. The outcome of this pipeline can be employed to construct immobilisation masks for Head-and-Neck cancer patients to be used in their radiotherapy treatment. The phases of the presented pipeline have been examined separately and then as a unit. A clinical trial has been conducted to allow the presented pipeline to be quantitatively evaluated. The results show that the presented pipeline is clinically viable. However, we conclude and summarise the work in this thesis by presenting the main outcomes and contributions.

#### **Removing image artefacts due to fixations in CT images**

We presented in this thesis a fast and automatic approach to remove image artefacts due to fixations in CT images. Our approach uses a fractional order Darwinian particle swarm optimisation of Otsu's method combined with morphological post-processing to classify pixels belonging to the mask. We applied our approach over five different CT data sets comprising a total of 738 image slices. The evaluation

indicates that the proposed approach is robust and of practical use. Some enhancements to speed up the process using PSO were also presented and tested in the thesis. The presented approach achieved an average specificity of 92.01% and sensitivity of 99.39%.

### **Image segmentation**

We applied five segmentation techniques in this thesis to segment the head from CT images. The five techniques are: Otsu, K-means, EM, DRLSE, and HMRF-EM. We found, when we evaluated their accuracy, that DRLSE is the most accurate one and this is expected as the level set methods have been successfully employed in the field of active contour models. In this context, we presented a procedure to set the level set binary function in order to segment CT images, and developed an algorithm to handle the case when more than one contour is found. The accuracy of segmentation, for the five techniques, were analysed slice by slice and the stability of results were addressed. We found that the DRLSE achieved 96.56% as a similarity ratio with a standard deviation equals 0.00796. All the generated figures encouraged us to employ the DRLSE in our pipeline.

### **Automatic 3D Alignment**

As one of the main parts of the evaluation process in this thesis is to compare between the laser-scan model as a ground-truth and the CT-derived model, a precise alignment between the two models is necessary. We presented a customised version of the ICP algorithm which shows better results than the conventional ICP algorithm in terms of speed, accuracy and convergence. We have applied our experiments to compare between the conventional ICP algorithm and our customised version of the ICP over three objects. In terms of execution time, the conventional ICP needed to align the three objects (61.80, 263.26, 423.45) seconds whereas the customised version needed (3.28, 26.96, 9.10) seconds respectively. In terms of the accuracy, the average

distances between the aligned models achieved by the conventional ICP are (2.8651, 3.5256, 0.7346)mm whereas the distances for the customised ICP are (0.60392, 0.6192, 0.47472)mm. The results show that the average distances between the two models, after applying the our customised version of the ICP algorithm, were smaller than the CT pixel-spacing value which ensures the reliability of the presented algorithm.

### **Overlap measurement for medical volumes**

An overlap measurement specifically designed to measure the ratio of overlap between two medical volumes is presented. The presented measurement generates figures representing the similarities along the axial, sagittal and coronal planes. Two strategies were used to test the proposed measurement. We examined the correlation between the proposed measurement and other widely used and accepted measurements. In addition to that, we examined methodically our outcomes for particular test cases in which we know in advance how the correct outputs should be. The average value of correlation between our overlap measurement and the RMSE is -0.7559 over our data sets and the average value that we got for the *p*<sub>value</sub> is 0.0018 which indicates that there are a very low probability of observing the null hypothesis. The extensive analysis of this measurement showed that this measurement is convenient to be used for medical volumes and to evaluate the outcomes of the segmentation and registration processes.

### **Automatic evaluation of segmentation techniques**

We presented in this thesis an automatic pipeline to be used to evaluate and compare the accuracies of different segmentation techniques. This pipeline supposes that we have a 3D model (e.g. laser-scan model) employed as a ground-truth. The experiments have been applied over homogeneous 3D printed objects of different shapes. The average similarity values that we got for the three objects are (96.96%, 99.40%, 98.61%). These outcomes indicate that the presented pipeline is reliable and can be

used to quantify the accuracy of segmentation of medical images.

#### **Automatic approach to construct immobilisation masks**

This thesis presented an automatic approach to construct immobilisation masks for use in radiotherapy treatment of HNC patients. The chapters of this thesis displayed in sequence all the required phases of this approach and examined the outcome of each phase separately. The whole approach was examined by conducting a clinical trial at the Norfolk and Norwich University Hospital. We found when we investigated the absolute measurements of the space between the surface of the CT-derived model and the external surface of the ground-truth that about 87% of points have distance-between-borders equals either (0.9765 mm) or (1.953 mm) which represent the thickness of the scanned mask. This makes the proposed approach of treatment which is presented in this thesis a promising alternative to the current immobilisation masks used nowadays in hospitals.

## **10.2 Future Work**

We have identified in this research two main points which we think are needed to be further investigated:

- Conducting a feasibility study in order to evaluate whether manufacturing immobilisation masks from an economic and operational standpoint is affordable and applicable. This requires us to communicate with companies in industry sector to show them our work and outcomes.
- Getting more patient specific data from our clinical trial by performing laser scanning for a cohort of patients and evaluating the outcomes. These outcomes will supply us with more comprehensive vision on the accuracy of the process when considering real human skin.

- Doing more enhancement over our customised version of the iterative closest point algorithm. This enhancement includes the employing of the FODPSO and other optimisation techniques to speed up the matching of corresponding points between two datasets.
- Testing our customised version of the ICP algorithm over different forms of meshes and generalise the presented approach to be of practical use not only in medical applications but in computer graphics applications in general.
- Evaluating the performance of the presented 3D overlap measurement over a benchmark dataset.
- Using the convolutional neural network and deep learning techniques to segment the skin/air boundary in humans.
- Publishing the novel pipeline that is presented in this thesis which performs an automatic evaluation of the accuracy of segmentation as well as the novel 3D overlap measurement.

# Bibliography

- [1] Globetech Media. MedImaging/Radiography. <http://www.medimaging.net/nuclear-medicine/articles/294766607/nano-based-masks-increase-radiation-therapy-comfort.html>. Accessed: 03-02-2017.
- [2] Chunming Li, Chenyang Xu, Changfeng Gui, and Martin D Fox. Distance regularized level set evolution and its application to image segmentation. *IEEE transactions on image processing*, 19(12):3243–3254, 2010.
- [3] Images published on webdocs of University of Alberta. <https://webdocs.cs.ualberta.ca/~btap/Images/>. Accessed: 24-01-2017.
- [4] Synthesizing geometries for 21st century electromagnetics. <http://emlab.utep.edu/ee5390em21/Lecture%2019%20-%20Interfacing%20MATLAB%20with%20CAD.pdf>. Accessed: 08-02-2017.
- [5] SD Laycock, M Hulse, CD Scrase, MD Tam, S Isherwood, DB Mortimore, D Emmens, J Patman, SC Short, and GD Bell. Towards the production of radiotherapy treatment shells on 3D printers using data derived from DICOM CT and MRI: preclinical feasibility studies. *Journal of Radiotherapy in Practice*, 14(01):92–98, 2015.
- [6] Head and Neck Cancer - Overview. <http://www.cancer.net/cancer-types/head-and-neck-cancer/overview>. Accessed: 27-11-2016.

- [7] Head and Neck Cancers. <https://www.cancer.gov/types/head-and-neck/head-neck-fact-sheet>. Accessed: 27-11-2016.
- [8] The Office for National Statistics Report. <https://www.ons.gov.uk/>. Accessed: 27-11-2016.
- [9] Head and Neck Cancer: Statistics. <http://www.cancer.net/cancer-types/head-and-neck-cancer/statistics>. Accessed: 27-11-2016.
- [10] Mohammad Hashem Ryalat, Stephen Laycock, and Mark Fisher. Automatic removal of mechanical fixations from CT imagery with particle swarm optimisation. In *International Conference on Bioinformatics and Biomedical Engineering*, pages 419–431. Springer, 2017.
- [11] Mark Fisher, Christopher Applegate, Mohammad Ryalat, Stephen Laycock, Mark Hulse, Daniel Emmens, Duncan Bell, et al. Evaluation of 3-D printed immobilisation shells for head and neck IMRT. *Open Journal of Radiology*, 4(04):322, 2014.
- [12] B Sanghera, A Amis, and M McGurk. Preliminary study of potential for rapid prototype and surface scanned radiotherapy facemask production technique. *Journal of medical engineering & technology*, 26(1):16–21, 2002.
- [13] The Engineering and Physical Sciences Research Council (EPSRC): Frontiers of physical intervention grand challenges. <https://www.epsrc.ac.uk/research/ourportfolio/themes/healthcaretechnologies/strategy/grandchallenges>, 2017. Accessed: 14-03-2017.
- [14] Jake Van Dyk, Tomas Kron, Glenn Bauman, and Jerry J Battista. Tomotherapy: a revolution in radiation therapy. *Physics in Canada*, 58(2):79–86, 2002.
- [15] FV Fossella, JB Putnam, and R Komaki. *Lung Cancer*. MD Anderson Cancer Care Series. New York: Springer, 2003.

- [16] R George, PJ Keall, VR Kini, SS Vedam, JV Siebers, Q Wu, MH Lauterbach, DW Arthur, and R Mohan. Quantifying the effect of intrafraction motion during breast imrt planning and dose delivery. *Medical physics*, 30(4):552–562, 2003.
- [17] P Elliott. A quicker target for therapy-algorithms developed under the covira programme to speed up producing anf 3-d radiation treatment planning. *Image Processing Magazine*, 6:32–32, 1994.
- [18] W Schlegel. Computer assisted radiation therapy planning. In *3D Imaging in Medicine*, pages 399–410. Springer, 1990.
- [19] William E Lorensen and Harvey E Cline. Marching cubes: A high resolution 3D surface construction algorithm. In *ACM siggraph computer graphics*, volume 21, pages 163–169. ACM, 1987.
- [20] Theodore S Lawrence, Randall K Ten Haken, and Amato Giaccia. Principles of radiation oncology. *Cancer: principles and practice of oncology. 8th ed. Philadelphia: Lippincott Williams and Wilkins*, 2008.
- [21] Richard Pazdur. *Cancer management: a multidisciplinary approach, medical, surgical & radiation oncology*. Cmp, 2004.
- [22] Ervin B Podgorsak. Review of radiation oncology physics: a handbook for teachers and students. *Vienna, International Atomic Energy Agency. Educational reports series*, 2003.
- [23] Radiological Society of North America Inc. linear accelerator. <http://www.radiologyinfo.org/en/info.cfm?pg=linac>, (last accessed: November, 2016). 1.
- [24] Christos Antypas and Evangelos Pantelis. Performance evaluation of a cyberknife® g4 image-guided robotic stereotactic radiosurgery system. *Physics in medicine and biology*, 53(17):4697, 2008.

- [25] Bin S Teh, Shiao Y Woo, and E Brian Butler. Intensity modulated radiation therapy (imrt): a new promising technology in radiation oncology. *The oncologist*, 4(6):433–442, 1999.
- [26] International Radiosurgery Association (IRSA). <http://www.irsa.org/>, 2017. Accessed: 14-03-2017.
- [27] Osama Dorgham. *High speed 2D/3D medical image registration*. PhD thesis, PhD Thesis, School of Computing Sciences, University of East Anglia, Norwich, 2010.
- [28] Andrew Webb and George C Kagadis. Introduction to biomedical imaging. *Medical Physics*, 30(8):2267–2267, 2003.
- [29] Robert A Novelline and Lucy Frank Squire. *Squire's fundamentals of radiology*. La Editorial, UPR, 2004.
- [30] Gerald F Marshall and Glenn E Stutz. *Handbook of optical and laser scanning*. CRC Press, 2011.
- [31] Zacharias Fourie, Janalt Damstra, and Yijin Ren. Application of cone beam computed tomography in facial imaging science. , 21(2):220–231, 2012.
- [32] Hee-Kyung Park, Jin-Woo Chung, and Hong-Seop Kho. Use of hand-held laser scanning in the assessment of craniometry. *Forensic science international*, 160(2):200–206, 2006.
- [33] Martin Friess, Leslie F Marcus, David P Reddy, and Eric Delson. The use of 3D laser scanning techniques for the morphometric analysis of human facial shape variation. *BAR Int Series*, 1049:31–5, 2002.
- [34] BV Karas and HF Beaubien. Three-dimensional laser scanning of cultural heritage: the deer stones of mongolia. *Scanning*, 28(3):187–188, 2005.
- [35] Mineo Yoshino, Hideaki Matsuda, Satoshi Kubota, Kazuhiko Imaizumi, and Sachio Miyasaka. Computer-assisted facial image identification system using a

3-d physiognomic range finder. *Forensic science international*, 109(3):225–237, 2000.

[36] Danilo De Angelis, Remo Sala, Angela Cantatore, Marco Grandi, and Cristina Cattaneo. A new computer-assisted technique to aid personal identification. *International journal of legal medicine*, 123(4):351–356, 2009.

[37] Chung How Kau, Stephen Richmond, Angela Incrapera, Jeryl English, and James Jiong Xia. Three-dimensional surface acquisition systems for the study of facial morphology and their application to maxillofacial surgery. *The International Journal of Medical Robotics and Computer Assisted Surgery*, 3(2):97–110, 2007.

[38] Fabian Rengier, A Mehndiratta, Hendrik von Tengg-Kobligk, Christian M Zechmann, Roland Unterhinninghofen, H-U Kauczor, and Frederik L Giesel. 3D printing based on imaging data: review of medical applications. *International journal of computer assisted radiology and surgery*, 5(4):335–341, 2010.

[39] Bettina Wendel, Dominik Rietzel, Florian Kühnlein, Robert Feulner, Gerrit Hülder, and Ernst Schmachtenberg. Additive processing of polymers. *Macromolecular materials and engineering*, 293(10):799–809, 2008.

[40] Steven J Esse, Phillip Berman, Allan I Bloom, and Jacob Sosna. Clinical applications of physical 3D models derived from mdct data and created by rapid prototyping. *American Journal of Roentgenology*, 196(6):W683–W688, 2011.

[41] Paul S D’Urso, David J Effeney, W John Earwaker, Timothy M Barker, Michael J Redmond, Robert G Thompson, and Francis H Tomlinson. Custom cranioplasty using stereolithography and acrylic. *British Journal of Plastic Surgery*, 53(3):200–204, 2000.

[42] Bethany C Gross, Jayda L Erkal, Sarah Y Lockwood, Chengpeng Chen, and Dana M Spence. Evaluation of 3D printing and its potential impact on biotechnology and the chemical sciences. *Analytical chemistry*, 86(7):3240–3253, 2014.

[43] Stephen D Laycock, Graham D Bell, David B Mortimore, Mark K Greco, Nick Corps, and Irving Finkle. Combining x-ray micro-ct technology and 3D printing for the digital preservation and study of a 19th century cantonese chess piece with intricate internal structure. *Journal on Computing and Cultural Heritage (JOCCH)*, 5(4):13, 2012.

[44] David Espalin, Danny W Muse, Eric MacDonald, and Ryan B Wicker. 3D printing multifunctionality: structures with electronics. *The International Journal of Advanced Manufacturing Technology*, 72(5-8):963–978, 2014.

[45] Adolf Müller, Kartik G Krishnan, Eberhard Uhl, and Gerson Mast. The application of rapid prototyping techniques in cranial reconstruction and preoperative planning in neurosurgery. *Journal of Craniofacial Surgery*, 14(6):899–914, 2003.

[46] Jiankang He, Dichen Li, Bingheng Lu, Zhen Wang, and Tao Zhang. Custom fabrication of a composite hemi-knee joint based on rapid prototyping. *Rapid Prototyping Journal*, 12(4):198–205, 2006.

[47] Ke-Rong Dai, Meng-Ning Yan, Zhen-An Zhu, and Yue-Hua Sun. Computer-aided custom-made hemipelvic prosthesis used in extensive pelvic lesions. *The Journal of arthroplasty*, 22(7):981–986, 2007.

[48] Matthew DBS Tam, Stephen D Laycock, Duncan G Bell, and Adrian Chojnowski. 3-d printout of a dicom file to aid surgical planning in a 6 year old patient with a large scapular osteochondroma complicating congenital diaphyseal aclasia. *Journal of radiology case reports*, 6(1):31–37, 2012.

[49] Abdulrazzaq Sulaiman, Loïc Boussel, Frédéric Taconnet, Jean Michel Serfaty, Hasan Alsaïd, Cherif Attia, Laurent Huet, and Philippe Douek. In vitro non-rigid life-size model of aortic arch aneurysm for endovascular prosthesis assessment. *European Journal of Cardio-Thoracic Surgery*, 33(1):53–57, 2008.

[50] Kimberley Knox, Charles W Kerber, SA Singel, MJ Bailey, and SG Imbesi. Rapid prototyping to create vascular replicas from CT scan data: making tools to teach, rehearse, and choose treatment strategies. *Catheterization and cardiovascular interventions*, 65(1):47–53, 2005.

[51] Jorge Faber, Patrícia Medeiros Berto, and Marcelo Quaresma. Rapid prototyping as a tool for diagnosis and treatment planning for maxillary canine impaction. *American journal of orthodontics and dentofacial orthopedics*, 129(4):583–589, 2006.

[52] E Maravelakis, K David, A Antoniadis, A Manios, N Bilalis, and Y Papahari-laou. Reverse engineering techniques for cranioplasty: a case study. *Journal of medical engineering & technology*, 32(2):115–121, 2008.

[53] Wellington Silva Paiva, Robson Amorim, Douglas Alexandre França Bezerra, and Marcos Masini. Application of the stereolithography technique in complex spine surgery. *Arquivos de neuro-psiquiatria*, 65(2B):443–445, 2007.

[54] C Hurson, A Tansey, B Odonnchadha, P Nicholson, J Rice, and J McElwain. Rapid prototyping in the assessment, classification and preoperative planning of acetabular fractures. *Injury*, 38(10):1158–1162, 2007.

[55] Keya Mao, Yan Wang, Songhua Xiao, Zhengsheng Liu, Yonggang Zhang, Xuesong Zhang, Zheng Wang, Ning Lu, Zhu Shourong, Zhang Xifeng, et al. Clinical application of computer-designed polystyrene models in complex severe spinal deformities: a pilot study. *European Spine Journal*, 19(5):797–802, 2010.

- [56] Michael S Kim, Adam R Hansgen, Onno Wink, Robert A Quaife, and John D Carroll. Rapid prototyping a new tool in understanding and treating structural heart disease. *Circulation*, 117(18):2388–2394, 2008.
- [57] A Armillotta, P Bonhoeffer, G Dubini, S Ferragina, F Migliavacca, G Sala, and S Schievano. Use of rapid prototyping models in the planning of percutaneous pulmonary valved stent implantation. *Proceedings of the Institution of Mechanical Engineers, Part H: Journal of Engineering in Medicine*, 221(4):407–416, 2007.
- [58] Silvia Schievano, Francesco Migliavacca, Louise Coats, Sachin Khambadkone, Mario Carminati, Neil Wilson, John E Deanfield, Philipp Bonhoeffer, and Andrew M Taylor. Percutaneous pulmonary valve implantation based on rapid prototyping of right ventricular outflow tract and pulmonary trunk from mr data 1. *Radiology*, 242(2):490–497, 2007.
- [59] C Canstein, P Cachot, A Faust, AF Stalder, J Bock, A Frydrychowicz, J Küffer, J Hennig, and M Markl. 3D mr flow analysis in realistic rapid-prototyping model systems of the thoracic aorta: Comparison with in vivo data and computational fluid dynamics in identical vessel geometries. *Magnetic resonance in medicine*, 59(3):535–546, 2008.
- [60] Jian Li, Xiaolong Li, Bin Yang, and Xingming Sun. Segmentation-based image copy-move forgery detection scheme. *IEEE Transactions on Information Forensics and Security*, 10(3):507–518, 2015.
- [61] Mohamad Forouzanfar, Nosratallah Forghani, and Mohammad Teshnehab. Parameter optimization of improved fuzzy c-means clustering algorithm for brain mr image segmentation. *Engineering Applications of Artificial Intelligence*, 23(2):160–168, 2010.
- [62] Zhen Ma, João Manuel RS Tavares, Renato Natal Jorge, and T Mascarenhas. A review of algorithms for medical image segmentation and their applications

to the female pelvic cavity. *Computer Methods in Biomechanics and Biomedical Engineering*, 13(2):235–246, 2010.

[63] MG Bueno. *Computer Aided Segmentation of Anatomical Structures in computed Tomographic Images*. PhD thesis, PhD Thesis, Coventry University, 1998.

[64] Wenshuo Gao, Xiaoguang Zhang, Lei Yang, and Huizhong Liu. An improved sobel edge detection. In *Computer Science and Information Technology (ICCSIT), 2010 3rd IEEE International Conference on*, volume 5, pages 67–71. IEEE, 2010.

[65] John Canny. A computational approach to edge detection. *IEEE Transactions on pattern analysis and machine intelligence*, (6):679–698, 1986.

[66] Rolf Adams and Leanne Bischof. Seeded region growing. *IEEE Transactions on pattern analysis and machine intelligence*, 16(6):641–647, 1994.

[67] Regina Pohle and Klaus D Toennies. Segmentation of medical images using adaptive region growing. In *Medical Imaging 2001*, pages 1337–1346. International Society for Optics and Photonics, 2001.

[68] Jaeyoun Yi and Jong Beom Ra. Vascular segmentation algorithm using locally adaptive region growing based on centerline estimation. In *Medical Imaging 2001*, pages 1329–1336. International Society for Optics and Photonics, 2001.

[69] Zhigeng Pan and Jianfeng Lu. A bayes-based region-growing algorithm for medical image segmentation. *Computing in Science & Engineering*, 9(4):32–38, 2007.

[70] Luc Vincent and Pierre Soille. Watersheds in digital spaces: an efficient algorithm based on immersion simulations. *IEEE transactions on pattern analysis and machine intelligence*, 13(6):583–598, 1991.

[71] Vicente Grau, AUJ Mewes, M Alcaniz, Ron Kikinis, and Simon K Warfield. Improved watershed transform for medical image segmentation using prior information. *IEEE transactions on medical imaging*, 23(4):447–458, 2004.

- [72] HP Ng, SH Ong, KWC Foong, PS Goh, and WL Nowinski. Medical image segmentation using k-means clustering and improved watershed algorithm. In *2006 IEEE Southwest Symposium on Image Analysis and Interpretation*, pages 61–65. IEEE, 2006.
- [73] Ghassan Hamarneh and Xiaoxing Li. Watershed segmentation using prior shape and appearance knowledge. *Image and Vision Computing*, 27(1):59–68, 2009.
- [74] Lee R Dice. Measures of the amount of ecologic association between species. *Ecology*, 26(3):297–302, 1945.
- [75] TT Tanimoto. An elementary mathematical theory of classification and prediction. 1958. *International Business Machines Corporation*.
- [76] P Jarccard. Nouvelles recherches sur la distribution floral. *Bull. Soc. Vard. Sci. Nat*, 44:223–270, 1908.
- [77] David J Rogers and Taffee T Tanimoto. A computer program for classifying plants. *Science (New York, NY)*, 132(3434):1115–1118, 1960.
- [78] Kelly H Zou, Simon K Warfield, Aditya Bharatha, Clare MC Tempany, Michael R Kaus, Steven J Haker, William M Wells, Ferenc A Jolesz, and Ron Kikinis. Statistical validation of image segmentation quality based on a spatial overlap index 1: Scientific reports. *Academic radiology*, 11(2):178–189, 2004.
- [79] Paolo Cignoni, Claudio Rocchini, and Roberto Scopigno. Metro: measuring error on simplified surfaces. In *Computer Graphics Forum*, volume 17, pages 167–174. Wiley Online Library, 1998.
- [80] Xin Liang, Ivo Lambrechts, Yi Sun, Kathleen Denis, Bassam Hassan, Limin Li, Ruben Pauwels, and Reinhilde Jacobs. A comparative evaluation of cone beam computed tomography (CBCT) and multi-slice CT (MSCT). part ii: On 3D model accuracy. *European journal of radiology*, 75(2):270–274, 2010.

- [81] Zacharias Fourie, Janalt Damstra, Rutger H Schepers, Peter O Gerrits, and Yijin Ren. Segmentation process significantly influences the accuracy of 3D surface models derived from cone beam computed tomography. *European journal of radiology*, 81(4):e524–e530, 2012.
- [82] Niansong Ye, Fan Jian, Junjie Xue, Sheng Wang, Lina Liao, Wenya Huang, Xing Yang, Yang Zhou, Wenli Lai, Jingtao Li, et al. Accuracy of in-vitro tooth volumetric measurements from cone-beam computed tomography. *American Journal of Orthodontics and Dentofacial Orthopedics*, 142(6):879–887, 2012.
- [83] Niansong Ye, Hu Long, Junjie Xue, Sheng Wang, Xin Yang, and Wenli Lai. Integration accuracy of laser-scanned dental models into maxillofacial cone beam computed tomography images of different voxel sizes with different segmentation threshold settings. *Oral surgery, oral medicine, oral pathology and oral radiology*, 117(6):780–786, 2014.
- [84] Steven M Seitz, Brian Curless, James Diebel, Daniel Scharstein, and Richard Szeliski. A comparison and evaluation of multi-view stereo reconstruction algorithms. In *Computer vision and pattern recognition, 2006 IEEE Computer Society Conference on*, volume 1, pages 519–528. IEEE, 2006.
- [85] Miet Loubele, Reinhilde Jacobs, Frederik Maes, Kathleen Denis, Stewart White, Walter Coudyzer, Ivo Lambrichts, Daniel van Steenberghe, and Paul Suetens. Image quality vs radiation dose of four cone beam computed tomography scanners. *Dentomaxillofacial Radiology*, 2014.
- [86] Miet Loubele, Frederik Maes, Dirk Vandermeulen, Kathleen Denis, Reinhilde Jacobs, SC White, Daniel van Steenberghe, Albert Van Bael, Dirk Loeckx, Ivo LAMBRICHTS, et al. Assessment of bone segmentation quality of CT scanners using laser scanning. 2006.
- [87] Willem P Engelbrecht, Zacharias Fourie, Janalt Damstra, Peter O Gerrits, and Yijin Ren. The influence of the segmentation process on 3D measurements

from cone beam computed tomography-derived surface models. *Clinical oral investigations*, 17(8):1919–1927, 2013.

[88] Massimo Martorelli, Pietro Ausiello, and Renato Morrone. A new method to assess the accuracy of a cone beam computed tomography scanner by using a non-contact reverse engineering technique. *Journal of dentistry*, 42(4):460–465, 2014.

[89] Joseph B Anstey, Erin Janine Smith, Brian Rasquinha, John F Rudan, and Randy E Ellis. On the use of laser scans to validate reverse engineering of bony anatomy. In *MMVR*, pages 18–24, 2011.

[90] Eero Huotilainen, Risto Jaanimets, Jiří Valášek, Petr Marcián, Mika Salmi, Jukka Tuomi, Antti Mäkitie, and Jan Wolff. Inaccuracies in additive manufactured medical skull models caused by the dicom to stl conversion process. *Journal of Cranio-Maxillofacial Surgery*, 42(5):e259–e265, 2014.

[91] Yu-qin Pan, Ruan Zheng, Fa-bing Liu, Wang Jing, Chen Yong, Xue-yan Liang, and Wu Bing. The use of CT scan and stereo lithography apparatus technologies in a canine individualized rib prosthesis. *International Journal of Surgery*, 12(1):71–75, 2014.

[92] Wael Nabha, Young-Min Hong, Jin-Hyoung Cho, and Hyeon-Shik Hwang. Assessment of metal artifacts in three-dimensional dental surface models derived by cone-beam computed tomography. *The Korean Journal of Orthodontics*, 44(5):229–235, 2014.

[93] Tong Xi, Ruud Schreurs, Wout J Heerink, Stefaan J Bergé, and Thomas JJ Maal. A novel region-growing based semi-automatic segmentation protocol for three-dimensional condylar reconstruction using cone beam computed tomography (cbct). *PloS one*, 9(11):e111126, 2014.

[94] Piotr Szymor, Marcin Kozakiewicz, and Raphael Olszewski. Accuracy of open-source software segmentation and paper-based printed three-dimensional models. *Journal of Cranio-Maxillofacial Surgery*, 2015.

[95] ABLE SOFTWARE CORP. <http://www.ablesw.com/3d-doctor/format.html>. Accessed: 19-01-2017.

[96] The Biomedical 3D Printing Community (embodi3D LLC). <https://www.embodi3d.com/>. Accessed: 19-01-2017.

[97] Nexus Training and Resources for Engineering,. <http://www.nexus-engineering.org/>. Accessed: 04-02-2017.

[98] Kenneth Clark, Bruce Vendt, Kirk Smith, John Freymann, Justin Kirby, Paul Koppel, Stephen Moore, Stanley Phillips, David Maffitt, Michael Pringle, et al. The cancer imaging archive (TCIA): maintaining and operating a public information repository. *Journal of digital imaging*, 26(6):1045–1057, 2013.

[99] The Cancer Imaging Archive. <http://doi.org/10.7937/K9/TCIA.2015.7AKGJUPZ/>. Bosch, Walter R. and Straube, William L. and Matthews, John W. and Purdy, James A. Data From Head Neck Cetuximab (2015).

[100] Kaiping Wei, Bin He, Tao Zhang, and Xianjun Shen. A novel method for segmentation of CT head images. In *2007 1st International Conference on Bioinformatics and Biomedical Engineering*, pages 717–720. IEEE, 2007.

[101] Wenan Chen, Rebecca Smith, Soo-Yeon Ji, and Kayvan Najarian. Automated segmentation of lateral ventricles in brain CT images. In *Bioinformatics and Biomedicine Workshops, 2008. BIBMW 2008. IEEE International Conference on*, pages 48–55. IEEE, 2008.

[102] Xiaohua Qian, Jiahui Wang, Shuxu Guo, and Qiang Li. An active contour model for medical image segmentation with application to brain CT image. *Medical physics*, 40(2):021911, 2013.

- [103] W Mimi Diyana W Zaki, M Faizal A Fauzi, R Besar, and WSH Munirah W Ahmad. Qualitative and quantitative comparisons of haemorrhage intracranial segmentation in CT brain images. In *TENCON 2011-2011 IEEE Region 10 Conference*, pages 369–373. IEEE, 2011.
- [104] Nobuyuki Otsu. A threshold selection method from gray-level histograms. *Automatica*, 11(285-296):23–27, 1975.
- [105] Raghavendra V Kulkarni and Ganesh Kumar Venayagamoorthy. Bio-inspired algorithms for autonomous deployment and localization of sensor nodes. *IEEE Transactions on Systems, Man, and Cybernetics, Part C (Applications and Reviews)*, 40(6):663–675, 2010.
- [106] Mohammad Hashem Ryalat, Daniel Emmens, Mark Hulse, Duncan Bell, Zainab Al-Rahamneh, Stephen Laycock, and Mark Fisher. Evaluation of particle swarm optimisation for medical image segmentation. In *Advances in Systems Science: Proceedings of the International Conference on Systems Science 2016 (ICSS 2016)*, volume 539, page 61. Springer, 2016.
- [107] Russ C Eberhart, James Kennedy, et al. A new optimizer using particle swarm theory. In *Proceedings of the sixth international symposium on micro machine and human science*, volume 1, pages 39–43. New York, NY, 1995.
- [108] Jason Tillett, T Rao, Ferat Sahin, and Raghuveer Rao. Darwinian particle swarm optimization. In B Prasad, editor, *Proceedings of the 2nd Indian International Conference on Artificial Intelligence (IICAI-05)*, pages 1474–1487, 2005.
- [109] Micael S Couceiro, Rui P Rocha, NM Fonseca Ferreira, and JA Tenreiro Machado. Introducing the fractional-order darwinian pso. *Signal, Image and Video Processing*, 6(3):343–350, 2012.

- [110] Mehmet Sezgin et al. Survey over image thresholding techniques and quantitative performance evaluation. *Journal of Electronic imaging*, 13(1):146–168, 2004.
- [111] Ping-Sung Liao, Tse-Sheng Chen, Pau-Choo Chung, et al. A fast algorithm for multilevel thresholding. *J. Inf. Sci. Eng.*, 17(5):713–727, 2001.
- [112] PD Sathya and R Kayalvizhi. Modified bacterial foraging algorithm based multilevel thresholding for image segmentation. *Engineering Applications of Artificial Intelligence*, 24(4):595–615, 2011.
- [113] Ming-Huwi Horng. Multilevel thresholding selection based on the artificial bee colony algorithm for image segmentation. *Expert Systems with Applications*, 38(11):13785–13791, 2011.
- [114] Ashish Kumar Bhandari, Vineet Kumar Singh, Anil Kumar, and Girish Kumar Singh. Cuckoo search algorithm and wind driven optimization based study of satellite image segmentation for multilevel thresholding using kapur’s entropy. *Expert Systems with Applications*, 41(7):3538–3560, 2014.
- [115] Pedram Ghamisi, Micael S Couceiro, Jón Atlí Benediktsson, and Nuno MF Ferreira. An efficient method for segmentation of images based on fractional calculus and natural selection. *Expert Systems with Applications*, 39(16):12407–12417, 2012.
- [116] Erik Cuevas, Daniel Zaldivar, and Marco Pérez-Cisneros. A novel multi-threshold segmentation approach based on differential evolution optimization. *Expert Systems with Applications*, 37(7):5265–5271, 2010.
- [117] Chih-Chin Lai and Din-Chang Tseng. A hybrid approach using gaussian smoothing and genetic algorithm for multilevel thresholding. *International Journal of Hybrid Intelligent Systems*, 1(3, 4):143–152, 2004.

- [118] Pedram Ghamisi, Micael S Couceiro, Fernando ML Martins, and Jon Atli Benediktsson. Multilevel image segmentation based on fractional-order darwinian particle swarm optimization. *IEEE Transactions on Geoscience and Remote sensing*, 52(5):2382–2394, 2014.
- [119] Samy Ait-Aoudia, El-Hachemi Guerrouat, and Ramdane Mahiou. Medical image segmentation using particle swarm optimization. In *2014 18th International Conference on Information Visualisation*, pages 287–291. IEEE, 2014.
- [120] Ahmed Afifi, Toshiya Nakaguchi, Norimichi Tsumura, and Yoichi Miyake. Particle swarm optimization based medical image segmentation technique. *Medical Imaging Technology*, 28(1):53–62, 2010.
- [121] Devraj Mandal, Amitava Chatterjee, and Madhubanti Maitra. Robust medical image segmentation using particle swarm optimization aided level set based global fitting energy active contour approach. *Engineering Applications of Artificial Intelligence*, 35:199–214, 2014.
- [122] Ehsan Shahamatnia and Mohamad Mehdi Ebadzadeh. Application of particle swarm optimization and snake model hybrid on medical imaging. In *2011 IEEE Third International Workshop on Computational Intelligence In Medical Imaging*, pages 1–8. IEEE, 2011.
- [123] Ivo Petrás. Fractional derivatives, fractional integrals, and fractional differential equations in matlab. *Engineering Education and Research Using MATLAB, InTech, kap*, 10:239–264, 2011.
- [124] Toma Marinov, Nelson Ramirez, and Fidel Santamaria. Fractional integration toolbox. *Fractional Calculus and Applied Analysis*, 16(3):670–681, 2013.
- [125] KB Oldham and J Spanier. (1974). the fractional calculus: Theory and applications of differentiation and integration to arbitrary order. New York. 2006.
- [126] Mohammad Hashem Ryalat, Stephen Laycock, and Mark Fisher. A fast and automatic approach for removing artefacts due to immobilisation masks in X-ray

CT. In *Biomedical & Health Informatics (BHI), 2017 IEEE EMBS International Conference on*, pages 33–36. IEEE, 2017.

[127] Pierre Soille. *Morphological image analysis: principles and applications*. Springer Science & Business Media, 2013.

[128] Rafael C.. Gonzalez, Richard E.. Woods, and Steven L.. Eddins. *Digital Image Processing Using MATLAB®*. McGraw Hill Education, 2010.

[129] James MacQueen et al. Some methods for classification and analysis of multivariate observations. In *Proceedings of the fifth Berkeley symposium on mathematical statistics and probability*, volume 1, pages 281–297. Oakland, CA, USA., 1967.

[130] ZhenSong Chen, ZhiQuan Qi, Fan Meng, Limeng Cui, and Yong Shi. Image segmentation via improving clustering algorithms with density and distance. *Procedia Computer Science*, 55:1015–1022, 2015.

[131] Suman Tatiraju and Avi Mehta. Image segmentation using k-means clustering, EM and normalized cuts. *University Of California Irvine*, 2008.

[132] Nameirakpam Dhanachandra, Khumanthem Manglem, and Yambem Jina Chanu. Image segmentation using k-means clustering algorithm and subtractive clustering algorithm. *Procedia Computer Science*, 54:764–771, 2015.

[133] Arnau Oliver, Xavier Munoz, Joan Batlle, Lluis Pacheco, and Jordi Freixenet. Improving clustering algorithms for image segmentation using contour and region information. In *Automation, Quality and Testing, Robotics, 2006 IEEE International Conference on*, volume 2, pages 315–320. IEEE, 2006.

[134] Vijay Jumb, Mandar Sohani, and Avinash Shrivastava. Color image segmentation using k-means clustering and otsus adaptive thresholding. *International Journal of Innovative Technology and Exploring Engineering (IJITEE)*, 3(9):72–76, 2014.

- [135] Alan Jose, S Ravi, and M Sambath. Brain tumor segmentation using k-means clustering and fuzzy c-means algorithms and its area calculation. *International Journal of Innovative Research in Computer and Communication Engineering*, 2(3):32–57, 2014.
- [136] Jianbo Shi and Jitendra Malik. Normalized cuts and image segmentation. *IEEE Transactions on pattern analysis and machine intelligence*, 22(8):888–905, 2000.
- [137] Arthur P Dempster, Nan M Laird, and Donald B Rubin. Maximum likelihood from incomplete data via the em algorithm. *Journal of the royal statistical society. Series B (methodological)*, pages 1–38, 1977.
- [138] Chad Carson, Serge Belongie, Hayit Greenspan, and Jitendra Malik. Blob-world: Image segmentation using expectation-maximization and its application to image querying. *IEEE Transactions on Pattern Analysis and Machine Intelligence*, 24(8):1026–1038, 2002.
- [139] Torsten Rohlfing, Daniel B Russakoff, and Calvin R Maurer. Performance-based classifier combination in atlas-based image segmentation using expectation-maximization parameter estimation. *IEEE transactions on medical imaging*, 23(8):983–994, 2004.
- [140] Chi Hau Chen and Gwo Giun Lee. Image segmentation using multiresolution wavelet analysis and expectation-maximization (em) algorithm for digital mammography. *International Journal of Imaging Systems and Technology*, 8(5):491–504, 1997.
- [141] Aristeidis Diplopoulos, Nikos Vlassis, and Theo Gevers. A spatially constrained generative model and an em algorithm for image segmentation. *IEEE Transactions on Neural Networks*, 18(3):798–808, 2007.
- [142] Sankar K Pal and Pabitra Mitra. Multispectral image segmentation using the rough-set-initialized em algorithm. *IEEE Transactions on Geoscience and Remote Sensing*, 40(11):2495–2501, 2002.

- [143] Jeff A Bilmes et al. A gentle tutorial of the em algorithm and its application to parameter estimation for gaussian mixture and hidden markov models. *International Computer Science Institute*, 4(510):126, 1998.
- [144] Geoffrey McLachlan and Thriyambakam Krishnan. *The EM algorithm and extensions*, volume 382. John Wiley & Sons, 2007.
- [145] Stuart Geman and Donald Geman. Stochastic relaxation, gibbs distributions, and the bayesian restoration of images. *IEEE Transactions on pattern analysis and machine intelligence*, (6):721–741, 1984.
- [146] Stan Z Li. *Markov random field modeling in image analysis*. Springer Science & Business Media, 2009.
- [147] Ciro D’Elia, Giovanni Poggi, and Giuseppe Scarpa. A tree-structured markov random field model for bayesian image segmentation. *IEEE Transactions on Image Processing*, 12(10):1259–1273, 2003.
- [148] Lei Zhang and Qiang Ji. Image segmentation with a unified graphical model. *IEEE Transactions on Pattern Analysis and Machine Intelligence*, 32(8):1406–1425, 2010.
- [149] Yongyue Zhang, Michael Brady, and Stephen Smith. Segmentation of brain mr images through a hidden markov random field model and the expectation–maximization algorithm. *IEEE transactions on medical imaging*, 20(1):45–57, 2001.
- [150] D-B Gu and J-X Sun. Em image segmentation algorithm based on an inhomogeneous hidden mrf model. *IEE Proceedings-Vision, Image and Signal Processing*, 152(2):184–190, 2005.
- [151] Kai-Wei Huang, Zhe-Yi Zhao, Qian Gong, Juan Zha, Liu Chen, and Ran Yang. Nasopharyngeal carcinoma segmentation via hmrf-em with maximum entropy. In *Engineering in Medicine and Biology Society (EMBC), 2015 37th Annual International Conference of the IEEE*, pages 2968–2972. IEEE, 2015.

- [152] Geming Wu, Xinyan Zhao, Shuqian Luo, and Hongli Shi. Histological image segmentation using fast mean shift clustering method. *Biomedical engineering online*, 14(1):24, 2015.
- [153] Hayder Saad Abdulbaqi, Mohd Zubir Mat, Ahmad Fairuz Omar, Iskandar Shahrim Bin Mustafa, and Loay Kadom Abood. Detecting brain tumor in magnetic resonance images using hidden markov random fields and threshold techniques. In *Research and Development (SCoReD), 2014 IEEE Student Conference on*, pages 1–5. IEEE, 2014.
- [154] Gilles Celeux, Florence Forbes, and Nathalie Peyrard. Em procedures using mean field-like approximations for markov model-based image segmentation. *Pattern recognition*, 36(1):131–144, 2003.
- [155] Balasrinivasa Rao Sajja, Sushmita Datta, Renjie He, Meghana Mehta, Rakesh K Gupta, Jerry S Wolinsky, and Ponnada A Narayana. Unified approach for multiple sclerosis lesion segmentation on brain mri. *Annals of biomedical engineering*, 34(1):142–151, 2006.
- [156] Stanley Osher and James A Sethian. Fronts propagating with curvature-dependent speed: algorithms based on hamilton-jacobi formulations. *Journal of computational physics*, 79(1):12–49, 1988.
- [157] Steffen Basting and Martin Weismann. A hybrid level set–front tracking finite element approach for fluid–structure interaction and two-phase flow applications. *Journal of Computational Physics*, 255:228–244, 2013.
- [158] Carles Montoliu, Néstor Ferrando, MA Gosálvez, Joaquín Cerdá, and RJ Colom. Implementation and evaluation of the level set method: towards efficient and accurate simulation of wet etching for microengineering applications. *Computer Physics Communications*, 184(10):2299–2309, 2013.
- [159] Juan Vidal, Gloria Bueno, John Galeotti, Marcial García-Rojo, Fernanda Relea, Oscar Déniz, et al. A fully automated approach to prostate biopsy segmentation

based on level-set and mean filtering. *Journal of pathology informatics*, 2(2):5, 2011.

[160] Mike Roberts, Jeff Packer, Mario Costa Sousa, and Joseph Ross Mitchell. A work-efficient gpu algorithm for level set segmentation. In *Proceedings of the Conference on High Performance Graphics*, pages 123–132. Eurographics Association, 2010.

[161] Lingfeng Wang and Chunhong Pan. Robust level set image segmentation via a local correntropy-based k-means clustering. *Pattern Recognition*, 47(5):1917–1925, 2014.

[162] Bin Wang, Xinbo Gao, Dacheng Tao, and Xuelong Li. A nonlinear adaptive level set for image segmentation. *IEEE transactions on cybernetics*, 44(3):418–428, 2014.

[163] Hong-Kai Zhao, Stanley Osher, and Ronald Fedkiw. Fast surface reconstruction using the level set method. In *Variational and Level Set Methods in Computer Vision, 2001. Proceedings. IEEE Workshop on*, pages 194–201. IEEE, 2001.

[164] Zhijie Xu, Hai Huang, Xiaoyi Li, and Paul Meakin. Phase field and level set methods for modeling solute precipitation and/or dissolution. *Computer Physics Communications*, 183(1):15–19, 2012.

[165] Hyungson Ki. Level set method for two-phase incompressible flows under magnetic fields. *Computer Physics Communications*, 181(6):999–1007, 2010.

[166] Joachim Weickert and Gerald Kühne. Fast methods for implicit active contour models. In *Geometric level set methods in imaging, vision, and graphics*, pages 43–57. Springer, 2003.

[167] Espen Jettestuen, Johan O Helland, and Maša Prodanović. A level set method for simulating capillary-controlled displacements at the pore scale with nonzero contact angles. *Water Resources Research*, 49(8):4645–4661, 2013.

- [168] Martin Burger. A framework for the construction of level set methods for shape optimization and reconstruction. *Interfaces and Free boundaries*, 5(3):301–329, 2003.
- [169] Ravi Malladi, James A Sethian, and Baba C Vemuri. Shape modeling with front propagation: A level set approach. *IEEE transactions on pattern analysis and machine intelligence*, 17(2):158–175, 1995.
- [170] Vicent Caselles, Francine Catté, Tomeu Coll, and Françoise Dibos. A geometric model for active contours in image processing. *Numerische mathematik*, 66(1):1–31, 1993.
- [171] Michael Kass, Andrew Witkin, and Demetri Terzopoulos. Snakes: Active contour models. *International journal of computer vision*, 1(4):321–331, 1988.
- [172] Gloria Bueno, R Gonzalez, Oscar Déniz, Marcial García-Rojo, J Gonzalez-Garcia, MM Fernández-Carrobles, Noelia Vállez, and Jesús Salido. A parallel solution for high resolution histological image analysis. *Computer methods and programs in biomedicine*, 108(1):388–401, 2012.
- [173] A Fenster and B Chiu. Evaluation of segmentation algorithms for medical imaging. In *2005 IEEE Engineering in Medicine and Biology 27th Annual Conference*, pages 7186–7189. IEEE, 2005.
- [174] Cornelis N de Graaf, André SE Koster, Koen L Vincken, and Max A Viergever. Validation of the interleaved pyramid for the segmentation of 3D vector images. *Pattern Recognition Letters*, 15(5):469–475, 1994.
- [175] Yousef Rezaeitabar and Ilkay Ulusoy. Automatic 3D segmentation of individual facial muscles using unlabeled prior information. *International journal of computer assisted radiology and surgery*, 7(1):35–41, 2012.
- [176] Szymon Rusinkiewicz and Marc Levoy. Efficient variants of the icp algorithm. In *3-D Digital Imaging and Modeling, 2001. Proceedings. Third International Conference on*, pages 145–152. IEEE, 2001.

- [177] Xiaozheng Mou and Han Wang. An improved approach for depth data based face pose estimation using particle swarm optimization. In *Computer Vision Theory and Applications (VISAPP), 2014 International Conference on*, volume 2, pages 534–541. IEEE, 2014.
- [178] Andrew M Day, David B Arnold, Sven Havemann, and Dieter W Fellner. Combining polygonal and subdivision surface approaches to modelling and rendering of urban environments. *Computers & Graphics*, 28(4):497–507, 2004.
- [179] Andrew J Stoddart and Adrian Hilton. Registration of multiple point sets. In *Pattern Recognition, 1996., Proceedings of the 13th International Conference on*, volume 2, pages 40–44. IEEE, 1996.
- [180] Ahmad Almhdie, Christophe Léger, Mohamed Deriche, and Roger Lédée. 3D registration using a new implementation of the icp algorithm based on a comprehensive lookup matrix: Application to medical imaging. *Pattern Recognition Letters*, 28(12):1523–1533, 2007.
- [181] Shuda Li and Andrew Calway. Rgbd relocalisation using pairwise geometry and concise key point sets. In *2015 IEEE International Conference on Robotics and Automation (ICRA)*, pages 6374–6379. IEEE, 2015.
- [182] Takeki Ogitsu and Manabu Omae. State observation and communication for cloud vehicle control. In *2015 IEEE 81st Vehicular Technology Conference (VTC Spring)*, pages 1–5. IEEE, 2015.
- [183] Marc Levoy, Kari Pulli, Brian Curless, Szymon Rusinkiewicz, David Koller, Lucas Pereira, Matt Ginzton, Sean Anderson, James Davis, Jeremy Ginsberg, et al. The digital michelangelo project: 3D scanning of large statues. In *Proceedings of the 27th annual conference on Computer graphics and interactive techniques*, pages 131–144. ACM Press/Addison-Wesley Publishing Co., 2000.

- [184] Mahdi Ben Ghorbel, Malek Baklouti, and Serge Couvet. 3D head pose estimation and tracking using particle filtering and icp algorithm. In *International Conference on Articulated Motion and Deformable Objects*, pages 224–237. Springer, 2010.
- [185] Farid Abedan Kondori, Shahrouz Yousefi, Haibo Li, Samuel Sonning, and Sabina Sonning. 3D head pose estimation using the kinect. In *Wireless Communications and Signal Processing (WCSP), 2011 International Conference on*, pages 1–4. IEEE, 2011.
- [186] Paul J Besl and Neil D McKay. Method for registration of 3-d shapes. In *Robotics-DL tentative*, pages 586–606. International Society for Optics and Photonics, 1992.
- [187] Yang Chen and Gérard Medioni. Object modelling by registration of multiple range images. *Image and vision computing*, 10(3):145–155, 1992.
- [188] Lena Maier-Hein, Alfred M Franz, Thiago R dos Santos, Mirko Schmidt, Markus Fangerau, Hans-Peter Meinzer, and J Michael Fitzpatrick. Convergent iterative closest-point algorithm to accomodate anisotropic and inhomogenous localization error. *Pattern Analysis and Machine Intelligence, IEEE Transactions on*, 34(8):1520–1532, 2012.
- [189] Greg Turk and Marc Levoy. Zippered polygon meshes from range images. In *Proceedings of the 21st annual conference on Computer graphics and interactive techniques*, pages 311–318. ACM, 1994.
- [190] Takeshi Masuda, Katsuhiko Sakaue, and Naokazu Yokoya. Registration and integration of multiple range images for 3-d model construction. In *Pattern Recognition, 1996., Proceedings of the 13th International Conference on*, volume 1, pages 879–883. IEEE, 1996.

- [191] Sebastian Weik. Registration of 3-d partial surface models using luminance and depth information. In *3-D Digital Imaging and Modeling, 1997. Proceedings., International Conference on Recent Advances in*, pages 93–100. IEEE, 1997.
- [192] Chu-Song Chen, Yi-Ping Hung, and Jen-Bo Cheng. A fast automatic method for registration of partially-overlapping range images. In *Computer Vision, 1998. Sixth International Conference on*, pages 242–248. IEEE, 1998.
- [193] Chu-Song Chen, Yi-Ping Hung, and Jen-Bo Cheng. Ransac-based darces: A new approach to fast automatic registration of partially overlapping range images. *IEEE Transactions on Pattern Analysis and Machine Intelligence*, 21(11):1229–1234, 1999.
- [194] Andrew Edie Johnson and Martial Hebert. Surface registration by matching oriented points. In *3-D Digital Imaging and Modeling, 1997. Proceedings., International Conference on Recent Advances in*, pages 121–128. IEEE, 1997.
- [195] Chitra Dorai, Juyang Weng, and Anil K. Jain. Optimal registration of object views using range data. *IEEE Transactions on Pattern Analysis and Machine Intelligence*, 19(10):1131–1138, 1997.
- [196] Olivier D Faugeras and Martial Hebert. The representation, recognition, and locating of 3-d objects. *The international journal of robotics research*, 5(3):27–52, 1986.
- [197] Fridtjof Stein and Gérard Medioni. Structural indexing: Efficient 3-d object recognition. *IEEE Transactions on Pattern Analysis and Machine Intelligence*, 14(2):125–145, 1992.
- [198] Gérard Blais and Martin D. Levine. Registering multiview range data to create 3D computer objects. *IEEE Transactions on Pattern Analysis and Machine Intelligence*, 17(8):820–824, 1995.
- [199] Peter Johannes Neugebauer. Geometrical cloning of 3D objects via simultaneous registration of multiple range images. In *Shape Modeling and Applications*,

1997. *Proceedings., 1997 International Conference on*, pages 130–139. IEEE, 1997.

[200] Jacques Feldmar and Nicholas Ayache. Locally affine registration of free-form surfaces. In *Computer Vision and Pattern Recognition, 1994. Proceedings CVPR'94., 1994 IEEE Computer Society Conference on*, pages 496–501. IEEE, 1994.

[201] Gregory C Sharp, Sang W Lee, and David K Wehe. Icp registration using invariant features. *IEEE Transactions on Pattern Analysis and Machine Intelligence*, 24(1):90–102, 2002.

[202] Kari Pulli. Multiview registration for large data sets. In *3-D Digital Imaging and Modeling, 1999. Proceedings. Second International Conference on*, pages 160–168. IEEE, 1999.

[203] Sébastien Granger, Xavier Pennec, and Alexis Roche. Rigid point-surface registration using an em variant of icp for computer guided oral implantology. In *International Conference on Medical Image Computing and Computer-Assisted Intervention*, pages 752–761. Springer, 2001.

[204] Shun’ichi Kaneko, Tomonori Kondo, and Atsushi Miyamoto. Robust matching of 3D contours using iterative closest point algorithm improved by m-estimation. *Pattern Recognition*, 36(9):2041–2047, 2003.

[205] Chitra Dorai, Gang Wang, Anil K Jain, and Carolyn Mercer. Registration and integration of multiple object views for 3D model construction. *IEEE Transactions on Pattern Analysis and Machine Intelligence*, 20(1):83–89, 1998.

[206] Leopoldo Armesto, Javier Minguez, and Luis Montesano. A generalization of the metric-based iterative closest point technique for 3D scan matching. In *Robotics and Automation (ICRA), 2010 IEEE International Conference on*, pages 1367–1372. IEEE, 2010.

- [207] Dmitry Chetverikov, Dmitry Stepanov, and Pavel Krsek. Robust euclidean alignment of 3D point sets: the trimmed iterative closest point algorithm. *Image and Vision Computing*, 23(3):299–309, 2005.
- [208] Andrew Edie Johnson and Sing Bing Kang. Registration and integration of textured 3D data. *Image and vision computing*, 17(2):135–147, 1999.
- [209] Jeff M Phillips, Ran Liu, and Carlo Tomasi. Outlier robust icp for minimizing fractional rmsd. In *3-D Digital Imaging and Modeling, 2007. 3DIM’07. Sixth International Conference on*, pages 427–434. IEEE, 2007.
- [210] S Rusinkiewicz and M Levoy. Efficient variants of the icp algorithm. in 3-d digital imaging and modeling, 2001. In *Proceedings. Third International Conference on*, pages 145–152.
- [211] Jon Louis Bentley. Multidimensional binary search trees used for associative searching. *Communications of the ACM*, 18(9):509–517, 1975.
- [212] David G Kendall. A survey of the statistical theory of shape. *Statistical Science*, pages 87–99, 1989.
- [213] William R Crum, Thomas Hartkens, and DLG Hill. Non-rigid image registration: theory and practice. *The British Journal of Radiology*, 2014.
- [214] Barbara Zitova and Jan Flusser. Image registration methods: a survey. *Image and vision computing*, 21(11):977–1000, 2003.
- [215] Terry Peters and Kevin Cleary. *Image-guided interventions: technology and applications*. Springer Science & Business Media, 2008.
- [216] David Jaffray, Patrick Kupelian, Toufik Djemil, and Roger M Macklis. Review of image-guided radiation therapy. *Expert review of anticancer therapy*, 7(1):89–103, 2007.

- [217] Matthew A Mauro, Kieran PJ Murphy, Kenneth R Thomson, Anthony C Venbrux, and Robert A Morgan. *Image-guided interventions: expert radiology series*. Elsevier Health Sciences, 2013.
- [218] Marc R Mayberg, Eric LaPresto, and Edwin J Cunningham. Image-guided endoscopy: description of technique and potential applications. *Neurosurgical focus*, 19(1):1–5, 2005.
- [219] Primoz Markelj, Dejan Tomažević, Bostjan Likar, and Franjo Pernuš. A review of 3D/2D registration methods for image-guided interventions. *Medical image analysis*, 16(3):642–661, 2012.
- [220] N Noguchi, M Tsuji, M Shigematsu, and M Goto. An orthognathic simulation system integrating teeth, jaw and face data using 3D cephalometry. *International journal of oral and maxillofacial surgery*, 36(7):640–645, 2007.
- [221] Tim Joda, Urs Brägger, and German Gallucci. Systematic literature review of digital three-dimensional superimposition techniques to create virtual dental patients. *International journal of oral & maxillofacial implants*, 30(2), 2015.
- [222] Joanneke M Plooij, Thomas JJ Maal, Piet Haers, Wilfred A Borstlap, Anne Marie Kuijpers-Jagtman, and Stefaan J Bergé. Digital three-dimensional image fusion processes for planning and evaluating orthodontics and orthognathic surgery. a systematic review. *International journal of oral and maxillofacial surgery*, 40(4):341–352, 2011.
- [223] Dinesh D Patil and Sonal G Deore. Medical image segmentation: a review. *International journal of computer science and mobile computing*, 2(1):22–27, 2013.
- [224] William R Crum, Oscar Camara, and Derek LG Hill. Generalized overlap measures for evaluation and validation in medical image analysis. *IEEE transactions on medical imaging*, 25(11):1451–1461, 2006.

[225] Emran Mohammad Abu Anas, Abtin Rasoulian, Alexander Seitel, Kathryn Darras, David Wilson, Paul St John, David Pichora, Parvin Mousavi, Robert Rohling, and Purang Abolmaesumi. Automatic segmentation of wrist bones in CT using a statistical wrist shape+ pose model. 2016.

[226] Bong Chul Kim, Chae Eun Lee, Wonse Park, Sang Hoon Kang, Piao Zheng-guo, Choong Kook Yi, and Sang-Hwy Lee. Integration accuracy of digital dental models and 3-dimensional computerized tomography images by sequential point-and surface-based markerless registration. *Oral Surgery, Oral Medicine, Oral Pathology, Oral Radiology, and Endodontology*, 110(3):370–378, 2010.

[227] Hoon Noh, Wael Nabha, Jin-Hyoung Cho, and Hyeyon-Shik Hwang. Registration accuracy in the integration of laser-scanned dental images into maxillofacial cone-beam computed tomography images. *American Journal of Orthodontics and Dentofacial Orthopedics*, 140(4):585–591, 2011.

[228] Niansong Ye, Hu Long, Songsong Zhu, Yunqiang Yang, Wenli Lai, and Jing Hu. The accuracy of computer image-guided template for mandibular angle ostectomy. *Aesthetic plastic surgery*, 39(1):117–123, 2015.

[229] Pietro Ausiello, Stefano Ciaramella, Franklin Garcia-Godoy, Antonio Gloria, Antonio Lanzotti, Saverio Maietta, and Massimo Martorelli. The effects of cavity-margin-angles and bolus stiffness on the mechanical behavior of indirect resin composite class ii restorations. *Dental Materials*, 33(1):e39–e47, 2017.

[230] Daniel P. Huttenlocher, Gregory A. Klanderman, and William J Rucklidge. Comparing images using the hausdorff distance. *IEEE Transactions on pattern analysis and machine intelligence*, 15(9):850–863, 1993.

[231] Manuel Pinheiro and JL Alves. A new level-set-based protocol for accurate bone segmentation from CT imaging. *IEEE Access*, 3:1894–1906, 2015.

[232] Bernhard Preim and Dirk Bartz. *Visualization in medicine: theory, algorithms, and applications*. Morgan Kaufmann, 2007.

[233] Krit Somkantha, Nipon Theera-Umporn, and Sansanee Auephanwiriyakul. Boundary detection in medical images using edge following algorithm based on intensity gradient and texture gradient features. *IEEE transactions on biomedical engineering*, 58(3):567–573, 2011.

[234] Peter C Tay, Christopher D Garson, Scott T Acton, and John A Hossack. Ultrasound despeckling for contrast enhancement. *IEEE Transactions on Image Processing*, 19(7):1847–1860, 2010.

[235] Jan Egger, Tina Kapur, Andriy Fedorov, Steve Pieper, James V Miller, Harini Veeraraghavan, Bernd Freisleben, Alexandra Golby, Christopher Nimsky, and Ron Kikinis. GBM volumetry using the 3D slicer medical image computing platform. *Scientific Reports* 3, (1364), 2013.

[236] Pankaj K Agarwal, Sariel Har-Peled, Micha Sharir, and Yusu Wang. Hausdorff distance under translation for points and balls. *ACM Transactions on Algorithms (TALG)*, 6(4):71, 2010.

[237] Abdel Aziz Taha and Allan Hanbury. Metrics for evaluating 3D medical image segmentation: analysis, selection, and tool. *BMC medical imaging*, 15(1):29, 2015.

[238] Sun-Jeong Kim, Soo-Kyun Kim, and Chang-Hun Kim. Discrete differential error metric for surface simplification. In *Computer Graphics and Applications, 2002. Proceedings. 10th Pacific Conference on*, pages 276–283. IEEE, 2002.

[239] Thabo Beeler, Bernd Bickel, Paul Beardsley, Bob Sumner, and Markus Gross. High-quality single-shot capture of facial geometry. In *ACM Transactions on Graphics (ToG)*, volume 29, page 40. ACM, 2010.

[240] Zacharias Fourie, Janalt Damstra, Peter O Gerrits, and Yijin Ren. Evaluation of anthropometric accuracy and reliability using different three-dimensional scanning systems. *Forensic Science International*, 207(1):127–134, 2011.

[241] M Dahmani-Causse, M Marx, O Deguine, B Fraysse, B Lepage, and B Escudé. Morphologic examination of the temporal bone by cone beam computed tomography: comparison with multislice helical computed tomography. *European annals of otorhinolaryngology, head and neck diseases*, 128(5):230–235, 2011.

[242] R Patcas, G Markic, L Müller, O Ullrich, T Peltomäki, CJ Kellenberger, and CA Karlo. Accuracy of linear intraoral measurements using cone beam CT and multidetector CT: a tale of two CTs. *Dentomaxillofacial Radiology*, 2014.

[243] Miet Loubele, Nele Van Assche, Karel Carpentier, Frederik Maes, Reinhilde Jacobs, Daniel van Steenberghe, and Paul Suetens. Comparative localized linear accuracy of small-field cone-beam CT and multislice CT for alveolar bone measurements. *Oral Surgery, Oral Medicine, Oral Pathology, Oral Radiology, and Endodontology*, 105(4):512–518, 2008.

[244] Juergen Medelnik, Klaus Hertrich, Stefanie Steinhäuser-Andresen, Ursula Hirschfelder, and Elisabeth Hofmann. Accuracy of anatomical landmark identification using different cbct-and msct-based 3D images. *Journal of Orofacial Orthopedics/Fortschritte der Kieferorthopädie*, 72(4):261–278, 2011.

[245] Olivier Pellerin, MingDe Lin, Nikhil Bhagat, Roberto Ardon, Benoit Mory, and Jean-François Geschwind. Comparison of semi-automatic volumetric vx2 hepatic tumor segmentation from cone beam CT and multi-detector CT with histology in rabbit models. *Academic radiology*, 20(1):115–121, 2013.

[246] Jack E Bresenham. Algorithm for computer control of a digital plotter. *IBM Systems journal*, 4(1):25–30, 1965.

[247] Jacob Cohen. Statistical power analysis. *Current directions in psychological science*, 1(3):98–101, 1992.

[248] Andrzej Buda and Andrzej Jarynowski. *Life Time of Correlations and Its Applications*. Andrzej Buda Wydawnictwo Naukowe, 2010.

- [249] Hod Lipson and Melba Kurman. *Fabricated: The new world of 3D printing*. John Wiley & Sons, 2013.
- [250] Sona Ghadimi, Hamid Abrishami Moghaddam, Reinhard Grebe, and Fabrice Wallois. Skull segmentation and reconstruction from newborn CT images using coupled level sets. *IEEE journal of biomedical and health informatics*, 20(2):563–573, 2016.
- [251] Chao Jin, Fei Shi, Dehui Xiang, Xueqing Jiang, Bin Zhang, Ximing Wang, Weifang Zhu, Enting Gao, and Xinjian Chen. 3D fast automatic segmentation of kidney based on modified aam and random forest. *IEEE transactions on medical imaging*, 35(6):1395–1407, 2016.
- [252] Karteek Popuri, Dana Cobzas, Nina Esfandiari, Vickie Baracos, and Martin Jägersand. Body composition assessment in axial CT images using fem-based automatic segmentation of skeletal muscle. *IEEE transactions on medical imaging*, 35(2):512–520, 2016.
- [253] Zeyang Xia, Yangzhou Gan, Jing Xiong, Qunfei Zhao, and Jie Chen. Crown segmentation from computed tomography images with metal artifacts. *IEEE Signal Processing Letters*, 23(5):678–682, 2016.
- [254] SMR Soroushmehr, A Bafna, S Schlosser, K Ward, H Derksen, and K Najarian. CT image segmentation in traumatic brain injury. In *2015 37th Annual International Conference of the IEEE Engineering in Medicine and Biology Society (EMBC)*, pages 2973–2976. IEEE, 2015.
- [255] Tiancheng He, Zhong Xue, and Stephen T Wong. A three-dimensional medical image segmentation app using graphic theory. In *2016 IEEE-EMBS International Conference on Biomedical and Health Informatics (BHI)*, pages 268–271. IEEE, 2016.

[256] HM Pinsky, S Dyda, RW Pinsky, KA Misch, and DP Sarment. Accuracy of three-dimensional measurements using cone-beam CT. *Dentomaxillofacial Radiology*, 2014.

[257] R Marmulla, R Wörtche, J Mühling, and S Hassfeld. Geometric accuracy of the newtom 9000 cone beam CT. *Dentomaxillofacial Radiology*, 2014.

[258] SA Stratemann, JC Huang, K Maki, AJ Miller, and DC Hatcher. Comparison of cone beam computed tomography imaging with physical measures. *Dentomaxillofacial Radiology*, 2014.

[259] CA Lascala, J Panella, and MM Marques. Analysis of the accuracy of linear measurements obtained by cone beam computed tomography (cbct-newtom). *Dentomaxillofacial Radiology*, 2014.

[260] A Anand Kumar, Abraham Phillip, Sathesh Kumar, Anuradha Rawat, Sakthi Priya, and V Kumaran. Digital model as an alternative to plaster model in assessment of space analysis. *Journal of pharmacy & bioallied sciences*, 7(Suppl 2):S465, 2015.

[261] Mika Salmi, Kaija-Stiina Paloheimo, Jukka Tuomi, Jan Wolff, and Antti Mäkitie. Accuracy of medical models made by additive manufacturing (rapid manufacturing). *Journal of Cranio-Maxillo-Facial Surgery*, 30:1e7, 2012.

[262] David B Arnold, AM Day, MR Goetz, A Courtenay, and HI Graham. Virtual teeth for endodontics training and practice. In *Information Visualization, 2000. Proceedings. IEEE International Conference on*, pages 597–604. IEEE, 2000.

[263] UK Clinical Trials Gateway. <https://ukctg.nihr.ac.uk/trials/trial-details/trial-details?trialNumber=NCT02930915>, 2016. Accessed: 25-03-2017.

[264] Acquisition of 3D facial geometry of patients scheduled for RT 1.0. <http://www.hra.nhs.uk/news/research-summaries/>

acquisition-of-3d-facial-geometry-of-patients-scheduled-for-rt-1-0/, 2016. Accessed: 25-03-2017.

[265] A service of the U.S. National Institutes of Health. <https://clinicaltrials.gov/ct2/show/NCT02930915>, 2016. Accessed: 25-03-2017.

[266] Dzung L Pham, Chenyang Xu, and Jerry L Prince. Current methods in medical image segmentation 1. *Annual review of biomedical engineering*, 2(1):315–337, 2000.

[267] Kjell Erlandsson, Irene Buvat, P Hendrik Pretorius, Benjamin A Thomas, and Brian F Hutton. A review of partial volume correction techniques for emission tomography and their applications in neurology, cardiology and oncology. *Physics in medicine and biology*, 57(21):R119, 2012.

[268] Miguel Angel Gonzalez Ballester, Andrew P Zisserman, and Michael Brady. Estimation of the partial volume effect in mri. *Medical Image Analysis*, 6(4):389–405, 2002.

[269] Miguel Angel Gonzalez Ballester, Andrew Zisserman, and Michael Brady. Segmentation and measurement of brain structures in mri including confidence bounds. *Medical Image Analysis*, 4(3):189–200, 2000.

[270] Emre H Kale, Erkan U Mumcuoglu, and Salih Hamcan. Automatic segmentation of human facial tissue by MRI–CT fusion: A feasibility study. *Computer methods and programs in biomedicine*, 108(3):1106–1120, 2012.

[271] Raphael Olszewski, Yang Liu, Thierry Duprez, TM Xu, and Hervé Reyhler. Three-dimensional appearance of the lips muscles with three-dimensional isotropic mri: in vivo study. *International journal of computer assisted radiology and surgery*, 4(4):349–352, 2009.

- [272] HPW Boom, PH Van Spronsen, FC Van Ginkel, RA Van Schijndel, JA Castelijns, and DB Tuinzing. A comparison of human jaw muscle cross-sectional area and volume in long-and short-face subjects, using mri. *archives of oral biology*, 53(3):273–281, 2008.
- [273] MA Yousuf and MN Nobi. A new method to remove noise in magnetic resonance and ultrasound images. *Journal of scientific research*, 3(1):81, 2010.
- [274] ME Farrugia, GM Bydder, JM Francis, and MD Robson. Magnetic resonance imaging of facial muscles. *Clinical radiology*, 62(11):1078–1086, 2007.
- [275] Corinne Devereux, Graham Grundy, and Philip Littman. Plastic molds for patient immobilization. *International Journal of Radiation Oncology\* Biology\* Physics*, 1(5-6):553–557, 1976.
- [276] Feng Ding, Hao Li, Yuan Cheng, and Wee Kheng Leow. Medical volume image summarization. In *Applications of Computer Vision (WACV), 2009 Workshop on*, pages 1–6. IEEE, 2009.
- [277] Ian Gibson. *Advanced manufacturing technology for medical applications: reverse engineering, software conversion and rapid prototyping*. John Wiley & Sons, 2006.
- [278] Michael Garland and Paul S Heckbert. Surface simplification using quadric error metrics. In *Proceedings of the 24th annual conference on Computer graphics and interactive techniques*, pages 209–216. ACM Press/Addison-Wesley Publishing Co., 1997.
- [279] Paul S Heckbert and Michael Garland. Optimal triangulation and quadric-based surface simplification. *Computational Geometry*, 14(1):49–65, 1999.
- [280] Michael Kazhdan, Matthew Bolitho, and Hugues Hoppe. Poisson surface reconstruction. In *Proceedings of the fourth Eurographics symposium on Geometry processing*, volume 7, 2006.

# Appendix A

## Applying our Overlap Measurement in Related Applications of Surface Simplification

This appendix presents the experimental work in which we employed our overlap measurement (*Dice\_3S*) in two different applications which are related to the quality of surface simplification of volume images. The ‘Pelvis’ and the ‘Knee’ data sets are used here to evaluate the experimental work.

### A.1 Introduction

Transmitting and displaying of medical volume images are two of the most technical difficulties in medical fields [276]. Reducing the size of medical volume images is one of the possible approaches to deal with those difficulties. The aim of reducing the size (surface simplification) is to produce high quality approximations of the original surface but in smaller size. Size reduction of medical volume images can have a significant impact on processing speed especially on low-end workstations [277] and it is considered an essential process when the computing resources (i.e. CPU, RAM, graphics card) is a matter. In addition to that, size reduction is used to export 3D medical image volumes for the production of physical biomodels [277]. There are different techniques used for reducing the size of volume images (down-sampling). 3D

overlap measurements are used as a measure to evaluate the validity of the techniques which are used for reducing the size of volume images.

The experiments in this appendix are designed to illustrate how *Dice\_3S* can be employed in useful applications for surface simplification in the field of medical images. We present two applications in this part:

- In the first application, we utilised *Dice\_3S* to compare between the Quadric Edge Collapse Decimation (QECD) technique [278] [279] and the Uniform Mesh Resampling (UMR) technique to determine which technique produces a higher level of similarity using different reduced versions of medical images. For each data set, 10 reduced versions of different sizes were generated using the QECD technique and another 10 reduced versions were generated using the UMR technique. The overlap measurement was run over each corresponding versions to find the technique that gives a higher level of similarity. Notice that UMR technique creates a new mesh that is a resampled version of the original one. The proportion of resampling depends on value of precision which is selected by the user.
- In the second application, we utilised *Dice\_3S* to be used to choose the optimal correction value (offsetting value) when a Poisson Surface Reconstruction (PSR) technique [280] is used. For each data set, a comparison between surfaces generated by 9 offsets was performed in order to find the optimal surface position.

## A.2 Comparing Two Surface-Simplification Techniques

Table A.1 displays the average similarity value generated by *Dice\_3S* when applied over the Pelvis and the Knee data sets using the QECD technique for surface simplification. The experiments are run over 11 resized versions of the same object (i.e each row represents one case). Each case of those represent a different percentage of reduction of the initial size.

Table A.1: Testing *Dice\_3S* on different reduced (simplified) versions of the pelvis and knee data sets. The QECD technique was used here to reduce the size of objects

Row#	Percentage	File-Size	Vertices	faces	Average With-filling	Overlap No-filling
<b>Pelvis</b>						
1	<i>Same</i>	750	7,625	15,350	<b>1.0000</b>	<b>1.0000</b>
2	90%	675	6,854	13,814	<b>0.9969</b>	<b>0.9785</b>
3	80%	600	6,090	12,279	<b>0.9908</b>	<b>0.9385</b>
4	70%	525	5,323	10,744	<b>0.9760</b>	<b>0.8591</b>
5	60%	450	4,556	9,210	<b>0.9613</b>	<b>0.7742</b>
6	50%	375	3,793	7,674	<b>0.9383</b>	<b>0.6801</b>
7	40%	300	3,030	6,140	<b>0.9231</b>	<b>0.6045</b>
8	30%	225	2,268	4,604	<b>0.9145</b>	<b>0.5569</b>
9	20%	150	1,505	3,070	<b>0.9013</b>	<b>0.4940</b>
10	10%	75	742	1,534	<b>0.8732</b>	<b>0.4119</b>
11	1%	8	70	152	<b>0.6089</b>	<b>0.1501</b>
<b>Knee</b>						
12	<i>Same</i>	2,665	26,651	53,314	<b>1.0000</b>	<b>1.0000</b>
13	90%	2,343	23,985	47,982	<b>0.9984</b>	<b>0.9535</b>
14	80%	2,132	21,319	42,650	<b>0.9965</b>	<b>0.8995</b>
15	70%	1,823	18,653	37,318	<b>0.9949</b>	<b>0.8475</b>
16	60%	1,562	15,988	31,988	<b>0.9921</b>	<b>0.7970</b>
17	50%	1,332	13,322	26,656	<b>0.9907</b>	<b>0.7535</b>
18	40%	1,042	10,656	21,324	<b>0.9886</b>	<b>0.7117</b>
19	30%	782	7,991	15,994	<b>0.9861</b>	<b>0.6755</b>
20	20%	521	5,325	10,662	<b>0.9841</b>	<b>0.6429</b>
21	10%	261	2,659	5,330	<b>0.9813</b>	<b>0.6099</b>
22	1%	27	261	532	<b>0.9511</b>	<b>0.2933</b>

Table A.2 displays the average similarity value generated by *Dice\_3S* when applied over the Pelvis and the Knee data sets using the UMR technique for surface simplification. The experiments are run over different resized versions (approximations) of the same object (i.e each row represents one case). Each case of those represent a different precision value. The resampling in UMR is performed by building a uniform volumetric representation where each voxel contains the signed distance from the original surface. The precision in this context refer to size of the cell where smaller cells produces better precision.

Figure A.1 illustrates and compares, as bar charts, the quality of the simplification between the QECD and the UMR techniques. It is obvious from the bar charts that the QECD technique produces a higher level of similarity ratio than the UMR technique for the same file size (i.e. the same percentage of approximation) which agrees with the results introduced in [278]. This applies for all the different test cases (i.e. all the file sizes) which leads to a conclusion that the QECD is more convenient than the UMR for approximation of volume medical images. The same test can be

Table A.2: Testing the overlap measurement on different reduced versions of the pelvis and knee data sets. The UMR technique was used here to reduce the size of objects

Row#	Precision	File-Size	Vertices	faces	Average With-filling	Overlap No-filling
<b>Pelvis</b>						
1	<i>Same</i>	750	7,625	15,350	<b>1.0000</b>	<b>1.0000</b>
2	1.5	747	7617	15280	<b>0.8858</b>	<b>0.4236</b>
3	2.0	403	4124	8247	<b>0.8558</b>	<b>0.3500</b>
4	2.5	241	2441	4928	<b>0.8247</b>	<b>0.3167</b>
5	3.0	165	1668	3358	<b>0.7817</b>	<b>0.2579</b>
6	3.5	111	1135	2270	<b>0.7461</b>	<b>0.2318</b>
7	4.0	81	824	1652	<b>0.7108</b>	<b>0.2018</b>
8	4.5	63	654	1284	<b>0.6568</b>	<b>0.1739</b>
9	5.0	46	487	934	<b>0.6181</b>	<b>0.1375</b>
10	5.5	34	367	694	<b>0.5357</b>	<b>0.1058</b>
11	6.0	28	294	560	<b>0.5348</b>	<b>0.1064</b>
12	6.5	24	248	472	<b>0.4507</b>	<b>0.0813</b>
13	7.0	18	197	362	<b>0.4414</b>	<b>0.0811</b>
14	7.5	18	191	366	<b>0.4712</b>	<b>0.0851</b>
15	10	7	82	140	<b>0.2211</b>	<b>0.0357</b>
<b>Knee</b>						
16	<i>Same</i>	2,665	26,651	53,314	<b>1.0000</b>	<b>1.0000</b>
17	1.5	605	6182	12384	<b>0.9765</b>	<b>0.5174</b>
18	2.0	324	3308	6624	<b>0.9670</b>	<b>0.4278</b>
19	2.5	207	2112	4228	<b>0.9574</b>	<b>0.3487</b>
20	3.0	139	1407	2830	<b>0.9391</b>	<b>0.2703</b>
21	3.5	100	1015	2034	<b>0.9230</b>	<b>0.2055</b>
22	4.0	75	757	1522	<b>0.9110</b>	<b>0.1747</b>
23	4.5	61	623	1238	<b>0.8952</b>	<b>0.1558</b>
24	5.0	43	438	876	<b>0.8637</b>	<b>0.1011</b>
25	5.5	37	378	756	<b>0.8578</b>	<b>0.0920</b>
26	6.0	33	332	668	<b>0.8504</b>	<b>0.0911</b>
27	6.5	23	234	464	<b>0.8206</b>	<b>0.0527</b>

used to compare between any size-reduction techniques to see which one gives a higher similarity ratio. The figures also support what we stated before, in Chapter 7 Section 7.6, on the stability of results generated by the overlap measurement either if we use or not the image filling. Moreover, the relation between the file size and the similarity ratio for the QECD is more linear than the UMR technique which is a good feature and makes the outcomes of this technique more reasonable.

### A.3 Determining the Optimal Correction Value in Poisson Surface Reconstruction Technique

We have utilised *Dice\_3S* to choose the optimal correction value (i.e. surface offsetting value or  $\alpha$ ) for the isosurface threshold when Poisson surface reconstruction (PSR)

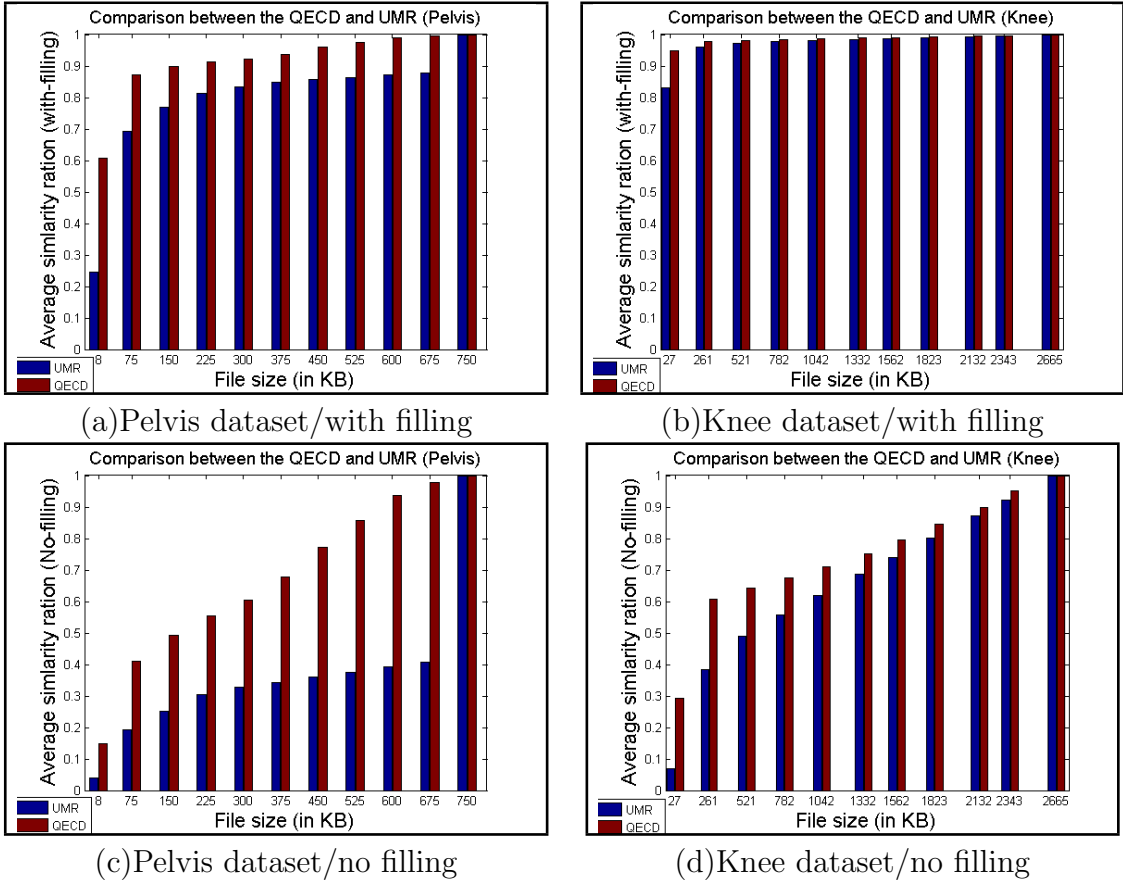


Figure A.1: Comparison between the QECD and the UMR techniques. Interpolation has been used to find the interpolated values at specific file sizes for the UMR

technique is used. Table A.3 displays the average similarity ratio for the pelvis and the knee data sets using different values for the parameter  $\alpha$  when PSR technique is applied to reduce the size of the mesh.

Figure A.2 plots the average similarity ratio for different values of  $\alpha$  when the PSR technique is used. The red ellipses in the figure represent the point at which the parameter  $\alpha$  reaches the maximum value of similarity ratio. It is obvious from the figures that choosing a value for  $\alpha$  to be in the range [0.90 - 1.0] will be the best choice to have the optimal similarity ratio.

Table A.3: The average similarity ratio for the pelvis and the knee data sets using different values for the parameter  $\alpha$ .

Row#	$(\alpha)$	File-Size	Vertices	faces	Average Overlap	
					With-filling	No-filling
<b>Pelvis</b>						
1	<i>Same</i>	750	7,625	15,350	<b>1.0000</b>	<b>1.0000</b>
2	0.25	840	8592	17192	<b>0.5731</b>	<b>0.0129</b>
3	0.50	781	7986	15980	<b>0.7421</b>	<b>0.1035</b>
4	0.75	712	7278	14568	<b>0.8320</b>	<b>0.2535</b>
5	0.875	680	6944	13908	<b>0.8400</b>	<b>0.2935</b>
6	1.0	638	6526	13052	<b>0.8408</b>	<b>0.3090</b>
7	1.25	562	5752	11492	<b>0.7506</b>	<b>0.2286</b>
8	1.5	459	4706	9384	<b>0.6029</b>	<b>0.1021</b>
9	1.75	325	3366	6652	<b>0.4143</b>	<b>0.0293</b>
10	2.0	194	1994	3968	<b>0.2293</b>	<b>0.0053</b>
<b>Knee</b>						
12	<i>Same</i>	2,665	26,651	53,314	<b>1.0000</b>	<b>1.0000</b>
13	0.25	456	4664	9324	<b>0.7478</b>	<b>0.0001</b>
14	0.50	442	4518	9032	<b>0.8318</b>	<b>0.0024</b>
15	0.75	429	4392	8784	<b>0.9069</b>	<b>0.0811</b>
16	0.875	427	4362	8724	<b>0.9324</b>	<b>0.1797</b>
17	1.00	426	4356	8712	<b>0.9424</b>	<b>0.2628</b>
18	1.25	415	4240	8480	<b>0.8892</b>	<b>0.0750</b>
19	1.50	386	3946	7888	<b>0.7943</b>	<b>0.0066</b>
20	1.75	341	3485	6970	<b>0.6570</b>	<b>0.0011</b>
21	2.00	235	2401	4794	<b>0.4516</b>	<b>0.0001</b>

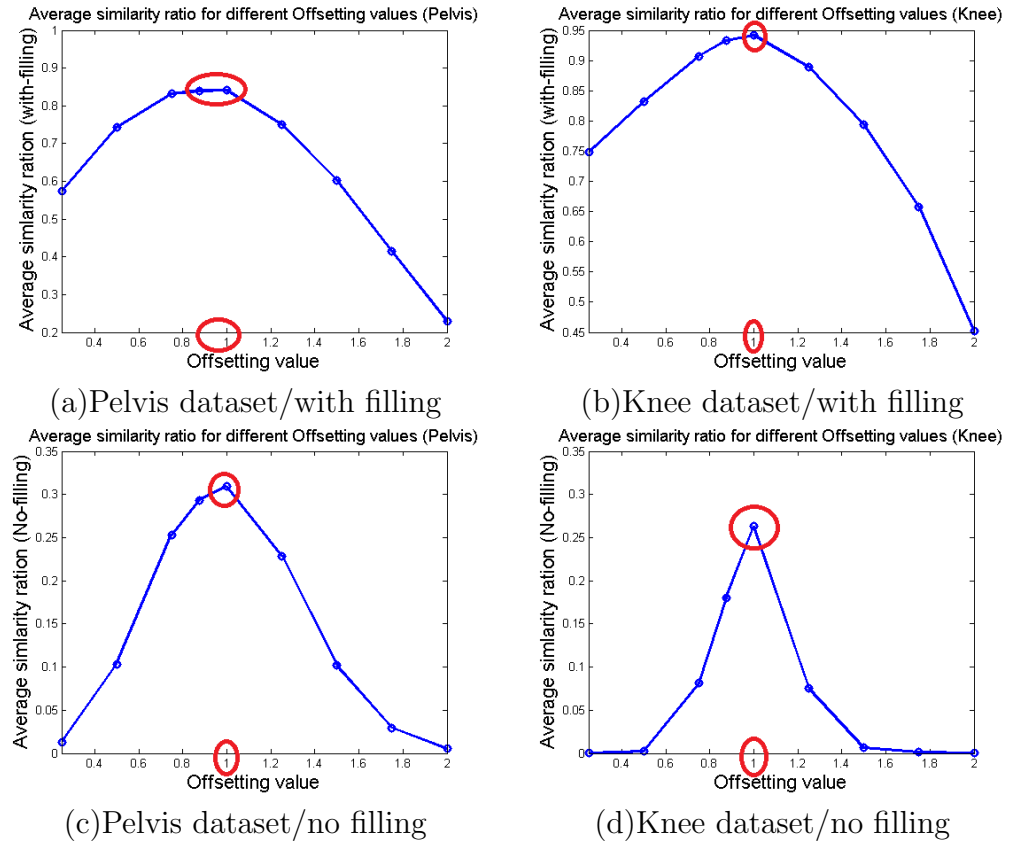


Figure A.2: Average similarity ratio for different Offsetting values. The red ellipses in the figure represent the point at which the parameter  $\alpha$  reaches the maximum value of similarity ratio.

## Appendix B

# Related Documents of the Clinical Trial

The following documents, which are related to our clinical trial, are attached to this appendix. This clinical trial is registered under the permission and approvals of the (Health Research Authority, NHS, UK) and the (Research Ethics Committee (REC), Yorkshire & The Humber, UK) and sponsored by the University of East Anglia, UK. It was given the following ID under the Integrated Research Application System (IRAS project ID:209119) and the following reference under the Research Ethics Committee (REC reference:16/YH/0485). Our clinical trial is posted online (see [263, 264, 265]).

- HRA approval (Health Research Authority approval)
- REC approval (Research Ethics Committee approval)
- Clinical trial protocol
- Participant information sheet (PIS)
- Consent form
- Good clinical practice certificate
- Letter of access for research

# **HRA Approval**

## **(Health Research Authority Approval)**

Mr Mohammad Ryalat  
University of East Anglia  
School of Computing Sciences  
UEA, Norwich.  
NR4 7TJ

Email: [hra.approval@nhs.net](mailto:hra.approval@nhs.net)

23 January 2017

Dear Mr Ryalat

**Letter of HRA Approval**

**Study title:** Feasibility Study: Acquisition of 3D facial geometry of patients' scheduled for head and neck Radiotherapy Treatment (RT).  
**IRAS project ID:** 209119  
**REC reference:** 16/YH/0485  
**Sponsor** University of East Anglia

I am pleased to confirm that **HRA Approval** has been given for the above referenced study, on the basis described in the application form, protocol, supporting documentation and any clarifications noted in this letter.

**Participation of NHS Organisations in England**

The sponsor should now provide a copy of this letter to all participating NHS organisations in England.

*Appendix B* provides important information for sponsors and participating NHS organisations in England for arranging and confirming capacity and capability. **Please read *Appendix B* carefully**, in particular the following sections:

- *Participating NHS organisations in England* – this clarifies the types of participating organisations in the study and whether or not all organisations will be undertaking the same activities
- *Confirmation of capacity and capability* - this confirms whether or not each type of participating NHS organisation in England is expected to give formal confirmation of capacity and capability. Where formal confirmation is not expected, the section also provides details on the time limit given to participating organisations to opt out of the study, or request additional time, before their participation is assumed.
- *Allocation of responsibilities and rights are agreed and documented (4.1 of HRA assessment criteria)* - this provides detail on the form of agreement to be used in the study to confirm capacity and capability, where applicable.

Further information on funding, HR processes, and compliance with HRA criteria and standards is also provided.

It is critical that you involve both the research management function (e.g. R&D office) supporting each organisation and the local research team (where there is one) in setting up your study. Contact details and further information about working with the research management function for each organisation can be accessed from [www.hra.nhs.uk/hra-approval](http://www.hra.nhs.uk/hra-approval).

## Appendices

The HRA Approval letter contains the following appendices:

- A – List of documents reviewed during HRA assessment
- B – Summary of HRA assessment

## After HRA Approval

The document “*After Ethical Review – guidance for sponsors and investigators*”, issued with your REC favourable opinion, gives detailed guidance on reporting expectations for studies, including:

- Registration of research
- Notifying amendments
- Notifying the end of the study

The HRA website also provides guidance on these topics, and is updated in the light of changes in reporting expectations or procedures.

In addition to the guidance in the above, please note the following:

- HRA Approval applies for the duration of your REC favourable opinion, unless otherwise notified in writing by the HRA.
- Substantial amendments should be submitted directly to the Research Ethics Committee, as detailed in the *After Ethical Review* document. Non-substantial amendments should be submitted for review by the HRA using the form provided on the [HRA website](http://www.hra.nhs.uk), and emailed to [hra.amendments@nhs.net](mailto:hra.amendments@nhs.net).
- The HRA will categorise amendments (substantial and non-substantial) and issue confirmation of continued HRA Approval. Further details can be found on the [HRA website](http://www.hra.nhs.uk).

## Scope

HRA Approval provides an approval for research involving patients or staff in NHS organisations in England.

If your study involves NHS organisations in other countries in the UK, please contact the relevant national coordinating functions for support and advice. Further information can be found at <http://www.hra.nhs.uk/resources/applying-for-reviews/nhs-hsc-rd-review/>.

If there are participating non-NHS organisations, local agreement should be obtained in accordance with the procedures of the local participating non-NHS organisation.

## User Feedback

The Health Research Authority is continually striving to provide a high quality service to all applicants and sponsors. You are invited to give your view of the service you have received and the application

procedure. If you wish to make your views known please email the HRA at [hra.approval@nhs.net](mailto:hra.approval@nhs.net). Additionally, one of our staff would be happy to call and discuss your experience of HRA Approval.

## HRA Training

We are pleased to welcome researchers and research management staff at our training days – see details at <http://www.hra.nhs.uk/hra-training/>

Your IRAS project ID is **209119**. Please quote this on all correspondence.

Yours sincerely

Beverley Mashegede  
Assessor

Email: [hra.approval@nhs.net](mailto:hra.approval@nhs.net)

Copy to: Ms Tracy Moulton, Sponsor Contact

Mr Michael Sheridan, Lead NHS R&D Contact

Dr Mark Fisher, Chief Investigator, Supervisor

## Appendix A - List of Documents

The final document set assessed and approved by HRA Approval is listed below.

Document	Version	Date
Covering letter on headed paper [Covering letter]	1.0	02 November 2016
IRAS Application Form [IRAS_Form_09122016]		09 December 2016
IRAS Application Form XML file [IRAS_Form_09122016]		09 December 2016
IRAS Checklist XML [Checklist_09122016]		09 December 2016
Letter from sponsor [Sponsor & Indemnity Letter]	1.0	03 November 2016
Non-validated questionnaire [Questionnaire]	2.0	02 November 2016
Other [List of Amendments]	1.0	17 November 2016
Other [IRAS Trial Form: Amendments]	1.0	09 December 2016
Participant consent form [Consent Form]	3.0	10 November 2016
Participant information sheet (PIS) [Participant Information Sheet]	3.0	17 November 2016
Research protocol or project proposal [Research Protocol]	3.0	10 November 2016
Summary CV for Chief Investigator (CI) [CV: Dr Mark Fisher]	1.0	02 November 2016
Summary CV for student [CV: Mohammad Ryalat]	1.0	02 November 2016
Summary CV for supervisor (student research) [CV: Dr Mark Fisher]	1.0	02 November 2016
Summary, synopsis or diagram (flowchart) of protocol in non-technical language [Flowchart]	1.0	02 November 2016

## Appendix B - Summary of HRA Assessment

This appendix provides assurance to you, the sponsor and the NHS in England that the study, as reviewed for HRA Approval, is compliant with relevant standards. It also provides information and clarification, where appropriate, to participating NHS organisations in England to assist in assessing and arranging capacity and capability.

**For information on how the sponsor should be working with participating NHS organisations in England, please refer to the, participating NHS organisations, capacity and capability and Allocation of responsibilities and rights are agreed and documented (4.1 of HRA assessment criteria) sections in this appendix.**

The following person is the sponsor contact for the purpose of addressing participating organisation questions relating to the study:

Name: Tracy Moulton

Tel: 01603 591482

Email: [t.moulton@uea.ac.uk](mailto:t.moulton@uea.ac.uk)

### HRA assessment criteria

Section	HRA Assessment Criteria	Compliant with Standards	Comments
1.1	IRAS application completed correctly	Yes	No comments
2.1	Participant information/consent documents and consent process	Yes	No comments
3.1	Protocol assessment	Yes	No comments
4.1	Allocation of responsibilities and rights are agreed and documented	Yes	The Sponsor contact confirmed that no Statement of Activities is expected as a form of agreement as UEA and NNUH have a joint working relationship with Joint SOPs.
4.2	Insurance/indemnity arrangements assessed	Yes	Where applicable, independent contractors (e.g. General Practitioners) should ensure that the professional indemnity provided by their medical defence organisation covers the activities expected of them for this

Section	HRA Assessment Criteria	Compliant with Standards	Comments
			research study.
4.3	Financial arrangements assessed	Yes	No funds will be provided to the participating organisation.
5.1	Compliance with the Data Protection Act and data security issues assessed	Yes	No comments
5.2	CTIMPS – Arrangements for compliance with the Clinical Trials Regulations assessed	Not Applicable	No comments
5.3	Compliance with any applicable laws or regulations	Yes	No comments
6.1	NHS Research Ethics Committee favourable opinion received for applicable studies	Yes	Provisional Opinion was issued 14 November 2016. Further Information FO issued 12 December 2016.
6.2	CTIMPS – Clinical Trials Authorisation (CTA) letter received	Not Applicable	No comments
6.3	Devices – MHRA notice of no objection received	Not Applicable	No comments
6.4	Other regulatory approvals and authorisations received	Not Applicable	No comments

## Participating NHS Organisations in England

*This provides detail on the types of participating NHS organisations in the study and a statement as to whether the activities at all organisations are the same or different.*

This is a non-commercial student (PhD Computing Sciences) and there is one site type.

The Chief Investigator or sponsor should share relevant study documents with participating NHS organisations in England in order to put arrangements in place to deliver the study. The documents should be sent to both the local study team, where applicable, and the office providing the research management function at the participating organisation. For NIHR CRN Portfolio studies, the Local LCRN contact should also be copied into this correspondence. For further guidance on working with participating NHS organisations please see the HRA website.

If chief investigators, sponsors or principal investigators are asked to complete site level forms for participating NHS organisations in England which are not provided in IRAS or on the HRA website, the chief investigator, sponsor or principal investigator should notify the HRA immediately at [hra.approval@nhs.net](mailto:hra.approval@nhs.net). The HRA will work with these organisations to achieve a consistent approach to information provision.

## Confirmation of Capacity and Capability

*This describes whether formal confirmation of capacity and capability is expected from participating NHS organisations in England.*

Participating NHS organisations in England **will be expected to formally confirm their capacity and capability to host this research.**

- Following issue of this letter, participating NHS organisations in England may now confirm to the sponsor their capacity and capability to host this research, when ready to do so. How capacity and capability will be confirmed is detailed in the *Allocation of responsibilities and rights are agreed and documented (4.1 of HRA assessment criteria)* section of this appendix.
- The [Assessing, Arranging, and Confirming](#) document on the HRA website provides further information for the sponsor and NHS organisations on assessing, arranging and confirming capacity and capability.

## Principal Investigator Suitability

*This confirms whether the sponsor position on whether a PI, LC or neither should be in place is correct for each type of participating NHS organisation in England and the minimum expectations for education, training and experience that PIs should meet (where applicable).*

A Principal Investigator is expected at the participating organisation.

GCP training is not a generic training expectation, in line with the [HRA statement on training expectations](#).

## HR Good Practice Resource Pack Expectations

*This confirms the HR Good Practice Resource Pack expectations for the study and the pre-engagement checks that should and should not be undertaken*

A Letter of Access or honorary contract is expected for external research team members undertaking any research activities that may impact on the quality of care of the participant.

Students supervised under close clinical supervision may not require honorary research contracts.

## Other Information to Aid Study Set-up

*This details any other information that may be helpful to sponsors and participating NHS organisations in England to aid study set-up.*

The applicant has indicated that they do not intend to apply for inclusion on the NIHR CRN Portfolio.

# **REC Approval**

## **(Research Ethics Committee Approval)**



**Health Research Authority**  
**Yorkshire & The Humber - Leeds East Research Ethics Committee**

Jarrow Business Centre  
Rolling Mill Road  
Jarrow  
NE32 3DT

Telephone: 0207 104 8081

03 November 2016

Mr Mohammad Ryalat  
NR4 7TJ  
University of East Anglia  
School of Computing Sciences  
UEA, Norwich.  
NR4 7TJ

Dear Mr Ryalat

**Study title:** Feasibility Study: Acquisition of 3D facial geometry of patients' scheduled for head and neck Radiotherapy Treatment (RT).  
**REC reference:** 16/YH/0485  
**IRAS project ID:** 209119

Thank you for your application for ethical review, which was received on 3<sup>rd</sup> November. I can confirm that the application is valid and will be reviewed by the Proportionate Review Sub-Committee on 14 November 2016. To enable the Proportionate Review Sub Committee to provide you with a final opinion within 10 working days your application documentation will be sent by email to Committee members.

One of the REC members is appointed as the lead reviewer for each application reviewed by the Sub-Committee. I will let you know the name of the lead reviewer for your application as soon as this is known.

Please note that the lead reviewer may wish to contact you by phone or email between 11<sup>th</sup> and 18<sup>th</sup> November to clarify any points that might be raised by members and assist the Sub-Committee in reaching a decision.

If you will not be available between these dates, you are welcome to nominate another key investigator or a representative of the study sponsor who would be able to respond to the lead reviewer's queries on your behalf. If this is your preferred option, please identify this person to us and ensure we have their contact details.

You are not required to attend a meeting of the Proportionate Review Sub-Committee.

Please do not send any further documentation or revised documentation prior to the review unless requested.

**Documents received**

The documents to be reviewed are as follows:

Document	Version	Date
Covering letter on headed paper [Covering letter]	1.0	02 November 2016
IRAS Application Form [IRAS_Form_03112016]		03 November 2016
IRAS Application Form XML file [IRAS_Form_03112016]		03 November 2016
IRAS Checklist XML [Checklist_03112016]		03 November 2016
Letter from sponsor [Sponsor & Indemnity Letter]	1.0	03 November 2016
Non-validated questionnaire [Questionnaire]	2.0	02 November 2016
Participant consent form [Consent Form]	2.0	03 November 2016
Participant information sheet (PIS) [Participant Information Sheet]	2.0	02 November 2016
Research protocol or project proposal [Research Protocol]	2.0	03 November 2016
Summary CV for Chief Investigator (CI) [CV: Dr Mark Fisher]	1.0	02 November 2016
Summary CV for student [CV: Mohammad Ryalat]	1.0	02 November 2016
Summary CV for supervisor (student research) [CV: Dr Mark Fisher]	1.0	02 November 2016
Summary, synopsis or diagram (flowchart) of protocol in non technical language [Flowchart]	1.0	02 November 2016

No changes may be made to the application before the meeting. If you envisage that changes might be required, you are advised to withdraw the application and re-submit it.

### **Notification of the Sub-Committee's decision**

We aim to notify the outcome of the Sub-Committee review to you in writing within 10 working days from the date of receipt of a valid application.

If the Sub-Committee is unable to give an opinion because the application raises material ethical issues requiring further discussion at a full meeting of a Research Ethics Committee, your application will be referred for review to the next available meeting. We will contact you to explain the arrangements for further review and check they are convenient for you. You will be notified of the final decision within 60 days of the date on which we originally received your application. If the first available meeting date offered to you is not suitable, you may request review by another REC. In this case the 60 day clock would be stopped and restarted from the closing date for applications submitted to that REC.

### **Setting up sites in the NHS**

All researchers and local research collaborators who intend to participate in this study at sites in the National Health Service (NHS) or Health and Social Care (HSC) in Northern Ireland should work with the relevant care organisation to ensure management permission is confirmed before the study begins. Guidance on how to work with sites is provided in the IRAS help section at <https://www.myresearchproject.org.uk/help/hlpnhshscr.aspx>

Final management permission will not be confirmed until after a favourable opinion has been given by this Committee, and all other relevant approvals for the research to begin are in place. Please contact the NHS R&D office at the lead site in the first instance for further guidance.

### **Communication with other bodies**

All correspondence from the REC about the application will be copied to the research sponsor and to the R&D office for Norfolk and Norwich University Hospitals NHS Foundation Trust. It will be your responsibility to ensure that other investigators, research

collaborators and NHS care organisation(s) involved in the study are kept informed of the progress of the review, as necessary.

### **HRA Training**

We are pleased to welcome researchers and R&D staff at our training days – see details at <http://www.hra.nhs.uk/hra-training/>

**16/YH/0485**

**Please quote this number on all correspondence**

Yours sincerely



**Katy Cassidy**

Email: nrescommittee.yorkandhumber-leedseast@nhs.net

Enclosure: [\[Further information about REC membership\]](#)

Copy to: *Ms Tracy Moulton  
Mr Michael Sheridan, Norfolk and Norwich University Hospitals NHS Foundation Trust  
Dr Mark Fisher, University of East Anglia*

# Clinical Trial Protocol

## **FULL/LONG TITLE OF THE STUDY**

Feasibility Study: Acquisition of 3D facial geometry of patients' scheduled for head and neck Radiotherapy Treatment (RT).

## **SHORT STUDY TITLE / ACRONYM**

Acquisition of 3D facial geometry of patients' scheduled for RT



Acquisition of 3D facial geometry of patients'  
scheduled for RT

## **RESEARCH REFERENCE NUMBERS**

IRAS 209119

## **PROTOCOL VERSION NUMBER AND DATE**

Version Number: 3.0 Date: 10.11.16

## **OTHER RESEARCH REFERENCE NUMBERS**

Norfolk & Norwich University Hospital NHS Foundation Trust R&D number: 82-03-16

## **SPONSOR / CO-SPONSORS / JOINT-SPONSORS**

University of East Anglia

## **RESEARCH REFERENCE NUMBERS**

**IRAS Number:** 209119

**SPONSORS Number:**

**FUNDERS Number:**



Acquisition of 3D facial geometry of patients'  
scheduled for RT

## **SIGNATURE PAGE**

The undersigned confirm that the following protocol has been agreed and accepted and that the Chief Investigator agrees to conduct the study in compliance with the approved protocol and will adhere to the principles outlined in the Declaration of Helsinki, the Sponsor's SOPs, and other regulatory requirement.

I agree to ensure that the confidential information contained in this document will not be used for any other purpose other than the evaluation or conduct of the investigation without the prior written consent of the Sponsor

I also confirm that I will make the findings of the study publically available through publication or other dissemination tools without any unnecessary delay and that an honest accurate and transparent account of the study will be given; and that any discrepancies from the study as planned in this protocol will be explained.

### **For and on behalf of the Study Sponsor:**

Signature: ..... Date: ...../...../.....

Name (please print):

Ms Tracy Moulton,

Position:

Contracts Manager, Research Enterprises, UEA.

### **Chief Investigator:**

Signature: ..... Date: ...../...../.....

Name: (please print):

Dr Mark Fisher, School of Computing Sciences, UEA.



**Acquisition of 3D facial geometry of patients' scheduled for RT**

## STUDY SUMMARY

Immobilisation for patients undergoing brain or head and neck radiotherapy is achieved using perspex or thermoplastic devices that require direct moulding to patient anatomy. The mould room visit can be distressing for patients and the shells do not always fit perfectly. In addition the mould room process can be time consuming. With recent developments in 3D printing technologies comes the potential to generate a treatment shell directly from a computer model of a patient. Typically, a patient requiring radiotherapy treatment will have had a CT scan and if a computer model of a shell could be obtained directly from the CT data it would reduce patient distress, reduce visits, obtain a close fitting shell and possibly enable the patient to start their radiotherapy treatment more quickly. However, extracting such a surface remains a challenge and is currently the focus of a PhD research project in the School of Computing Sciences, UEA that aims to develop software capable of creating physical models of treatment shells directly from CT scans. This study will provide patient specific data that will in turn enable algorithms developed as part of the PhD to be quantitatively evaluated and compared, thus allowing us determine if the approach is clinically viable.

Study Title	Feasibility Study: Acquisition of 3D facial geometry of patients' scheduled for head and neck Radiotherapy Treatment (RT).
Internal ref. no. (or short title)	Acquisition of 3D facial geometry of patients' scheduled for RT
Study Design	
Study Participants	Adults (age 18-69 inclusive). Patients undergoing radiotherapy treatment for tumours affecting their head and neck.
Planned Size of Sample (if applicable)	12
Follow up duration (if applicable)	N/A
Planned Study Period	01.12.2016 – 31.01.2017
Research Question/Aim(s)	Can an automatic system generate 3-D printed immobilisation masks having performance comparable to existing head and neck immobilisation systems from a CT scan?  How do 3-D facial models built from CT and laser-scanner data sets compare in terms of accuracy and precision?



Acquisition of 3D facial geometry of patients'  
scheduled for RT

#### **FUNDING AND SUPPORT IN KIND**

<b>FUNDER(S)</b> (Names and contact details of ALL organisations providing funding and/or support in kind for this study)	<b>FINANCIAL AND NON FINANCIAL SUPPORT GIVEN</b>
University of East Anglia	Sponsor, limited Financial Support (PhD Bench Fees)
University Campus Suffolk	Loan of 3D Laser Scanner and technical support
Norfolk and Norwich University Hospital NHS Foundation Trust	Clinical support



Acquisition of 3D facial geometry of patients' scheduled for RT

## KEY STUDY CONTACTS

Chief Investigator	Dr Mark Fisher, Senior Lecturer, School of Computing Sciences, University of East Anglia, Norwich Research Park, Norwich, NR4 7TJ.  Email: <a href="mailto:mark.fisher@uea.ac.uk">mark.fisher@uea.ac.uk</a> Phone: 01603 592671 Fax: 01603 593345
Study Co-ordinator	As Above
Sponsor	Ms Tracy Moulton, Contracts Manager, Research and Enterprise Services, University of East Anglia, Norwich Research Park, Norwich, NR4 7TJ.  Email: <a href="mailto:t.moulton@uea.ac.uk">t.moulton@uea.ac.uk</a> Phone:
Joint-sponsor(s)/co-sponsor(s)	N/A
Funder(s)	University of East Anglia - Support in Kind  University Campus Suffolk - Support in Kind  Norfolk & Norwich University Hospital NHS Trust - Support in Kind
Key Protocol Contributors	Sarah Barber, Trials and Research Radiographer, Norfolk & Norwich University Hospital NHS Foundation Trust, Colney Centre, East Block Level 1, Colney Lane, Norwich, Norfolk, NR4 7UY.  Email: <a href="mailto:sarah.barber@nnuh.nhs.uk">sarah.barber@nnuh.nhs.uk</a>  Michal Sheridan, Research Study & Recruitment Facilitator (General Surgery, Haematology, Oncology, Plastic Surgery & Urology], R&D office, Level 3 East Norfolk & Norwich University Hospitals NHS Foundation Trust Colney Lane, Norwich, NR4 7UY.  Email: <a href="mailto:michael.sheridan@nnuh.nhs.uk">michael.sheridan@nnuh.nhs.uk</a>  Mark Hulse, Senior Lecturer, Radiotherapy and Oncology, Faculty of Health Science, University Campus Suffolk, Ipswich, IP4 1QJ  Email: <a href="mailto:m.hulse@UCS.AC.UK">m.hulse@UCS.AC.UK</a>
Committees	



Acquisition of 3D facial geometry of patients'  
scheduled for RT

## **ROLE OF STUDY SPONSOR AND FUNDER**

The clinical trial is the next step in a programme of research investigating the use of 3D printing of patient immobilisation masks and it is a key component of a research project carried out by Mr Mohammad Ryalat, a PhD student at UEA. UEA are the sponsor. The PhD is supervised by Dr Mark Fisher (Co-supervisor Dr Stephen Laycock), in the School of Computing Sciences, UEA.

Mohammad Ryalat is funded by Al-Balqa' Applied University, 19117 Al-Salt, Jordan

The project is part of an ongoing collaboration between the University of East Anglia, University Campus Suffolk, and Norfolk and Norwich University Hospital NHS Foundation Trust. The initial stages of the project attracted funding from BigC cancer charity (<http://www.big-c.co.uk/>), but this small clinical study has no direct funding, apart from the student's bench fees.

## **ROLES AND RESPONSIBILITIES OF STUDY MANAGEMENT COMMITTEES/GROUPS & INDIVIDUALS**

### **Study Steering Groups**

As this represents a small pilot study, involving only 12 patients, there is no formal management group.

### **Protocol contributors**

Aim: To describe all the contributors to the protocol.

The protocol has been developed in consultation with clinical partners, principally:

Sarah Barber, Trials and Research Radiographer, Norfolk & Norwich University Hospital NHS Foundation Trust, Colney Centre, East Block Level 1, Colney Lane, Norwich, Norfolk, NR4 7UY.

Email: [sarah.barber@nnuh.nhs.uk](mailto:sarah.barber@nnuh.nhs.uk)

Michal Sheridan, Research Study & Recruitment Facilitator [General Surgery, Haematology, Oncology, Plastic Surgery & Urology], R&D office, Level 3 East Norfolk & Norwich University Hospitals NHS Foundation Trust Colney Lane, Norwich, NR4 7UY.

Email: [michael.sheridan@nnuh.nhs.uk](mailto:michael.sheridan@nnuh.nhs.uk)

Alison Vinall, Consultant Physicist, Head of Radiotherapy Physics, Norfolk and Norwich University Hospital NHS Trust. Colney Centre, East Block Level 1, Colney Lane, Norwich, Norfolk, NR4 7UY.

Email: [alison.vinall@nnuh.nhs.uk](mailto:alison.vinall@nnuh.nhs.uk)

Mark Hulse, Senior Lecturer, Radiotherapy and Oncology, Faculty of Health Science, University Campus Suffolk, Ipswich.

Email: [m.hulse@UCS.AC.UK](mailto:m.hulse@UCS.AC.UK)

Tom Roques, Consultant Oncologist, Norfolk and Norwich University Hospital NHS Trust.

Email: [TOM.ROQUES@nnuh.nhs.uk](mailto:TOM.ROQUES@nnuh.nhs.uk)

The sponsor (UEA) will provide indemnity insurance.

### **KEY WORDS:**

External Beam Radiotherapy; Patient Immobilisation; Head and Neck Cancer; 3D Printing



Acquisition of 3D facial geometry of patients'  
scheduled for RT

## LIST of CONTENTS

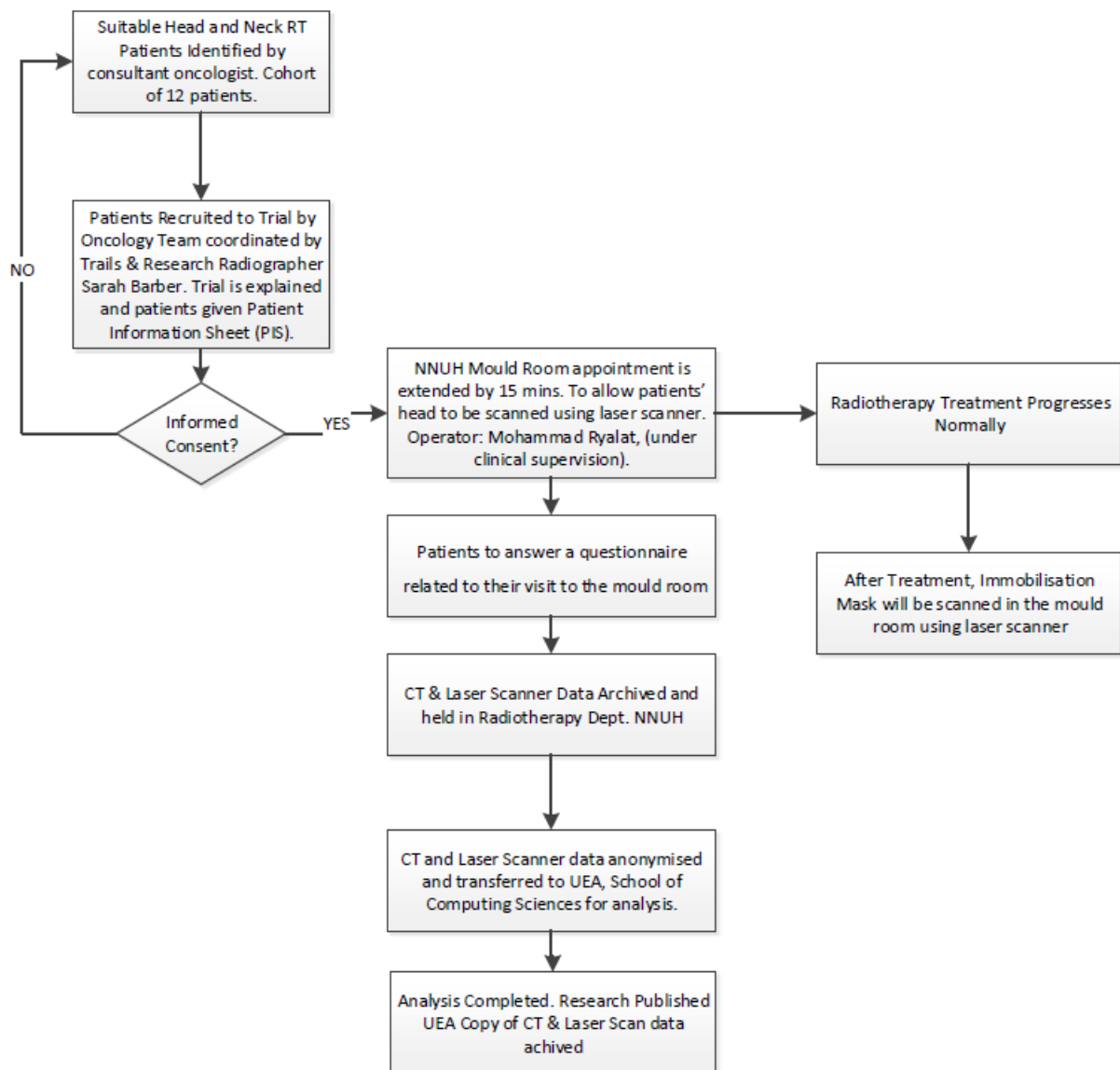
<b>GENERAL INFORMATION</b>	<b>Page No.</b>
TITLE PAGE	1
RESEARCH REFERENCE NUMBERS	2
SIGNATURE PAGE	3
STUDY SUMMARY	4
FUNDING	5
KEY STUDY CONTACTS	6
ROLE OF SPONSOR AND FUNDER	7
ROLES & RESPONSIBILITIES OF STUDY STEERING GROUPS AND INDIVIDUALS	7
LIST of CONTENTS	8
STUDY FLOW CHART	9
SECTION	
1. BACKGROUND	10
2. RATIONALE	10
3. THEORETICAL FRAMEWORK	11
4. RESEARCH QUESTION/AIM(S)	11
5. STUDY DESIGN/METHODS	11
6. STUDY SETTING	12
7. SAMPLE AND RECRUITMENT	12
8. ETHICAL AND REGULATORY COMPLIANCE	14
9. DISSEMINATION POLICY	16
10. REFERENCES	16



Acquisition of 3D facial geometry of patients' scheduled for RT

## STUDY FLOW CHART

Aim: To give readers a schematic overview of the study



Acquisition of 3D facial geometry of patients'  
scheduled for RT

## **STUDY PROTOCOL**

Feasibility Study: Acquisition of 3D facial geometry of patients' scheduled for head and neck Radiotherapy Treatment (RT).

### **1 BACKGROUND**

Aim: To place the study in the context of available evidence.

The background should be supported by appropriate references to published literature on the area of interest:-

Accurately targeting radiation therapy treatment is critical to minimise side-effects and achieve a successful treatment outcome. Immobilisation of patients is essential when treating tumours located in the head and neck to ensure adequate target coverage and to minimise dose to organs at risk (OARs) most notably the eyes, spinal cord and brain stem. To ensure proper immobilisation and treatment reproducibility custom made thermoplastic face masks (beam directional shells) are usually used. These are tailor made for each patient by a specialist team of technicians in the Mould Room. Creating a plaster positive can be rather messy and some patients find it uncomfortable and distressing. An alternative approach that creates a thermo-plastic mesh shell directly can be equally unpleasant. The long-term objective of the project is to use rapid prototyping technology to generate immobilisation shells non-invasively from 3D volumetric data acquired from the CT used for treatment planning.

Patient immobilisation and the modelling of geometrical uncertainty are important topics that are generally well represented in the literature on radiotherapy physics. Research has shown that rigid immobilization could improve targeting in radiotherapy reducing the dose to normal tissue and potentially increasing the dose to the target [Verhey, 2006]. Verhey outlines the challenges of immobilizing patients with tumours in the head and neck due to the flexibility of the neck and the location of the tumour relative to organs at risk (OARs). A variety of immobilisation devices and techniques have been developed to minimise inter and intra fraction target registration error and beam directional shells (BDS) constructed from thermoplastic [Christiansen et al. 2012] are often employed. The processes involved in constructing these devices is a specialised task and can be distressing and inconvenient (e.g. requiring the removal of facial hair) for the patient.

With modern manufacturing and rapid prototyping comes the possibility of determining the shape of the immobilisation device from the CT-scan of the patient directly, alleviating the need for making physical moulds from the patients' head. Earlier work funded by a Big-C research grant demonstrated that masks to fit the contours of a Phantom [Hulse et al., 2012][Laycock et al., 2015][Fisher et al, 2014] could be automatically generated. However, extracting the facial geometry from human subjects is more challenging as the facial tissue is heterogeneous and automatically determining the skin / air interface in CT is challenging. This trial provides data and a framework to evaluate computer algorithms designed to solve this problem, and to compare printed thermoplastic immobilisation solutions.

### **2 RATIONALE**

Aim: To explain why the research questions/aim(s) being addressed are important and why closely related questions are not being covered.

A previous study using a rando-phantom demonstrated the feasibility of printing immobilisation masks but was not able to determine if their performance was comparable to existing systems, because the



**Acquisition of 3D facial geometry of patients'  
scheduled for RT**

task of automatically locating the 'skin' / air boundary is trivial since the phantom is encapsulated in epoxy (i.e. homogeneous material). Facial skin is heterogeneous and it is far more challenging to build automatic systems that address this segmentation task. To develop and evaluate computer algorithms that are able to accurately reconstruct a model of the skin surface from CT imagery we need both CT data and a ground truth model of the patient's facial features. A laser scanner is widely accepted as the most accurate method of obtaining ground truth. A trial involving a small number of patients is needed to provide data to evaluate our algorithms and measure errors between surface models reconstructed from CT and those reconstructed from laser scan data.

### **3 THEORETICAL FRAMEWORK**

Aim: To describe the theoretical framework for the study.

We plan to repeat the study reported by [Fisher et al, 2014] but using human subjects rather than a radio-phantom. Standard metrics will be used to compare the two surface models derived from CT and laser scan data, e.g. [Crum et al. 2006].

### **4 RESEARCH QUESTION/AIM(S)**

Aim: To define the primary research question/aim(s)

#### **4.1 Objectives**

Aim: To clearly define the study's objectives (there may be more than one).

1. To determine if a computer vision system can automatically generate 3-D printed immobilisation masks having performance comparable to existing head and neck immobilisation systems from a CT scan?
2. To compare 3-D models of facial geometry built from CT and laser-scanner data sets in terms of accuracy and precision?
3. To identify if patients find the experience of making a facial mould using plaster of paris distressing and painful?

#### **4.2 Outcome**

Aim: To outline potential broad outcomes for the study which will reflect the research question aim(s).

1. We will place the mask on the patient's face (virtually, using 3-D computer modelling) and report errors measured between the immobilisation shell and the patient's skin. This will enable us to benchmark a range of algorithms used to segment the CT and extract a surface contour that could be used to print a shell.
2. By comparing results of computer modelling with those reported for thermoplastic masks we can determine if the approach is viable.
3. Patient responses to the questionnaire data will provide limited insight into their experience in the mould room.



Acquisition of 3D facial geometry of patients'  
scheduled for RT

## **5 STUDY DESIGN and METHODS of DATA COLLECTION AND DATA ANALYSIS**

Aim: To describe the study design. To clearly describe the data collection methods and outline the roles involved in data collection. To clearly describe the data analysis methods.

A suitable design should be chosen to reflect the aim(s) of the study and the chosen theoretical framework. A suitable design might include ethnography, interviews, focus groups, documents, and so on.

The study aims to evaluate computer algorithms for automatically generating immobilisation masks. . CT data that is required, together with an accurate (ground truth) 3D facial model, for a small cohort of patients. An accurate surface model can be acquired in a few minutes using a hand-held laser scanner. The algorithms are implemented in MATLAB™ a computer language used for prototyping and modelling. This software environment allows us to construct a 3D models derived from the CT and laser scanner data. The CT-derived model will be evaluated and compared with the acquired laser model, using the same programming tool. We have tested this approach with other objects, e.g. Rando-Phantom, 3D printed Geometric Objects etc. using CT data acquired at Ipswich Hospital NHS Trust [Ryalat 2016]. We now need to show the approach works in a clinical setting.

Patients are asked to complete a short questionnaire regarding their experience in the mould room and their responses are recorded on a Likert scale. Since the cohort is only 12 patients the results will not be subject to statistical analysis. The questionnaire results may be used to inform a secondary research question and to motivate a future study involving a larger number of participants.

## **6 STUDY SETTING**

- Aim: To state where the data will be collected, explain what activities will take place in that site, and justify the choice of site and any special requirements.

Twelve patients undergoing radiotherapy treatment for head and neck cancer at the Norfolk and Norwich University Hospital (NNUH) NHS Foundation Trust will be recruited by the oncology team. Their treatment will progress normally and the CT planning data will be archived and anonymised and copied to researchers at UEA. Additional data, captured by a hand held laser scanner will be gathered by Mohammad Ryalat. This will take place at NNUH (under clinical supervision). The laser scanning is non-intrusive and the scan can be completed in approximately 15 minutes. The scanning process involves the patient sitting in a chair while a researcher performs the scan. As a precautionary measure we require the patient to wear an eye mask as although the scanner is CE marked and completely safe patients' may have read reports in the press of eye damage resulting from the illegal use of higher powered lasers. The process can be completed in stages (e.g. 3 x 5 minutes) with a break of 2-3 minutes between each session. The laser scanner will then be moved around the patient to obtain a set of 3D points forming the surface of the patient's head.

Patients will follow a normal treatment pathway, using an immobilisation shell manufactured normally (i.e. 'soft-drape' or 'hard-shell'). Once the mask has been manufactured (by mould room technicians) it will be scanned (in the mould room) using the laser scanner.

## **7 SAMPLE AND RECRUITMENT**

### **7.1 Eligibility Criteria**

Aim: To define the study population/sample



Acquisition of 3D facial geometry of patients' scheduled for RT

12 subjects will be selected by NNUH consultant oncologists.

### **7.1.1 Inclusion criteria**

12 Patients undergoing radiotherapy treatment for tumours affecting their head and neck at NNUH.

Age - 18-69 years inclusive. Ethnicity and Socio economic grouping are not critical factors.

### **7.1.2 Exclusion criteria**

Patients who are not able to give written informed consent (in English) and those who are outside of age range 18-69.

## **7.2 Sampling**

Aim: To clearly explain and justify the detail of sampling in terms of volume and technique.

### **7.2.1 Size of sample**

Aim: to explain the rationale behind the size of the sample.

Total sample size is 12 subjects. The sample size was decided considering this is the first clinical study addressing 3D printed fixations for radiotherapy. The sample size (12) is considered as sufficient for a pilot feasibility study (i.e. suitable for inclusion in a PhD Thesis). The CT data sets comprise a far greater (in the order of 1000's) number of voxels indicative of air/skin interface.

### **7.2.2 Sampling technique**

Aim: To describe the selection of participants.

This section should detail the methods of selection used for example:

- At random, snowball, convenience sampling, purposive sampling?
- Where has the sample been derived from?
- What is the rationale for this sampling strategy? The rationale should reflect the methodological and theoretical framework for the study.

The oncology department, Norfolk and Norwich University Hospital will identify patients who are planned to have head and neck radiotherapy.

## **7.3 Recruitment**

Aim: To describe how participants are identified and recruited.



**Acquisition of 3D facial geometry of patients'  
scheduled for RT**

This section should give details of the participant eligibility screening process for the project including methods of identifying eligible participants/sample.

### **7.3.1 Sample identification**

The oncology department, liaising with consultant oncologists at Norfolk and Norwich University Hospital will identify patients who are planned to have head and neck radiotherapy. The identification of potential participants does not involve reviewing or screening the identifiable personal information of patients, service users or any other person. No participants will be recruited neither by publicity through posters, leaflets, adverts or websites nor by Patient Identification Centres (PICs). Research participants will not receive any payments, reimbursement of expenses or any other benefits or incentives for taking part in this research.

### **7.2.2 Consent**

Participants' oncology consultant will identify the participants at their initial meeting. Trials and research radiographer, Sarah Barber will discuss with them about the nature and objectives of the study and possible risks associated with their participation. Patients will be informed of the study and given the Patient Information Sheet. The research radiographer will follow up on any patients who are willing to take part in the study, answer any questions and obtain informed consent. Potential participants will be given a minimum of 7 days to decide whether or not to take part and we will not recruit any participants who are involved in current research or have recently been involved in any research prior to recruitment. The patient information sheet explains that participants are free to withdraw at any time without giving any reason and without their medical care or legal rights being affected.

## **8 ETHICAL AND REGULATORY CONSIDERATIONS**

**Aim:** To explain how the research question/aim(s) and design/methods fit into the ethical and regulatory framework. A clear explanation of the risk and benefits to the participants should be included as well as addressing any specific needs/considerations of the sample. State how the data collection methods used uphold the dignity of the participants.

The protocol should also include a justification of how the protocol is in line with relevant legislation.

### **8.1 Assessment and management of risk**

**Aim:** To describe a risk analysis plus risk management if the researcher were to come into information which had safeguarding implications.

There are no clinical risks associated with this study. The laser used by the laser scanner is completely safe. Since we aim to capture facial features there is risk that the data may compromise patient anonymity. To mitigate this possibility and distinguishing features which appear in publications will be redacted.

### **8.2 Research Ethics Committee (REC) review & reports**



**Acquisition of 3D facial geometry of patients'  
scheduled for RT**

Aim: to demonstrate that the study will receive ethical review and approval from the necessary body  
Ethical approval via IRAS will be sought before the trial commences.

**8.3 Peer review**

Aim: to describe the peer review process for the study which should be instigated and/or approved by the sponsor.

Publications arising from the preclinical research have been subject to peer review. Some reviewers identified the need for a clinical study, and their comments motivate this trial.

**8.4 Patient & Public Involvement**

Aim: to describe the involvement of the Public in the research

Anecdotal evidence from patients (reported by Macmillan Cancer Support) suggests they find the mould room experience rather unpleasant and uncomfortable.

**8.5 Regulatory Compliance**

Aim: to demonstrate that the study will comply with regulations

NNUH R&D management committee has approved the study.

**8.6 Protocol compliance**

Aim: to demonstrate how protocol compliance will be managed

Protocol deviations represent a low risk and do not affect the patients' treatment.

**8.7 Data protection and patient confidentiality**

Aim: To describe how patient confidentiality will be maintained and how the study is compliant with the requirements of the Data Protection Act 1998

All investigators and study site staff will comply with the requirements of the Data Protection Act 1998 with regards to the collection, storage, processing and disclosure of personal information and will uphold the Act's core principles. Data will be stored on NHS hospital computers in the Colney centre. Pseudonymised data will then be encrypted and transferred to university computers at UEA for data analysis. The stored data complies with UEA's Information Security Policy, which includes security standards, procedures and guidelines developed in accordance with ISO27001. The physical security arrangements for storage of personal data during the study will be under the UEA General Information Security Policy, V4.2. Each patient will be given a unique study identifier. A key to link the data to the patient will be held separately in a filing cabinet in the locked office of Mr Tom Rogues, NNUH Foundation Trust, Norwich, only accessible to Mr Rogues. Only NHS clinical staff will have access to personal data. Research monitors from the University of East Anglia may need to see data for the study to ensure best practice is maintained in line with University policy. Data will be made available to the institutional review board (IRB) if necessary. Pseudonymised data generated by the study will



**Acquisition of 3D facial geometry of patients'  
scheduled for RT**

be analysed by researchers in the School of Computing Sciences, UEA. Ms Sarah Barber (Trials & Research Radiographer at Norfolk & Norwich University Hospital NHS Foundation Trust) will have control of and act as the custodian for the data generated by the study. The data held at UEA will be destroyed 12 months after the end of the study. A data archive (DVD) will be held at Colney Centre, NNUH for 10 years.

**8.8 Indemnity**

Aim: to fully describe indemnity arrangements for the study

The sponsor (UEA) is responsible for insurance and indemnity

**8.9 Amendments**

Aim: to describe the process for dealing with amendments

Any necessary amendments will be discussed and agreed with

Michal Sheridan, Research Study & Recruitment Facilitator (General Surgery, Haematology, Oncology, Plastic Surgery & Urology], R&D office, Level 3 East Norfolk & Norwich University Hospitals NHS Foundation Trust Colney Lane, Norwich, NR4 7UY.

and we will seek further ethical approvals is necessary.

**8.10 Access to the final study dataset**

Aim: to describe who will have access to the final dataset

NNUH Colney Centre will have access to the final dataset.

**9 DISSEMINATION POLICY**

**9.1 Dissemination policy**

Aim: to describe the dissemination policy for the study

NNUH Colney Centre owns the data captured by the trial and will be acknowledged in publications arising from the study. The study will be reported in Mohammad Ryalat's PhD Thesis, planned submission date: September 2017. The thesis will act as the final study report. Results will also be presented at appropriate UK conferences and an article will appear in a relevant scientific journal.

**9.2 Authorship eligibility guidelines and any intended use of professional writers**

Aim: to describe who will be granted authorship on the final study report

Mohammad Ryalat (See 9.1).

**10 REFERENCES**

[Christiansen et al. 2012] Christiansen, R., Hansen, C., Nielsen, T., Johansen, J. and Brink, C. Comparison of Three Immobilisation Systems for Radiation Therapy in Head and Neck Cancer. Radiotherapy & Oncology, 103, S106, 2012. [http://dx.doi.org/10.1016/S0167-8140\(12\)70609-6](http://dx.doi.org/10.1016/S0167-8140(12)70609-6)



**Acquisition of 3D facial geometry of patients'  
scheduled for RT**

[Crum et al. 2006] Crum, W., Camara, O., Hill, D., Nov. 2006. Generalized overlap measures for evaluation and validation in medical image analysis. *Medical Imaging, IEEE Transactions on* 25 (11), 1451–1461.

[Fisher et al, 2014] Fisher, M., Applegate, C., Ryalat, M., Laycock, S., Hulse, M., Emmens, D., Bell, D. (2014) Evaluation of 3D Printed Immobilisation Shells for Head and Neck IMRT in *Open Journal of Radiology* 04. pp. 322-328, 2014. <http://dx.doi.org/10.4236/ojrad.2014.44042>

[Hulse et. al, 2012] M. Hulse, M. Tam, S. Isherwood, C. Scrase, S. Laycock, D. Mortimore, J. Patman, S. Short and D. Bell, Production of 3-D printer-generated radiotherapy shells using DICOM CT, MRI or 3-D surface laser scan – Acquired STL files: Preclinical feasibility studies, 8th NCRI Cancer Conference, Liverpool, November 2012.

[Laycock et al., 2015] Laycock, S. D., Hulse, M., Scrase, C. D., Tam, M. D., Isherwood, S., Mortimore, D. B., Emmens, D., Patman, J., Short, S. C., Bell, G. D. (2015) Towards the production of radiotherapy treatment shells on 3D printers using data derived from DICOM CT and MRI: preclinical feasibility studies in *Journal of Radiotherapy in Practice* 14. pp. 92-98).

[Ryalat 2016] Mohammad Hashem Ryalat, Daniel Emmens, Mark Hulse, Duncan Bell, Zainab Al-Rahamneh, Stephen Laycock, and Mark Fisher (2016). Evaluation of Particle Swarm Optimisation for Medical Image Segmentation, In J. Swiatek and J.M. Tomczak (eds.), *Advances in Systems Science, Advances in Intelligent Systems and Computing* 539, DOI 10.1007/978-3-319-48944-5\_6

[Verhey, 2006] Verhey, L.J., Immobilizing and positioning patients for radiotherapy, *Seminars in Radiation Oncology*, 2006.



# **Participant Information Sheet (PIS)**

**Clinical Trial: Acquisition of 3-D facial geometry of patients' scheduled for head and neck RT.**

---

**PARTICIPANT INFORMATION SHEET**

---

The School of Computing Sciences, UEA in collaboration with University Campus Suffolk and Norfolk and Norwich University Hospital NHS Trust are investigating an alternative non-invasive technique for manufacturing immobilisation masks used during radiotherapy treatment. Methods for creating computer models for the mask are being investigated as part of a PhD at UEA and we seek your cooperation to help the student complete his research.

You have been invited to participate in this study because you have been prescribed a course of radiotherapy treatment that requires an immobilisation mask. The manufacture and fitting of the mask will involve a visit to the Mould Room. It would be helpful if you would tell us something about your experience of this process by completing a short questionnaire after your visit.

This study aims to evaluate a new approach to manufacturing immobilization masks but the new masks will not be used in your treatment. If you decide not to take part in the study then your treatment will progress normally. However, if you agree to take part in the trial, further measurements of your head will be made using a hand held laser scanner. This procedure is non-invasive and completely safe but it will take about 15 minutes of your time.

We hope to develop a process that allows the immobilization mask to be manufactured by a 3-D printer using a model constructed from your CT scan. The digital information we collect will allow us to build a digital 3-D model of your head that in turn will allow us to assess the accuracy of the model built from CT. We do not need to physically manufacture a printed immobilisation mask to assess the accuracy of the model as we can do this using a computer simulation. The information we collect will be stored and analysed by the School of Computing Sciences, UEA and results of the analysis will be published in a PhD thesis and presented at relevant conferences and in journals. If successful, we hope that in the future, our non-invasive approach to manufacturing immobilisation masks may be adopted within the NHS and plaster of Paris moulds will no longer be needed.

To ensure patient confidentiality, the data is anonymised and only a fragment of the model will be included in any published work arising from the study.

Your participation in this study is entirely voluntary and will not affect your treatment outcome. Anonymised data generated by the study will be analysed by researchers in the School of Computing Sciences, UEA. Ms Sarah Barber (Trials & Research Radiographer at Norfolk & Norwich University Hospital NHS Foundation Trust) will manage the anonymization process and Dr Mark Fisher, School of Computing sciences, UEA will act as custodian for the data generated by the study. The data held at UEA will be destroyed after a period of 10 years. All information which is collected about you during the course of the study will be kept within the hospital. Any information about you which leaves the hospital will have your name and address removed so that you cannot be recognised. Measurements gathered as part of this study will enable approaches developed as part of the PhD to be quantitatively evaluated and compared, thus allowing researchers determine if the approach is clinically viable. Your treatment will progress normally and so there is very little risk involved in participating in the study. However, if you have any concern about any aspect of this study, you should ask to speak to Ms Sarah Barber. She will do her best to answer your questions. You may withdraw from the study at any time without affecting your planned treatment and any data or models collected as part of the study will be destroyed.

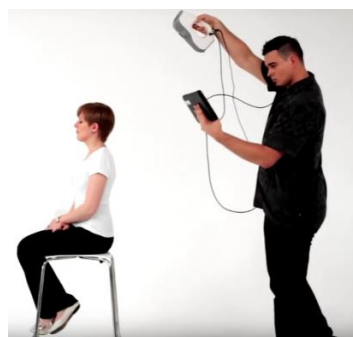
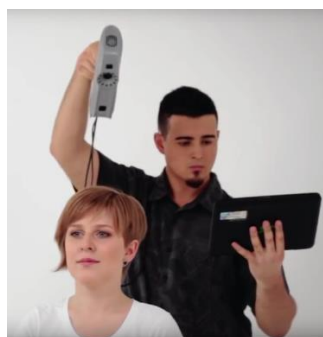
Radiotherapy treatment is part of your routine care. If you take part in this study you will not undergo any additional radiotherapy sessions and the radiotherapy dose you receive will not be affected. Radiotherapy treatment involves the use of ionising radiation to form images of your body, kill cancerous cells and provide your doctor with other clinical information. However, ionising radiation can cause cell damage that may, after many years or decades, turn cancerous. The chances of this happening to you are the same whether you take part in this study or not.

### Laser-scanning session

After completing the questionnaire we will ask you to sit in an office chair and the PhD student, supervised by a nurse or radiographer, will be scan your head using a hand held laser scanner, held at a distance of 20-60 cm, as illustrated below. The procedure will take about 15 minutes and during this time you will be asked to wear an eye mask. The procedure is non-invasive, try to relax during the session and feel free to ask for breaks at any time.

### Is the laser scanner safe?

The low power laser used in the scanner is no more powerful than a laser pointer. The laser machine is CE marked which means that the machine complies with the essential requirements of the relevant European health, safety and environmental protection legislation. However, there is a small risk of eye damage if one looks directly at a laser and for this reason we will cover your eyes while being scanned.



If you have any concerns about participating in the project, require any further information about the project, or would like to receive a summary of the results of the research please contact either:

Dr Mark Fisher, School of Computing Sciences, UEA, Norwich, NR4 7TJ.  
Tel: 01603 592671 Email: [mark.fisher@uea.ac.uk](mailto:mark.fisher@uea.ac.uk)

Ms Sarah Barber, Trials & Research Radiographer at Norfolk & Norwich University Hospital NHS Foundation Trust. Colney Centre, East Block Level 1, Colney Lane, Norwich, Norfolk, NR4 7UY.  
Tel: 01603 646736 Email: [sarah.barber@nnuh.nhs.uk](mailto:sarah.barber@nnuh.nhs.uk)

Thank you.

# **Consent Form**

**Project Lead: Mark Fisher**  
**School of Computing Sciences**  
**University of East Anglia**  
**Norwich Research Park,**  
**Norwich, NR4 7TJ**

Centre Number:

Study Number:

Patient Identification Number for this trial:

---

**CONSENT FORM**

---

Title of Project: **Construction of 3D-Printed Immobilisation Masks for Use in Radiotherapy Treatment of Head-and-Neck Cancers.**

Name of Researcher: **Mohammad Ryalat**

**Initial Box**

1. I confirm that I have read and understand the information sheet dated 10.11.16 (version 3.0) for the above study. I have had the opportunity to consider the information, ask questions and have had these answered satisfactorily.

**Initial Box**

2. I understand that my participation is voluntary and that I am free to withdraw at any time without giving any reason, without my medical care or legal rights being affected.

**Initial Box**

3. I understand that relevant sections of my medical notes and data collected during the study may be looked at by individuals from the NHS Trust, from regulatory authorities or from The University of East Anglia, where it is relevant to my taking part in this research. I give permission for these individuals to have access to my records.

**Initial Box**

4. I agree to take part in the above study.



---

**Name of Participant  
in full**

---

**Date in full**

---

**Signature**

---

**Name of Person taking  
consent in full, as per  
study Delegation Log**

---

**Date in full**

---

**Signature**

**1 for patient; 1 for researcher; 1 to be kept with hospital notes**

# Good Clinical Practice Certificate (GCP)

# CERTIFICATE of ACHIEVEMENT

This is to certify that

**Mohammad Ryalat**

has completed the course

Introduction to Good Clinical Practice eLearning (Secondary Care)

June 29, 2016

**Modules completed:**

Introduction to Research in the NHS

Good Clinical Practice and Standards in Research

Study Set Up and Responsibilities

The Process of Informed Consent

Data Collection and Documentation

Safety Reporting

*This course is worth 4 CPD credits*



# **Letter of Access for Research**



Mohammad Hashem Ryalat  
School of Computing Sciences  
University of East Anglia  
Norwich Research Park  
Norwich  
NR4 7TJ

23/01/2017

Research and Development Department  
Level 3, East Block, Room 032  
Norfolk & Norwich University Hospitals NHS Foundation Trust  
Colney Lane  
Norwich  
NR4 7UY  
Direct Dial: 01603 597305  
e-mail: [rdoffice@nnuh.nhs.uk](mailto:rdoffice@nnuh.nhs.uk)  
Website: [www.nnuh.nhs.uk](http://www.nnuh.nhs.uk)

Dear Mr Ryalat,

**Re: 209119 - Feasibility Study: Acquisition of 3D facial geometry of patients' scheduled for head and neck Radiotherapy Treatment (RT).**

**Letter of access for research**

This letter confirms your right of access to conduct research through Norfolk & Norwich University Hospitals NHS Foundation Trust for the purpose and on the terms and conditions set out below. This right of access commences on **24<sup>th</sup> January 2017** and ends on **31<sup>st</sup> December 2017** unless terminated earlier in accordance with the clauses below.

You have a right of access to conduct such research as confirmed in writing in the letter of permission for research from this NHS organisation. Please note that you cannot start the research until the Principal Investigator for the research project has received a letter from us giving permission to conduct the project.

The information supplied about your role in research at Norfolk & Norwich University Hospitals NHS Foundation Trust has been reviewed and you do not require an honorary research contract with this NHS organisation. We are satisfied that such pre-engagement checks as we consider necessary have been carried out.

You are considered to be a legal visitor to Norfolk & Norwich University Hospitals NHS Foundation Trust premises. You are not entitled to any form of payment or access to other benefits provided by this NHS organisation to employees and this letter does not give rise to any other relationship between you and this NHS organisation, in particular that of an employee.

While undertaking research through Norfolk & Norwich University Hospitals NHS Foundation Trust, you will remain accountable to your employer the **University of East Anglia** but you are required to follow the reasonable instructions of **Alison Vinall** in this NHS organisation or those given on her behalf in relation to the terms of this right of access.

Where any third party claim is made, whether or not legal proceedings are issued, arising out of or in connection with your right of access, you are required to co-operate fully with any investigation by this NHS organisation in connection with any such claim and to give all such assistance as may reasonably be required regarding the conduct of any legal proceedings.

You must act in accordance with Norfolk & Norwich University Hospitals NHS Foundation Trust policies and procedures, which are available to you upon request, and the Research Governance Framework.

You are required to co-operate with Norfolk & Norwich University Hospitals NHS Foundation Trust in discharging its duties under the Health and Safety at Work Act 1974 and other health and safety legislation and to take reasonable care for the health and safety of yourself and others while on Norfolk

& Norwich University Hospitals NHS Foundation Trust premises. You must observe the same standards of care and propriety in dealing with patients, staff, visitors, equipment and premises as is expected of any other contract holder and you must act appropriately, responsibly and professionally at all times.

You are required to ensure that all information regarding patients or staff remains secure and *strictly confidential* at all times. You must ensure that you understand and comply with the requirements of the NHS Confidentiality Code of Practice ([https://www.gov.uk/government/uploads/system/uploads/attachment\\_data/file/200146/Confidentiality%20-%20NHS%20Code%20of%20Practice.pdf](https://www.gov.uk/government/uploads/system/uploads/attachment_data/file/200146/Confidentiality%20-%20NHS%20Code%20of%20Practice.pdf)) and the Data Protection Act 1998. Furthermore you should be aware that under the Act, unauthorised disclosure of information is an offence and such disclosures may lead to prosecution.

You should ensure that, where you are issued with an identity or security card, a bleep number, email or library account, keys or protective clothing, these are returned upon termination of this arrangement. Please also ensure that while on the premises you wear your ID badge at all times, or are able to prove your identity if challenged. Please note that this NHS organisation accepts no responsibility for damage to or loss of personal property.

We may terminate your right to attend at any time either by giving seven days' written notice to you or immediately without any notice if you are in breach of any of the terms or conditions described in this letter or if you commit any act that we reasonably consider to amount to serious misconduct or to be disruptive and/or prejudicial to the interests and/or business of this NHS organisation or if you are convicted of any criminal offence. As from 26 July 2010, your HEI employer may initiate your Independent Safeguarding Authority (IISA) registration (where applicable), and thereafter, will continue to monitor your ISA registration status via the on-line ISA service. Should you cease to be ISA-registered, this letter of access is immediately terminated. Your employer will immediately withdraw you from undertaking this or any other regulated activity. You **MUST** stop undertaking any regulated activity.

Your substantive employer is responsible for your conduct during this research project and may in the circumstances described above instigate disciplinary action against you.

Norfolk & Norwich University Hospitals NHS Foundation Trust will not indemnify you against any liability incurred as a result of any breach of confidentiality or breach of the Data Protection Act 1998. Any breach of the Data Protection Act 1998 may result in legal action against you and/or your substantive employer.

If your current role or involvement in research changes, or any of the information provided in your Research Passport changes, you must inform your employer through their normal procedures. You must also inform your nominated manager in this NHS organisation.

Yours sincerely



Julie Dawson  
Research Services Manager

cc: HR department of the substantive employer